The Smoothness Constraint in Spatially Informed Minimum Norm Approaches for the Reconstruction of Neuroelectromagnetic Sources

The Smoothness Constraint in Spatially Informed Minimum Norm Approaches for the Reconstruction of Neuroelectromagnetic Sources

Dissertation

zur Erlangung des akademischen Grades

Doktoringenieur (Dr.-Ing.)

vorgelegt der Fakultät für Informatik und Automatisierung
der Technischen Universität Ilmenau

von Dipl.-Ing. (FH) Mirco Fuchs
geboren am 21. Januar 1982 in Leipzig

1. Gutachter: Univ.-Prof. Dr.-Ing. habil. Jens Haueisen
(Technische Universität Ilmenau)

2. Gutachter: PD Dr.-Ing. habil. Thomas R. Knösche
(Max-Planck-Institut für Kognitions- und Neurowissenschaften Leipzig)

3. Gutachter: Prof. Dr. rer. nat. habil. Christoph Braun
(Universitätsklinikum Tübingen)

Tag der Einreichung: 2. Dezember 2016

Tag der wissenschaftlichen Aussprache: 1. August 2017

urn:nbn:de:gbv:ilm1-2017000312

Abstract

Neuronal processes in the brain give rise to electromagnetic signals that can be measured by means of EEG/MEG. However, the ambiguity of the bioelectromagnetic inverse problem limits the localizability of the underlying generators. The solution of the inverse problem requires additional assumptions. A very common method is to model brain activity using distributed sources. In that case, a large number of equivalent current dipoles covers the volume in which activity is expected (usually the cortex). Reconstruction methods on the basis of distributed sources allow the incorporation of additional information on the functional similarity between sources (i.e. information on the spatial structure of brain activity). This kind of information can be derived from prior knowledge, for instance from the subdivision of the cortex into distinct functional areas (i.e. parcellations) or from fMRI.

The work presented here is based on a previously published method that combines a general smoothness constraint with priori knowledge on the (binary) similarity between neighboring sources by means of a 2$^{\text{nd}}$ order spatial derivative operator (PatchLORETA). The first part of this work addressed the systematic evaluation on how the integration of prior knowledge into the derivative operator affects the estimation of *a priori* assumed source covariances. It turned out that the method introduced incorrect prior assumptions. Consequently, some extensions were proposed to generalize the approach. These are an additional normalization operator and an additional parameter to encode arbitrary mutual similarity between neighbors. Moreover, a technique was developed to adjust the correlation structure according to a desired smoothness level. The final method (called informed LORETA) is particularly suited for the use of functio-anatomical boundaries.

The second part addressed the systematic evaluation of the question whether the use of prior knowledge (derived from parcellations) can improve source localization. This was done using Monte-Carlo simulations. A main focus was the evaluation on how potential errors / uncertainties in the prior knowledge influence the reconstruction performance. Finally, informed LORETA was used for the localization of auditory evoked potentials from experimental data. It turned out that spatially informed methods provide very plausible reconstruction results.

Zusammenfassung

EEG/MEG ermöglicht die Messung elektrischer Gehirnaktivität, die durch neuronale Prozesse im Gehirn hervorgerufen wird. Die Lokalisierbarkeit der Aktivität ist aufgrund der fehlenden Eindeutigkeit des bioelektromagnetischen inversen Problems allerdings eingeschränkt. Zur Lösung sind Zusatzannahmen erforderlich. Eine Klasse von Lösungsverfahren basiert auf der Verwendung verteilter Quellenmodelle. Dabei werden im gesamten wahrscheinlichen Quellraum (typischerweise im Cortex) Stromdipole modelliert, um schließlich eine räumliche Verteilung der Dipolstärken zu bestimmen. Dieser Ansatz erlaubt es, Zusatzannahmen über die funktionelle Ähnlichkeit zwischen den Dipolen (d.h. über die räumliche Strukturierung von Gehirnaktivität) zu formulieren. Derartiges Wissen kann zum Beispiel aus der Unterteilung des Cortex in funktional unterschiedliche Areale (Parzellierungen) oder mittels fMRI gewonnen werden.

Diese Arbeit befasst sich mit einer bereits zuvor publizierten Technik, bei der Zusatzwissen über die funktionelle Ähnlichkeit benachbarter Quellen in einen Differentialoperator integriert und mit einer allgemeinen Glattheitsannahme kombiniert wird (*PatchLORETA*). Im ersten Teil dieser Arbeit wurde systematisch untersucht, wie sich eine derartige Integration auf die tatsächliche Korrelationsstruktur auswirkt. Dabei wurden verschiedene Probleme identifiziert, die zu fehlerhaften *a priori* Annahmen führen. Aus diesem Grund wurde die Methode um einen Normalisierungsoperator, lokale Ähnlichkeitsparameter, und ein Verfahren zur Einstellung einer definierten Glattheitsannahme erweitert. Im Ergebnis liegt ein als *informed LORETA* bezeichnetes Verfahren vor, in das grundsätzlich beliebige Ähnlichkeitsinformation eingebunden werden kann. Es ist besonders zur Integration funktio-anatomischer Grenzen geeignet.

Im zweiten Teil dieser Arbeit wurde die Nutzbarkeit informierter linearer inverser Verfahren mithilfe von Monte-Carlo-Simulationen und unter Verwendung von Parzellierungen systematisch untersucht. Im Fokus stand dabei vor allem der Einfluss möglicher Fehler im Zusatzwissen auf die Rekonstruktionsqualität. Abschließend wurde *informed LORETA* zur Lokalisierung auditorisch evozierter Aktivität aus EEG/MEG-Daten eingesetzt. Dabei konnte gezeigt werden, dass die Plausibilität der rekonstruierten Quellenverteilung durch die Integration von Zusatzwissen deutlich gesteigert werden kann.

Acknowledgement

"Experience is what you get when you didn't get what you wanted.", Randy Pausch

. . . and, for sure, I gained a lot of experience throughout this long-term project. It was an exciting time in which I was often faced with new challenges in both my life and work. Therefore, it was sometimes difficult to sustain the motivation to complete this project. Now, however, I feel very satisfied that I am finally able to present the results that I achieved. This would not have been possible without the support of many people, to whom I would like to express by deepest gratitude.

I would like to thank Prof. Jens Haueisen for accepting me as a PhD student. He acted as my supervisor at the Ilmenau University of Technology and helped me to navigate the administrative requirements of that institution. I am thankful to Dr. Thomas Knösche and Dr. Burkhard Maeß, my mentors and supervisors at the Max Planck Institute for Human Cognitive and Brain Sciences, who had the idea for this project. Thank you for extensive discussions, your support, encouragement and excellent guidance but also constructive criticism - not only regarding this thesis, but also for the collaboration in other projects.

A thank also goes to my former colleagues in the MEG group in Bennewitz, in particular to Dr. Margit Schönherr, Hermann Sonntag, and Yvonne Wolff-Rosier. I always enjoyed the warm and constructive working atmosphere, and I am thankful for a lot of interesting discussion that we had.

I am very grateful to Prof. Matthias Sturm, who not only supported me all the way through my studies at the Leipzig University of Applied Sciences but also thereafter - until now. I would not have had the opportunity to pursue a doctorate without him. He always encouraged and motivated me to finish this project. Thanks also to Dr. Gerold Bausch. It is great to know that other people not only pursue the same goals, but also share the same spirit and enthusiasm. It is a pleasure for me to work by your sides and to navigate our research group - the Laboratory for Biosignal Processing - through fairly rough terrain. I am very looking forward to exciting challenges that lie ahead of us.

I would also like to thank my colleagues at the LaBP group, in particular Fabian Schrumpf. Thank you for a lot of lively and inspiring conversations.

I am thankful to my family who always encouraged me to pursue my goals. Special thanks go to my parents who supported me in various ways. I would also like to thank my cousin Heike who read the final version of my manuscript and supported me with valuable tips and helpful remarks.

My deepest thanks go to Jana, my beloved girlfriend, and our wonderful children Nicklas and Jasmin. You opened my eyes for the really valuable things in life. Thank you for being there and enriching my life.

– Mirco Fuchs
Leipzig, November 2016

Contents

Symbols and Abbreviations

$\vec{B}$	Vector of magnetic flux density
C_d	Data covariance matrix ($n \times n$)
C_ϵ	Noise covariance matrix ($n \times n$)
C_q	Source covariance matrix ($m \times m$)
$\vec{d}, d$	n element data vector
$\vec{J}$	Electric current density
$\vec{l}_i$	Leadfield vector of dipole i
L	Leadfield matrix ($n \times m$), Leadfield
m	Number of source dipoles (ECDs)
n	Number of channels (sensors)
p_{ij}	Similarity between source i and j
$\vec{q}, q$	m element dipole magnitude vector
$\vec{Q}$	Dipole moment vector
r_{ij}	Euclidian distance between source i and j
$\vec{r}$	Position of sensor (measurement)
$\vec{r}'$	Position of source
R_q	Normalized source covariance matrix ($m \times m$)
W	Source weighting matrix ($m \times m$)
α	Tikhonov regularization parameter
ϵ	n element measurement noise vector
Θ_i	Set of direct grid neighbours of dipole i
$\lvert\Theta_i\rvert$	Number of direct grid neighbours of dipole i
λ_B	Regularization parameter for the Laplace operator
μ	Magnetic permeability
Ξ_a	Set of activated sources in a reference source distribution q_{ref}
Ξ_i	Subset of all inactive sources in a reference source distribution q_{ref}
σ	Electric conductivity
σ_d^2	Data variance (including noise)
σ_{ref}^2	Signal variance (noise-free data from reference activity)
σ_ϵ^2	Noise variance in sensor space
σ_q^2	Mean source variance, regularization parameter
Φ	Electric scalar potential

Φ_{ij}	Solid angle spanned by source i with neighbour j
Ω	Diagonal matrix for depth weighting / leadfield normalization
AUC	Area under curve
BA	Brodmann area
BEM	Boundary element method
CAV	Cluster activity variability
COR	Correlation coefficient
CSF	Cerebrospinal fluid
DE	Displacement error
ECD	Equivalent current dipole
EEG	Electroencephalography
FACE	Functional area constrained estimator
FEM	Finite element model
fMRI	Functional magnetic resonance imaging
GOF	Goodness of fit
LORETA	Low resolution electromagnetic tomography
MAP	Maximum a posteriori
MC	Monte-Carlo (simulations)
MEG	Magnetoencephalography
MN	Minimum norm
MRI	Magnetic resonance imaging
PAF	Patch activation frequency
PDF	Probability density function
PET	Positron emission tomography
PRF	Patch reconstruction frequency
PRFI	Patch reconstruction frequency index
PSF	Point spread function
RE	Relative energy
ROC	Receiver operating characteristic
SNR	Signal-to-noise ratio
WMN	Weighted minimum norm

1 Introduction

1.1 General Introduction and Problem Statement

The functioning of the brain is based on biochemical and bioelectrical processes, which are the basis for information transfer between neural cells. These processes generate electrical currents. It can be distinguished between so called primary currents, occurring in the close vicinity of electrically active neurons, and secondary currents far away from active regions, flowing through the different tissues in the whole head. It would be great if a direct image of primary currents could be drawn because this would allow to map brain functions to real neuronal processes.

The detection of primary currents using imaging techniques, such as positron emission tomography (PET) and functional magnetic resonance imaging (fMRI), is not possible. They utilize effects of metabolism and, therefore, are not sensitive to any electrical activity. Moreover, it is usually not possible to sense these currents directly inside the brain. Thus, the only practical solution is to detect their electromagnetic effects on the head surface (skin) using electroencephalography (EEG) and outside the head using magnetoencephalography (MEG) (Andrä and Nowak, 2006).

EEG is based on measuring potential differences between electrodes. These differences occur due to currents, which are driven by neuronal activity, flowing through the different tissues of the head, including skull and skin. Thus, EEG highly depends on the volume conducting properties. In contrast, MEG is sensitive to the magnetic field generated by the currents inside the head. While the magnetic field itself is not prone to volume conducting properties, the measured signals are superpositions of fields generated by primary and secondary currents. Hence, neither EEG nor MEG measure electromagnetic effects which are exclusively related to primary currents.

The reconstruction of electrical brain activity from EEG and MEG measurements is referred to as the bioelectromagnetic inverse problem. Due to its ambiguity, i.e. the fact that an infinite number of different source configurations can explain the same EEG/MEG signals (von Helmholtz, 1853), a unique solution can only be found by defining additional assumptions about the sources. Several components are required to tackle the inverse problem. First, it is necessary to define a source model that already reflects fundamental assumptions about the brain activity, for example, concerning the number of sources (see Sec. 2.2.1). The model must contain free parameters, which can be optimized in the light of data, for example location and orientation of source activity. Second, a volume conductor model, which describes the conductivity properties inside the head, and a model of the sensors is required to calculate a forward solution (see Sec. 2.2.2). Given that, EEG/MEG data that would be generated given a certain source configuration can be determined. The goal function, which is the third component, is necessary to optimize the model parameters such that estimated sensor values are in sufficient accordance with real sensor values (see Sec. 2.3). Thereby, it is possible to constrain the model parameters using additional assumptions or even knowledge from independent information. The optimization result represents one possible inverse solution.

A very common method is to model brain activity using distributed sources. In that case, a large number of equivalent current dipoles (ECD) covers the volume in which activity is expected. The strengths of all ECDs are the only free parameters, that is, locations and orientations are fixed. This approach allows a linear solution of the inverse problem, given that a suitable goal function is selected (see Sec. 2.3). Moreover, it is easily possible to encode information on the correlations between neuronal sources (Dale and Sereno, 1993). This is a key point for this work because it is the basis to incorporate prior knowledge on the spatial correlation structure of brain activity. Such information can be derived, for instance, from the functio-anatomical organization of the cortex (for example, parcellations), which describes the relationship between common anatomical properties of neuronal sites (for example, regarding cytoarchitecture and structural connectivity) and their functional similarity (that means, whether their activity correlates).

The present work utilizes functio-anatomical prior knowledge to constrain the linear inverse problem. In fact, this kind of spatial information has been combined with linear inverse problems before (Cottereau et al., 2012, Knösche et al., 2013). The key concept in these two methods is the use of information on the belonging of sources to functional areas to define *a priori* correlations between sources. In the former method (i.e. functional area constrained estimator (FACE), Cottereau et al., 2012) this is realized by the explicit definition of source correlations. In the latter one (PatchLORETA, Knösche et al., 2013), the correlations are rather estimated on the basis of a second order spatial derivative operator. This operator, known from the low resolution electromagnetic tomography (LORETA) method (Pascual-Marqui et al., 1994), introduces a general similarity assumption between all neighboring sources. In PatchLORETA, this similarity assumption is modified according to functio-anatomical prior knowledge. However, PatchLORETA is limited to the use of parcellations (i.e. patch information) to define prior assumptions. More importantly, the method introduces artifacts into the estimated source covariance matrix, which implies unapparent *a priori* assumptions on the solution. Another issue is that the benefit of using functio-anatomical prior knowledge with linear reconstruction methods has not been sufficiently studied yet. Therefore, this work has two main focuses.

The first one is the generalization of the PatchLORETA method. This includes the exploration of the smoothness operator based integration of functio-anatomical prior knowledge, the reduction of artifacts (that means, implausible *a priori* assumptions) in the source covariance matrix, which are inherent with LORETA-based methods, and the extension of PatchLORETA in such a way that alternative functio-anatomical prior knowledge can be used. This is relevant since, for example, it has not been investigated yet if the correlation between sources estimated on the basis of the smoothness constraint (i.e. based on a spatial derivative operator) is actually consistent with the expected underlying *a priori* assumption. The result presented in this work is an informed LORETA method that accounts for major artifacts, and allows to use even general functional borders such as, for instance, the course of major sulcus lines (see Sec. 2.5.3). Moreover, it provides a solution to systematically control the *a priori* correlation structure with respect to the spatial resolution of the source space, which is another issue that has not been considered so far.

The second focus of this work relates to the question how the use of functio-anatomical prior information influences the reconstruction results of linear source reconstruction methods. On the one hand, this comprises the identification of characteristic properties of spatially informed linear source reconstruction methods. On the other hand, it is evaluated under which conditions minimum norm based source reconstruction methods can benefit from incorporating prior knowledge on the functional organization of the cortex. This includes studying the reconstruction quality given that the imposed prior is either consistent or inconsistent to the underlying activity. This is accomplished by using both full parcellations, i.e. a complete subdivision of the cortical surface into distinct functional areas, and local parcellations, i.e. multiple subsets of patches drawn from full parcellations, to express a belief on the underlying source configuration. The results are highly relevant for the analysis of realistic EEG/MEG data.

1.2 Outline of this Thesis and Contributions

The subsequent chapter 2 gives, first, a condensed overview on the main ingredients of source localization in general, including source model, forward solution and goal function. Then, it focuses on linear inverse problems using distributed source models and, in particular, on the derivation of the inverse solution using Bayesian inference and Tikhonov regularization. Their relationship provides an important basis for the smoothness based inverse solutions addressed in this thesis. The chapter will then shed light on possible sources from which *a priori* knowledge on the spatial correlation structure of brain activity can be derived. Finally, two approaches for informed linearly constrained source localization will be introduced - these are PatchLORETA (Knösche et al., 2013) and FACE (Cottereau et al., 2012).

Chapter 3 covers the extension and improvement of PatchLORETA and deals with the plausibility of LORETA-based source covariance estimates in the light of the underlying *a priori* assumptions. As mentioned above, PatchLORETA has several limitations, which will shortly be summarized in Sec. 3.1. Section 3.2 introduces an extension that allows to encode information on the mutual similarity between neighboring sources. This is the basis for the use of alternative functio-anatomical information. Section 3.3 considers the estimation of *a priori* source covariances by means of the inversion of a second order spatial derivative operator (Laplace operator), which is crucial for LORETA methods. In particular, it will be pointed out that the modification of this Laplacian using prior knowledge introduces discrepancies between intended and actually imposed *a priori* assumptions. Moreover, an additional normalization operator is presented, which effectively reduces some of these artifacts. Section 3.4 focuses on the adjustment of the Laplacian regularization parameter to control the estimated correlation structure. The proposed method eliminates the influence of the spatial resolution of the source space on the estimated spatial correlations.

Chapter 4 is focused on the evaluation of spatially informed linear inverse methods. Two different types of simulations are used: (1) Simulations with carefully controlled activation patterns, and (2) Monte-Carlo (MC) simulations. The former are subject of Sec. 4.3. The source patterns are defined manually in these simulations, and their agreement to prior knowledge is systematically varied. Thus, the effects of incorporating prior knowledge into linear source reconstruction methods on the localization results are presented in an illustrative manner. The MC simulations are subject of Sec. 4.4-4.6. Here, several parameters for generating source patterns are determined by random sampling. This is the basis to examine main characteristics of the reconstruction results and to assess the benefit of using prior knowledge for linear source reconstruction. Moreover, it allows to evaluate the accuracy of spatially informed methods with respect to uncertainties in the volume conductor model, which occur, for instance, due to co-registration errors.

Chapter 5 covers the application of informed LORETA-based linear inverse methods to reconstruct evoked brain activity from EEG/MEG data recorded in a language experiment. Section 5.2 describes the methods used for the analysis, i.e. the experimental setup, EEG/MEG data preprocessing, the forward model, prior information, the estimation of the noise and data covariance matrix used for the determination of the Tikhonov regularization parameter, and criteria for the assessment of the localization results. The reconstruction results are shown in Sec. 5.3, separately for EEG and MEG, and are discussed in Sec. 5.4.

Finally, chapter 6 contains a summary and conclusions of the results presented in this thesis.

Two key points are targeted in this thesis. Chapter 3 contributes to the improved integration of functio-anatomical prior information into the linear inverse problem. Chapter 4 and 5 provide important insight into the characteristics of informed smoothness based inverse methods and how such approaches might facilitate EEG/MEG source reconstruction. The original contributions listed below are given to the best of the author's knowledge of existing literature.

1. A novel extension of the LORETA-Laplacian allows to encode the mutual similarity (i.e. even gradual information) between neighbors. Such similarity information can be derived from functio-anatomical prior knowledge (for example, parcellations, course of major sulcus lines). Chapter 3.

2. A study on the plausibility of source variances and covariances estimated using an existing spatially informed LORETA-based inverse method (i.e. PatchLORETA) revealed that the modification of the Laplacian introduces undesired *a priori* assumptions (i.e. artifacts) into the source covariance matrix. Chapter 3.

3. An additional normalization operator is introduced to compensate for major artifacts in the estimated source covariance matrix. Chapter 3.

4. A measure is presented that allows to adjust the Laplacian regularization parameter according to a desired smoothness criterion. It allows to carefully vary the strength of the smoothness constraint and, more importantly, to control the covariance structure independently of the spatial resolution of the source space. Chapter 3.

5. A simulation study, in which several subsets of a realistic parcellation are used as a prior for informed LORETA, underpins that the consistency between *a priori* information and the "true" activity pattern is of crucial importance to avoid only prior-driven source localization results. Chapter 4.

6. Main characteristics of source distributions (i.e. features as the spatial extent) estimated on the basis of spatially informed linear inverse methods are determined. This is done using Monte-Carlo (MC) simulations. Chapter 4.
7. MC simulations are used to asses the benefit of incorporating functio-anatomical prior knowledge into linear source reconstruction. Chapter 4.
8. The informed LORETA approach is used to analyze experimental EEG/MEG data recorded in a spoken language experiment. Chapter 5.

2 Theoretical Background

2.1 Overview

The reconstruction of brain activity from bioelectromagnetic data requires to model electrical sources (Section 2.2.1), tissues inside the head (volume conductor) and the solution of the forward problem (Section 2.2.2), that is, the prediction of the magnetic field and the electric potential at sensors given a known activation. The goal of the reconstruction is the estimation of the free model parameters using a certain goal function. Due to the ambiguity of the neuroelectromagnetic inverse problem, the integration of prior knowledge to constrain both fixed (Section 2.2.3) and free model parameters (Section 2.3) is important.

This thesis focuses on the use of distributed source models, which allow to reconstruct a spatial activity distribution (Section 2.3). A linear solution can be derived by means of optimization using Lagrange multipliers, for instance Tikhonov regularization (Section 2.4.3), and on the basis of probability theory using Bayes's law (Section 2.4.2). Their relationship with respect to the definition of additional assumptions on the functional similarity between sources is particularly important (Section 2.4.4).

On the one hand, information on the functional similarity can be based on assumptions. For example, the LORETA method (Section 2.4.5) employs a general smoothness assumptions. This assumption introduces a certain degree of correlation between sources, particularly between sources which are close to each other . LORETA is the basis for the reconstruction method that is extended in this work (see below). On the other hand, functional similarity between sources can be derived using explicit knowledge, e.g., drawn from other functional modalities (Section 2.5.2) or the functio-anatomical organization of the cortex (Section 2.5.3). An example for the latter one are parcellations, which were recently integrated in two linear reconstruction methods. (1) The FACE method (Cottereau et al., 2012) encodes such knowledge on the basis of the explicit definition of source correlations (Section 2.5.5). (2) PatchLORETA (Knösche et al., 2013) utilizes parcellations by means of a spatial derivative operator whose intrinsic smoothness constraint is lifted at boundaries (Section 2.5.4). This method is the basis for the generalization to utilize functio-anatomical information presented in chapter 3. The improved method and the FACE method mentioned above are used for the evaluation carried out in chapter 4.

2.2 EEG/MEG Source Modeling and the Forward Solution

2.2.1 Source Models

The solution of the bioelectromagnetic inverse problem aims at reconstructing the primary current density of neuronal processes. Therefore, a model of the current density is required. If the current density concentrates in a small area whose extent is much smaller than its distance to sensors , a so called equivalent current dipole (ECD) can be used to model the current density (cmp., for instance, Knösche, 1997). An ECD describes a quasi-pointlike current flow and is parameterized by location, orientation and strength. ECDs are the atomic elements in most source reconstruction methods.

Two general approaches to utilize ECDs can be distinguished. (1) Single- and multiple dipole methods might be used to model focal brain activity, either on the basis of moving, rotating, or fixed dipoles. Moving dipole methods estimate location, orientation and strengths of the ECDs. In contrast, the location is fixed in rotating dipole methods, only orientations and strengths may vary. Single-/Multiple dipole models are particularly useful if a small number of active sources (focal activity) can be expected. This is the case, for instance, in the field of analyzing epileptic seizures (da Silva, 2008). (2) An alternative is the use of so called distributed source models (Singh et al., 1984), where a large number of fixed dipoles (i.e. ECDs with fixed location and orientation) is used to sample the volume in which activity is expected. In contrast to single- or multiple dipole models, the concurrent reconstruction of all dipole strengths provides a spatial current density distribution. Either multiple dipoles, i.e. typically three orthogonal dipoles[1], or only a single ECD are placed at each location, see Section 2.2.3.

The present work is based on the use of distributed source models. Before the estimation of source parameters from EEG/MEG data is possible, the solution of the so called forward problem is required. This is addressed in the subsequent section. Moreover, it is often useful to constrain the source model using additional prior knowledge, e.g. on the likely location of the generators. This is subject of Section 2.2.3.

2.2.2 Forward Solution

The forward solution draws the relationship between the source parameters and the sensor values. This requires to consider the volume conductor properties, i.e. the conductivity structure of the tissues, fluids and bone inside and on the head. This section gives a condensed overview on the calculation of the forward solution. A much more detailed explanation of this topic can be found in literature (e.g. Grunwald, 1996).

Following the law of *Biot-Savart*, a current density $\vec{J}$ impressed in the volume V located at r' generates the magnetic flux density

$$\vec{B}(\vec{r}) = \frac{\mu_0}{4\pi} \int_V \frac{\vec{J}(\vec{r}\,') \times (\vec{r} - \vec{r}\,')}{|\vec{r} - \vec{r}\,'|^3} d\vec{r}\,' \tag{2.1}$$

at the sensor location r. The parameter μ_0 is the magnetic constant. Likewise, the electric

---

[1] For source localization based on MEG data it is common to use only two orthogonal ECDs because radial source components cannot be detected.

potential at the distance r in a medium with the conductivity σ is

$$\Phi(\vec{r}) = \frac{1}{4\pi}\int_V \frac{\vec{J}(\vec{r}\,')\cdot(\vec{r}-\vec{r}\,')}{\sigma\cdot|\vec{r}-\vec{r}\,'|^3}\,d\vec{r}\,'. \tag{2.2}$$

Under the assumption that the extent of V is small in comparison to its distance to sensors, the current density at r' can be approximated using a current dipole, i.e. $\vec{Q} = \int_V \vec{J}(\vec{r}\,')\,d\vec{r}\,'$. Consequently, Eq. 2.1 and 2.2 change to

$$\vec{B}_D(\vec{r}) = \frac{\mu_0}{4\pi}\frac{\vec{Q}\times(\vec{r}-\vec{r}\,')}{|\vec{r}-\vec{r}\,'|^3} \tag{2.3}$$

and

$$\Phi_D(\vec{r}) = \frac{1}{4\pi\sigma}\frac{\vec{Q}\cdot(\vec{r}-\vec{r}\,')}{|\vec{r}-\vec{r}\,'|^3}. \tag{2.4}$$

The parameters of $\vec{Q}$ are its magnitude, orientation, and location. Equations 2.3 and 2.4 allow to calculate the magnetic flux density and the electric potential generated by a current dipole in an infinite and homogeneous volume conductor. Hence, they are the fundamental basis for the forward solution in the neuroelectromagnetic inverse problem. Signals generated by multiple ECDs as used, for example, in multi and distributed source models can be derived from the superposition of the individual components.

However, two issues must be taken into account in practice. First, although one is only interested in estimating the primary currents, the effect of secondary currents, which particularly depend on the volume conducting properties, need to be considered. Second, the conductivity distribution and the physical structure of a realistic volume conductor is very complex. Thus, an adequate model of the head with its various compartments is mandatory in order to reliably predict the magnetic field and the electric potential.

The compartments of the head in which secondary currents flow are scalp, skull, cerebrospinal fluid (CSF) and brain tissues. These compartments can be segmented from magnetic resonance imaging (MRI) data using, for example with the Neuroelectromagnetic Forward Head Modeling Toolbox (NFT) (Acar and Makeig, 2010) or using Freesurfer (Fischl, 2012). The compartments are mainly arranged as concentric areas. That means it is in principle suitable to assume that the conductivity profile changes much stronger in radial direction than within the compartments themselves. The first approach to construct a model of the volume conductor is to use spheres to approximate the boundaries between these compartments. In this case, the analytic solution of the bioelectromagnetic forward problem is still possible (Munck, 1989, Sarvas, 1987). The second approach is to use the boundary element method (BEM) to model the inter-compartment boundaries by means of triangulated meshes (Fuchs et al., 2001, Hämäläinen and Sarvas, 1989). This is also the method of choice in this thesis. It requires a numerical solution of the forward problem (see, e.g., Bommel et al., 1993, Mosher et al., 1999, Zanow, 1997, Zanow and Peters, 1995) but allows a more realistic approximation of the individual, non-spherically shaped boundaries. The most sophisticated approach to model realistic volume conductors, which is also based on a numerical solution, is the finite element method (FEM) (see, e.g., Haueisen, 1996, Wolters et al., 2002). In contrast to BEM, where the conductivity inside the head is piecewise constant and isotropic, FEM is based on the subdivision of the whole head volume into many volume elements and allows to account for inhomogeneity and anisotropy in the different compartments. For example, the natural structure of the human skull causes inhomogeneities in the conductivity. These inhomogeneities finally influence source localization results (Pohlmeier et al., 1997). The accuracy and the quality of the volume conductor model are of crucial importance for the quality of source reconstruction (Dannhauer et al., 2011, Güllmar et al., 2006, Lanfer et al., 2012).

The combination of a realistic volume conductor model and sensor information (i.e. sensor position, orientation and physical properties) allows to determine a so called leadfield operator for each pair of ECD and sensor. This operator describes the relationship between the dipole parameters and the sensor values. In case of one dipole with fixed orientation and location as, e.g., used in distributed source models, the evaluation of the leadfield operator yields the scalar value l which transforms the dipole magnitude to a sensor value by means of a linear projection. Consequently, the forward solutions for one ECD and a set of n sensors can be condensed in the leadfield vector $\vec{l} \in \mathbb{R}^n$. Finally, in a distributed source space with m sources, all m leadfield vectors, $\vec{l}_i, i \in 1 \dots m$, span the leadfield matrix $L \in \mathbb{R}^{n \times m}$, which will subsequently be shortly denoted as the so called Leadfield. Thus, the Leadfield defines the forward model. The projection of the dipole magnitudes $\vec{q} \in \mathbb{R}^m$ of m fixed ECDs to the sensor space using the Leadfield defines the linear forward solution

$$\vec{d} = L\vec{q}, \tag{2.5}$$

where $\vec{d} \in \mathbb{R}^n$ contains n sensor values. Subsequently, these vectors will be denoted as d and q.

2.2.3 Using *a priori* Knowledge for the Source Model

Different approaches to generate source models based on ECDs were summarized in Section 2.2.1. In practice, it is often useful to employ additional knowledge to constrain the fixed parameters of the ECDs, that means to restrict the source model. This effectively narrows down the space of possible solutions. Note that constraining fixed parameters is different from employing prior knowledge on the free parameters of ECDs (see Section 2.3): While the latter are optimized in the light of the data, the former are taken as *ground truth* so that these *a priori* assumptions cannot be rejected during source reconstruction. Thus, constraints on the source model have a very strong influence on the solution.

The parameters that are usually constrained are number, location and orientation of dipoles. Sources for this kind of information are, for example, general anatomical and physiological knowledge and functional knowledge drawn from imaging modalities such as, for instance, functional magnetic resonance imaging (fMRI). The use of such information will be shortly outlined below. The main focus is on constraining distributed source models.

The main contributors to measurable EEG/MEG signals are the pyramidal cells of the cortex (da Silva and van Rotterdam, 1999, Nunez and Srinivasan, 2006). Therefore it is, first, often reasonable to restrict the sources to the cortical sheet, that means to constrain the location of dipoles to tissue in which the measurable fields are likely to be generated. Dale and Sereno (1993) proposed to approximate the cortical surface using a triangular mesh, where ECDs are placed on each grid node. This consequently pursues the idea of distributed sources. A location constraint was also employed by Im et al. (2005b), who placed rotating dipoles at certain locations in the cortical sheet. The dipole locations were chosen according to the peaks of a spatial source distribution pattern that was identified from a prelocalization of EEG/MEG data with a linear reconstruction method (Dale and Sereno, 1993, Dale et al., 2000). Similarly, Scherg and Berg (1991) used multiple dipoles whose locations (and orientations) were constrained according to their relative distance to match main aspects of cortical gyri.

Second, the pyramidal cells are usually oriented perpendicular to the interface between gray and white matter. It is therefore reasonable to align the ECDs in a similar way. This is possible for single- and multiple dipole models (Scherg and Berg, 1991) and for distributed source models (Dale and Sereno, 1993). For example, it is straightforward to place a single perpendicular dipole at each node of a triangular mesh (see above, Dale and Sereno, 1993). However, the estimated perpendicular direction is prone to errors from the MRI based segmentation and subsequent tessellation of brain tissues, which is needed in order define a cortical mesh. An alternative to this strict orientation constraint is to place multiple dipoles on each mesh node. All dipoles together define an effective orientation. Deviation from this orientation is possible by means of, e.g., a projection matrix (known as loose orientation constraint, Lin et al., 2006a) or based on a tripod with non-orthogonal components (Knösche et al., 2013). Another alternative to prevent such uncertainties was presented by Phillips et al. (2002). Firstly, they used a voxel space that covers the whole cortical sheet rather than only a two dimensional hypersurface (i.e. a folded cortical surface). Secondly, they placed one ECD in the center of each voxel and aligned it towards the interface between gray and white matter. Thirdly, they assigned a probability to each source. The probability expresses how likely it is that the source is covered by gray or white matter.

Another type of prior information is functional knowledge which can be drawn from functional imaging modalities. Imaging techniques measure second order effects of neuroelectric activity. For example, PET indicates ongoing metabolic processes in neuronal cells based on radioactive markers. fMRI detects the blood oxygenation level dependent (BOLD) contrast that results from changes in blood flow due to the energy demand in neuronal active and inactive areas (Magistretti et al., 1999). There is considerable evidence from both studies in animals (Grinvald et al., 1986, Logothetis et al., 2001, Malonek and Grinvald, 1996) and humans (Benson et al., 1996, Puce et al., 1995, 1997) for a general correlation between the spatial distributions of electrical brain activity and hemodynamic changes during a given task. It is therefore obvious to constrain EEG/MEG source estimates using the (local) fMRI response or the PET signals as prior knowledge.

One possibility to incorporate functional information to constrain the source model can be seen as an extension to the cortical location constraint (Dale and Sereno, 1993). Baillet and Garnero (1997) restricted the source space only to voxels that are simultaneously active (patches) during hemodynamic measurements. Similarly, Fujimaki et al. (2002) subdivided large fMRI activation volumes and placed single ECDs in the center of each subvolume. Obviously, approaches like these give a very strong weight to fMRI prior knowledge in that sources without significant support from the functional modality are completely discarded from the source model and, therefore, from EEG/MEG source reconstruction.

Unless otherwise noted, a cortical mesh with high spatial resolution is used in this work as the source space. In this case, potential uncertainties concerning the perpendicular orientation of dipoles are less problematic (Lin et al., 2006a). Thus, only the strict orientation constraint will be applied. No additional prior knowledge is incorporated into the source model. However, prior information is used to constrain the free parameters, i.e. the dipole magnitudes, in the inverse problem (see Section 2.3 and 2.5).

2.3 The Inverse Solution and Constraints from Independent Prior Information

The goal of the solution of the bioelectromagnetic inverse problem the determination of the free parameters of the source model in the light of EEG/MEG data. A variety of methods have been developed to estimate electric brain activity. This includes methods based on single- and multiple dipoles, e.g. dipole fitting (Scherg and Berg, 1991, Scherg and von Cramon, 1985, 1986), multiple signal classification (MUSIC, Mosher et al., 1992), beamforming (Robinson and Vrba, 1999, van Veen et al., 1997), and methods based on distributed sources where the solution is found using an iterative optimization scheme (e.g. Gorodnitsky et al., 1992) or by means of a linear inverse mapping (Hämäläinen and Ilmoniemi, 1994, Pascual-Marqui et al., 1994), which is sometimes also referred to as Leadfield imaging. An overview on this topic can also be found in literature (see, e.g., Baillet et al., 2001, Grech et al., 2008, Wendel et al., 2009).

Moreover, there are a variety of possibilities to incorporate independent prior information to constrain the free parameters. For example, the strength and location in a multiple dipole approach can be fitted subject to the cortical location and orientation constraint (Auranen et al., 2007). Similarly, these dipoles could be replaced by compact patches which cover an area of predefined size (Kincses et al., 1999, Lütkenhöner et al., 1995). Other approaches minimize the distance between the EEG/MEG inverse solution and the fMRI subspace or use statistical maps drawn from fMRI to control a statistical prior on source locations (Jun et al., 2008). For the use of distributed source models, it is very common to employ independent prior knowledge into weights for the dipole magnitudes. Since this is also a key concept in this work, it is discussed separately in Section 2.5.

The estimation of a unique solution, which determines the free model parameters, requires a so called goal function. For single- and multiple dipole models, for which the inverse problem is overdetermined since the number of free parameters is much smaller than the number of channels, the goal function needs to balance the agreement between predicted and recorded data. In contrast, the number of ECDs employed in distributes source models usually exceeds the number of senors by far. In order to find a unique solution to this underdetermined problem, the goal function additionally needs to balance the agreement between the estimated solution and *a priori* assumptions, e.g. by means of regularization. In principle, there are many different ways to derive a goal function. However, two are of particular importance for this thesis and, therefore, they will be outlined below briefly. They are discussed in some more detail with respect to distributed source models in Section 2.4.

First, a widely used technique is the optimization of a functional which consists of several terms (e.g. Marquardt, 1963, Tikhonov and Arsenin, 1977). Each of these terms measures a certain agreement (i.e. a certain constraint on the solution, see above) by means of some ℓ-norm. They are combined using a weighted sum to scale their individual impact on the solution. This is also known as a regularization approach (see Section 2.4.3) and can be understood as an optimization using Lagrange multipliers. Typically, the minimization of the functional using non-linear or linear algorithms (see, for instance, Section 2.4.3) provides a unique solution. Constraints can either be formulated with or without using additional prior information. In the latter case, additional weights determined by independent prior knowledge are usually used for weighting free model parameters.

The second strategy with relevance for this work is the derivation of a goal function on the basis of probabilistic theory, particularly on Bayesian inference (see Section 2.4.2). In this case, all parameters are treated as random variables with a dedicated probability density function (PDF). According to the law of Bayes, a *likelihood*, that means a PDF of the forward solution (see Section 2.4.2), and a *prior*, that means a PDF of the free model parameters which are known *a priori*, allow to determine the *posterior*, i.e. the PDF of the free parameters in the light of both data and *prior*, by means of conditional probabilities. Theoretically, Bayesian inference is very powerful and allows source analysis in a probabilistic sense, for instance to answer the question if it is likely that the activity strength in a certain region exceeds a certain threshold (Schmidt et al., 1999). However, this requires the full determination of the posterior, which is usually not possible (see Section 2.4.2). Therefore, most methods are based on the evaluation of prominent features of the posterior (cmp., e.g., Friston et al., 2002, Trujillo-Barreto et al., 2004), for example the maximum probability density. Similarly to regularization based optimization, this allows to define a unique representative solution. Others sample the posterior by means of Markov Chain Monte Carlo (MCMC) methods (e.g. Jun et al., 2008, Schmidt et al., 1999), which is a technique that tries to estimate the probability distribution of the posterior.

Bayesian inference provides a formal means of incorporating independent prior information. In practice, however, the PDF of the prior information does not exist, at least not by means of an analytic function. It is therefore common to approximate the *prior* using a model function, for example a Gaussian distribution, whose parameters serve for the encoding of independent prior information. Thus, prior information is encoded by means of statistical parameters, whereas regularization based approaches employ prior information by the definition of weight factors. The relationship between these different approaches is of crucial importance for prior information which embodies assumptions on the spatial correlation structure of brain activity (see Section 2.5). This kind of information is employed in this thesis.

2.4 Approaches to Solve the Inverse Problem using Distributed Sources

2.4.1 Introductory Remarks

Main aspects of the biomagnetic inverse problem were outlined in the previous sections, for example possible approaches for its solution and the integration of independent prior knowledge. Since distributed source models are of key importance in the present work, their use for the solution of the bioelectromagnetic inverse problem is discussed in more detail in this very section.

According to Eq. 2.5, the electric potential and the magnetic field, respectively, recorded at n sensors and generated by usually $m \gg n$ dipoles with fixed location and orientation is given by

$$d = Lq + \epsilon. \tag{2.6}$$

This means that the data is composed of a projection of the dipole magnitudes into sensor space through the Leadfield, and of noise, $\epsilon \in \mathbb{R}^n$. Noise contains both technical noise of the sensors and background activity in the brain, that means activity which is expected to be uncorrelated to activity which aims to be reconstructed[2]. The dipole magnitudes are the free model parameters which have to be estimated in the light of the data. Due to the ill-posed nature of the inverse problem, there is an infinite number of possible solutions which can explain a certain measurement, d. A unique solution can only be found with the help of additional constraints.

Various ways exist to derive such a solution, see, for instance, Liu et al. (2002), Mosher et al. (2003) and Hauk (2004) for an overview. A lot of them lead to a linear inverse solution. Two of these methods are of particular interest for the present work: Bayesian inference and the Tikhonov regularization based solution (Tikhonov and Arsenin, 1977). These two methods will be introduced and compared in the subsequent sections. Finally, the linear inverse method which employs a generic smoothness constraint (LORETA, Pascual-Marqui et al., 1994) will be introduced. It is fundamental for the method proposed by Knösche et al. (2013) to employ functio-anatomical prior information. This, in turn, the basis for the method developed in this work.

2.4.2 Bayesian Inference

Bayesian inference provides a generalized framework to solve inverse problems. As already stated in Section 2.3, the Bayesian approach relies on the definition of probability density functions for noise, i.e. the likelihood, and for *a priori* assumptions on the free parameters (*prior*).

The noise is usually assumed to be normally distributed with zero mean. Following this assumption and Eq. 2.6, the likelihood can be expressed as a function of the source strengths, i.e. using a multivariate Gaussian distribution given by

$$\rho(d|q) \propto \exp\left(-\frac{1}{2}(d-Lq)^T C_\epsilon^{-1}(d-Lq)\right). \tag{2.7}$$

The noise covariance matrix, $C_\epsilon \in \mathbb{R}^{n\times n}$, contains variances and covariances of the noise. The likelihood, $\rho(d|q)$, defines the conditional probability of the data given the particular model parameters.

As stated above, Bayesian inference provides a formal means of incorporating independent prior knowledge. This means that any arbitrary PDF that describes the probability of the source strengths in absence of the data could be used. While a precise, quantitative definition of the *prior* would be desirable, it is simply not possible to derive it from other modalities, e.g. fMRI, since their relationship to electrical brain activity is highly non-linear and still not fully understood.

Therefore, the *prior*, $\rho(d)$, is usually expected to follow a Gaussian distribution with zero mean as well. This leads to a so-called shrinkage prior, that means the mean activity is expected to be zero. The variance controls the possibility to diverge from zero. A large variance renders the activation of a source more likely and vice versa. In principle, the use of non-zero expectation values is possible. However, it is only hardly possible to derive a precise expecta-

---

[2] A typical application of source reconstruction is the localization of event related potentials, i.e. of signals which are expected to be correlated to some event as, e.g., a certain visual, auditory or motor stimulation. Background activity, i.e. spontaneous activity somewhere in the brain, is expected to be uncorrelated to such events.

tion value from other knowledge as well. Finally, the shrinkage prior is given by

$$\rho(q) \propto \exp\left(-\frac{1}{2} q^T C_q^{-1} q\right). \tag{2.8}$$

The source covariance matrix, $C_q \in \mathbb{R}^{m \times m}$, defines *a priori* source variances and covariances between sources. It eventually allows to encode independent prior knowledge.

According to Bayes' Theorem, the *posterior*, $\rho(q|d)$, can be inferred from the joint PDF of *likelihood* and *prior*, i.e.

$$\rho(q|d) = \frac{\rho(d|q)\rho(q)}{\rho(d)}. \tag{2.9}$$

The model evidence, $\rho(d)$, is defined as

$$\rho(d) = \int \rho(d|q)\rho(q)\partial q. \tag{2.10}$$

This is the marginal probability distribution of the measurement and it can be treated as a constant. In practice, its calculation is usually computationally not tractable. That means that the *posterior* cannot be fully determined. However, since both *likelihood* and *prior* are Gaussian functions, the posterior is a Gaussian as well. Thus, the model evidence can be omitted if the evaluation of the *posterior* is limited to features of the Gaussian. This is, in fact, common practice.

A multivariate normal distribution is characterized by two parameters, i.e. a vector of expectation values and a covariance matrix. The former defines the location of the maximum of the probability density function. This point can easily be determined by means of linear optimization (Tarantola, 2005), for instance by minimizing the exponent of the joint PDF $\rho(d|q)\rho(q)$, i.e.

$$\hat{q} = \underset{q}{\arg\min}\left\{(d - Lq)^T C_\epsilon^{-1}(d - Lq) + q^T C_q^{-1} q\right\}. \tag{2.11}$$

The solution of this minimization problem is

$$\hat{q} = C_q L^T \left(L C_q L^T + C_\epsilon\right)^{-1} d, \tag{2.12}$$

which is referred to as the linear *maximum a posteriori* (MAP) estimate. Thus, the solution to the inverse problem is represented by a single 'best' estimate of the dipole magnitudes. This estimate corresponds to the maximum probability density.

The linear solution in Eq. 2.12 requires a quantitative *a priori* definition of source variances and covariances. Usually, however, only qualitative information is available. It is obvious that an arbitrary source variance information, which is encoded in C_q, gives rise to an imbalance between predicted signal strengths and noise. To account for this, consider multiplying the right hand side of Eq. 2.12 with the scalar σ_q^2/σ_q^2 where σ_q^2 denotes the unknown mean source variance. Then, C_q/σ_q^2 can be replaced by the normalized covariance matrix, $R_q \in \mathbb{R}^{m \times m}$. This matrix encodes qualitative rather than quantitative prior knowledge. This can be, for instance, correlation between sources or arbitrary weights on the variance (de Peralta Menendez and Gonzalez Andino, 1998, 2002, Phillips et al., 2002). In other words, this matrix allows to employ information on relative covariances. For example, it is possible to express the belief that source A is more likely to be activated than source B, or that source A has a stronger connection to source B than to source C. Given this, Eq. 2.12 changes to

$$\hat{q} = R_q L^T \left(L R_q L^T + \frac{1}{\sigma_q^2} C_\epsilon \right)^{-1} d. \tag{2.13}$$

The unknown mean source variance σ_q^2, which is the remaining free parameter, serves as a regularization parameter to scale the signal-to-noise ratio. It might be fitted from the data, for example by means of an L-Curve method. An alternative is to estimate σ_q^2 from the noise and data covariance matrix. The basis for this is a technique proposed by Smith (1992). They estimated the full source covariance matrix (i.e. not only variances) from sensor signals on the basis of two essential assumptions. First, they assumed that signals and noise are uncorrelated. Second, none of the projections of active sources to the sensor domain is part of the nullspace, that means any activity is visible in the data. Knösche (1997) followed this idea and estimated the source variance in a least squares sense for the case that the noise is uncorrelated over channels. Here, however, it is necessary to consider spatially correlated noise. Therefore, a more general formulation of the underlying problem was employed here. Consider the following expression:

$$\mathrm{tr}(L \sigma_q^2 R_q L^T) = \mathrm{tr}(C_d) - \mathrm{tr}(C_\epsilon). \tag{2.14}$$

C_d is the covariance matrix of the noisy data and $\mathrm{tr}(\cdot)$ denotes the trace of the matrix. The equation states that the predicted accumulated variance in the sensor domain equals the accumulated measured variance of the noise-free signals. Solving for σ_q^2 reveals

$$\sigma_q^2 = \frac{\mathrm{tr}(C_d) - \mathrm{tr}(C_\epsilon)}{\mathrm{tr}\left(L R_q L^T \right)}. \tag{2.15}$$

This estimation of the source variance is the basis for both simulations and the analysis of experimental data carried out in this work.

2.4.3 Tikhonov Regularization

Another approach to derive a unique solution $\hat{q}$ that explains the measurement d can be found by solving a constrained minimization problem. Based on Eq. 2.6 (data term) and an additional (arbitrary) ℓ^2-norm based assumption on the dipole magnitudes (model term), the problem states as

$$\arg\min_q \left\| W q \right\|_2^2 \qquad \text{subject to the constraint} \qquad \left\| d - L q \right\|_2^2 = 0. \tag{2.16}$$

It can be written as a combined optimization problem using Tikhonov regularization (Tikhonov and Arsenin, 1977):

$$\hat{q} = \arg\min_q \left\{ \left\| d - L q \right\|_2^2 + \alpha^2 \left\| W q \right\|_2^2 \right\}. \tag{2.17}$$

The regularization parameter α scales between the influence of the data term and the model term on the solution. The matrix $W \in \mathbb{R}^{m \times m}$ allows to constrain the source parameters with different assumptions (see below). Since Eq. 2.17 is based on squared norms, it is straightforward to derive a linear solution, i.e.

$$\hat{q} = \left(W^T W\right)^+ L^T \left(L\left(W^T W\right)^+ L^T + \alpha^2 I\right)^{-1} d, \tag{2.18}$$

where $(\cdot)^+$ denotes the regularized inverse matrix.

If $W = I$ is the identity matrix, Eq. 2.18 simplifies to the well-known minimum norm (MN) solution (Hämäläinen and Ilmoniemi, 1984, 1994),

$$\hat{q} = L^T \left(LL^T + \alpha^2 I\right)^{-1} d, \tag{2.19}$$

where the solution matrix $G = L^T \left(LL^T + \alpha^2 I\right)^{-1}$ corresponds to the Moore–Penrose pseudoinverse (Golub and van Loan, 1996) of L in the absence of additional constraints ($\alpha = 0$). The MN method tends to prefer superficial sources because they have a larger impact on the sensors (Fuchs et al., 1999, Jeffs et al., 1987). To account for this bias it is common to apply the so-called leadfield normalization (Crowley et al., 1990, Hämäläinen and Ilmoniemi, 1984, 1994, Jeffs et al., 1987, Köhler et al., 1996, Wang et al., 1993), which weights each source according to its impact on all sensors. This can be done using a diagonal weighting matrix, i.e. $W = \Omega$, with a definition of the elements according to Köhler et al. (1996), i.e.

$$\Omega_{ii} = \sqrt{\|L_{\cdot i}\|_2}. \tag{2.20}$$

This definition ensures an equal balance between deep and superficial sources (Fuchs et al., 1999), given that the ℓ^2-norm is used to penalize the dipole magnitudes. This is commonly referred to as the weighted minimum norm (WMN) solution. Another approach involves the ℓ^2-norm of the solution weighted by a smoothness operator, which approximates the second spatial derivative (Laplacian) and, therefore, imposes a general source correlation pattern. This technique has been put forward as Low Resolution Electromagnetic Tomography (LORETA) by Pascual-Marqui and colleagues 1994. It selects a solution with both small current strengths and high smoothness. It will be discussed in Section 2.4.5 in more detail.

MN solutions produce a rather blurred image of the brain activity. This reflects the non-uniqueness of the inverse problem and the limitations in quantity (number of sensors) and quality (signal-to-noise ratio) of EEG/MEG data (de Peralta Menendez and Gonzalez Andino, 2000). Less blurred images can be obtained by employing an ℓ^1-norm to constrain the dipole magnitudes (Gorodnitsky et al., 1995, Nagarajan et al., 2006, Uutela et al., 1999). This, however, requires non-linear optimization techniques. Of course, such an approach does not increase the spatial resolution of EEG/MEG but only expresses the assumption that solutions are sparse or focused. To some extent, this is similar to the use of single- and multiple dipole models.

2.4.4 A Bayesian Perspective on Tikhonov Regularization

The aim of this section is to emphasize the relationship between linear solutions derived using Bayesian inference and Tikhonov regularization. This relationship is a very important basis for the incorporation of prior knowledge on the spatial correlation structure. The mere comparison between Eq. 2.13 and 2.18 reveals the two following relations:

$$R_q = \left(W^T W\right)^+ \tag{2.21}$$

$$\frac{1}{\sigma_q^2} C_\epsilon = \alpha^2 I. \tag{2.22}$$

Equation 2.21 describes the formal relationship between the weighting matrix employed with the regularization approach and the normalized source covariance matrix. It means that - given a suitable definition of W - the inversion of the squared weighting matrix allows to estimate the source covariance structure, which is encoded in R_q (see below). Equation 2.22 relates to noise. It is only valid under the assumption of uncorrelated homoscedastic noise, i.e. $C_\epsilon = \sigma_\epsilon^2 I$. It follows that the Tikhonov regularization approach implicitly assumes an uncorrelated zero mean Gaussian distribution for the noise. This means that EEG/MEG data needs to be prewithend before source reconstrucion. In contrast, Bayesian inference directly employs the noise covariance matrix. The regularization parameter defines as $\alpha^2 = \sigma_\epsilon^2/\sigma_q^2$, that means it scales with the noise variance. Hence, the model term in the Tikhonov approach becomes more influential if the uncertainty of the observed data increases.

Additionally, one can also assume uncorrelated homoscedastic source strengths, i.e. $R_q = I$. Substituting this expression into Eq. 2.12 leads to the MN solution (Eq. 2.19). Thus, it can be concluded that the MN approach implicitly assumes uncorrelated zero mean Gaussian distributions for source strengths and noise (Lewis et al., 1995). Likewise, the WMN approach assumes that sources are uncorrelated, but have different variances. Since this weighting attenuates superficial sources with respect to deep sources, the latter ones are expected to have a larger *a priori* variance, that means they are more likely to diverge from zero. However, it is very likely that superficial sources are the main contributors to measured EEG/MEG signals. This emphasizes that leadfield normalization is a rather arbitrary assumption.

The analysis of Eq. 2.21 is particularly interesting for LORETA based methods. Again, it states that the inversion of W provides an estimate of the source correlations encoded in R_q. LORETA is based on a general smoothness assumption, that means it employs information on the correlation structure (see Section 2.4.5 for a detailed description). However, this is not based on the definition of correlations but rather on a spatial derivative operator. In other words, LORETA provides a means of defining a correlation structure without the need for an explicit definition of correlations. This is interesting for several reasons. For instance, it allows to impose a rather strong smoothness assumption, which actually implies that a lot of sources are correlated to each other, at least to some small (i.e. non-zero) extent. The integration of such an assumption directly in R_q would be inefficient since a huge number of non-zero elements drastically reduces the sparsity of R_q. This is particularly problematic if the cortical sheet is approximated using a high spatial resolution grid. In contrast, W is always sparse since it defines a local smoothness criterion (i.e. it only depends on weighting neighboring sources), which is finally transformed into the global smoothness assumption by means of the efficient inversion of $W^T W$[3].

It can be summarized that Tikhonov approach provides an efficient way to impose assumptions on the spatial correlation structure by means of the weighting matrix W. This is particularly important for informed smoothness based methods (e.g. Knösche et al., 2013, see below), in which the degree of correlation depends on both the geodesic distance and the functional similarity between sources. However, it must be considered that the inverse of the squared weighting matrix only provides an estimate of R_q. Hence, it depends on the properties of W and the inversion procedure whether the estimated correlations are plausible. Equation 2.21 can be used to verify whether certain assumptions formulated by means of W lead to a desired correlation structure[4]. It will be shown in Section 3.3 that this is not always the case, particularly when functio-anatomical prior knowledge is employed.

This work utilizes both the Tikhonov regularization approach and the Bayesian solution. The latter one allows the definition of noise covariance matrix, while the former one provides an effect way to encode correlation assumptions. Therefore, Eq. 2.21 is substituted into 2.13. Hence, the linear solution which is used for simulations and experimental evaluation in this work defines as

$$\hat{q} = \left(W^T W\right)^+ L^T \left(L\left(W^T W\right)^+ L^T + \frac{1}{\sigma_q^2} C_\epsilon\right)^{-1} d. \tag{2.23}$$

Using Eq. 2.15 and the relationship $R_q = \left(W^T W\right)^+$, the estimation of σ_q^2 is straightforward.

2.4.5 Low Resolution Electromagnetic Tomography (LORETA)

As introduced above, the LORETA method, which has been put forward by Pascal-Marqui and colleagues (1995, 1994), exhibits a general spatial smoothness assumption. It is the basis for the informed smoothness based method proposed by Knösche et al. (2013) and, therefore, essential for the method presented in this thesis.

The general smoothness constraint is defined by means of a second order spatial derivative operator, i.e. the Laplacian $B \in \mathbb{R}^{m \times m}$. It encodes a functional dependence between neighboring sources in the weighting matrix W. In LORETA, the Laplacian is combined with a leadfield normalization operator, i.e.

$$W = B\Omega. \tag{2.24}$$

The definition for B depends on the underlying source space (see below). Given this, the full LORETA solution writes as

$$\hat{q} = \Omega^{-1}\left(B^T B\right)^+ \Omega^{-1} L^T \left(L\Omega^{-1}\left(B^T B\right)^+ \Omega^{-1} L^T + \frac{1}{\sigma_q^2} C_\epsilon\right)^{-1} d. \tag{2.25}$$

Since Ω is a diagonal matrix it is obvious that B imposes the correlation structure. This has already been pointed out by Pascual-Marqui (1995). In general, the Laplacian is defined as the

---

[3] The explicit calculation of the inverse would lead to a similar problem as directly defining R_q. However, the inverse does not have to be calculated for the solution of Eq. 2.18 since LU-decomposition can be applied to solve $(W^T W)^+ L^T$ (Golub and van Loan, 1996).

[4] In practice, this is only possible for source models that consist of a rather small number of sources. The explicit inversion of a matrix is computationally intensive and the inverse requires approximately $m^2 \cdot 4 \cdot 10^{-6}$ MB of memory.

divergence of the gradient. Its application to a scalar field of dipole magnitudes determines the strength of the variation of the magnitudes. Hence, the Laplacian actually constrains both the curvature and the norm of the spatially distributed source activity. The simultaneous minimization of these two constraints leads to a compromise between the activation of topologically close sources and those with similar leadfields (e.g. sources on opposite sides of a sulcus).

LORETA was originally introduced on a cubic grid with three orthogonal dipoles per node. Pascual-Marqui et al. (1994) approximated a Laplacian for such a grid using

$$\begin{aligned} B_{ii} &= -\frac{6}{r^2} \\ B_{ij} &= \frac{6}{r^2} \cdot \frac{6+|\Theta_i|}{12 \cdot |\Theta_i|} \quad j \in \Theta_i . \end{aligned} \tag{2.26}$$

Θ_i is the set of all dipoles that belong to the direct neighborhood of dipole i, $|\Theta_i|$ denotes the number of neighbors of i (usually six for inner voxels), and r the euclidean distance between two neighboring dipoles. Note that sources with a different number of neighbors (i.e. less than six) are treated differently. Knösche et al. (2013) demonstrated that this leads to a punishment of sources in edge, corner and surface voxels, i.e. activity is suppressed there. They introduced a row normalization of B to account for this issue (see below).

The fundamental assumption of LORETA is that close reconstruction points exhibit similar source activity. This was criticized since the actual scale of neural smoothness is different from the smoothness scale imposed by LORETA (Hämäläinen, 1995, Ilmoniemi, 1995, Nunez, 1995). In fact, the smoothness constraint has no neurophysiological justification at all, neither between neighbors on a volumetric source space nor between reconstruction points on a 2D hypersurface. The latter is often used to restrict the sources to the folded cortical sheet. The smoothness constraint is rather a means of expressing the inherent uncertainty of the neuroelectromagnetic inverse problem.

The approximation of a Laplacian on a folded source space is somewhat more difficult. Usually, distances and angles between neighbors vary on a triangulated grid (see Fig. 2.1). Moreover, the number of neighbors is not necessarily constant. While Pascual-Marqui (1995) presented an simplistic definition for B on a 2D surface, the operator proposed by Huiskamp (1991) is better suited and has actually been applied to LORETA on a folded cortical surface

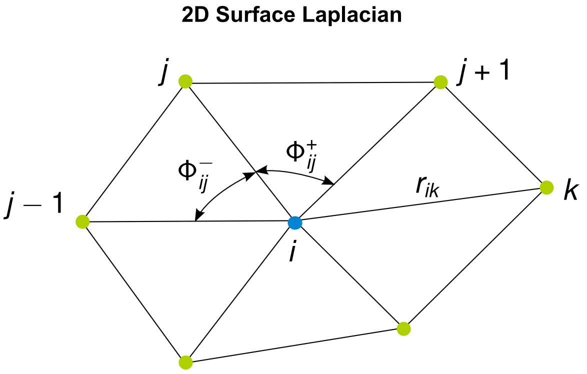

Figure 2.1: Approximation of a Laplacian on a triangulated 2D surface. Angles and distances are not constant, the number of neighbors can vary.

(Riera et al., 1996, Trujillo-Barreto et al., 2008). As already pointed out by Knösche et al. (2013), this operator is an approximation for a planar 2D grid, that means it disregards the curvature of the cortical surface. In order to minimize possible negative effects, the curvature between spatial neighbors should be as small as possible. This can be achieved by a sufficiently high spatial resolution.

Knösche et al. (2013) combined the Laplacian introduced by Huiskamp (1991) with the previously mentioned row normalization and proposed the surface Laplacian

$$\begin{aligned}
B_{ii} &= -1 - \lambda_B \\
B_{ij} &= \begin{cases} \dfrac{\gamma_{ij}}{\sum\limits_k \gamma_{ik}} & j,k \in \Theta_i \\ 0 & j,k \notin \Theta_i \end{cases} \qquad (2.27) \\
\gamma_{ij} &= \frac{\Phi_{ij}}{r_{ij}} = \frac{1}{r_{ij}} \left(\frac{1-\cos\Phi_{ij}^{+}}{\sin\Phi_{ij}^{+}} + \frac{1-\cos\Phi_{ij}^{-}}{\sin\Phi_{ij}^{-}} \right)
\end{aligned}$$

The angles Φ_i and distances r_{ij} are defined as depicted in Fig. 2.1. The regularization parameter λ_B is required since B is singular due to the normalization. Note that such a parameter was not required with previously introduced Laplacians (e.g. Huiskamp, 1991, Pascual-Marqui, 1995, Pascual-Marqui et al., 1994), because irregularities of the grid, e.g. a varying number of neighbors or varying distances between neighbors, actually embody regularization.

The normalization to the row sum of all off-diagonal elements is important for the 2D Laplacian. The potential differences between the number of neighbors is certainly not as large than on a cubic grid, for which a corner voxel with three neighbors has only half as much neighbors as an inner voxel with six neighbors. However, the 2D mesh is comprised of irregularities which may introduce an additional bias. The normalization accounts for both aspects and ensures the same overall weighting of each source. Moreover, this normalization becomes particularly important when the regular neighborhood is modified using prior knowledge (see Section 2.5.4, Knösche et al., 2013), which may lead to a rather large variation in the number of neighboring sources.

2.5 Prior Knowledge for the Source Covariance Matrix

2.5.1 Background

As introduced in Section 2.4, the source covariance matrix can be used to encode prior information for the localization of brain activity from EEG/MEG data by means of distributed source models. The diagonal entries control the probability for a source to be activated during reconstruction. Large values with respect to others increase this probability and vice versa. Off-diagonal elements can be used to encode functional similarity, that means if it is likely that two sources are concurrently activated. The methods mentioned in previous sections are based on rather arbitrary assumptions on source covariances. The subsequent sections deal with the integration of independent prior knowledge on source covariances drawn from functional measurements (Section 2.5.2) and from the functional organization of the cortex (Section 2.5.3).

The present work is focused on the use of functio-anatomical prior knowledge (see below), e.g. given by the functional organization in terms of a cortex parcellation. The use of such information for linear source reconstruction was proposed by Cottereau et al. (2012) and Knösche et al. (2013). Since their methods, i.e. FACE (Cottereau et al., 2012) and PatchLORETA (Knösche et al., 2013), are part of the evaluation in chapter 4, they will be outlined in Sections 2.5.5 and 2.5.4. Moreover, PatchLORETA is the basis for the method developed in this thesis introduced in chapter 3.

2.5.2 Encoding Functional Information into the Source Covariance Matrix

As introduced in Section 2.2.3, it can reasonably be assumed that the spatial distributions of electrical brain activity and hemodynamic changes during a given task are correlated. Hence, BOLD activity drawn from fMRI can be used to constrain EEG/MEG source reconstruction.

An alternative to the restriction of the source space, as it was outlined above, is to encode fMRI in the diagonal elements to constrain the source variances. Thus, regions with strong BOLD signals are preferred for reconstruction. This was proposed in several publications, e.g. Babiloni et al. (1998), Dale et al. (2000), Im et al. (2005a), Liu et al. (1998, 2002), Sato et al. (2004). A common strategy is to binarize the BOLD information using some threshold. Assuming zero variance for voxels without significant fMRI activity corresponds to the restriction of the source space proposed by Baillet and Garnero (1997). Since, however, the time scales of BOLD and neuroelectric activity are highly different, Liu and He (2008) presented a time dependent prior on the source variance. fMRI appears as a prior on the integrated source variance over a time window (averaged evoked response) and EEG data is used to retrieve the temporal variation of the source variance within this time window. Alternatively, one can employ the PEB framework introduced before to encode fMRI into multiple source covariance components (Henson et al., 2010, 2011). Since this framework usually employs a minimum norm like weighting in addition to the defined components, it does not require evidence from fMRI for a source to be reconstructed.

Besides the derivation of source variances, one can also account for the functional coupling between sources. This can be done by encoding the correlation between hemodynamic time courses in the off-diagonal elements of the source covariance matrix (Babiloni et al., 2002, 2003). Likewise to the PEB framework, this is an alternative to exclude sources without significant fMRI activity. An overview on integrating EEG/MEG source reconstruction with fMRI can be found in, e.g., Dale and Halgren (2001) and Liu et al. (2006).

All approaches that integrate fMRI into EEG/MEG source reconstruction imply a strong relation between BOLD and electrical source activity that might not always be justified for the following reasons. First, the paradigms for the imaging and EEG/MEG experiments are often different, even within the same study. Second, fMRI integrates activity mainly over time and EEG/MEG over space, that means time and spatial resolution, respectively, are fundamentally different. Third, the actual relationship between neural activity and the BOLD effect is still not fully known and certainly non-linear. Even if BOLD and EEG/MEG sources generally have good correlations, they have different origins and errors in one measure might bias the other (Nunez and Silberstein, 2000). Fourth, EEG and MEG reflect only part of the neural activity, namely temporally coherent activity of spatially aligned pyramidal cells. This restriction does not apply to fMRI or any other functional imaging method. A more reliable approach towards EEG/MEG and fMRI integration might be the establishment of joint generative source models (Babajani and Soltanian-Zadeh, 2006, Sotero and Trujillo-Barreto, 2008) with an inverse framework that explains both hemodynamic measurements and neuronal activity at the same time (Daunizeau et al., 2007).

2.5.3 Source Covariance Constraints drawn from the Functional Cortex Organization

On a microscopic scale, brain function is based on interacting neurons that influence each other due to biochemical and biophysical processes. On a macroscopic scale, a certain function usually exhibits correlated activation in a certain brain region (Durbin and Mitchison, 1990, Tononi et al., 1992) and, often, involves several areas. It is therefore reasonable to employ prior information on the functional similarity structure between sources in the brain, which can be effectively encoded in the source covariance matrix.

In principle, assumptions on similarity open a whole new world of possible sources for prior knowledge. While it is impossible to infer the neural activity from anatomical properties, like cytoarchitecture or long-range connectivity drawn by means of tractography methods (Behrens et al., 2003, Catani et al., 2002, Koch et al., 2002) from diffusion weighted MRI (dwMRI) (Beaulieu, 2002, Bihan et al., 2001, Mori and van Zijl, 2002, Pierpaoli et al., 1996), in a particular experimental condition, it is much more reasonable to assume that similar structural properties coincide with similar functional properties (Barbas and Rempel-Clower, 1997, Felleman and van Essen, 1991, Passingham et al., 2002).

Often, the similarity structure of functional or anatomical properties of the cortex is discontinuous, featuring structurally and functionally distinct areas with relatively constant properties, e.g. cytoarchitecture (Knösche and Tittgemeyer, 2011), separated by more or less sharp boundaries. Such a parcellation is known for cytoarchitecture (Brodmann, 1909), myeloarchitecture (Braitenberg, 1962, Vogt, 1910, 1911), and neurotransmitter receptor density (Zilles et al., 1996, 2004). Unfortunately, individual parcellations of the cortex based on these properties are only available post-mortem. The only possibility to utilize such information is the generation of standardized maps from empiric measurements that can be projected to the individual cortical surface. Today, individual parcellations are available in vivo. For example, long-range connectivity information drawn from dwMRI (Anwander et al., 2007, Johansen-Berg et al., 2004, 2005, Rushworth et al., 2006), correlation between BOLD signals drawn from task-related fMRI (Neumann et al., 2006), and low-frequency correlations in BOLD derived in the absence of any task (Wig et al., 2014), i.e. resting state functional connectivity (Biswal et al., 1995), has successfully been employed to derive parcellations of several parts of the human brain.

Parcellations can be utilized in different ways for source reconstruction. First, it is possible to assign a certain variance for all sources within a functional area (patch). For example, if there is any reason to assume that a certain region is likely to be active, the variance of the sources can be increased. Regions which are expected to be inactive can be attenuated by lowering the source variances. For example, Cottereau et al. (2012) increased the variance of sources in visual areas for the analysis of experimental data recorded under visual stimulation. Alternatively, the Bayesian model averaging (BMA) Trujillo-Barreto et al. (2004) framework employs one diagonal source covariance matrix for each patch and selects a certain combination of patches by means of the model evidence to represent the solution.

Second, a parcellation represents a functio-anatomical structure of the cortex which can be encoded in the off-diagonal elements of the source covariance matrix. This is based on the assumption that (neighboring) sources within a patch exhibit a certain degree of functional correlation, while sources in different regions are expected to be uncorrelated. Cottereau et al. (2012) (Section 2.5.5) and Knösche et al. (2013) (Section 2.5.4) pursued this idea and proposed different linear reconstruction schemes, where the functio-anatomical structure defined by the parcellation is effectively approximated in the covariance matrix. However, the particular encoding of the prior knowledge is different.

Changes of the functio-anatomical properties (similarity structure) of the tissue can also be expected at other functional borders, e.g. drawn from even purely macroanatomical information. There is evidence that some of the fundus lines of the major sulci, which can be extracted from individual MRI (Goualher et al., 1999, Kao et al., 2007, Tu et al., 2007), represent strong functional boundaries and, thus, clearly separate distinct functio-anatomical areas (Hinds et al., 2009, Toro and Burnod, 2005, Welker and Campos, 1963). This is supported by the theory that functional fields rapidly grow during the early development of the brain, which leads to the formation of gyri and, finally, renders fundus lines as functional borders between gyri (Sanides, 1962, Welker, 1990).

It is straightforward to employ functional borders similarly to parcellations for linear source reconstruction (Knösche et al., 2013), e.g. by encoding an approximation of the functional similarity structure in the off-diagonal elements of the source covariance matrix.

2.5.4 PatchLORETA: Informed LORETA-based Source Reconstruction

PatchLORETA (Knösche et al., 2013) allows the incorporation of a cortex parcellation into the linear inverse problem. It is based on a general smoothness assumption, that means close sources should exhibit similar activity. However, the smoothness is expected to end at boundaries between adjacent functio-anatomical sites.

The method utilizes a spatial derivative operator, i.e. a Laplacian as defined in LORETA, which imposes a smoothness constraint on the solution. The smoothness constraint is bro-

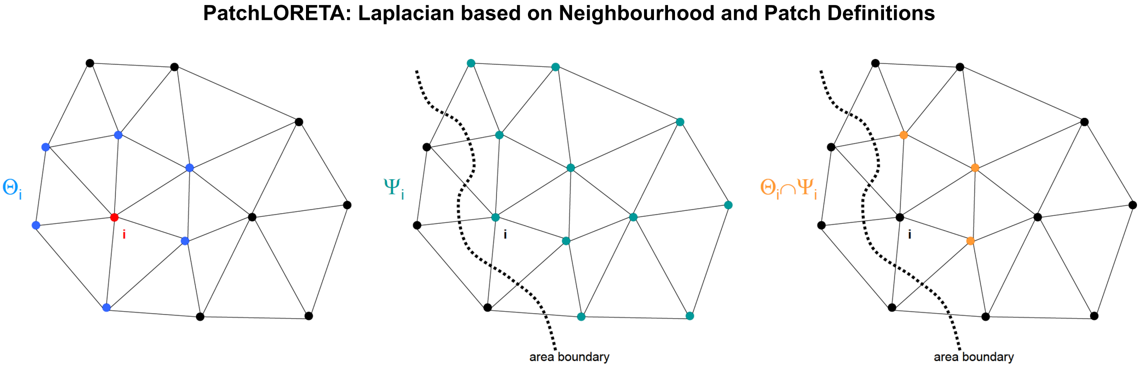

Figure 2.2: Neighborhood and patch definitions for PatchLORETA. Left: topological neighborhood of node i (blue), middle: patch affiliation including node i (petrol), right: intersection of neighborhood and patch affiliation defines modified neighborhood for PatchLORETA1 (orange). Reprinted from Knösche et al. (2013) with permission from Elsevier.

ken up at patch boundaries. This Laplacian is modified according to patch affiliations drawn from parcellations. Two derivations of the algorithm were proposed: PatchLORETA1 effectively lifts the smoothness criterion at patch boundaries while preserving smoothness within patches. PatchLORETA2 extends the smoothness criterion by treating all sources within a patch as neighbors.

In general, PatchLORETA is based on definitions for the topological neighborhood Θ_i and the patch belonging Ψ_i for each node. The former contains all direct grid neighbors of node i (Fig. 2.2, left). The latter is a patch definition which contains all nodes of the patch in which i is located (Fig. 2.2, middle).

PatchLORETA1 is based on the Laplacian in Eq. 2.27, however, with a modification of the neighborhood definition. Given Θ_i and Ψ_i, the intersection $\Xi_i = \Theta_i \bigcap \Psi_i$ determines a modified neighborhood (Fig. 2.2, right), which replaces the node neighborhood Θ_i in the definition for the surface Laplacian. This effectively lifts the spatial smoothness constraint at patch boundaries, that means it allows a more or less independent activation of different functional units.

PatchLORETA2 completely ignores the topological neighborhood and only accounts for the patch belonging Ψ_i. This is used to define the patch neighborhood of node i, i.e. $\Xi_i = \Psi_i - \{i\}$. This way, all nodes in the same patch as i are defined as (direct) functional neighbors of node i. The Laplacian now defines to (Knösche et al., 2013)

$$\begin{aligned} B_{ii} &= -1 - \lambda_B \\ B_{ij} &= \begin{cases} \dfrac{1}{|\Xi_i|} & j \in \Xi_i \\ 0 & j \notin \Xi_i \end{cases}, \end{aligned} \tag{2.28}$$

with $|\Xi_i|$ being the number of patch neighbors of i. Compared to PatchLORETA1, this definitions imposes a much stronger intra patch-correlation constraint.

2.5.5 FACE: Informed Correlation-based Linear Source Reconstruction

Cottereau et al. (2012) proposed a linear reconstruction scheme (Eq. 2.13) which is based on a so called functional area constrained estimator (FACE). It aims at constraining brain activity to functional areas. Information on the functio-anatomical organization of the cortex is directly encoded into the source covariance matrix. While they derived information on the functional organization from retinotopic maps of the visual field drawn from fMRI, their method can be used with any parcellation.

Given is a set of K distinct regions defined by a parcellation, each consisting of m_k sources with $\sum_{k=1}^{K} m_k \leq m$. All sources in area k span the submatrix R_k in the full normalized covariance matrix R_q. The diagonal elements in R_q are defined according to, e.g., the minimum norm constraint, i.e. $R_q = I$. The off-diagonal elements in R_k can be used to introduce functional correlations between sources in k. The correlation $R_k(i,j)$ for each pair (i,j) of sources can be modeled by a function $f(d_{ij})$ of their distance d_{ij}. For the sense of simplicity, the distance measure is realized in terms of 1^{st} or 2^{nd} order neighborhood relationship. Then, the submatrix R_k of R_q for a region defines as

$$R_k(i,j)_{i\neq j} \quad = \begin{cases} \alpha_1 & \text{if} j \in N_i(1), \\ \alpha_2 & \text{if} j \in N_i(2), \\ 0 & \text{otherwise}, \end{cases} \tag{2.29}$$

with $\alpha_2 \leq \alpha_1 \leq 1$ encoding the strength of the correlation. $N_i(1)$ contains the set of sources in region k which are directly connected to i. $N_i(2)$ contains the neighbors of the sources in $N_i(1)$, except both i itself and those which are already connected to i. Based on this definition, Cottereau et al. (2012) distinguished between two different algorithms: (1) Focal FACE with rather small scaling parameter values, i.e. $\alpha_1 = 0.2$ and $\alpha_2 = 0.1$, to enforce focal solutions. (2) Extended FACE with larger values, i.e. $\alpha_1 = 0.6$ and $\alpha_2 = 0.4$ to obtain a more widespread reconstruction.

Moreover, Cottereau et al. (2012) proposed to prefer sources within predefined functional regions by increasing their *a priori* variance using

$$R_k(i,i) = \alpha. \tag{2.30}$$

Again, two algorithms were distinguished: (1) Autocorrelated FACE which does not consider the correlations defined in Eq. 2.29. (2) Combined FACE where the submatrix R_k is composed of Eq. 2.29 and 2.30. Note that information on α is not derived from the parcellation but only from arbitrary assumptions on regions that are likely to be active due to the particular experimental paradigm.

3 Generalization of Informed LORETA-based Source Reconstruction

3.1 Introductory Remarks, PatchLORETA's limits

The PatchLORETA method proposed by Knösche et al. (2013) can be used to incorporate parcellations into the linear inverse problem. It is an efficient alternative to the FACE method Cottereau et al. (2012), in which functio-anatomical information (i.e. derived from parcellations) is directly encoded by means of correlations. However, its original definition as presented in Sec. 2.5.4 has certain limitations and problems, which are summarized briefly below. Content of this chapter is to solve these issues and to provide a generalized informed LORETA-based source reconstruction method.

PatchLORETA is limited to the use of parcellations since the incorporation of prior information is based on the affiliation of sources to patches. This means that only patch boundaries can be used to introduce discontinuities in the local similarity structure. However, changes of the functio-anatomical properties of the tissue can also be expected at other functional borders, e.g. drawn from purely macroanatomical information (cmp. Sec. 2.5.3). The extension presented in Sec. 3.2 allows to utilize alternative information on functio-anatomical cortex organization by means of a mutual similarity parameter. This allows the use of general functional boundaries and even supports the usage of non-binary (i.e. gradual) prior knowledge. The latter, however, is not straightforward, which is also discussed in this section.

Generally, linear inverse methods are based on the definition of a source covariance matrix to pose *a priori* assumptions or to integrate prior information. In LORETA - and PatchLORETA as well - this matrix is not defined directly but estimated by means of the inversion of a Laplace operator. It turned out that this inversion introduces an additional bias to each source. This bias apparently depends on the size of the patch in which a source is located. This emphasizes that it is necessary to investigate the estimation of the covariance matrix more closely before spatially informed LORETA-based methods can safely be used for source reconstruction. Section 3.3 starts with considering some basic properties of the Laplace operator and inevitably properties of its inverse, which is major component of the source covariance matrix. Subsequently, it is analyzed how modifications of the smoothness constraint specifically affect the source covariance matrix. The particular focus lies on the question whether the estimated (co-)variances are, in fact, consistent with the prior assumptions expressed in the smoothness operator. Moreover, an additional normalization operator is introduced which accounts for major artifacts.

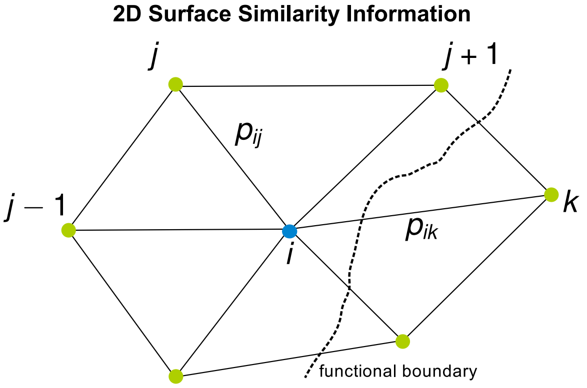

Figure 3.1: Encoding of prior information on the local functional similarity using the mutual similarity parameter p. Here, a low similarity value would be assigned to edges crossed by the functional border, e.g. edge $\overline{ik}$.

The inversion of the Laplacian requires regularization. The regularization parameter has a fixed heuristically chosen value in PatchLORETA. The careful selection of this parameter is, however, of crucial importance. It controls the strength of the smoothness constraint and, therefore, strongly influences the estimated correlation structure. A method to adjust this parameter is presented in Sec. 3.4. It ensures that the estimated correlations are independent of the spatial resolution of the source space.

3.2 Mutual Similarity based Formulation of Spatially Informed LORETA

3.2.1 Surface Laplacian with Similarity Information

The Laplace operator used in LORETA-based inverse methods imposes a smoothness constraint on the solution, that means, it introduces a functional dependency between neighboring sources. Its modification according to the patch affiliation of sources proposed in PatchLORETA aims at lifting the smoothness constraint at patch boundaries. Here, a more general approach is proposed. It even allows to use alternative functio-anatomical prior information such as, in particular, the course of functional boundaries.

The basis for the proposed extension is the introduction of the similarity parameter p_{ij}. It defines the *a priori* mutual functional similarity between directly neighboring sources, i.e. i and j. Hence, a unique similarity value is assigned to each edge of the mesh that approximates the cortical surface (see Fig. 3.1). The combination of the mutual similarity p_{ij} with the topological neighborhood Φ_i changes the Laplacian defined in Eq. 2.27 to:

$$\begin{aligned} B_{ii} &= -1 \\ B_{ij} &= \begin{cases} \dfrac{p_{ij}\gamma_{ij}}{\sum\limits_k p_{ik}\gamma_{ik}} & j,k \in \Theta_i; p_{ij} \in [0,1] \\ 0 & j,k \notin \Theta_i \end{cases} \\ \gamma_{ij} &= \frac{1}{r_{ij}} \left(\frac{1-\cos\Phi^+_{ij}}{\sin\Phi^+_{ij}} + \frac{1-\cos\Phi^-_{ij}}{\sin\Phi^-_{ij}} \right) \end{aligned} \tag{3.1}$$

Angles Φ_i and distances r_{ij} are defined as depicted in Fig. 2.1. The off-diagonal elements in B define the effective weighting between neighboring sources. Here, this weighting depends on both common geometrical properties and *a priori* assumptions on their neural activity.

The similarity parameter has the following effect: If, on the one hand, $p_{ij} = \text{const.} \forall j \in \Theta_i$, the weighting for node i corresponds to the uninformed LORETA surface Laplacian (Eq. 2.27). This means that only geometrical properties of the mesh are relevant. If, on the other hand, $p_{ik} < p_{ij}$ for $j, k \in \Theta_i$, the impact of neighbor k on source i is reduced relative to the impact of j on i. This lifts the spatial smoothness constraint in the direction of k. The relative weighting is important and will be discussed more detailed in Section 3.2.2.

Note that the Laplacian regularization parameter λ_B (cmp. Eq. 2.27) vanished from the definition of the Laplacian presented in Eq. 3.1. Regularization is now directly applied to the estimator of the source correlation structure (cmp. Sections 2.4.4 and 2.4.5), i.e.

$$(B^T B)^+ = (B^T B + \lambda_B I)^{-1}. \tag{3.2}$$

While this is only a minor modification, it allows a slightly simpler notation of both the full inverse solution (Eq. 2.25) and of the Laplacian normalization matrix, which is introduced in Section 3.3.6 of this thesis.

The following section discusses the actual effect of encoding similarity information in the Laplacian. Section 3.2.3 considers the question how such information can be derived from available functio-anatomical knowledge.

3.2.2 Possibilities and Limitations for Encoding Mutual Similarity

The introduction of a continuous similarity parameter allows the incorporation of gradual rather than only binary similarity information. Hence, any value between zero and one can be used to describe the *a priori* functional similarity between anatomically connected sources. A parameter value less than one reduces the functional connection between two sources. However, the actual smoothness constraint that results when adjusting this value also depends on the similarity parameters used for all other sources in the neighborhood. This follows from the fact that off-diagonal elements in the Laplacian are normalized to the corresponding row sum (cmp. Eq. 3.1).

As already stated in Section 3.2.1, Eq. 3.1 implies the same weighting for the i^{th} source as the uninformed surface LORETA operator (Eq. 2.27) in case that all similarity parameters in its neighborhood are equal, i.e. $p_{ij} = \text{const.} \forall j \in \Theta_i$. Given that, the following two scenarios can be considered. Suppose that prior knowledge provides evidence that a source exhibits maximum functional similarity with its neighbors (i.e. $p_{ij} = 1$). Applying this information to the Laplacian leads to a smoothness constraint that is consistent to the prior. Now, let the *a priori* similarity between all neighboring sources be almost zero and equal[1]. The neighbors are now considered to be similar since the smoothness constraint is preserved. This clearly reflects a contradiction to the imposed prior knowledge. Note that this characteristic holds for any value of p, that means equal similarity between a source and its neighbors results in the maximum smoothness constraint. The strength of the contradiction between the smoothness constraint and prior

---

[1] $p_{ij} = 0 \forall j \in \Theta_i$ would introduce division by zero and render Eq. 3.1 invalid.

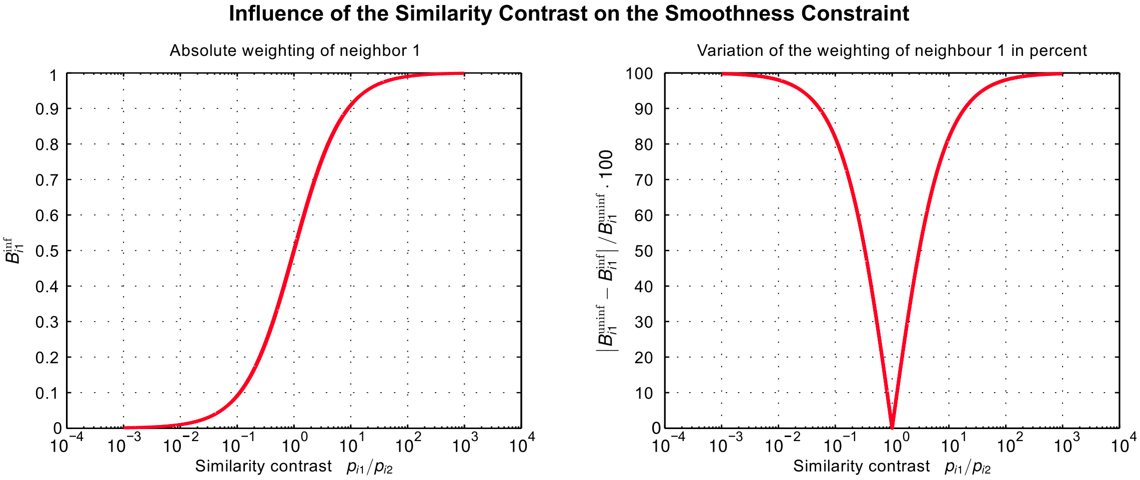

Figure 3.2: Effect of similarity based weighting on the Laplacian demonstrated using a toy example (see text). The superscripts *inf* and *uninf* refer to informed LORETA and uninformed LORETA, respectively.

knowledge increases for lower values of p.

The following toy example illustrates similarity based weighting. Given is a source with only two neighbors. The two geometrical weighting parameters are assumed to be identical, i.e. $\gamma_{i1} = \gamma_{i2} = 0.5$. The corresponding *a priori* functio-anatomical similarity is defined by the parameters p_{i1} and p_{i2}. The ratio between these two parameters, i.e. p_{i1}/p_{i2}, reflects the similarity contrast in the neighborhood of source i. Given that, the Laplacian B is evaluated with respect to this contrast. The result is shown in Fig. 3.2. The left panel shows the resulting absolute weighting (i.e. the off-diagonal element in the Laplacian) of the first neighbor. The right panel illustrates how strong the weighting on source i changes compared to the uninformed Laplacian (Eq. 2.27). The main findings are:

1. The similarity parameters have no impact on the Laplacian if their values are equal, i.e. $B_{i1}^{\text{inf}} = B_{i1}^{\text{uninf}} = 0.5$ for $p_{i1} = p_{i2}$.
2. The absolute weighting of a neighbor varies between 0 (e.g. $p_{i1} << p_{i2}$) and 1 (e.g. $p_{i1} >> p_{i2}$). Thus, a sufficiently large ratio between both parameters suppresses the impact of one neighbor.
3. A major impact on the smoothness constraint can only be observed in case of a high similarity contrast. For example, the ratio $p_{i1}/p_{i2} = 1:2$ leads to an absolute weighting of $B_{i1}^{\text{inf}} = 0.35$. This corresponds to a change of only 30 % with respect to the case of equal similarities. In other words, both neighbors still have a strong influence. A significant change of 90 % requires a much stronger ratio of $p_{i1}/p_{i2} = 1:19$. This emphasizes that a rather strong similarity contrast is required to affect the smoothness constraint. Prior knowledge that implies more or less balanced similarity information (i.e. parameters in the same order of magnitude) is ineffective. From this perspective, the use of gradual similarity information is inappropriate.

It is straightforward to generalize these findings for realistic meshes with more than two neighbors per source. Finally, the possibilities to incorporate prior knowledge can be summarized as follows. Equation 3.1 allows to incorporate quantitative similarity information. Due to the row normalization in the Laplacian, however, its actual effect depends on the similarity contrast in the neighborhood of each source[2]. When the contrast is low, the smoothness constraint is almost unaffected since all weights of all neighbors become similar. This effect is independent from the absolute similarity values. More importantly, the smoothness constraint expressed by the Laplacian is only consistent with prior knowledge if the functional similarity between a source and at least one of its neighbors is high. It follows that cases where the similarities in the whole neighborhood are low must be prevented[3], for instance by using a sufficiently high spatial resolution of the mesh.

3.2.3 Derivation of Prior Information on Mutual Similarity

In principle, similarity information could be derived from various types of prior knowledge as, for example, functio-anatomical properties, correlation between fMRI time courses, and correlation between long-range connectivity patterns. The Laplace operator as given in Eq. 3.1 requires the definition of a similarity value for each edge of the mesh. However, it is difficult - if not impossible - to derive such fine-grained information for each pair of neighboring sources on the whole cortical surface. Neither do imaging modalities provide suitable similarity parameters on a high spatial resolution, nor does the mapping of more general functional knowledge on the individual cortical surface, for instance derived from a cytoarchitectonic parcellation, provide such information. Available prior knowledge must therefore be utilized differently.

A suitable technique that has already been used by Knösche et al. (2013) is to assume similarity between all neighbors ($p_{ij} = 1$) unless it is evident from prior knowledge that neighboring sources are functionally different. In such a case, p_{ij} is reduced and the smoothness constraint lowers accordingly. Thus, only information on the course of functional similarity borders rather than detailed information on the *a priori* functio-anatomical similarity for each reconstruction point is required. A special case of this approach is to use a binary similarity measure, that means $p_{ij} = 0$ at functional borders and $p_{ij} = 1$ elsewhere. This ensures a maximum similarity contrast. Fig. 3.3 illustrates the influence of functional boundaries on the Laplacian in analogy to Fig. 2.2.

Prior knowledge must provide information on sharp boundaries to follow this approach. Such information can be derived from various sources. It is generally accepted that functional correlation between sources inside homogeneous cytoarchitectonic areas is much higher than between sources that belong to different regions (Fischl et al., 2008, Hasnain et al., 2001). Therefore, the outline of such areas (e.g. drawn from a parcellation) can be taken as a functio-anatomical border which separates nodes inside a patch from all others on the cortical surface. In PatchLORETA, these borders are indirectly expressed by means of patch affiliations. The similarity parameter introduced in this work allows to directly encode the boundaries. Moreover, it is now possible to use only a part of the outline of a patch as a functional border, while the other part of the patch boundary can be ignored. This could be used, for instance, to incorporate only boundaries between neighboring patches which are functionally different. Boundaries between neighboring patches which have a similar function, or for which only poor prior infor-

---

[2] Renouncing row normalization would ensure an absolute impact of prior information, but it would also introduce a similarity dependent bias of sources (cmp. Section 2.4.5).

[3] Anyway, this case would require some regularization to prevent false high similarity contrast.

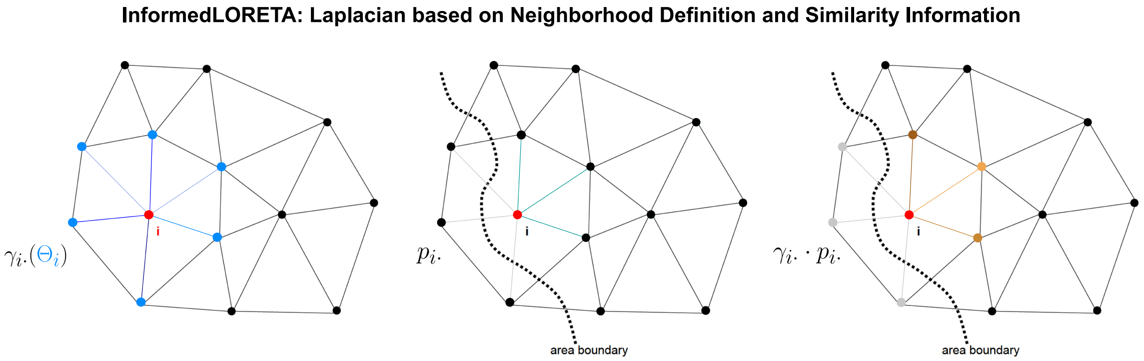

Figure 3.3: Edge based weighting used in the Laplace operator defined in Eq. 3.1. Left: Edge weights for node i derived from the topological neighborhood (blue, varying edge colors due to grid inhomogeneities). Middle: Edge weights for node i derived from prior information (petrol = edges connecting nodes in the same functional entity as i, gray = edges between nodes with no similar function). Right: Combining topological and prior based weighting reveals a new neighborhood weighting for i (orange). Adapted from Knösche et al. (2013).

mation on the similarity is available, can be omitted. The fundus lines are of the major sulci are another source for this kind of priors. There is evidence that these lines represent strong functional boundaries and, thus, clearly separate distinct functio-anatomical areas (Hinds et al., 2009, Welker and Campos, 1963). Fundus lines can automatically be extracted from individual MRI datasets (Lohmann, 1998, Seong et al., 2010, Troter et al., 2012).

It can be summarized that the limitation of similarity based encoding of functio-anatomical prior knowledge to boundaries is useful for several reasons. First, it ensures a high similarity contrast between different functional sites. Therefore, prior knowledge has a strong effect on the Laplacian. Second, drawing information on the course of functional boundaries seems to be much easier than deriving similarity information for all neighbors on the cortex. In contrast to PatchLORETA, similarity based weighting allows the explicit definition of boundaries. That means that it is possible to follow any boundary on the cortical surface for which a strong discontinuity of the functional similarity between neighboring sources can be expected. Although Eq. 3.1 introduces the possibility to utilize any similarity measure, the studies and evaluations in this work are limited to the use of binary similarity information. Such knowledge is easily available and the strongest effects can be expected.

3.3 Plausibility of LORETA-based Source Covariance Matrix Estimates

3.3.1 Motivation

LORETA-based source reconstruction methods involve the estimation of the source covariance matrix by means of Laplacian inversion (cmp. Sec. 2.4.4). In this inversion process, the smoothness constraint is transformed into a kind of correlation information. More precisely, the correlation between all pairs of sources is predicted. The correlation between two sources is expected to decrease the more distant they are. Since, however, the inversion is a highly non-linear procedure, it needs to be ensured that the covariance matrix estimate is consistent with the *a priori* assumption expressed by the Laplacian. In particular, the question needs to be answered whether the modification of the Laplacian, which is a key concept in informed

LORETA, can lead to a somehow inconsistent matrix estimate as, for instance, an undesired bias of sources. In fact, Knösche et al. (2013) raised concerns that sources in small patches might be less constrained by the smoothness criterion with respect to sources in larger patches. This would correspond to an undesired and patch size dependent bias of sources. So far, however, no effort was made to investigate this issue. In their study, such errors were prevented by using the simplification that all patches are equal in size. The application of informed LORETA to a realistically shaped folded cortical surface, which is comprised of differently sized and shaped functional areas, requires a closer examination of the covariance matrix estimation based on Laplacian inversion. This is looked at in the subsequent sections.

To study this issue, the source covariance matrix must explicitly be derived. In other words, the calculation of the inverse matrix as defined in Eq. 3.2 is necessary. Note that this is generally not required to solve the linear inverse problem (cmp. Eq. 2.25). This calculation is, however, not trivial for practical reasons. The inversion is highly computationally expensive, that means the typical complexity to calculate the full inverse of matrix $A \in \mathbb{R}^{n\times n}$ is $\mathcal{O}(n^3)$. Moreover, the inverse matrix is usually dense, that means that at least about n^2 elements need to be stored in memory. It is due to these restrictions that the verification of the estimated source covariance matrix is virtually impossible for realistic grids (i.e. with typically more than 200 000 sources). Moreover, drawing relations between the Laplacian and the covariance matrix is more difficult for complex grids (as, for example, the folded cortical surface). For these reasons, and without the loss of generality, the following investigations are restricted to the use of (1) simple toy and test examples for which the LORETA-based normalized source covariance matrix $R_q = \Omega^{-1}(B^TB)^{+}\Omega^{-1}$ can be directly calculated. Furthermore, (2) leadfield normalization is omitted by using $\Omega = I$, i.e. $R_q = (B^TB)^{+} = (B^TB + \lambda_B I)^{-1}$.

3.3.2 Properties of the LORETA-based Source Covariance Matrix

The basis for the estimation of the source covariance matrix R_q is the smoothness constraint as defined in the Tikhonov regularization approach (see Eq. 2.17), , i.e. $\arg\min_q \|Bq\|_2^2$. The Laplacian B introduces a functional coupling between neighboring sources. The i^{th} row in $R_q = (B^TB+\lambda_B I)^{-1}$ corresponds to the point spread function (PSF) of the i^{th} source, that means the i^{th} row describes the activity pattern arising through the activation of source i. Obviously, a uniform activation of all sources minimizes the penalty term. In this case, all covariances would be constant. The estimation of R_q is mainly influenced by (1) Laplacian regularization using λ_B and (2) the modification of the smoothness criterion using the functional similarity parameter p_{ij}. This has consequences for the resulting source covariances:

1. The regularization parameter λ_B controls the balance between main and off-diagonal elements in the Laplacian. The larger its value, the smaller amplitudes of the neighboring sources are required to minimize the penalty term. In other words, the smoothness constraint is reduced in this case. Consequently, the covariances in the PSF decrease towards larger distances between sources.

2. Regularization has another implication for R_q. Since each row sum in $(B^TB+\lambda_B I)$ equals λ_B, each row sum in R_q equals $1/\lambda_B$. This relationship can be derived as follows. The row sums of the symmetric matrix $A = A^T = (B^TB + \lambda_B I)$, $A \in \mathbb{R}^{m\times m}$ can be expressed as

$At = \lambda_B t$, with $t \in \mathbb{R}^m$ and $t_i = 1 \;\; \forall i = 1 \ldots m$. Similarly, $A^{-1} t = x$, $x \in \mathbb{R}^m$ defines the row sums of the inverse. The right handside multiplication of both equations reveals

$$Att^T \left(A^{-1}\right)^T = \lambda_B t x^T \tag{3.3}$$

Since the expression on the left handside is symmetric, the resulting matrix on the right handside is symmetric too. From that it follows that all elements in x must be equal. The left handside multiplication of above equations results in

$$t^T A^T A^{-1} t = \lambda_B t^T x. \tag{3.4}$$

Since $A^T A^{-1} = I$ and $t^T t = m$, this can be written

$$m = \lambda_B \sum_i^m x_i. \tag{3.5}$$

Finally, applying the constraint derived from Eq. 3.3 that all elements in x are equal, i.e. $\sum_i^m x_i = m x_i$, leads to the final relation $x_i = 1/\lambda_B$. It is shown below that this relation significantly influences the source variances and covariance estimates.

3. Another effect of Laplacian regularization is that the covariance $R_{q_{ij}}$ can be negative. This occurs if the corresponding element in the Laplacian (i.e. B_{ij}) is zero and if $\lambda_B > 0$ exceeds a certain threshold[4]. A negative covariance between two sources implies that their activity is shifted by a phase of 180°. However, such an *a priori* assumption cannot be drawn by means of functio-anatomical prior knowledge. In this respect, the LORETA-based source covariance matrix estimation introduces implausible *a priori* assumptions. Therefore, it needs to be considered whether strong artifacts must be expected by this effect.

4. The similarity parameter p_{ij} controls the functional coupling between neighboring sources. It is used to introduce discontinuities in the similarity structure. As a consequence, the PSF in R_q is different for each source. More precisely, a particular PSF strongly depends on the geodesic distance of a source to a discontinuity. For example, a source with a relatively large distance will have a homogeneous covariance structure in its vicinity, whereas the PSF for a source close to a discontinuity is anisotropic. This is discussed in more detail below.

Based on these general properties it is possible to substantiate the assumptions on (co-)variances estimated in informed LORETA when a binary similarity measure is used[5]. These assumptions are briefly summarized below and discussed in more detail subsequently using several toy examples.

Firstly, the estimated variance of a source depends on its distance to a discontinuity (i.e. a cut) in the similarity structure. This is due to the fact that the row sums in the covariance matrix

---

[4] A practical approach to verify this statement is given in appendix A.1.

[5] This is much more difficult for the use of gradual similarity information. It is hardly possible to express a believe on the point spread function for any non-sharp similarity contrast. Besides that, the full *a priori* similarity model is different even if only one similarity value p_{ij} changes. Since Laplacian regularization always affects the whole model, comparisons using, for instance, test examples are not straightforward.

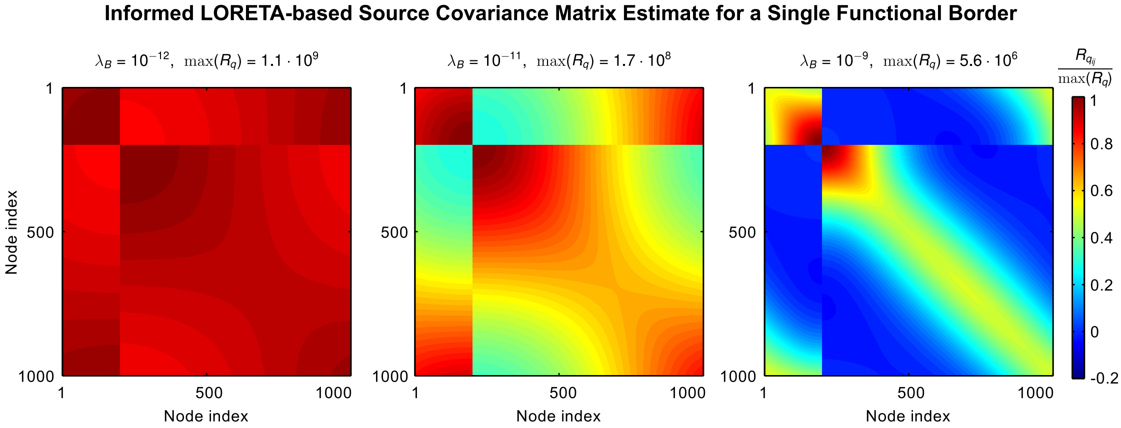

Figure 3.4: Estimated source covariance matrix for different λ_B. The values correspond to a strong smoothness constraint on the left and a weaker constraint on the right. Each matrix is normalized to its maximum, i.e. $\max(R_q)$. The matrix elements are color coded. All results refer to the same color bar. Arbitrary units.

are constant (item 2), and that the covariance structure is inhomogeneous (item 4). Particularly sources close to a discontinuity will have larger variances than other ones. Secondly, it also follows from these two aspects that the variances of sources located in fully separated areas (i.e. patches) depend on the patch size. Larger source variances can be expected in smaller patches. Thirdly, the fact that Laplacian regularization renders the covariance as a function of the distance between sources (item 1) implies that negative covariances (item 3) have rather small absolute values in R_q with respect to positive covariances. By analogy with filter theory, negative covariances in connection with the smoothness constraint can also be explained with the well known overshoot of low pass filters at the transition from pass to stop band. It is therefore likely that this implausible *a priori* assumption has only a weak impact.

3.3.3 General Effect of Discontinuities in the Similarity Structure

The objective of this section is to examine how discontinuities in the similarity structure actually influence the estimation of the source covariance matrix. The toy example used for this purpose is based on a one-dimensional annular grid consisting of 1000 nodes (node index increases in clockwise direction). According to Eq. 3.1, the LORETA Laplacian for node i with its left and right neighbor j and k (i.e. $p_{ij} = p_{ik} = 1$ and $\gamma_{ij} = \gamma_{ik} = 1$) defines as $B_{ii} = -1$ and $B_{ij} = B_{ik} = 0.5$.

This grid is now cut at one position, for example $v = 200$. The *a priori* similarities are $p_{v,v+1} = p_{v+1,v} = 0$. The Laplacian at index v changes to $B_{v,v} = -1$, $B_{v,v-1} = 1$ and $B_{v,v+1} = 0$, and for the index $(v+1)$ to $B_{v+1,v+1} = -1$, $B_{v+1,v} = 0$ and $B_{v+1,v+2} = 1$. This means that nodes v and $v+1$ are no more directly coupled.

Figure 3.4 shows the estimated source covariance matrix R_q for three different values of λ_B. The smallest regularization parameter implies the strongest smoothness constraint. As expected, the variances are not constant and the covariance structure is inhomogeneous. In particular, it can be seen that the variance of a source depends on its shortest distance to the interruption of the grid. The larger this distance, the smaller the variance. This becomes even

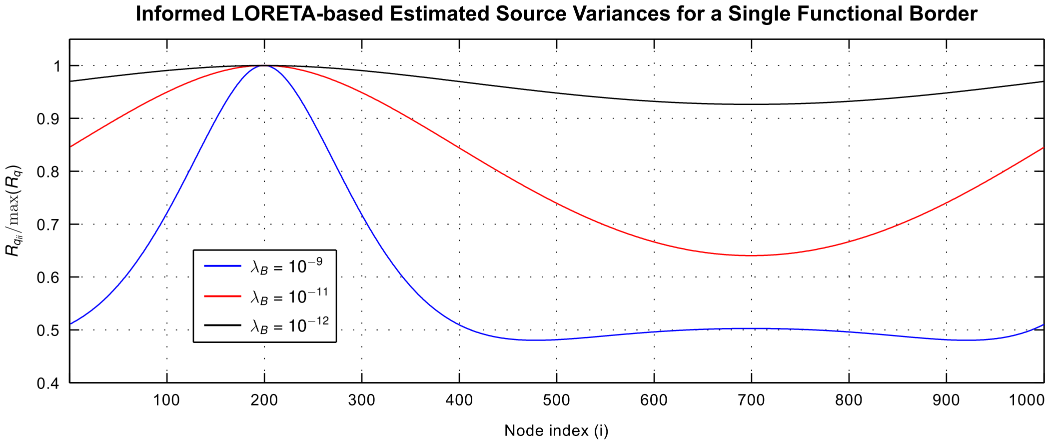

Figure 3.5: Main diagonal elements of R_q for different λ_B. The values for each curve are normalized to the corresponding $\max(R_q)$. The discontinuity in the similarity structure is at node $i = 200$. Arbitrary units.

more obvious in Fig. 3.5, which only shows the source variances. Another important aspect can be noticed. The ratio between the minimum and maximum variance reduces when the regularization becomes stronger. However, it does not significantly drop below ≈0.5 but rather converges towards this value. This corresponds to the strongest bias that can occur on the one-dimensional grid given that only a single cut is used to modify the Laplacian. The variance bias and its particular dependence on regularization is a direct result of equal row sums in R_q and of the anisotropy of the smoothness constraint. It can be explained as follows.

First, it is assumed that the regularization parameter λ_B has a large value (right matrix in Fig. 3.4). In this case the covariances decrease to zero in each row of R_q. It can be seen that the covariance structure is more or less symmetric for sources which have a large distance to a cut (i.e. the covariance continuously decreases in both directions). That means, the functional similarity unfolds into both grid directions roughly in the same manner. This implies that always two sources in a row of R_q have a very similar covariance. In contrast, the functional similarity for sources close to a cut unfolds into only one grid direction. As a consequence, the covariance in a certain distance is unique in such a row. However, the row sum must be constant in both cases. This is only possible if the variance and the corresponding covariances are larger in the latter case. More precisely, they must be twice as large as for the source with the largest distance to the cut. Therefore, it can be concluded that the variance of sources which are close to a cut is larger than the variance of sources with a larger distance. Moreover, the smallest possible ratio between the minimum and maximum variance depends on the number of neighboring sources. Since each source has two neighbors in the given toy example, the smallest ratio is ≈0.5.

In the previously discussed case (i.e. strong regularization), each row contains a different number of covariances which are zero. Now it is assumed that the regularization parameter λ_B is reduced. As a consequence, more and more elements in R_q become non-zero. This effect continues until all elements are non-zero in a particular row (i.e. $R_{q_{i\cdot}}/R_{q_{ii}} > 0$). It will first appear in the row that belongs to the source with the largest distance to the cut (that means, rows of closer sources still contain covariances being zero). This can be explained with the de-

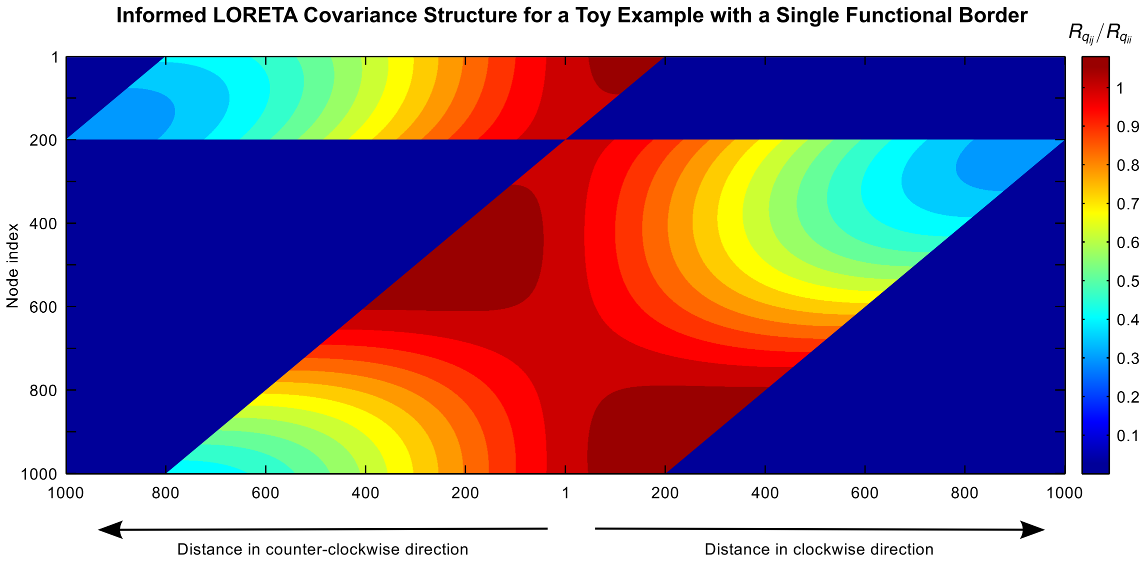

Figure 3.6: Source covariance structure derived from R_q ($\lambda_B = 1 \times 10^{-11}$, see Fig. 3.4, middle panel) using the following procedure: (1) Normalization of each element in the i$^{\text{th}}$ row (i.e. $R_{q_{ij}}$) to the corresponding variance $R_{q_{ii}}$, (2) centering each row to the main diagonal element $R_{q_{ii}}$, (3) rearrangement of the row elements such that sources in clockwise direction (towards the cut at $i = 200$) are located in the right part of the figure (i.e. sources in counterclockwise direction in the left part). The normalized matrix elements are color coded. Arbitrary units.

pendence of the covariance structure for a given source on its distance to the cut. A further reduction of λ_B causes larger row sums in R_q and, therefore, leads to an increases of all elements (i.e. the variance and covariances) in this row. Consequently, the variance bias in R_q reduces (i.e. variances become more balanced, cmp. Fig. 3.5). It completely disappears for a sufficiently small λ_B. This is almost the case for the weakest regularization in Fig. 3.4.

It is useful to remove the variance bias to study further effects on the covariance structure. This can be achieved by normalizing all row elements, i.e. $R_{q_{i.}}$ in the i^{th} row, to the corresponding variance, i.e. $R_{q_{ii}}$. Moreover, it is useful to distinguish between a covariance structure in clockwise and counterclockwise direction. This can be done separately for each source. The starting point for the direction dependent assessment of the covariance is the source position. The interruption of the grid marks the endpoint. The distance between the two sources whose connection is cut corresponds to the maximum possible distance in each direction. Fig. 3.6 shows the direction dependent covariance structure for R_q with $\lambda_B = 1 \times 10^{-11}$. The following conclusions can be drawn:

1. Assuming zero similarity between two sources when constructing the Laplacian does not necessarily imply that their estimated correlation is zero too. For example, row 199 of R_q reveals that the covariance between the sources 199 and 200 (i.e. at a distance of 1000 sources) is ≈ 0.3. Hence, the functional similarity between the two sources is not fully lifted in this case. The estimated covariance rather depends on Laplacian regularization, which controls the function according to which the covariance decreases with respect to the distance.

2. The covariance structure is anisotropic. That means that the covariance is not only a

   function of the distance but also of the direction. The covariances consistently decrease along the longer path between the source and the discontinuity in the similarity structure, and the covariances are constant or even slightly increase along the shorter path. The latter aspect implies a very strong functional coupling. This kind of coupling leads to a preferred distribution of the source activity towards functional borders.

3. The covariance is not only a function of both direction and distance but also of the source position. This means that the covariance in a certain distance and for a given direction is different for each source. However, these differences seem to depend on Laplacian regularization. Fig. 3.4 shows that a very strong (left matrix) and a very weak smoothness constraint (right matrix) reduce this effect. In both cases, the covariance-distance function is only minor dependent on the source position. In case of moderate regularization, however, the covariance-distance function strongly depends on the source position. This can also be seen in Fig. 3.6.

It can be summarized that the incorporation of functio-anatomical borders influences the estimated variances and covariances in an undesired manner. Especially the variance bias is rather strong (cmp. Fig. 3.5) and needs to be compensated (see Sec. 3.3.6). In contrast, the effect on covariances seems to be weak. Nonetheless, both effects are important for the incorporation of multiple discontinuities in the similarity structure. This is relevant for incorporating parcellations. Their use is discussed in the following section.

3.3.4 Effect of Incorporating Distinct Functional Units

The incorporation of distinct functional units (i.e. patches) requires to define multiple discontinuities (i.e. $p_{ij} = 0$) in the similarity structure. As a result, only sources belonging to the same functional region are connected. As discussed in the last section, each cut causes a bias on variances and covariances. Here, it is of particular interest if non-uniform patch sizes introduce an additional bias.

Again, the annular grid from above is used. The incorporation of patches is trivial in the given toy example. Each additional cut in the similarity structure automatically creates an additional patch, that means two cuts form two patches. In the first example used here, the grid is cut at three positions (i.e. $v = \{300, 800, 1000\}$). This is realized by assigning the similarities $p_{v,v+1} = p_{v+1,v} = 0$. The Laplace operator entries for the indices v change to $B_{v,v} = -1$, $B_{v,v-1} = 1$ and $B_{v,v+1} = 0$, and for the indices $(v+1)$ to $B_{v+1,v+1} = -1$, $B_{v+1,v} = 0$ and $B_{v+1,v+2} = 1$. Figure 3.7 shows R_q and Fig. 3.8 the source variances for three regularization levels.

First, it can be seen at the right panel (Fig. 3.7) that every single cut influences the (co-)variances in the way that was discussed above. The closer a source is located to a cut, the higher is its variance as well as the covariance to sources in the same patch. These effects reduce when the smoothness constraint becomes stronger (middle panel). Obviously, the patch size starts influencing the matrix elements. The bias of the (co-)variances almost completely depends on the patch size in case of a very strong smoothness constraint (left matrix).

The influence of the patch size is closely related to the regularization parameter dependent (co-)variance bias. It occurs as soon as at least one source in a patch, e.g. source i, exhibits a non-zero correlation to all other sources in the same patch, i.e. $R_{q_{ij}}/R_{q_{ii}} > 0, j \in \Psi_i$. The effect

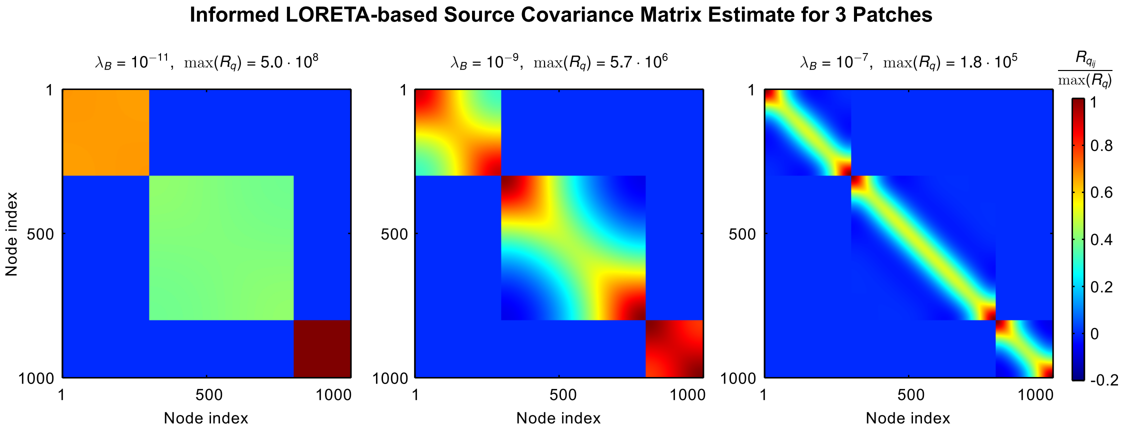

Figure 3.7: Estimated source covariance matrix for different λ_B. The values correspond to a strong smoothness constraint on the left and a weaker constraint on the right. Each matrix is normalized to its maximum, i.e. $\max(R_q)$. The matrix elements are color coded. All results refer to the same color bar. Arbitrary units.

can be explained with the characteristic that all row sums in the source covariance matrix are equal. When the row sum increases due to a lower regularization parameter value, the non-zero elements $R_{q_{ii}}$ and $R_{q_{ij}}, j \in \Psi_i$ corresponding to the i$^{\text{th}}$ source increase as well. In fact, this reflects a relationship between the size of the patch in which a source is located and the corresponding entries in the covariance matrix. The patch bias effect can also be seen in Fig. 3.8 in which only the source variances are displayed. As already discussed in Sec. 3.3.3, the variance of a source is a function of the distance between its position and a discontinuity in the similarity structure. It turned out that the ratio between the smallest and the largest variance never dropped below 0.5 on an annular grid, independently of the regularization parameter. The illustration shown here reveals that - given a sufficiently small regularization parameter - the smallest ratio significantly drops below this value. This effect can be explained with the

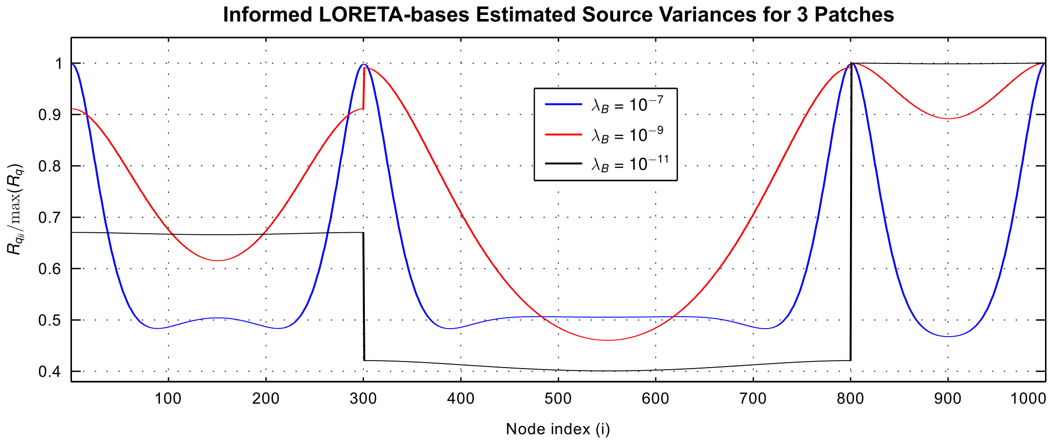

Figure 3.8: Main diagonal elements of R_q for different λ_B. The values for each curve are normalized to the corresponding maximum variance, i.e. $\max(R_q)$. The cuts in the similarity structure are at nodes 300, 800, and 1000. Arbitrary units.

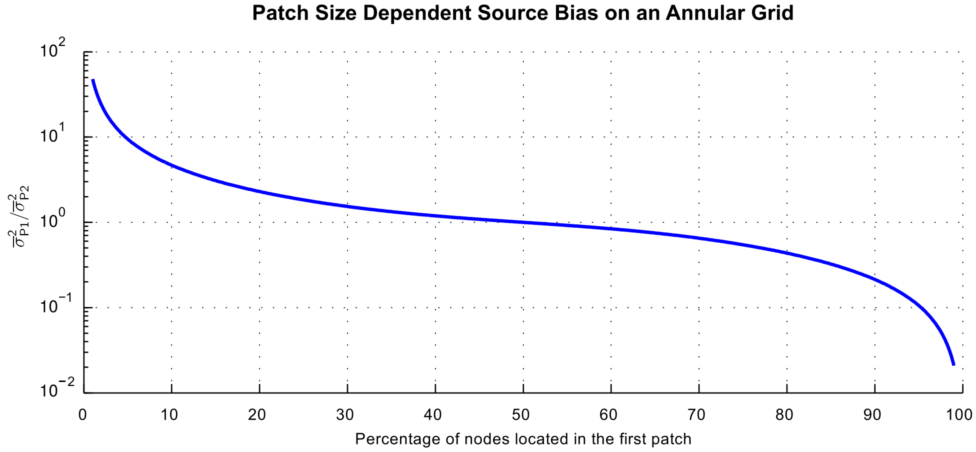

Figure 3.9: Dependence of the source variance bias from the patch size demonstrated using a toy example with an annular grid and two patches (see text). The abscissa denotes the percentage of all nodes located in the first patch (this is equivalent to its size), and the ordinate denotes the ratio between the mean variances in both patches. Minimum patch size is 10 (i.e. 1 % of all nodes), $\lambda_B = 1 \times 10^{-10}$ ensures a strong correlation constraint.

different patch sizes. Hence, this corresponds to a patch size dependent bias of sources.

In order to quantify the patch size dependent bias, a second toy example is used. It is also based on the annular grid from above. Now, only two rather than three areas are constructed. The patch sizes are systematically varied by shifting one border, while the second border has a fixed position. A very small regularization parameter λ_B is used to ensure a strong patch size dependent bias effect. Figure 3.9 shows the ratio between the mean variances in both patches with respect to the size of the first patch. A ratio of $\overline{\sigma}^2_{P1}/\overline{\sigma}^2_{P2} > 1$ means that sources in the first patch have a larger a priori variance, that means they might preferably be activated to explain data. The most salient aspects are briefly summarized.

The variances in both patches are equal if both functional areas have the same size. If the first patch comprises only 1 % of all sources, its mean variance is about 50 times larger than that of the second patch. In contrast, the variances are 50 times smaller if 99 % of all sources are located in the first patch. It seems unrealistic that patch size differences like these are relevant in practice. They can, however, reasonably be expected when, for instance, using a realistic parcellation and a folded cortical surface with high spatial resolution. For example, the parcellations used in chapter 5 contain functional areas which consist of less than 1000 nodes. The triangulated grid, however, consists of approximately 250 000 nodes. The use of only one of these patches as prior information would imply that only 0.4 % of all sources are located in this patch. This means that their mean variance may become even more than 50 times larger than the variance of all other sources.

The toy examples used so far were based on a very simplistic Laplacian. It is therefore useful to verify the patch size bias on a more realistic grid such as a triangulated surface, which is usually used to approximate the source space. The following example is based on this kind of grid. The weighting between neighbors now additionally depends on geometrical properties (see Eq. 3.1) because the distance and angles between all neighboring sources are usually not equal.

Given is a grid consisting of 4574 vertices. It represents the envelope of the brain (see Fig.

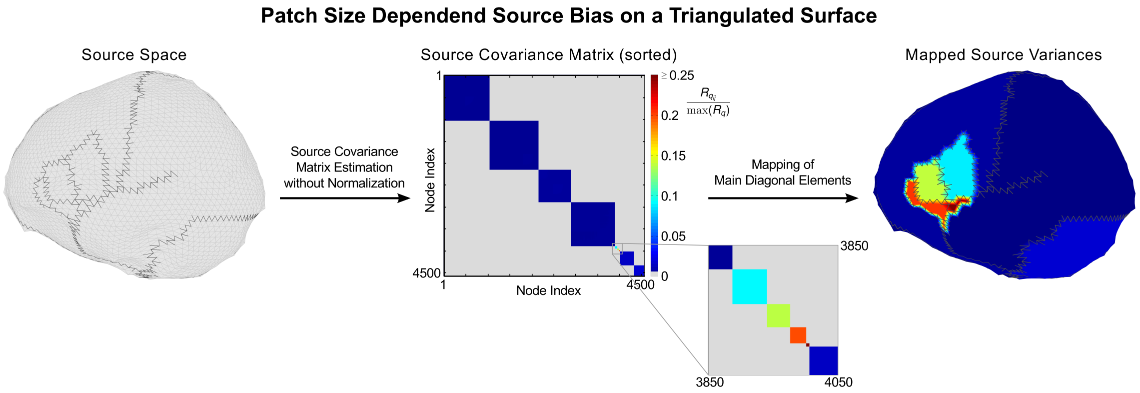

Figure 3.10: Demonstration of the patch size dependent source variance bias. Left: triangulated surface with functio-anatomical borders (similarity $p_{ij} = 0$ at black edges). Middle panel: PatchLORETA-based source covariance matrix ($\lambda_B = 1 \times 10^{-10}$). Right panel: Main diagonal elements mapped on the surface (same color coding). Conclusion: the smaller the patch size, the larger the estimated source variance. Arbitrary units.

3.10, left panel). Multiple functio-anatomical borders on the surface model several functional areas. These borders approximate the outline of the Brodmann areas (BA) 44, 45, and 47, and the stretch of the central, lateral, and interhemispheric sulcus (Fig. 3.10, black edges in left panel). The *a priori* functional similarity between neighboring sources located in different functional areas is zero, i.e. $p_{ij} = 0 \forall j \notin \Psi_i$, and $p_{ij} = 1$ otherwise. Figure 3.10 (middle panel) shows the estimated source covariance matrix (Eq. 3.2, $\lambda_B = 1 \times 10^{-10}$).

As before, the source variances are not equal. The covariances reflect the patchy organization of the cortex. Note that not only the patches themselves but also the functional boundaries form distinct functional regions. This is due to the fact that some of the borders are crossing each other. To associate the different color coded covariance blocks to patches, the source variances are mapped on the brain surface (Fig. 3.10, right panel). The result confirms that larger variances are estimated for sources in smaller areas.

The patch size bias is a serious problem for source localization. It reflects an artifact that occurs through the inversion of the second order spatial derivative operator used in LORETA-based approaches. Generally, such a bias is undesired and, more importantly, implausible with respect to the underlying prior knowledge on functional similarity (that means it is implausible that the incorporation of prior knowledge on the functional similarity increases the probability that certain sources are activated). For that reason it is absolutely necessary to account for this bias in source covariance matrix estimation. This is the topic in section 3.3.6.

3.3.5 Occurrence and Impact of Negative Covariances

It was mentioned in Sec. 3.3.2 that the occurrence of negative covariance entries is inevitable in LORETA-based source covariance matrix estimation. Any element $R_{q_{ij}}$ can become negative if the corresponding element B_{ij} is zero. Such an *a priori* assumption implies a 180° phase shift, which is implausible with respect to the kind of prior knowledge applied here, i.e. functio-anatomical information. Negative covariances between sources might produce more focused solutions, particularly if the leadfields of these sources are similar. It would therefore be problematic if the negative covariances become too strong. It depends on the regularization parameter whether and how strong a certain element in the covariance matrix becomes negative. Due to the smoothness constraint, however, it can be expected that their absolute values are rather small with respect to the largest positive covariances in each row. This assumption will be examined in this very section.

As above, the starting point is an annular grid consisting of 1000 sources. This grid is the basis for a total of 4 test cases: Informed LORETA with one ($v = 200$), two ($v = \{200, 1000\}$), and three cuts ($v = \{300, 800, 1000\}$) as well as uninformed LORETA (i.e. no cuts). The Laplacian defines according to Eq. 3.1 with $B_{v,v} = -1$, $B_{v,v-1} = 1$ and $B_{v,v+1} = 0$, and $B_{v+1,v+1} = -1$, $B_{v+1,v} = 0$ and $B_{v+1,v+2} = 1$. The parameter λ_B is systematically varied to compute multiple source covariance matrix estimates for each test case. Each matrix is then analyzed row by row using the measure

$$R_q^{\text{neg}}(i) \Big/ R_q^{\text{abs}}(i) = \sum_{j=1}^{N} \begin{cases} -R_{q_{ij}}, & \text{if } R_{q_{ij}} < 0 \\ 0, & \text{otherwise} \end{cases} \Big/ \sum_{j=1}^{N} \left| R_{q_{ij}} \right| \tag{3.6}$$

which determines the ratio between the sum of all negative covariances and the sum of the absolute values of all covariances in the i^{th} row. The measure is zero when all elements are positive and becomes one when all are negative. Calculating Eq. 3.6 for each row in a matrix allows to create a boxplot for any value of λ_B. Figure 3.11 shows the results for all test cases. Each boxplot allows to conclude whether negative covariances occur in the matrix and how strong their effect differs between rows.

The analysis for uninformed LORETA (top left) reveals, first, that the ratio (i.e. Eq. 3.6) is equal in all rows. This is kind of trivial since no additional prior knowledge is applied and, therefore, all sources have identical covariance structures. Second, negative covariances only occur in a range of $10^{-9} \leq \lambda_B \leq 10^{3}$. Values smaller than 10^{-9} represent the case of maximum smoothness, that means all sources are positively correlated to each other. Values larger than $\lambda_B = 10^{3}$ fully suppress any smoothness constraint (i.e. any correlation between neighboring sources). Therefore, negative covariances cannot occur at all. Third, the maximum ratio is ≈ 0.062, which is a very low value. It emphasizes that the influence of negative covariances is rather small.

The results for the informed LORETA test cases are similar to the results obtained for uninformed LORETA in several ways. First, negative covariances only occur in a certain range as well. It can be seen that the lower bound of this range shifts towards larger regularization parameter values when the number of cuts increases. This can be explained by the different patch sizes in the test examples. More precisely, the size of a patch defines the strength of regularization that is needed to achieve non-negative covariances. The upper bound of this range is very similar between both the informed LORETA examples and uninformed LORETA. In particular, the medians of the measure are almost identical for $\lambda_B \geq 10^{-4}$. This emphasizes that the smoothness constraint and, therefore, incorporated prior knowledge has no effect if too strong regularization is applied. Second, the maximum ratio is ≈ 0.062 as well. This is important since it means that the prior knowledge does not increase the maximum effect of negative covariances.

The boxplots belonging to informed LORETA clearly reflect that the negative covariances are strongly different between the matrix rows. These differences are a direct result of the inhomogeneous covariance structure (cmp. Sec. 3.3.3, Fig. 3.6). However, strong differences only occur

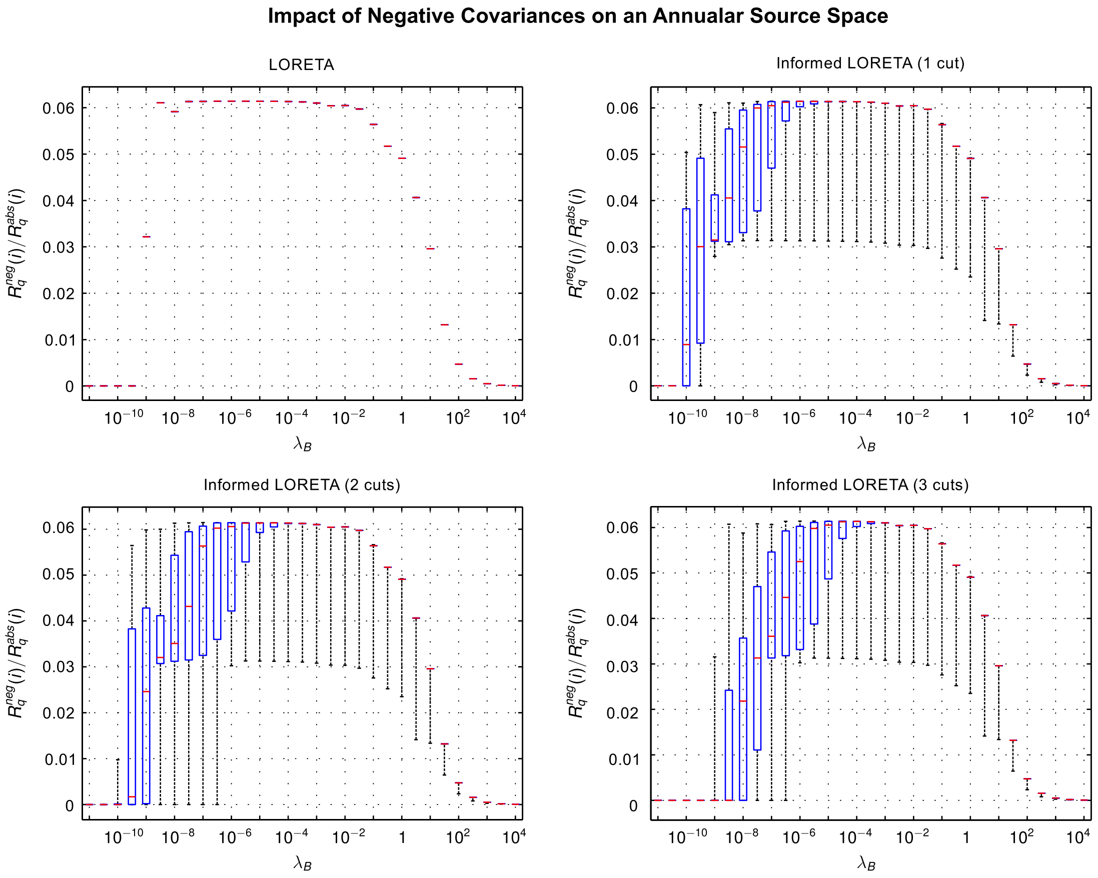

Figure 3.11: Illustration of the regularization parameter dependent ratio between the sum of negative covariances and of all absolute values in each row (i.e. $R^{\text{neg}}_{q_{ij}} \Big/ R^{\text{abs}}_{q_{ij}}$, Eq. 3.6) using an annular source space. The measure is determined for uninformed (i.e. no cuts) and informed LORETA (for 1, 2, and 3 cuts; see text). Shown are the ranges between lower and upper quartile (blue boxes), the median (red bars) and the minimum and maximum values.

in the transition between total smoothness (i.e. for very small λ_B) and a moderate smoothness constraint.

The tests performed above were repeated using different annular grids to examine if the impact of negative covariances depends on the number of sources. Grids with up to 5000 sources were used for this purpose. All tests revealed rather similar results. This means that the number of sources does not influence negative covariances.

The test setup used so far reflects a best case scenario. That means that using a one-dimensional equidistantly sampled source space avoids the influence of any inhomogeneous geometrical properties. Another toy example is used to examine potential implications of inhomogeneities. It is based on the triangulated surface already presented in Sec. 3.3.4. The source space consists of 4574 sources and is much more realistic compared to the annular grid. Prior knowledge is defined according to Fig. 3.10. The measure defined in Eq. 3.6 is applied to the corresponding uninformed and informed LORETA-based source covariance matrix. The results are depicted in Fig. 3.12.

Two aspects are important. First, the strength of negative covariances is different in each

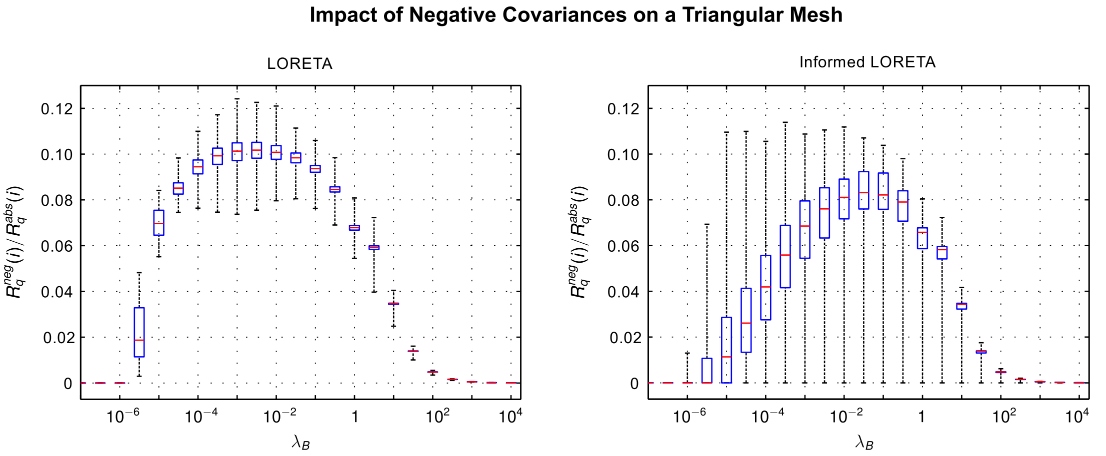

Figure 3.12: Illustration of the regularization parameter dependent ratio between the sum of negative and positive covariances in each row (i.e. $R^{\text{neg}}_{q_{ij}} \big/ R^{\text{abs}}_{q_{ij}}$, Eq. 3.6) using a triangulated surface. The measure is determined for uninformed (i.e. no cuts) and informed LORETA (see Fig. 3.10 for prior knowledge). Shown are the ranges between lower and upper quartile (blue boxes), the median (red bars) and the minimum and maximum values.

row, even for uninformed LORETA. These differences, however, seem to be rather small in most cases. Otherwise, the inter quartile range would be much larger. This effect can be explained with varying geometrical properties, that means an inhomogeneous grid structure. Since angles and distances between neighboring sources are different for each node, the resulting covariance estimate must be different as well. Some rows (indicated by the extreme points), however, significantly deviate from the median. Negative covariances in these rows are either particularly strong or particularly weak. This is a result of strong irregularities in certain areas of the triangulated[6]. A second aspect is that the strength of negative covariances is generally higher compared to the results obtained for the annular grid. This emphasizes that the grid structure and the general organization of the neighborhood ha a certain impact on the covariances. Nonetheless, the strength of negative covariances is small enough to assume that their influence on source localization is rather low.

Finally, an important conclusion can be drawn from all these examples. The occurrence of negative covariances is only a minor problem for LORETA-based source reconstruction. It is common practice to approximate the source space using a triangulated surface. Therefore, it is reasonable to assume that the findings discussed above also apply for practical applications. This is an important fact because it would only be hardly possible to reduce or even remove these effects.

3.3.6 Main Diagonal Normalization of the Source Covariance Matrix

The previous sections disclosed several artifacts in the LORETA-based source covariance matrix. In order to pose plausible *a priori* assumptions on the solution, it is particularly necessary to reduce the variance bias. Otherwise, several sources are preferred over others during source

---

[6] A test revealed that 98.8 % of the grid nodes have 6 neighbors, whereas some nodes have only four and five or even seven and eight neighbors. Compared to the majority of nodes, they have very different geometrical properties in their neighborhood.

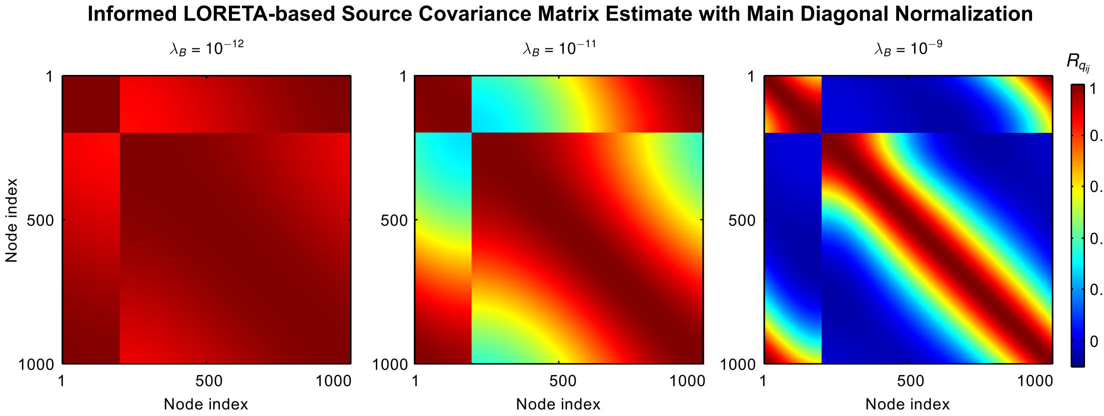

Figure 3.13: Estimated source covariance matrix with subsequent normalization to its main diagonal elements (Eq. 3.8) for different λ_B. The values correspond to a strong smoothness constraint on the left and a weaker constraint on the right. The matrix elements are color coded. All results refer to the same color bar. Arbitrary units.

localization. As shown above, the variance bias depends on the proximity of a source to a discontinuity in the functio-anatomical similarity structure. In case of parcellations, the bias additionally depends on the patch size. This section introduces a solution that eliminates the variance bias and, moreover, reduces the bias on covariances.

The problem is solved by introducing an additional normalization operator, i.e. $\Gamma \in \mathbb{R}^{m\times m}$, to the LORETA estimator of the source covariance matrix. The resulting estimator writes as $\Gamma^{-1}\left(B^TB\right)^+\Gamma^{-1}$. The matrix Γ defines as

$$\Gamma = \operatorname{diag}\left[\left(B^TB+\lambda_B I\right)^{-1/2}\right]. \tag{3.7}$$

It is a diagonal matrix and contains the square roots of the main diagonal elements of the estimated covariance matrix. This effectively normalizes each off-diagonal element to its two adjacent main diagonal elements and sets each main diagonal element to one. Hence, this normalization ensures an equal variance for all sources. According to Eq. 2.21 and 2.24, the complete source covariance matrix then writes as

$$\begin{aligned} R_q &= \left(\Omega^{-1}\Gamma^{-1}\left(B^TB+\lambda_B I\right)^{-1}\Gamma^{-1}\Omega^{-1}\right) \\ &= \left(\Omega\Gamma\left(B^TB+\lambda_B I\right)\Gamma\Omega\right)^{-1}. \end{aligned} \tag{3.8}$$

In order to calculate Γ, however, it is necessary to derive the main diagonal elements of the source covariance matrix. That means that the Laplacian-based operator needs to be inverted, which is a serious problem. It is shown in the end of this section how this can be achieved for practical problems. Before that, the actual effect of this normalization is illustrated. This is done on the basis of an annular grid consisting of $m = 1000$ sources and with a single cut defining a discontinuity in the functio-anatomical similarity structure. This is the same toy example as already used in in Sec. 3.3.3. Figure 3.13 shows R_q for different levels of regularization when main diagonal normalization is applied (cmp. Fig. 3.4 for the results without normalization). It provides the following insights.

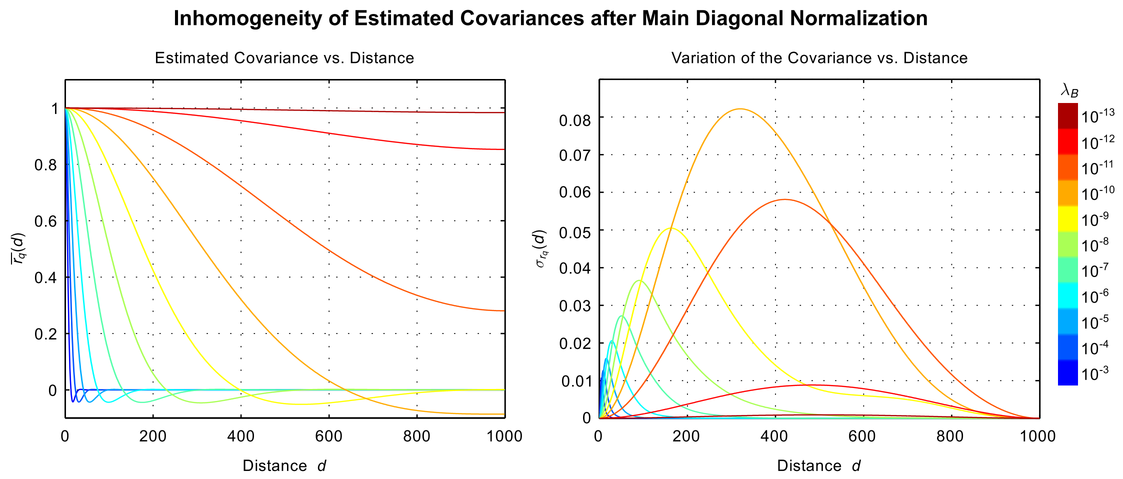

Figure 3.14: Distance dependent variation of covariances after normalization of the informed LORETA-based source covariance matrix for an annular source space comprised of a single functional border. Shown is the mean (left) and the standard deviation of the covariances (right) in dependence of the distance d between two sources. The colors encode the results for different regularization parameters. Arbitrary Units.

First, the results in Fig. 3.13 emphasize that the proposed normalization successfully removes the source position dependent variance bias. Second, the off-diagonal elements are always smaller than or equal to the corresponding main diagonal element. That means, the covariance is a descending function of the distance between sources. The gradient of this function depends, however, on the proximity of a source to the functional discontinuity and is therefore different in each row of R_q. It is therefore useful to examine this effect somewhat more closely.

Given R_q, one can define the vector $r_q(d)$, $r_q \in \mathbb{R}^m$, whose i^{th} element describes the covariance to the i^{th} source at the distance d. The distance may vary between $1 \le d \le m$[7]. Note that this approach deliberately does not distinguish between clockwise and counterclockwise direction. To quantify the variation of the covariances in a certain distance, it is straightforward to determine both the mean, i.e. $\overline{r_q}(d)$, and the standard deviation of r_q, i.e. $\sigma_{r_q}(d)$. Both functions are shown in Fig. 3.14 for a broad range of regularization parameter values.

It can be seen in the left panel that the function $\overline{r_q}(d)$ systematically depends on Laplacian regularization. In contrast, the standard deviation $\sigma_{r_q}(d)$ (right panel) exhibits a non-continuous dependence on both the distance and Laplacian regularization. Two aspects are particularly interesting. First, the variation of the covariances is different at any distance and has a unique maximum. Second, the strength of the variation strongly depends on λ_B. The standard deviation is very small when the smoothness constraint is very strong and increases significantly with growing λ_B. It then reaches a maximum (here at $\lambda_B = 1 \times 10^{-10}$) and decreases again when λ_B grows further. At the same time, the maximum of $\sigma_{r_q}(d)$ shifts towards smaller distances. Altogether, the standard deviation of the covariances is always small compared to its mean in a certain distance. This is an important fact and there is no reason to believe that this effect is fundamentally different on other grids.

The bias effect on the covariances is much more complex compared to the variance bias. The

---

[7] This results from the cut that interrupts the similarity structure, cmp. Sec. 3.3.3.

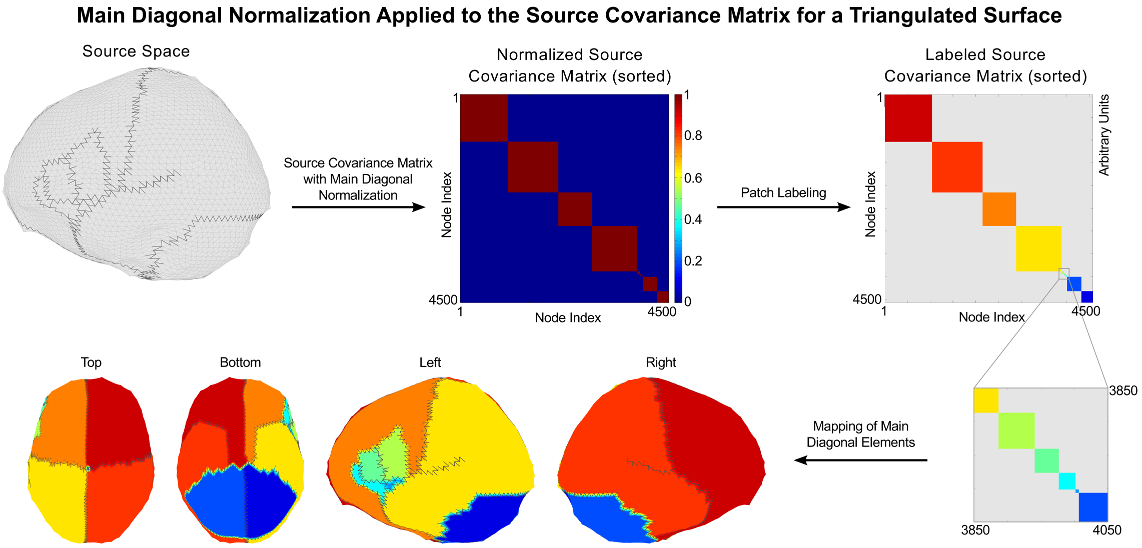

Figure 3.15: Demonstration example to verify that main diagonal normalization of the source covariance matrix (Eq. 3.8, $\lambda_B = 1 \times 10^{-10}$) removes the patch size dependent source bias (cmp. Fig. 3.10). The mapping of the labeled main diagonal elements on the surface illustrates the distinct functional regions.

problem is that a slightly different smoothness constraint is imposed on each source. Since it is difficult to predict the particular effect in each row, it is also hardly possible to counteract, e.g., by means of suitable algorithms. However, the results presented above suggest that the differences between the covariance structure for each source are in a rather small order of magnitude. Therefore, there is reason to believe that the covariance bias only has a minor impact on source localization. Moreover, the minimum norm constraint itself favors smeared solutions and, therefore, is less affected by variations of *a priori* covariances. Thus, it can safely be assumed that the overall effect on source localization is certainly weak.

The proposed main diagonal normalization of the source covariance matrix not only accounts for the location dependent bias on variances but also for the patch size dependent bias. This is demonstrated using the triangulated mesh from Sec. 3.3.4 (cmp. Fig.3.10). The corresponding unbiased estimate of the source covariance matrix, which results from normalizing the surface Laplacian, is shown in Fig. 3.15.

The last focus in this section is the calculation of Γ, which in turn requires the calculation of R_q. This appears to counteract one important advantage of informed LORETA-based source reconstruction: the possibility to compute the inverse solution by means of LU decomposition (Golub and van Loan, 1996). That means that the explicit inversion of the Laplacian (i.e. the Laplacian-based smoothness operator) is not necessary in order to calculate the inverse solution (cmp. Sec. 2.4.4). This excellent feature allows to apply spatial similarity constraints even on a source space with high spatial resolution[8]. In order to calculate the normalization operator Γ it is only necessary to determine the main diagonal elements of the source covariance matrix. The covariance matrix is the the inverse of the operator $(B^T B + \lambda_B I)$, which is a sparse matrix.

---

[8] For example, a mesh consisting of $m = 240.000$ sources has a Laplacian with dimensions $m \times m$. The sparsity leads to approx. less than 10 MB of required memory. In contrast, the inverse $(B^T B)^+$ is fully occupied, ending up in a total of 214 GB using single-precision representation (float). Furthermore, the computation of this full inverse is a serious computational problem.

Fortunately, the inversion of a sparse matrix for the purpose of deriving only the main diagonal elements of the inverse is a frequent problem in a variety of scientific disciplines. These elements can be computed with a method described by Takahashi et al. (1973). Its extension and realization in MATLAB (Davis, 2011) performs well even on huge problems. The comparison of this method with the results of traditional inversion algorithms for several low-dimensional test examples revealed an excellent agreement. Thus, this sparse matrix inversion algorithm is an important tool to apply the proposed normalization of the source covariance matrix in realistic problems.

3.4 Determination of the Laplacian Regularization Parameter

3.4.1 Problem Statement

The LORETA-based estimation of the source covariance matrix requires the regularization of the Laplacian. The parameter λ_B controls the balance between main- and off-diagonal elements in $B^T B$, that means the strength of the smoothness constraint[9]. Thereby, the transition from total smoothness to a non-smooth prior assumption occurs in a narrow range (e.g. cmp. results in Sec. 3.3.5) from which λ_B has to be selected carefully. Knösche et al. (2013) proposed to determine the Laplacian regularization parameter empirically in a way that ensures both a stable inversion of the smoothness operator and that preserves the LORETA effect in the reconstructed source distribution (i.e. the smoothing effect must be visible). Here, an objective approach is introduced. It allows to determine λ_B such that the smoothness constraint can be adjusted according to a desired strength.

The need for an objective determination of λ_B becomes even more clear when considering properties of the Laplacian somewhat more closely. The row normalization introduced in Eq. 2.27 eliminates any information on the distance between neighboring sources. That means, the weighting between a source and its neighbors is independent of the spatial resolution of the source space. As a result, the regularization defines how the correlation structure for a given source (i.e. actually for all sources) changes with respect to the neighborhood order. However, it would be rather useful to select the parameter λ_B in a way that allows to define a certain correlation assumption with respect to the distance between sources. Thus, the correlation structure for a given parameter λ_B must be evaluated. This is essential to ensure clearly defined prior assumptions which are independent of the spatial resolution of the source space.

3.4.2 Laplacian Regularization Parameter Estimation

This section introduces a method to systematically determine the regularization parameter for the Laplacian. The main objective is to select λ_B according to the source correlation structure defined by $\left(\Gamma\left(B^T B + \lambda_B I\right)\Gamma\right)^{-1}$ (cmp. Eq. 3.8). This requires a suitable measure which provides sufficient information on the estimated spatial correlations.

As shown previously, the LORETA-based covariance matrix changes from the identity matrix for large parameters to a dense matrix when λ_B converges towards zero. In the latter

---

[9] In contrast, the Tikhonov regularization parameter α (cmp. Eq. 2.17) balances between a term fitting the data and a model term as, for instance, a smoothness constraint. Hence, it controls the impact of the smoothness constraint on the solution, whereas Laplacian regularization controls the particular spatial correlation structure.

case, the covariance between all elements that belong to the same functional area is one. This finally leads to a fully occupied matrix with all elements being one in case of uninformed LORETA. A straightforward approach to assess the covariance structure in this matrix is to compute its Frobenius norm as a function of λ_B, i.e. $g(\lambda_B) = \left\| \left(\Gamma \left(B^T B + \lambda_B I\right) \Gamma\right)^{-1} \right\|_F$. It converges towards $g_{\min} = \min\left(g(\lambda_B)\right) = \sqrt{m}$ when λ_B increases and towards a fixed maximum value $\sqrt{m} < g_{\max} = \max\left(g(\lambda_B)\right) \leq m$ when it decreases. The actual value of $g_{\max}$ depends on prior knowledge. For uninformed LORETA, this value corresponds to number of sources, i.e. $g_{\max} = m$. Several smoothness levels can be identified if this measure is computed for a suitable range of regularization parameter values. This is the basis to select λ_B according to a desired smoothness level.

A major drawback of computing the Frobenius norm is that it requires the explicit calculation of the LORETA-based source covariance matrix, i.e. the computation of the inverse. As outlined in Sec. 3.3.1 this is only hardly possible in most cases. This problem can be circumvented as follows. The computation of the Frobenius norm requires to sum up the squared values of all matrix elements. If one can be sure that covariances are non-negative (see below), it is sufficient to directly sum up the non-squared values to assess the covariance structure in dependence of λ_B, i.e. $g(\lambda_B) = \sum_i \sum_j \left(\Gamma \left(B^T B + \lambda_B I\right) \Gamma\right)^{-1}$, $i, j = 1 \ldots m$. This measure converges towards $g_{\min} = m$ when λ_B increases and towards a fixed value $m < g_{\max} \leq m^2$ when it decreases. The major advantage is that this sum of matrix elements can be expressed in terms of a vector-matrix-vector multiplication. The finally proposed measure to asses the covariance structure is

$$\begin{aligned} g(\lambda_B) &= \vec{1}^T \left(\Gamma \left(B^T B + \lambda_B I\right) \Gamma\right)^{-1} \vec{1} \\ f(\lambda_B) &= g(\lambda_B) / \max\left(g(\lambda_B)\right). \end{aligned} \tag{3.9}$$

$\vec{1} \in \mathbb{R}^m$ is a vector with all elements being one. This allows for an effective inversion procedure by solving a linear system of equations. The function f, which is normalized to the maximum value $g_{\max}$ to eliminate the dependence on the number of sources, is a relative measure that expresses the topological smoothness level independently of the number of sources. It varies between $f_{\max} = \max\left(f(\lambda_B)\right) = 1$ and $f_{\min} = \min\left(f(\lambda_B)\right) = m/g_{\max}$. Usually $g_{\max} \gg m$ and it follows that $f_{\min} \approx 0$.

As already mentioned, this approach implies the assumption that all matrix elements are non-negative. In fact, it was discussed in Sec. 3.3.2 that negative covariances occur as an artifact of Laplacian inversion. These negative entries might falsify the proposed smoothness measure. However, the results in Sec. 3.3.5 have shown that the absolute value of the sum of negative elements is always rather small compared to the sum of positive values in the source covariance matrix. It can therefore safely be assumed that the influence of this effect, i.e. of negative covariances, on the proposed measure is small. Hence, it is useful to ignore potential artifacts in favor of the efficiency of this method.

Equation 3.9 allows to select a regularization parameter according to the smoothness level. The question which level should be used depends on the prior information. If, for example, it can be expected that the sources within the *a priori* defined functional regions are highly spatially correlated the smoothness level should be high. This might be useful when a full parcellation with particularly small patches is used. When the areas are rather large, a low smoothness level seems reasonable. For example, this is the case for uninformed LORETA, which actually implies the incorporation of a single patch comprising the whole cortical sheet. It is very much plausible to select a low smoothness level in this case.

The selection of any value in between these two extremes is not straightforward and depends on the homogeneity of the size of the incorporated functional areas. If all regions are approximately equal in size, the smoothness level adjusted by means of λ_B is identical in each area. For example, this is the case for informed LORETA with prior knowledge defined according to a full homogeneous parcellation, and for uninformed LORETA. If, however, prior information is comprised of inhomogeneously sized and/or extremely differently shaped functional regions, the correlation structure in the distinct regions can be very different. As a consequence, the actual degree of smoothness in each patch may strongly deviate from the desired smoothness level. Examples for such a case are the use of only a subset of patches from a full parcellation to inform LORETA, or the use of a full parcellation with inhomogeneously sized patches. In such a case, only the selection of a regularization parameter close to the maximum or the minimum smoothness level ensures a predictable source correlation structure. A particularly important feature of the proposed method to adjust λ_B is to account for the spatial resolution of the source space. This feature is illustrated in the following section.

3.4.3 Demonstration Examples

This section aims at illustrating the usage and properties of the proposed method for estimating the Laplacian regularization parameter. First, this is done using toy examples similar to the one employed in Sec. 3.3.3. Given are three annular source models consisting of $m = \{500, 1000, 2000\}$ sources. They are supposed to approximate the same physical solution space at different spatial resolutions. All grids are cut at the same relative location at index $v = 0.2 \cdot m$. The Laplacians are constructed like above. The source covariance matrix for each grid denotes as R_q^m.

The first step is to compute the smoothness measure according to Eq. 3.9 for each source space. The result is depicted in Fig. 3.16. It is obvious that the measure systematically shifts towards smaller λ_B when the number of sources increases. More precisely, doubling the number of sources shifts the measure by approximately one order of magnitude. It is now interesting whether the source covariance matrices for the different grids are similar given the same smoothness level. Therefore, three different λ_B corresponding to distinct smoothness levels, i.e. $f(\lambda_B) = \{0.9, 0.5, 0.1\}$, are selected to compute three R_q^m for each source space. Fig. 3.17 shows the comparison of the results.

The top panel shows the covariance matrix R_q^{500} for each smoothness level. It is expected that the matrices for $m = 1000$ and $m = 2000$ exhibit a very similar covariance structure. To verify this, the courses of the mean covariance of R_q^m are compared. More precisely, the columnwise mean of R_q^m denoted as $c^m(j_r)$ is calculated as a function of the relative column index $j_r = j/m$, j being the column index, for each smoothness level. The results shown in the lower panel of Fig. 3.17 reveal a high similarity between the different functions. Additionally, the differences between these functions are assessed by means of the standard deviation of the mean covariances, i.e. $\sigma_{c^m}(j_r)$. It is computed for those 500 indices which are common for all three source models. The mean standard deviation, i.e. $\overline{\sigma}_{c^m}$, for each smoothness level is given in Fig. 3.17. These values emphasize that the differences between the mean covariances are

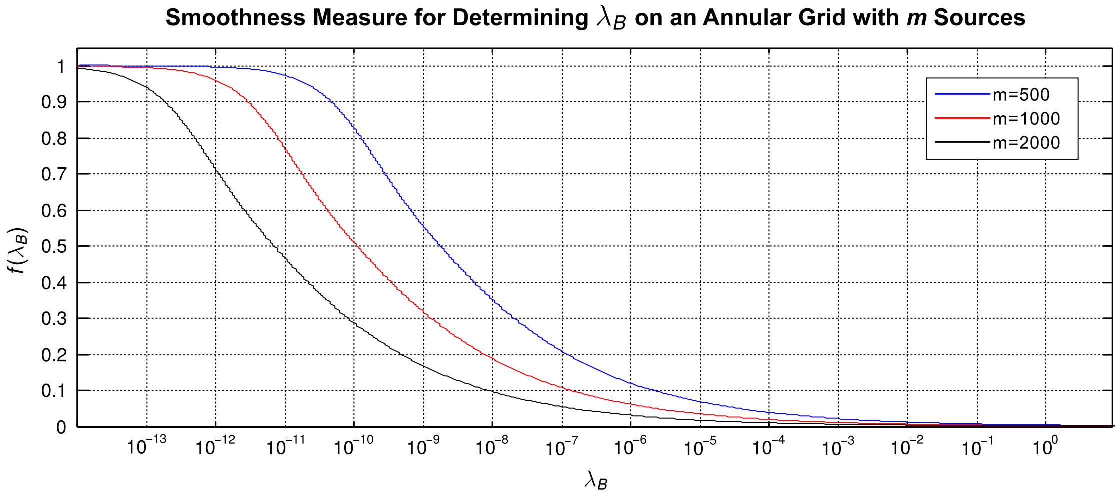

Figure 3.16: Result of calculating the smoothness measure, i.e. $f(\lambda_B)$, according to Eq. 3.9 for three annular source models with different spatial resolution.

very small. Overall, the results suggest that the *a priori* source covariance structure estimated for source models with different spatial resolution is similar if, first, λ_B is adjusted according to the smoothness measure defined in Eq. 3.9 and, second, the source models including the prior knowledge are equivalent.

A second example demonstrates that the method also works on a source space which is defined on a triangular mesh. It focuses on the relation between the spatial resolution of the source space and the source localization result. That means, it is demonstrated that consistent reconstruction results can be obtained for various discretizations of this mesh when λ_B is adjusted according to a desired smoothness level (i.e. by means of the proposed method). The example is based on the mesh and the prior knowledge already used in Sec. 3.3.4 (cmp. Fig. 3.10). For the purpose of source localization, three orthogonal dipoles are placed on each vertex to construct the source model. This leads to a total of $m = 13722$ sources. Two additional source models are defined. The first is a subset of the original source space. It contains only $m = 4578$ sources. The second is obtained by refining the original mesh. The resulting source space consists of $m = 41154$ sources. All grids are shown in Fig. 3.18. Although the prior information is derived using the same functio-anatomical boundaries, it is obvious that the representation of the prior information by means of local discontinuities (i.e. black edges) is slightly different on each grid. Therefore, sizes and shapes of patches can be slightly different as well. Next, the smoothness measure according to Eq. 3.9 is calculated for both informed and uninformed LORETA. The results are shown at the bottom of Fig. 3.18. It can be seen that, as above, the transition from high to low smoothness systematically shifts towards smaller λ_B when the spatial resolution increases. The smoothness measure for the finest granularity has a slightly different shape compared to the two other source models (i.e. particularly for informed LORETA). This reflects differences concerning the incorporated prior knowledge.

As a next step, an EEG leadfield is computed for each source space. Details on the volume conductor and senor model are given in Sec. 4.2.2. An artificial data set is generated afterwards using the source space with $m = 13722$ sources. All source dipoles in BA 45 are activated in such a way that a radial orientation and unit length of the effective dipole at each vertex is reached.

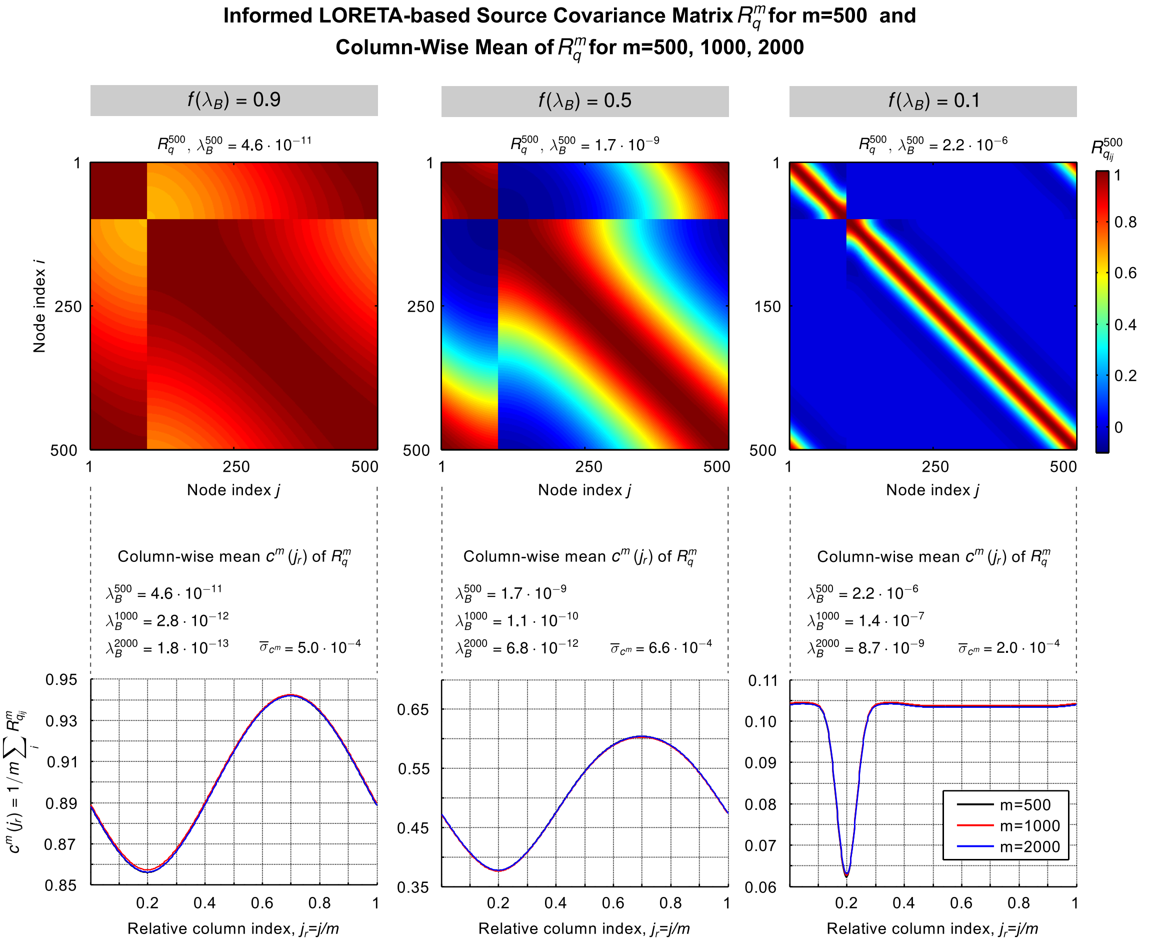

Figure 3.17: Comparison of source covariance matrices R_q^m estimated for three different annular source models at three smoothness levels. Top panel: Source covariance matrix R_q^{500} for smoothness levels $f(\lambda_B) = \{0.9, 0.5, 0.1\}$. The matrix elements are color coded, all results refer to the given color bar. Bottom panel: Column-wise mean $c^m(j_r)$ of R_q^m for each smoothness level. For details on c^m, j_r and $\overline{\sigma}_{c^m}$, see text. The legend (right plot) and the description of the ordinate (left plot) apply for all graphs. The black function for $m = 500$ is almost completely overlayed. The Laplacian regularization parameters are denoted as λ_B^m.

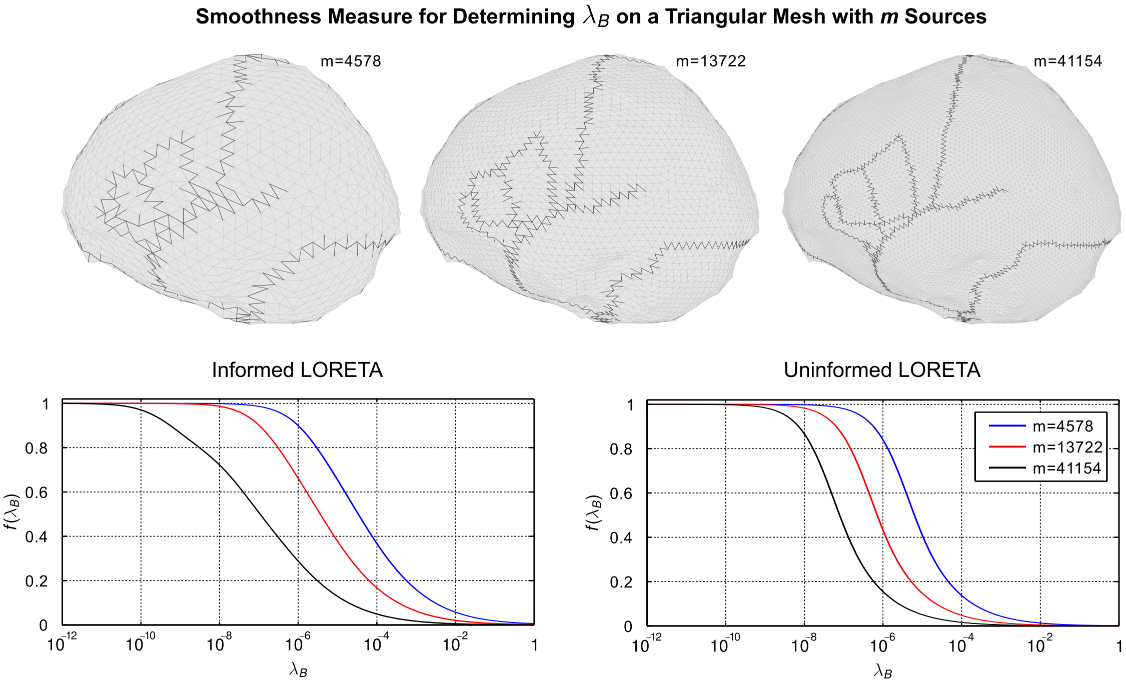

Figure 3.18: Top panel: Three discretizations of the same surface, which approximates the envelop of the brain. Black edges denote functional boundaries used for informed LORETA. Bottom panel: Smoothness measure determined for informed and uninformed LORETA for the three source models. Legend applies to both plots.

Finally, this activation pattern is used to compute the forward solution (details in Sec. 4.2.4, SNR=1×10^8) in order to perform the source reconstruction (details in Sec. 4.2.5). Figure 3.19 shows uninformed and informed LORETA reconstruction results for three different smoothness levels.

The following conclusions can be drawn. The reconstructed activity patterns on the different source models are highly similar for each smoothness level. Hence, the objective determination of λ_B is crucial. Yet another aspect can be seen: For informed LORETA, the reconstructed pattern is more and more focused on a single patch when the smoothness level increases. In contrast, the activation for uninformed LORETA becomes more focal towards lower smoothness levels. This emphasizes that the smoothness constraint not only depends on Laplacian regularization but also on the prior knowledge itself. This is a very important aspect. It underpins the need to select a desired smoothness level in accordance with the incorporated prior knowledge. In case of uninformed LORETA, for example, the whole source space forms a unique functional region and it is implausible to assume that all sources within this region are correlated. Hence, a low smoothness level is useful. For informed LORETA, the incorporated regions are much smaller and it might be very likely that sources in these regions exhibit a high correlation. In this case a higher smoothness level seems plausible.

Finally, it is worth to note that Laplacian regularization is also an issue for the original LORETA method as defined in Eq. 2.26, or any derivative of this approach, which does not employ a row normalization of the Laplace operator as introduced in Eq. 2.27. These Laplacians are usually invertible and therefore do not require additional regularization. Instead, the definition of main- and off-diagonal elements itself introduces a kind of regularization which has a very

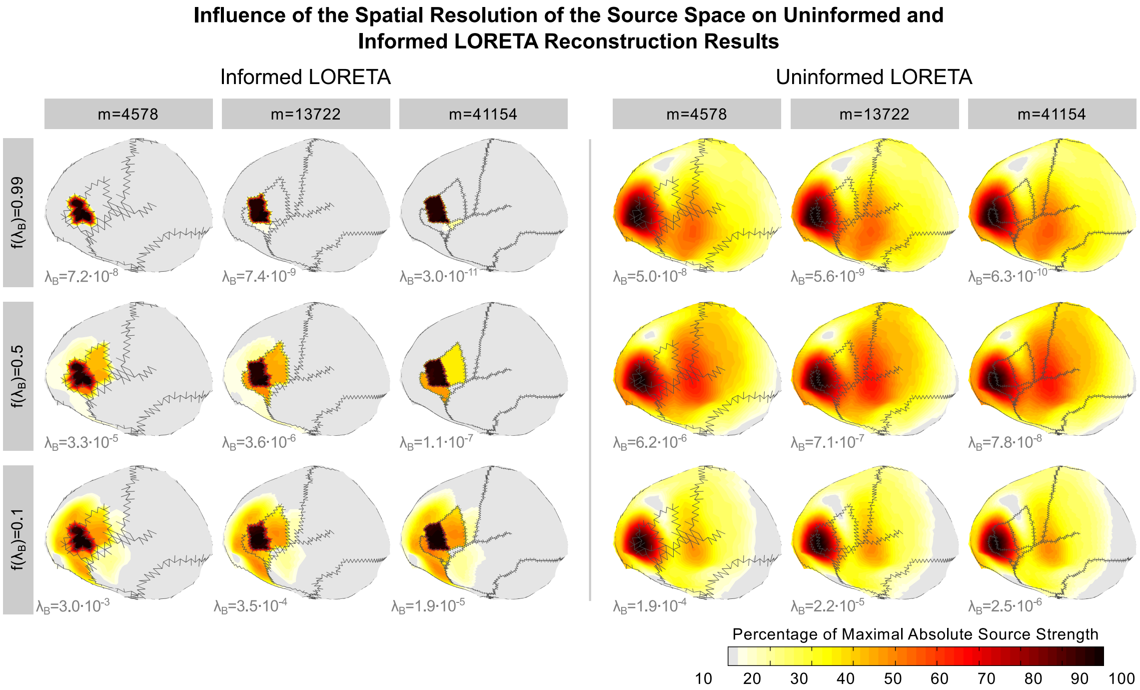

Figure 3.19: Results of reconstructing source activity in BA 45 (dark red colored region in informed LORETA results). λ_B is adjusted according to three smoothness levels for each grid. The source model comprises three dipoles per vertex, plotted are the strength of the effective dipole at each vertex. Results normalized to the maximum strength in each plot. Arbitrary units.

similar effect as the one discussed here. However, it is neither possible to determine nor to control the smoothness level that results from this implicit regularization. This should be kept in mind when employing such methods for source reconstruction.

3.4.4 An Alternative Method for Laplacian Regularization Parameter Estimation

The smoothness measure introduced in Eq. 3.9 turned out to be particularly suited to adjust the Laplacian regularization parameter λ_B according to some smoothness level. However, an alternative approach is tested in this work. It is briefly summarized in this section.

The approach is based on the idea to assess the similarity between a matrix and its inverse. More precisely, $g(\lambda_B) = \left\| \left(B^T B\right)\left(B^T B + \lambda_B I\right)^{-1} - I \right\|_F$ defines the dissimilarity between the LORETA weighting operator and its regularized inverse. This measure converges towards $g_{\min} = \min\left(g\left(\lambda_B\right)\right) = 0$ when regularization is reduced and towards $g_{\max} = \max\left(g\left(\lambda_B\right)\right) = \|I\|_F = \sqrt{m}$ when regularization increases, respectively. In contrast to Eq. 3.9, $g_{\max}$ is independent of prior knowledge such that a normalized measure can be written as $f\left(\lambda_B\right) = g\left(\lambda_B\right)/\sqrt{m}$. Furthermore, the left and right hand side multiplication with the Leadfield matrix and its transposed, respectively, effectively projects the similarity measure to sensor space and allows for an efficient inversion. The final normalized measure then writes as

$$f\left(\lambda_B\right) = \left\| L\left(B^T B\right)\left(B^T B + \lambda_B I\right)^{-1} L^T - LL^T \right\|_F / \left\| LL^T \right\|_F . \tag{3.10}$$

The function $f\left(\lambda_B\right)$ is reversed to that in Eq. 3.9. It varies between zero and one. A low value implies a high similarity between both matrices and, therefore, a strong smoothness constraint, and vice versa. As above, the normalization eliminates the dependence on the number of sources and effectively accounts for the spatial resolution of the source space. This measure does not require the source variances to be equal. Hence, it also works for PatchLORETA as introduced by Knösche et al. (2013). Anyway, the use of PatchLORETA is not recommended for the several reasons discussed above. The alternative method is also less influenced by negative variances.

The main disadvantage of this method is that $f(\lambda_B)$ does not directly relate to the underlying smoothness level. Thus, it is only hardly possible to predict a covariance structure for a given regularization value. Moreover, the proposed Leadfield projection suppresses certain source configurations. This might be undesired. Therefore, the method introduced in Sec. 3.4.2 is preferred for adjusting λ_B. It is used for all subsequent simulations and the analysis of experimental data.

3.5 Summary and Conclusion

The aim of this chapter was the analysis and optimization of PatchLORETA. This method allows to incorporate prior knowledge on the affiliation of sources to functional regions into LORETA-based source reconstruction. First of all, a redefinition of the surface Laplacian was presented in Sec. 3.2. The newly defined Laplacian allows the use of more general information on the mutual functional similarity between neighboring sources (i.e. even gradual information). However, the results of a closer examination revealed that gradual similarity information might be rather unsuited in order to obtain a strong impact on source localization. Instead, a sufficiently strong similarity contrast in the local similarity structure is mandatory. For example, boundaries representing a strong functional separation between distinct functional areas are particularly useful. The use of this kind of prior information with informed LORETA might also be referred to as LineLORETA (Fuchs et al., 2012).

The subsequent analysis of the LORETA-based source covariance matrix in Sec. 3.3 revealed several issues. The estimated variance of a source depends on (1) its distance to a discontinuity in the similarity structure and (2) on the size of the patch in which the source is located (i.e. when a parcellation is used as prior knowledge). Moreover, the estimated covariance between two sources, e.g. A and B, not only depends on their distance to each other, but also (3) on the distance of A and (4) the distance of B to a discontinuity in the similarity structure. The analysis has additionally shown that (5) the estimated covariance between two sources can be negative. The first two issues are particularly problematic, that means they need to be solved in order to use informed LORETA. An additional normalization operator introduced in Sec. 3.3.6 removes both effects. The issues 3-5 are of minor importance.

The regularization of the Laplace operator and its important role for informed LORETA was evaluated and discussed in another part of this chapter. In simple terms, the Laplacian regularization parameter defines a relation between the covariance and the distance between two sources. In other words, it defines a smoothness level. Strong regularization leads to a weak smoothness level and, generally, reduces spatial correlations. Weak regularization implies a high smoothness level. That means, lowering the regularization parameter increases the smoothness level until all sources within a functional unit are fully correlated. Note that this case corresponds to PatchLORETA2 (see Eq. 2.28), which, however, employs a patch-based neighborhood definition to achieve such a strong intra-area correlation. In contrast, the approach presented here relies on the local neighborhood.

The strong relation between Laplacian regularization and the source covariance matrix estimate emphasizes the need for a careful selection of λ_B. A suitable method was proposed in Sec. 3.4.2. It allows to adjust λ_B according to the smoothness level. The method is based on a measure that is directly related to the underlying source covariance structure. The larger its value, the larger is the imposed smoothness inside functional areas. However, not only the measure itself but also the incorporated prior knowledge are important in order to select a suitable regularization parameter. For example, uninformed LORETA effectively implies that the cortex exhibits a unique functional area. In this case, it is rather implausible to assume the highest possible degree of smoothness between sources since this would render all sources to be highly correlated. Hence, a low smoothness level should be selected. Another case would be the use of a parcellation consisting of a large number of small sized patches for informed LORETA. The selection of a high smoothness level would be quite useful since it implies a very strong intra-patch correlation – which seems rather plausible in this situation. The most important property of the measure is its ability to adjust the regularization parameter independently of the spatial resolution of the underlying source space.

Altogether, the informed LORETA method proposed in this chapter can be used to incorporate functio-anatomical prior information for linear source reconstruction. The method in general as well as the use of this kind of prior knowledge is evaluated in the following two chapters of this thesis.

4 Evaluation of Spatially Informed Linear Inverse Methods

4.1 Introduction

The method introduced in the previous chapter allows the incorporation of functio-anatomical similarity information into LORETA-based source reconstruction. The corresponding *a priori* source covariance matrix estimate is free of artifacts on the source variances. This is an important requirement for its practical application. Subject of this chapter is the evaluation how the use of such prior knowledge constrains linear source reconstruction in practice. It focuses on the main characteristics of the source estimates as, for instance, the spatial dispersion of reconstructed activity. Another focus is the actual benefit that the use of priors might bring to linear source reconstruction. This is of particular interest for two reasons. First, the accuracy of the course of functio-anatomical borders is certainly limited. Second, the estimated covariance structure is, at best, only a rough approximation of the real spatial correlation structure. Therefore, the use of prior knowledge is evaluated under several conditions. That includes scenarios in which the use of priors in fact improves source reconstruction since the priors and the sources that generated the data are in a good agreement with. Other scenarios show how reconstruction results are affected when the prior deviates from the likely generators.

The simulations in Sec. 4.3 target a qualitative characterization of informed LORETA reconstruction results. It is evaluated how functio-anatomical information and in particular its accordance to the activation pattern influences source reconstruction.

Section 4.4 aims to characterize the spatial properties of different informed linear inverse methods in a quantitative manner. This includes derivatives of FACE, i.e. focal and extended FACE (cmp. Sec. 2.5.5), as well as informed LORETA for which several regularization levels are used. The evaluation is done using Monte-Carlo (MC) simulations on the basis of artificially generated parcellations.

The simulations in Sec. 4.5 are based on both full and local parcellations. The latter contain only a subset of patches of a full parcellation. In linear inverse methods the a priori source covariance matrix expresses knowledge or at least a belief on spatial correlations between the sources which generated the data. Its estimation based on a general smoothness constraint, which is combined with prior knowledge, may introduce unforeseen prior assumptions. For example, the use of a full parcellation implies the occurrence of correlated activity in each patch of the cortex. This is often a rather unrealistic assumption (e.g. for the analysis of event related activity). This issue is particularly problematic when the smoothness constraint is strong.

Moreover, it is independent of the fact if the incorporated functio-anatomical borders accurately match the true functional boundaries. The simulations demonstrate how the restriction of prior information to patches in a certain cortical area affects source reconstruction and which coinciding effects must be taken into account.

The simulations performed in Sec. 4.3-4.5 are ideal in the sense that the forward models used for the generation of simulated data and its reconstruction are identical. This is also known as inverse crime and might cause overestimated measures of the reconstruction quality. It is evaluated in Sec. 4.6 how spatial inaccuracies between these models, for example caused by co-registration errors, affect the source reconstruction quality of the employed algorithms.

4.2 Methods

4.2.1 Overview

This section gives a short overview of methods that are used for the simulations in this chapter. This includes forward models, prior knowledge, the generation of simulated data, reconstruction algorithms, and the metrics for the evaluation of the results. The detailed simulation setup is presented in the individual sections.

The general simulation procedure employed throughout this chapter can be summarized as follows: (1) computation of the EEG leadfield matrix, (2) parameterization of reconstruction algorithms according to prior knowledge, (3) activation of a set of dipoles on the source space, (4) prediction of EEG sensor values using the pre-computed leadfield matrix, (5) addition of noise, (6) reconstruction of a source distribution for each algorithm under test, and (7) evaluation of the results.

4.2.2 Source Models and Forward Solution

Two different source models were used for the simulations. The first was based on a triangulated surface approximating the envelope of the brain. It was derived from the Montreal Standard Brain (Collins et al., 1994) by shifting the inner skull surface inwards about 1 cm. Three orthogonal dipoles were placed on each vertex, which leads to a total number of 13 722 sources (cmp. Fig. 3.19, second column). Among these surfaces, the outer skull and outer skin surface were used to construct a three-compartment BEM model with the conductivities 0.33 S/m for brain and skin and 0.0042 S/m for the skull compartment. The SIMBIO toolbox (Fingberg et al., 2003) was used to calculate the forward solution at 85 EEG sensor positions arranged according to the 10-10 system (Chatrian et al., 1985).

The second head model was constructed from an individual subject's MRI data set. Therefore, the pial cortex surface (≈ 122 000 nodes per hemisphere), the inner and outer skull surface, and the outer skin surface were segmented using Freesurfer (Fischl et al., 2002). A single ECD with perpendicular orientation was placed on each vertex of the pial surface to built up the source space. Inner and outer skull surface and the outer skin surface each consist of 5120 vertices. Finally, a three-compartment volume conductor model was constructed with the same conductivities as above. The leadfield was computed using SIMBIO for a given set of 60 EEG sensor positions (placed according to the 10-10 system).

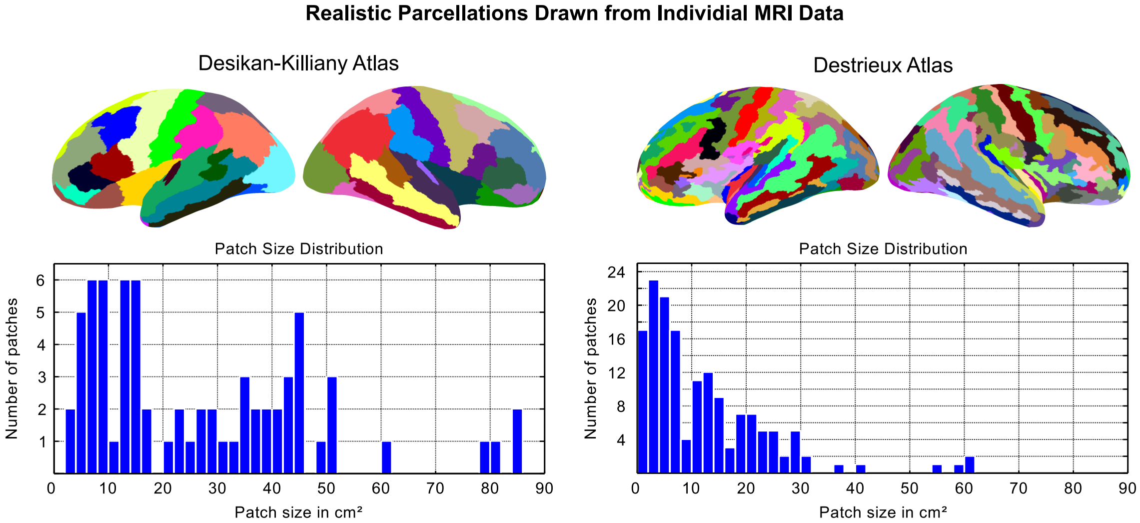

Figure 4.1: Top panel: Two realistic parcellations mapped on the inflated cortical surface. Arbitrary patch colors. Bottom panel: Histograms of the patch sizes for each parcellation; $2\,\mathrm{cm}^2$ bin width. Left/right parcellation contains 70/156 parcels.

4.2.3 Prior Knowledge

The functio-anatomical prior information used in the simulations was derived from various parcellations. Generally, parcellations embody the binary similarity structure and are therefore perfectly suited for the use with informed LORETA. Full and local parcellations are distinguished. While the former assign all sources to a dedicated functional area, the latter only contain a subset of patches of a full parcellation. That means that several sources are unlabeled. The selection of patches to construct local parcellations is discussed in the simulation setup for a particular simulation. Here, the derivation of full parcellations is outlined.

The simulations on the folded cortical surface in Sec. 4.3 are based on realistic parcellations according to the Desikan-Killiany-Atlas (Desikan et al., 2006) and the Destrieux-Atlas (Destrieux et al., 2010). They were drawn from the individual subject's MRI data using automated parcellation procedures provided by Freesurfer (Fischl et al., 2004). These parcellations as well as a histogram of their patch sizes are illustrated in Fig. 4.1. Since both parcellations embody a different concept to define functio-anatomical borders, the distributions of their patch sizes are significantly different as well. Both are useful for the desired simulations. However, the patch sizes are distributed over a rather large range. Moreover, certain intrinsic properties of these parcellations might distort the analysis (for instance, areas with a certain size might only be located in a particular area of the brain, and this would introduce a systematic bias). To safely exclude that patch size differences or other parcellation specific characteristics have a relevant influence on the reconstruction result, a more controlled setup regarding the prior knowledge seems reasonable. Therefore, artificial parcellations were generated and used for the MC simulations in Sec. 4.4-4.6. the sizes of the distinct functional areas are well controlled in these parcellations.

Two types of artificial parcellations are distinguished: homogeneous and inhomogeneous ones. The former consist of patches which are all equal in size. The latter contain parcels whose sizes belong to discrete equally spaced levels (7 levels were used, each with approxi-

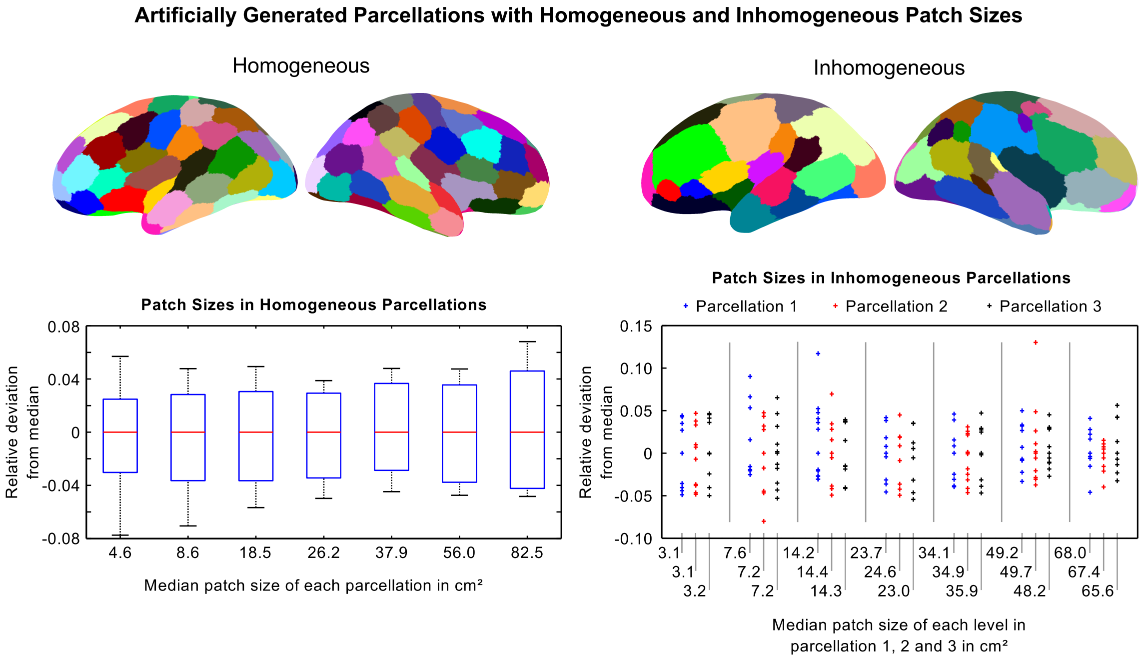

Figure 4.2: Artificial parcellations mapped on the inflated cortical surface and illustration of their patch sizes. Arbitrary patch colors. Top left: Homogeneous parcellation with a median patch size of 18.5 cm^2. Top right: Inhomogeneous parcellation no. 3 (see legend). Bottom left: Boxplots showing the variation of the patch size for each homogeneous parcellation. Bottom right: Scatter plot of the patch sizes in inhomogeneous parcellations, grey bars separate patch size levels.

mately the same number of patches) between a minimum and a maximum patch size. These parcellations were generated using an iterative procedure, which is briefly summarized in the following steps: (1) random selection of a seed point on the triangular mesh from the set of unlabeled sources, (2) assignment of the seed point and adjacent sources within a certain geodesic distance (which depends on the desired patch size) to a new patch, (3) repetition of step 1 until no further patch can be created without significantly overlapping existing ones, (4) assignment of sources in unlabeled regions to neighboring patches, thereby taking the patch size and the length of the patch boundary into account, and finally (5) iterative exchange of sources between neighboring patches until the size of all patches is in a range of ±5 % from the median. For an inhomogeneous parcellation, this constraint applies to each patch size level.

The mentioned procedure was used to generate a total of seven homogeneous and three inhomogeneous parcellations. The results are depicted in Fig. 4.2. The patch sizes in the homogeneous parcellations roughly cover the range of sizes found in the realistic parcellations (see above). The three inhomogeneous parcellations were generated in such a way that their individual patch size levels are approximately equal and, as before, that they cover a reasonable range of patch sizes. In fact, the size of some patches in both homogeneous and inhomogeneous parcellations is located outside the desired five percent interval. However, these outliers are, first, rather seldom and, second, still small enough to ignore potential side effects on the analysis. Homogeneous parcellations are referenced as the combination of the prefix HP with the integer digit of the corresponding median patch size throughout this chapter. For example, HP18 denotes the parcellation with 18.5 cm^2 sized patches. The three inhomogeneous parcellations are referenced with IP and the number 1, 2 or 3 (cmp. Fig. 4.2).

4.2.4 Source Activity and Simulated EEG data

The generation of simulated data is based on the activation of one or multiple compact sets of source dipoles. These sets are either defined manually (Sec. 4.3) or randomly based on the following steps. The first one is the selection of seed point(s) on the folded cortical surface. In a second step, sources in the vicinity of each seed point are used to generate an active cluster. Therefore, sources are selected according a maximum geodesic distance, which depends on the desired cluster size. Both the location of the seed points and the cluster sizes are random variables. Activation patterns in agreement or in deviation to prior information are distinguished. In the former case, functio-anatomical borders confine the spatial extent of active clusters. The latter case allows activity to spread over boundaries. This represents incorrect or at least uncertain prior information. The final step for generating the activation pattern is to assign the same random amplitude to all sources of a cluster. This ensures a homogeneous activation within clusters. This kind of activation is preferred over a rugged one. It is consistent with the prior assumption imposed by smooth reconstruction algorithms. Moreover, a discontinuous activation would produce very similar EEG/MEG data anyway.

The activation pattern q_{ref} is then projected to sensor space using the precomputed EEG leadfield matrix, i.e. $d_{\text{ref}} = Lq_{\text{ref}}$. Finally, uncorrelated zero mean Gaussian noise with the variance $\sigma_\epsilon^2 = \sigma_{\text{ref}}^2/\text{SNR}$ is added to the data, i.e. $d = d_{\text{ref}} + \epsilon$. σ_{ref}^2 is the variance over channels of the noise-free data, i.e. of d_{ref}, and SNR is a random variable or set to a fixed value, depending on the particular simulation.

4.2.5 Source Reconstruction Algorithms

This section summarizes the inverse algorithms and their parameterization employed for the simulations. The basis for all algorithms is the linear inverse solution presented in Eq. 2.13. With the assumption of uncorrelated noise, i.e. $C_\epsilon = \sigma_\epsilon^2 I$, it can be written as

$$\hat{q} = R_q L^T \left(LR_q L^T + \alpha^2 I\right)^{-1} d. \tag{4.1}$$

$\alpha^2 = \sigma_\epsilon^2/\sigma_q^2$ is the Tikhonov regularization parameter (cmp. Sec. 2.4.3). According to Eq. 2.15, assuming homoscedastic signals, i.e. $\text{tr}(C_d) = \text{tr}(\sigma_d^2 I) = \sigma_d^2 \cdot n$, and with $\text{tr}(C_\epsilon) = \sigma_\epsilon^2 \cdot n$ the parameter estimates to

$$\alpha^2 = \frac{\sigma_\epsilon^2 \cdot \text{tr}\left(LR_q L^T\right)}{n \cdot (\sigma_d^2 - \sigma_\epsilon^2)} = \frac{\text{tr}\left(LR_q L^T\right)}{n \cdot \text{SNR}}. \tag{4.2}$$

A similar estimate for α^2 has been used in other studies (Ahlfors and Simpson, 2004, Lin et al., 2004, 2006b, Liu et al., 2002, Molins et al., 2008). The linear source reconstruction methods that are used for the simulations in this chapter are summarized below. All are based on Eq. 4.1 and 4.2 .

The first algorithm under test is informed LORETA with R_q defined as proposed in Eq. 3.8. The Laplacian regularization parameter λ_B is selected according to the smoothness measure defined in Eq. 3.9. This measure is calculated for each set of incorporated boundaries, that means for each parcellation. Finally, multiple values for λ_B are selected according to the smoothness level used for the particular simulation.

The second method is uninformed LORETA with the source weighting matrix as defined in Eq. 2.24 and the surface Laplacian given in Eq. 2.27. It serves as a reference method in which nothing but general spatial smoothness is assumed *a priori*. As above, multiple values for the regularization parameter λ_B are selected on the basis of the smoothness measure (Eq. 3.9) to adjust the smoothness constraint.

Third, the FACE method is employed for the simulations. The off-diagonal elements of sources which are located in functional areas are defined as proposed in Eq. 2.29. The main diagonal elements of R_q are set to one. Both focal FACE ($\alpha_1 = 0.2$, $\alpha_2 = 0.1$) and extended FACE ($\alpha_1 = 0.6$, $\alpha_2 = 0.4$) are used. R_q is defined for each parcellation. Autocorrelated FACE or even combined FACE is not used in this study since, here, the source variance should not be defined *a priori*.

Finally, the WMN method (Eq. 2.20) is used as another reference method since it does not imply any assumption on the spatial correlation structure at all.

4.2.6 Evaluation Metrics

The evaluation of the results is based on comparisons between the reconstructed source distribution $\hat{q}$ and the simulated activation pattern q_{ref}. Given these patterns, the normalized energy $\hat{e}, e_{\text{ref}} \in \mathbb{R}^{\text{m}}$ for the i^{th} source defines as

$$\begin{aligned} \hat{e}(i) &= \hat{q}(i)^2 \Big/ \max\left(\left|\hat{q}(i)\right|\right)^2 \quad \text{and} \\ e_{\text{ref}}(i) &= q_{\text{ref}}(i)^2 \Big/ \max\left(\left|q_{\text{ref}}\right|\right)^2 . \end{aligned} \tag{4.3}$$

The set of sources $\Xi_a \in \Xi$ in the reference distribution q_{ref} whose normalized energy is nonzero, that means $e_{\text{ref}}(i) > 0$, are denoted as active sources. $\Xi \in [1, m]$ corresponds to the set of all sources in q_{ref}. Among visual inspection, the following evaluation metrics are used throughout this chapter. Moreover, statistical comparison between different distributions is performed using Kolmogorov-Smirnov tests.

The **relative energy** (RE) for a given source estimate $\hat{q}$ defines the total normalized energy produced by the set of originally activated sources Ξ_a with respect to the total normalized energy produced by all sources. It writes as

$$\text{RE} = \sum_{i \in \Xi_a} \hat{e}(i) \Bigg/ \sum_{i \in \Xi} \hat{e}(i) \tag{4.4}$$

A perfect reconstruction leads to a value of one. The value is zero if no activity is recovered in the activated region.

The **correlation coefficient** (COR) indicates how well the original pattern q_{ref} is reconstructed by the source estimate $\hat{q}$ for a given algorithm. It is particularly suited to assess the quality of algorithms producing smooth results. A value of one corresponds to a perfect reconstruction.

The **area under curve** (AUC, Grova et al., 2006) quantifies how well an inverse algorithm detects true active and true inactive sources. It is based on the receiver operating characteristic (ROC, Metz, 1986) of a detection method. The ROC can be constructed as follows. First, one selects a range of thresholds $\beta \in [0,1]$ and determines the number of true positive (TP, simulated and estimated source are active), true negative (TN, simulated and estimated source are inactive), false positive (FP, simulated source is inactive, estimated source is active) and false negative (FN, simulated source is active, estimated source is inactive) sources for each value of β. A source is active if its normalized energy is above this threshold (i.e. $\hat{e}, e_{\text{ref}} \geq \beta$). These quantities allow to define the

$$\begin{aligned} &\text{sensitivity}\left(\beta\right) = \text{TP}\left(\beta\right) / \left(\text{TP}\left(\beta\right) + \text{FN}\left(\beta\right)\right) \qquad \text{and the} \\ &\text{specificity}\left(\beta\right) = \text{TN}\left(\beta\right) / \left(\text{TN}\left(\beta\right) + \text{FP}\left(\beta\right)\right). \end{aligned} \tag{4.5}$$

Evaluating the $\text{sensitivity}\left(\beta\right)$ against $\left(1 - \text{specificity}\left(\beta\right)\right)$ gives the ROC curve as well as the AUC value being the area under this curve. According to Grova et al. (2006), a detection method is considered as accurate if its AUC exceeds 0.8. They reported the AUC to be biased for the evaluation of distributed reconstruction methods since the number of active sources is usually much smaller than the number of inactives (i.e. sources with zero activity). Therefore, these authors proposed to define a reduced set of $\text{card}\left(\Xi_a\right)$ inactive sources $\Xi_i \in \Xi \setminus \Xi_a$ to compute an appropriate AUC. Similarly to Cottereau et al. (2012), two selections for Ξ_i are used here resulting in the measures $\text{AUC}_{\text{close}}$ and AUC_{far}. The former is based on the set $\Xi_i^{\text{close}} \in \Xi_a^k\left(\Xi_a\right) \setminus \Xi_a$ containing only the closest inactive sources. $\Xi_a^k\left(\Xi_a\right)$ denotes the set of sources up to the k^{th} neighborhood of the seed point i that is used to generate Ξ_a. The neighborhood level k is chosen such that the number of sources in the two sets are approximately balanced, i.e. $\text{card}\left(\Xi_a\right) \approx \text{card}\left(\Xi_i^{\text{close}}\right)$. The $\text{AUC}_{\text{close}}$ index quantifies the ability of a method to focus on the originally activated region. The AUC_{far} index is determined using the strongest sources in the reconstructed distribution $\hat{q}$ which are located outside the region considered for $\text{AUC}_{\text{close}}$ and outside the originally activated region, $\Xi_i^{\text{far}} \in \Xi \setminus \left(\Xi_i^{\text{close}} \bigcup \Xi_a\right)$. It indicates whether spurious sources are generated far from the activated region. Both measures are combined to

$$\text{AUC} = 1/2 \left(\text{AUC}_{\text{close}} + \text{AUC}_{\text{far}}\right). \tag{4.6}$$

The **displacement error** (DE) refers to the distance between an activated cluster and the location of the nearest reconstructed cluster (i.e. a compact activation in the vicinity of a local maximum). The calculation of this measure requires the selection of unique sources from $\hat{q}$ and q_{ref}. This is done similarly as proposed by Im et al. (2003). First, a reference source in the originally activated cluster needs to be selected. Therefore, the source k_i in the i^{th} active cluster with the smallest error $\left\| L(\cdot,k_i) / \|L(\cdot,k_i)\|_2 - l_i^c \Big/ \left\| l_i^c \right\|_2 \right\|_2$, $l_i^c \in \mathbb{R}^{\text{n}}$ being the sum of leadfield vectors in cluster i, is taken as the reference location r_i^k of cluster i. Given the set of active sources, the selected source provides the best approximation for the leadfield of the whole cluster. Second, a reference source in the reconstructed source distribution needs to be selected. Therefore, the source k_j in the j^{th} reconstructed cluster (local maximum) in $\hat{q}$ with the strongest activity $\hat{e}\left(k_j\right) > \hat{e}\left(v\right), v \in \Xi(k_j)^3$, $\Xi(k_j)^3$ denoting the third order neighborhood of k_j, is used as the reference location r_j^k in cluster j. Afterwards, the geodesic distance between each reconstructed cluster (i.e. r_j^k) and the reference cluster (i.e. r_i^k) is calculated. DE corresponds to the smallest calculated distance. When multiple clusters are activated, this procedure is repeated for each activated cluster. The mean value of all shortest distances is computed to determine a unique value for DE in this case. This allows to calculate DE even if the number of activated and reconstructed clusters is different.

The **cluster activity variability** (CAV) is an original measure which indicates the homogeneity of activity within a given set of sources as, for instance, a patch of a parcellation. It is defined as the average squared relative difference between the normalized energies and the maximum normalized energy in given cluster. It writes as

$$\mathrm{CAV} = 1/N_c \sum_{i\in\Xi_c} \left(\hat{e}(i)/\hat{e}_c^{\max} - 1\right)^2 \tag{4.7}$$

with $\hat{e}_c^{\max} = \max(\hat{e}(\Xi_c))$ being the strongest activity in the selected cluster Ξ_c, and $N_c = \mathrm{card}(\Xi_c)$ being the number of sources in Ξ_c. The CAV value is zero when all sources have the same normalized energy, that means when the reconstruction method provides a homogeneous activation of the cluster. In the following simulations, clusters are the unique parcels of a parcellation. The CAV then indicates whether a smooth reconstruction method gives preference to the full activation of patches. The CAV is determined for both the patch in which the global reconstructed maximum is located (this is denoted as $\mathrm{CAV}^{\mathrm{global}}$) and for all patches containing local maxima. The mean of all local CAV values is computed to define $\mathrm{CAV}^{\mathrm{local}}$. Note that only one corresponding local maximum for each activated cluster is selected.

The **patch reconstruction frequency index** (PRFI) is another original measure. It is determined for every patch in a parcellation and defines as the relative difference between the patch reconstruction frequency (PRF) and the patch activation frequency (PAF), i.e. $\mathrm{PRFI}_i = (\mathrm{PRF}_i - \mathrm{PAF}_i)/\mathrm{PAF}_i$, $i \in [1, N_p]$. N_p is the number of patches in the parcellation. PRF_i corresponds to the absolute number of trials in which the maximum normalized energy is located in the i$^{\mathrm{th}}$ patch. PAF_i is given by the number of simulations in which sources are active in the i$^{\mathrm{th}}$ patch. A PRFI value smaller than zero corresponds to the case that sources in a particular patch are less frequently reconstructed than they are activated. Similarly, a positive PRFI value indicates that sources are more frequently reconstructed than activated. Determining the PRFI requires a significantly large number of repetitive simulations with random activation patterns in which always one cluster (not necessarily restricted to a single patch) is active. The measure is used in simulations with artificially generated inhomogeneous parcellations (see Sec. 4.2.3). It supports the identification of patch size dependent biases of a reconstruction method.

4.3 Informed LORETA: An Illustrative Demonstration

4.3.1 Objective

The simulations carried out in this section demonstrate principal characteristics of informed LORETA based source reconstruction. It is demonstrated how the algorithm performs when the prior knowledge is consistent to the true underlying activation. Moreover, it is shown how a potential mismatch between prior knowledge and true activation generally affects the inverse solution. This is basically done using manually defined activation patterns. The results provide a general insight into the capabilities of informed linear source reconstruction. A systematic quantitative analysis is carried out in Sec. 4.4-4.6.

4.3.2 Simulation Setup

This section includes three different simulations. The first is based on a simplified forward model with sources placed along the brain envelope (see Sec. 4.2.2). Prior knowledge was defined manually using several lines. They mimic both multiple functional areas and major sulcus lines (cmp. Sec. 3.3.4 and Fig. 4.3). Source activity was generated manually by activating compact regions. That means that all dipoles within a certain region were activated. The effective dipole at each vertex has a unit length and radial orientation. The generated source patterns were assigned to one of the following categories: (A) Activity is inside patches, (B) activity is far away from any patch, and (C) activity is in the close vicinity of patches (this includes the case where activity overlaps patch boundaries). The two latter ones represent a mismatch between prior information and true activity. WMN, uninformed and informed LORETA were employed for source reconstruction. The smoothness level $f(\lambda_B) = 0.5$ was used for Laplacian regularization (i.e. $\lambda_B^i = 3.6 \times 10^{-6}$ and $\lambda_B^u = 7.1 \times 10^{-7}$). The superscripts i and u denote informed and uninformed LORETA. The simulations were carried out without noise, i.e. $\mathrm{SNR} = 10^8$.

The second simulation is based on a realistic forward model (see Sec. 4.2.2). Functio-anatomical prior information was derived by selecting a subset of patches from the Desikan-Killiany-Atlas (cmp. Fig. 4.1), namely pars opercularis, pars triangularis and pars orbitalis of the inferior frontal gyrus (the selected areas can be seen in Fig. 4.4). These areas roughly correspond to BA 44, 45 and 47. Like above, compact source patterns were generated (manually) and assigned to one of the three categories. However, only one dipole needs to be activated at each vertex. Noise at several SNR levels was added to the generated data. The regularization parameters for informed and uninformed LORETA are $\lambda_B^i = 3.0 \times 10^{-10}$ and $\lambda_B^u = 2.8 \times 10^{-10}$.

The third simulation employs the realistic forward model as well. Two different setups for the prior knowledge are distinguished. The first is subsequently referred to as the *full model*. It consists of all patches given by the Destrieux-Atlas (see Fig. 4.1). The second is the *language model*. It only contains areas in the temporal lobe and the inferior frontal part of the cortex (see separate box in Fig. 4.5). These areas are commonly assumed to be involved in language processing[1]. Activity was generated as follows. Between 1 and 19 patches were randomly drawn from the full parcellation. All sources in these patches were activated with unit strength. A total of 1000 source patterns were generated for each number of concurrently active patches. Finally, noise according to several SNR levels in the range from 1 to 10^8 was added to the forward solution of each generated source pattern. The simulation setup implies that a mismatch between prior knowledge and true activation can only occur for the language model. WMN, uninformed and informed LORETA were employed for source reconstruction. Now, three different smoothness levels were used for the LORETA methods, i.e. $f(\lambda_B) = 0.01$ for low smoothness, $f(\lambda_B) = 0.5$ for medium smoothness, and $f(\lambda_B) = 0.99$ for a high smoothness level. The related parameters are: $\lambda_B^{\mathrm{uh}} = 3.2 \times 10^{-12}$, $\lambda_B^{\mathrm{um}} = 3 \times 10^{-10}$ and $\lambda_B^{\mathrm{ul}} = 1.1 \times 10^{-7}$ for uninformed LORETA; $\lambda_B^{\mathrm{ih\_fu}} = 1.2 \times 10^{-10}$, $\lambda_B^{\mathrm{im\_fu}} = 3.9 \times 10^{-8}$ and $\lambda_B^{\mathrm{il\_fu}} = 9.4 \times 10^{-5}$ for uninformed LORETA with the full model; $\lambda_B^{\mathrm{ih\_la}} = 1.9 \times 10^{-12}$, $\lambda_B^{\mathrm{im\_la}} = 2.3 \times 10^{-10}$ and $\lambda_B^{\mathrm{il\_la}} = 1.3 \times 10^{-7}$ for uninformed LORETA with the language model. The additional subscript letters *h*, *m* and *l* denote the smoothness level (high / medium / low) and the abbreviations *fu* and *la* the prior models

---

[1] The *language model* was used for the prospect of analyzing experimental language data in chapter 5.

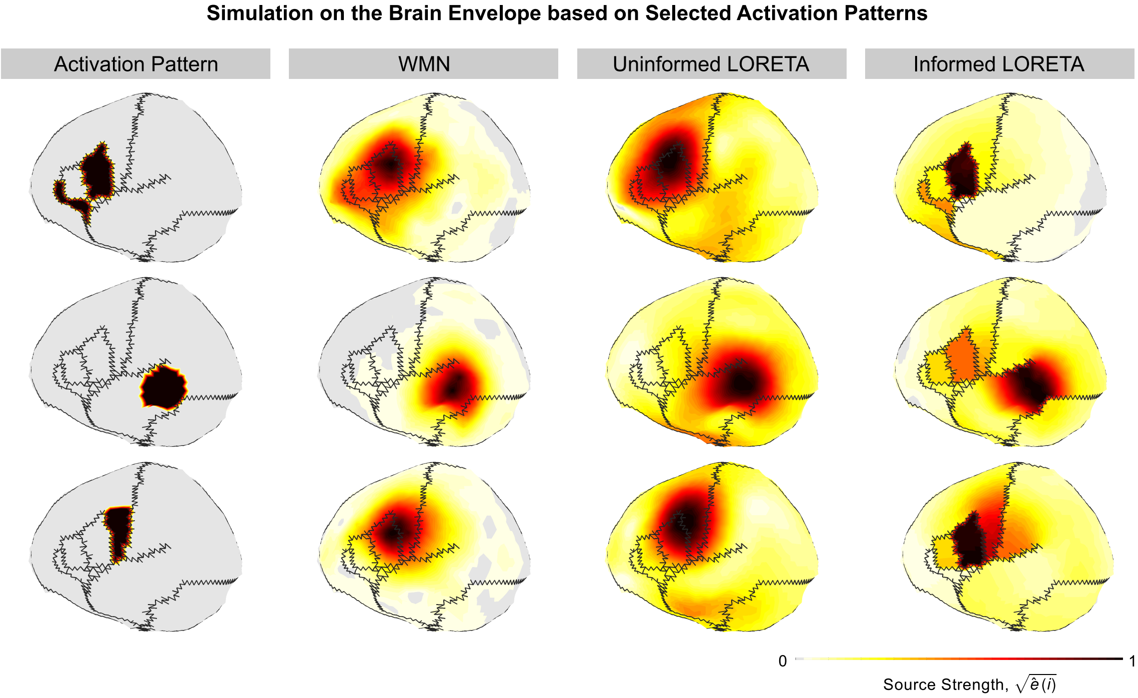

Figure 4.3: Representative examples of reconstructed source distributions. Upper/Middle/Lower row refers to category A (activity inside patches) / B (activity far from any patch) / C (activity in the close vicinity of patches). Black edges mimic functio-anatomical boundaries. Arbitrary units.

full and language, respectively. Finally, the COR metric was used to assess the results.

4.3.3 Results

The results for the simulations on the brain envelope are presented in Fig. 4.3. One representative activation pattern and the related reconstructed source distributions are shown for each category. Generally, uninformed LORETA and WMN produce blurred activity distributions with a maximum peak inside or at least very close to the activated region. For category A, informed LORETA produces homogeneous distributions inside the activated patches with a strong change of source strengths at boundaries. The visual correspondence between reconstructed and activated source pattern is remarkably high. For category B, informed and uninformed LORETA solutions are largely similar. However, informed LORETA sometimes produces an additional local peak in patch areas. Besides that, the example emphasizes that non-patch boundaries constrain the spatial distribution as well. For category C, informed LORETA solutions are characterized by the fact that the strongest activity is reconstructed inside a patch close to the original activation. All sources within this patch usually have similar strength. In contrast to category A, however, some activity is also produced outside patches.

Figure 4.4 shows representative results for the second simulation. WMN and uninformed LORETA solutions are now generally much more different in comparison to the simulation on the brain envelope. The category A results for informed LORETA are strongly dominated by prior knowledge. In contrast to the uninformed methods, informed LORETA separates multiple sources even in the presence of moderate noise (i.e. here BA 44 and 47). Functio-anatomical

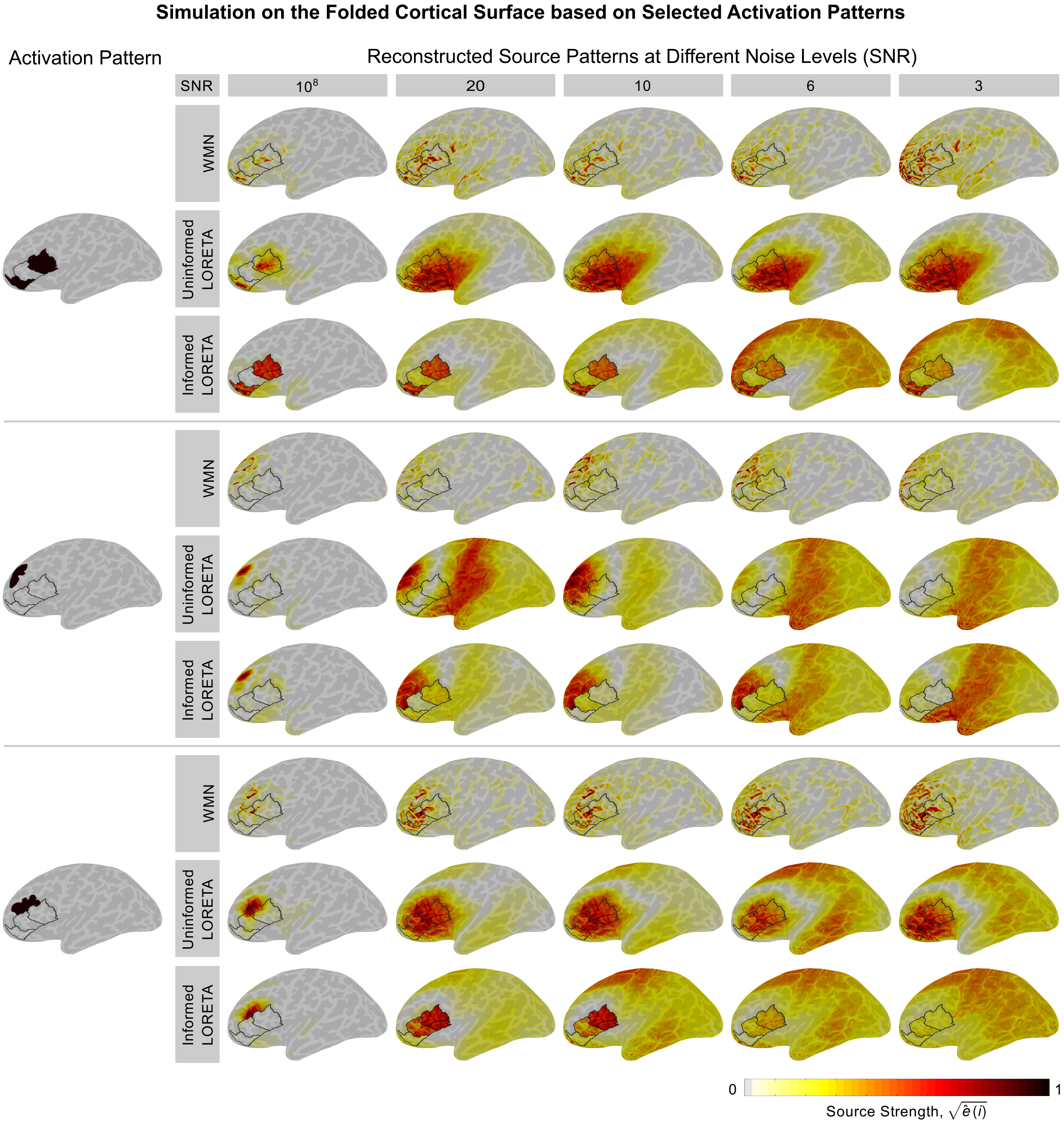

Figure 4.4: Representative examples of reconstructed source distributions shown on the inflated cortex. Upper/Middle/Lower row refers to category A / B / C. Black edges mimic functio-anatomical boundaries. Arbitrary units.

prior information is much less dominant in category B reconstruction results. This is even the case for low SNR values. Uninformed and informed LORETA solutions become more and more similar towards lower SNR levels. Interestingly, the influence of prior information for category C is strong in the presence of noise but very much reduced in the noise-free case.

The third simulation provides a more quantitative analysis. Figure 4.5 shows the performance of informed LORETA in dependence of the number of concurrently active clusters and the SNR level. The colored surface in each graph represents the median of the COR values. Similarly the upper gray shaded surface represents the 95 % percentile and the lower surface the 5 % percentile. Figure 4.6 shows the median COR values determined from simulations with

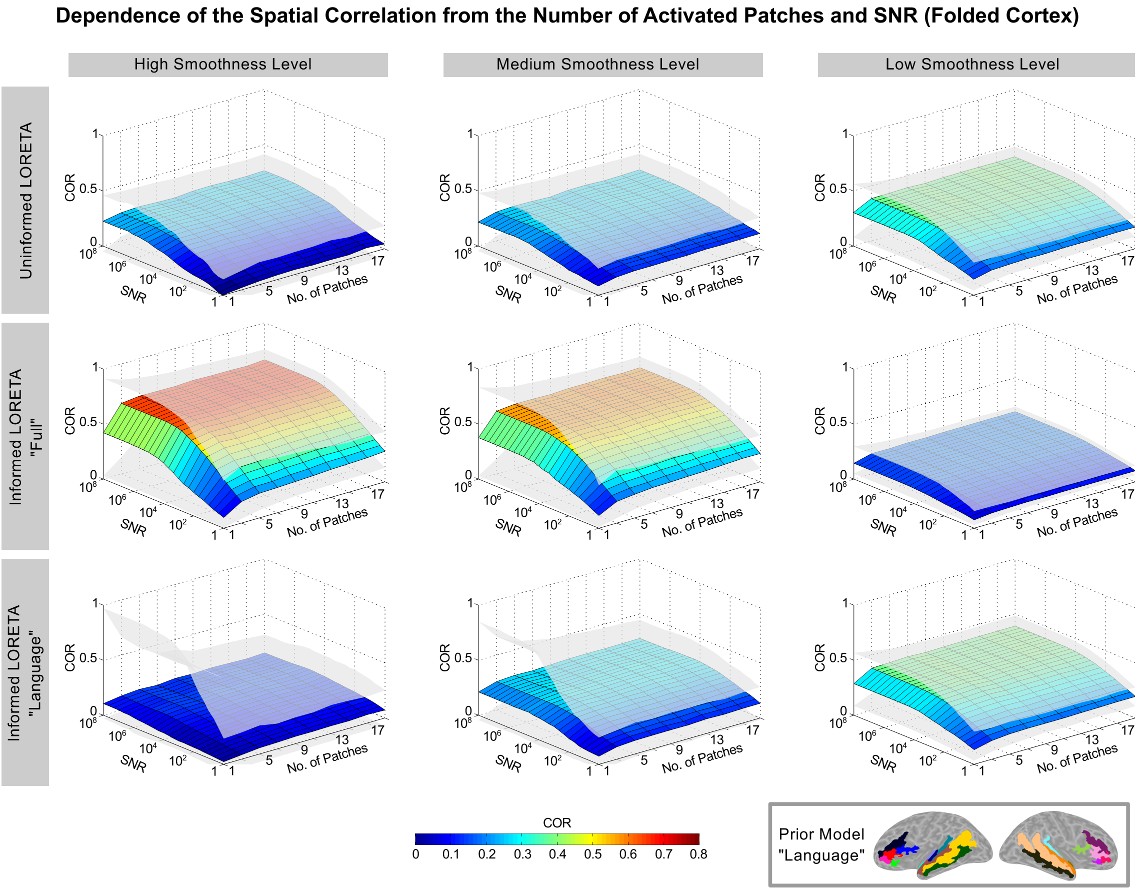

Figure 4.5: Characteristic values of the COR distribution derived from integrating over patches. See text for an explanation on the different surfaces. The colorbar encodes median COR values. Arbitrary colors are used to illustrate the patches in the language model.

source patterns in which only single patches were active. The results are integrated over noise levels. The following major conclusions can be drawn from these complementary figures.

In general, the overall reconstruction quality given by the median COR values reduces towards higher smoothness levels for uninformed LORETA and informed LORETA employing the language model while it improves for informed LORETA with the full model. It can be observed that the COR values obtained for informed LORETA with the full model and for a strong smoothness constraint are quite high for the majority of patches. In contrast, only a small subset of patches receives high values with the language model. It is particularly important, however, that activity in some areas (e.g. Heschl's gyri) can only be reconstructed using the language model. The highly different numbers of patches with low and high COR values in both models explain the shape of both their median and 95-percentile surface shown in Fig. 4.5. For informed LORETA with the language model, the median of the COR values can only be close to one if all activated patches are part of the prior model. It is obvious that this is very unlikely when multiple patches are activated.

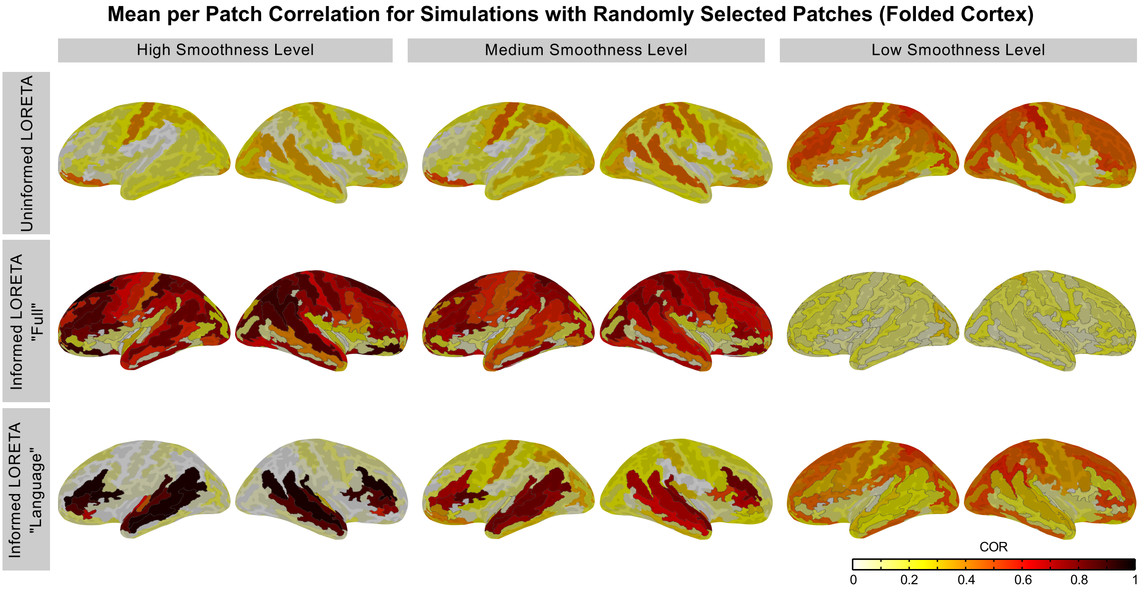

Figure 4.6: Median of each per-patch COR distribution derived from integrating over noise levels mapped on the inflated cortical surface (by assigning the median of a patch to all of its vertices).

4.3.4 Discussion

Three simulations were carried out in this section. The main objective was to study the performance of informed LORETA in two generally different situations. In the first, prior knowledge and generated source activity are consistent. In the second case, prior knowledge and source activity deviate from each other. The simulations ought to provide a first general impression how the prior assumptions based on different smoothness levels influence the source distribution.

The first simulation effectively isolated the effect of match and mismatch between prior knowledge and activation. Therefore, the influence of noise was discarded, and manually defined patch-like activation patterns, a simplistic forward model, and a fixed smoothness level were used. In general, the results show that lifting the functional coupling between neighboring sources somewhere on the cortex constrains the spread of the whole source distribution. It can be seen that activity inside the small patches is always homogeneously distributed. This is the result of the strong smoothness constraint that was used for informed LORETA. In fact, such a homogeneous pattern is the best solution subject to the constraint of minimizing the second order spatial derivative. This explains the very good correspondence between generated and reconstructed patterns in category A. The results also reveal that informed LORETA suppresses activity in the vicinity of the patches. In such a case, the algorithm prefers activity inside patches. This leads to spurious sources for category B and to a mislocalization for category C. These results clearly demonstrate that the performance of informed LORETA with a strong smoothness level strongly depends on the correspondence between true activity and prior knowledge.

The second simulation aimed to study the performance of informed LORETA for category A source patterns under more realistic conditions. Therefore, a realistic forward model and noisy data were used. Tests using a realistic source model are important because the surface LORETA approach embodies two different constraints on the folded cortical surface. The first one is the minimum norm constraint, which is based on leadfield similarity. The second one is the smoothness constraint, which enforces similarity between neighboring sources. Both constraints can be in a contradiction. For example, two sources on the opposite walls of a sulcus have similar leadfields, but a rather large geodesic distance (that means that the minimum norm constraint might support their co-activation, while the smoothness constraint does not). Interestingly, the results presented by Knösche et al. (2013) suggested that this potential conflict might reduces the effect of the smoothness constraint when the reconstruction is performed on the folded cortex. Consequently, also the effect of incorporating of function-anatomical boundaries (i.e. prior knowlegde) would be low. According to the authors, only the patch-based smoothness approach (i.e. PatchLORETA2, cmp. Sec.2.5.4) would provide a spatial smoothness constraint which is stronger than the constraint on leadfield similarities. The results presented here, however, are not in agreement with these findings. The comparison between WMN and uninformed LORETA results reveals a significant difference between the reconstructed spatial distributions. This clearly emphasizes that the smoothness constraint in fact has a strong influence on the folded cortex. Moreover, the informed LORETA results show a clear effect of incorporating functional boundaries. These apparently different findings can be explained with the strength of the smoothness constraint, which is controlled by Laplacian regularization. In contrast to Knösche et al. (2013), the simulations here are based on a systematic adjustment of the regularization parameter to enforce a high smoothness level. In fact, this is comparable to the patch-based smoothness approach (i.e. PatchLORETA2). These results underpin the importance of Laplacian regularization, even though the regularization parameter was not systematically varied at all. Finally, the results exhibit a good visual correspondence between activated and reconstructed source patterns even for lower SNR ratios given that the underlying activation and prior knowledge are consistent[2]. Hence, the incorporation of prior knowledge improves source localization in this particular case.

The third simulation provides brief insight on how the use of different prior models (i.e. a certain set of functional boundaries) and smoothness levels affects source reconstruction. The following considerations are useful before analyzing the results. Each prior model divides the cortex into a fixed number of separated areas. The language model divides the cortical sheet into a small number of patches and a huge unlabeled area on each hemisphere. Likewise, even uninformed LORETA implies a separation of the source space into two huge areas, i.e. the left and right hemisphere. In case of the full model, the subdivision of the cortex is consistent with the full parcellation. It should be noted that the combination of any of these subdivisions with a certain smoothness level defines a unique prior model.

Let us first consider the results for the highest smoothness level. Hence, sources within each cortical area are expected to be correlated (cmp. Sec. 3.4.2). Consequently, the full model embodies the *a priori* assumption that the data can be explained with activity that can be located anywhere on the cortex and that exactly follows the shape of patches. In contrast, the language model assumes patch-like activity only in certain regions. Outside these rather small regions (that means in the unlabeled areas), extremely wide-spread solutions are expected. It is obvious that this kind of extreme smoothness constraint penalizes activity which exhibits a

---

[2] In fact, this is an inherent assumption when employing prior knowledge for the analysis of real data.

clear maximum in this region (i.e. focal solutions and even moderately distributed solutions are rather unlikely). For uninformed LORETA, such wide-spread solutions are expected anywhere. Therefore, the full model perfectly fits to the data generation procedure. This explains the generally good reconstruction quality that can be observed for this method. The other two methods impose an *a priori* assumption that is in conflict to the data either anywhere on the cortex (uninformed LORETA) or only in certain regions (informed LORETA with the language model). This explains why a good reconstruction quality for the latter one can only be observed when the activation occurs in an *a priori* defined patch. It is important, however, that the language model performs better than the full model when activity is generated in certain areas. For instance, activity from areas in the inferior frontal sulcus and the lateral fissure, e.g. Heschl's gyri, are poorly reconstructed using the full model. It seems that activity in these regions is rather explained by means of activity in superficial regions as, for instance, the superior temporal gyrus. In contrast, the language model comprises some of these deeper patches and provides much better reconstruction results for them (cmp. Fig. 4.6). This means that the prior information (which only contains information on the functional boundaries) causes a bias of the solution towards the a priori defined regions. This is particularly interesting since the incorporation of these functional boundaries into the Laplacian does not increase the *a priori* variances of these sources. Hence, the method can, for instance, be used to reconstruct evoked brain activity from deeper brain areas.

Next, the reduction of the smoothness constraint is considered. It was shown in Sec. 3.4.3 that the estimated correlation between two sources only depends on their geodesic distance (i.e. for a fixed smoothness level). The patch size has no influence on the correlation. However, the maximum geodesic distance between two sources (in the same patch) depends on the patch size. In other words, a source in a large patch can be correlated to more distant sources in comparison to a source in a small patch. This leads to the effect that a reduction of the smoothness level at first affects the correlation structure in large patches. As a consequence, the patch sizes (or rather the differences between the sizes of separated areas) have a strong impact on the changes in the *a priori* covariance structure that occur when the smoothness level is reduced. For uninformed LORETA, the two areas are approximately equal in size. Hence, the changes in covariance structure are similar in each area. The lower the smoothness level, the more focal sources can be reconstructed. This is also reflected by the simulation results. Consequently, a high smoothness level is inappropriate to reconstruct patch-like or even focal activity using uninformed LORETA. Likewise, the areas in the full model are approximately equal in size as well[3]. Thus, lowering the smoothness level affects the estimated covariance structure in each patch in a more or less similar manner. The reconstruction quality reduces towards lower smoothness levels since homogeneous source strengths inside separated areas (which are also used for data generation) are more and more penalized. By the way, this suggests that it is in principle possible to formulate a prior assumption which prefers the partial activation of patches. The areas in the language model are much less homogeneous in size. The unlabeled regions are much larger than the incorporated patches. Hence, a reduction of the smoothness level affects the covariance structure in the two large areas before changes in the smaller areas can be expected. A reduced smoothness constraint in the larger areas reduces the bias effect

---

[3] In fact, all patches are slightly different in size (cmp. Fig. 4.1). It is analyzed in Sec. 4.4 whether such differences might produce any significant bias on the solution.

(i.e. the penalty for less smooth solution reduces as well) towards the smaller areas. Again, this is clearly reflected in the simulation results. It is interesting, however, that this bias is already remarkably low at a level of 0.5, for which the correlation in the large areas is still expected to be wide-spread. This discussion emphasizes that the underlying functional organization defined by prior knowledge must be considered to select a meaningful smoothness level.

Finally, the results for the lowest smoothness level are shortly discussed. Although the results of the methods converge with increasing regularization, they are still very different for the lowest smoothness level used here. This can be explained with the calculation of the smoothness measure (Eq. 3.9). The calculation includes a normalization to the maximum sum of covariances. This number depends on the largest separated area in each prior model. For that reason, models containing larger areas (e.g. uninformed LORETA) are more similar to the identity matrix for the largest Laplacian regularization parameters used here.

4.4 Spatial Characteristics of Informed Linear Source Estimates

4.4.1 Objective

It is particular interesting whether the source localization results of informed reconstruction methods depend on certain spatial features of both the incorporated functio-anatomical prior knowledge and the underlying source activity. This section aims at a systematic evaluation on the basis of MC simulations and using prior knowledge derived from arbitrary parcellations. The evaluation focuses on the following questions, which are raised with respect to the findings presented in chapter 3: (1) Do variations of the patch sizes contained in a parcellation affect the reconstruction result (i.e. do they bias the solution)? (2) Does any method produce certain spatial patterns independently of the underlying activity, that means is there a tendency to focal or widespread solutions or some bias towards certain regions? (3) How does the performance of a method depend on the spatial extent of the underlying activity? All simulations are carried out under the assumption that the incorporated boundaries are in agreement with the likely generators of the data and under noise-free conditions.

4.4.2 Simulation Setup

The simulations in this section are based on the realistic forward model (see Sec. 4.2.2 for details). The artificial parcellations described in Sec. 4.2.3 were used as prior information. A total of 5000 independent trials for each parcellation were generated as follows: Data was generated by means of the random activation of compact clusters with unique source strengths (see Sec. 4.2.4). The target size of the cluster was selected from a range between $22\,\mathrm{mm}^2$ (also being the step width) and 1.1 times the size of the respective patch. Activity was always consistent with prior knowledge. that means it did not overlap functional boundaries. Sources close to or even inside the interhemispheric fissure were not activated. An SNR of 1×10^8 was used for the simulations to suppress any side effects that might be introduced by noise.

Focal FACE, extended FACE, informed LORETA for six smoothness levels (i.e. 0.01, 0.2, 0.4, 0.6, 0.8, and 0.99), and WMN were employed for source reconstruction. See Sec. 4.2.5 for details and appendix B.1 for the corresponding Laplacian regularization parameters for each parcellation. Finally, the size of the activated area and the metrics COR, AUC, DE, $\mathrm{CAV}^{\mathrm{local}}$, and

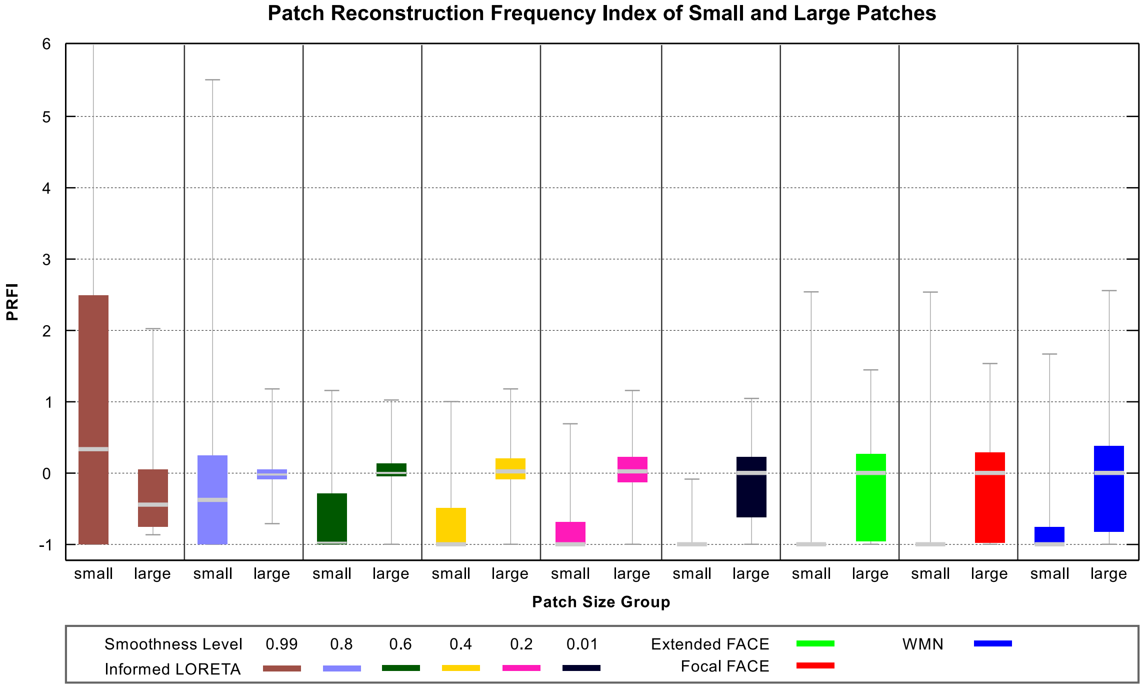

Figure 4.7: Distributions of PRFI derived from inhomogeneous parcellations. The boxplots indicate first and last quartile, median, and extreme points of the PRFI distributions. The latter are truncated in some cases in favour of a suitable resolution for all distributions. The left/right bar for each algorithm comprises the PRFI for all patches belonging to the 2 smallest/largest patch size levels of the 3 inhomogeneous parcellations. Median patch size in small/large group is 709 mm^2/5361 mm^2.

CAV$^{\text{global}}$ were computed for each reconstruction result. Besides that, the PRFI was determined for each patch.

4.4.3 Results

Effect of patch size differences: Based on the discussion in Sec. 4.3.4 there is reason to believe that patch size differences within a parcellation cause undesired side-effects in the solution. For example, a strong smoothness constraint for informed LORETA might lead to a preferred reconstruction of sources in small patches. The first analysis is based on the results for the three different inhomogeneous parcellations, each of which consisting of seven patch size levels. Figure 4.7 shows the PRFI for all small and large patches from these parcellations. Patches belonging to the two smallest size levels are joined together in the *small* group ($N = 43$ patches), patches from the two largest levels are joined in the *large* group ($N = 55$). The observations obtained for the small and the large group are statistically different for each reconstruction method ($P < 2 \times 10^{-3}$, Kolmogorov-Smirnov).

The standard deviation and the median of the informed LORETA results for the small group reduce when the smoothness levels becomes lower. The median converges to -1 (with respect to lower smoothness levels). That means that most of these patches are poorly reconstructed. In contrast, the median in the large group is approximately zero for all smoothness levels below 0.99 and the standard deviation systematically increases when the smoothness constraint is reduced. This means that some of these patches are more frequently reconstructed than

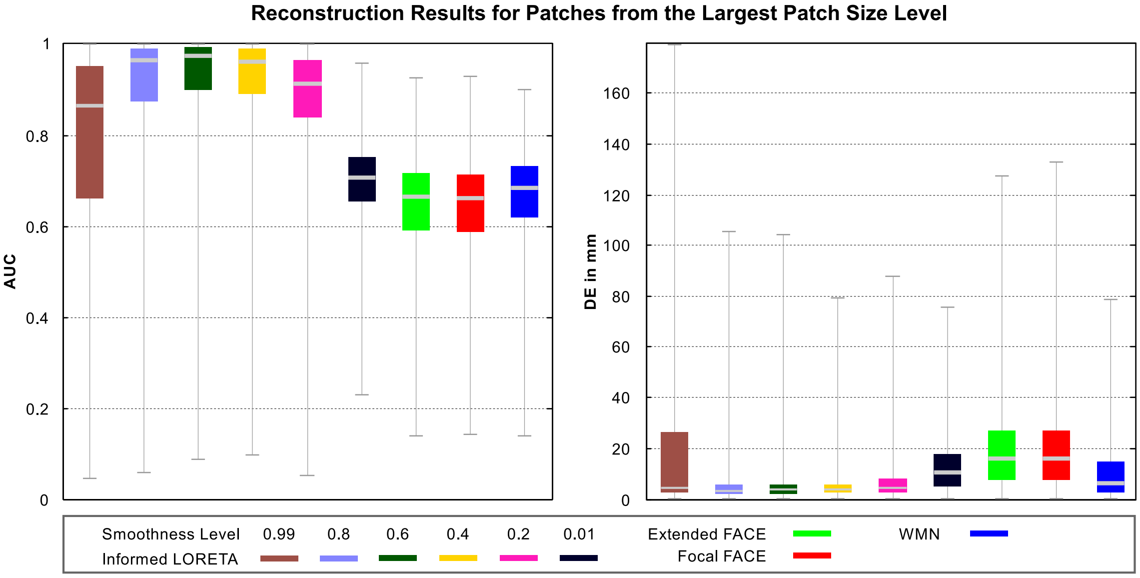

Figure 4.8: AUC and DE distributions derived from simulation trials with active sources inside patches belonging to the largest patch size level of the inhomogeneous parcellations (median patch size is 6404 mm^2). The boxplots indicate first and last quartile, median, and extreme points of the distributions.

others in this group. The obvious concentration of activity to a subset of large patches can be explained with the minimum norm effect. Lowering the smoothness constraint increases the degrees of freedom and, therefore, also the tendency to focussed activity in superficial regions. These regions are only covered by a few patches. Moreover, it is more likely that these regions are covered by large patches than that a smaller patch covers a superficial region (remember that the number of patches in each patch size level is approximately equal). This explains why a subset of large patches is preferred for low smoothness levels. The results for the strongest smoothness level clearly indicate a bias towards small patches. First, the majority of small patches (median of the PRFI values is 0.33) is reconstructed much more frequently[4] than they are activated. Second, the majority of large patches has negative PRFI values (median is minus 0.43) and is therefore less frequently activated. This effect, which indicates a considerable bias towards small patches, is already significantly reduced at a smoothness level of 0.8.

Information on a smoothness level dependent bias can also be drawn from AUC and DE distributions. The distributions shown in Fig. 4.8 are derived from simulation trials with activity located in large patches (i.e. patches from the largest level of the inhomogeneous parcellations). Each distribution comprises $N = 8541$ observations and all are statistically different from each other (AUC: $P < 1 \times 10^{-7}$, DE: $P < 0.03$), except for the two FACE distributions (AUC: $P = 0.07$, DE: $P = 0.7$). Particularly the smoothness levels 0.8, 0.6, and 0.4 outperform the other informed LORETA derivatives as well as FACE and WMN. A weak smoothness constraint (which can also be assumed for eFACE, fFACE and WMN) obviously reduces the AUC and increases DE. As above, this can be explained with the minimum norm constraint and the tendency to superficial sources. The results for the strongest smoothness constraint clearly indicate a bias towards smaller patches since the reconstruction quality of large patches is significantly re-

---

[4] An PRFI of 1 denotes a twice times more frequent reconstruction than activation.

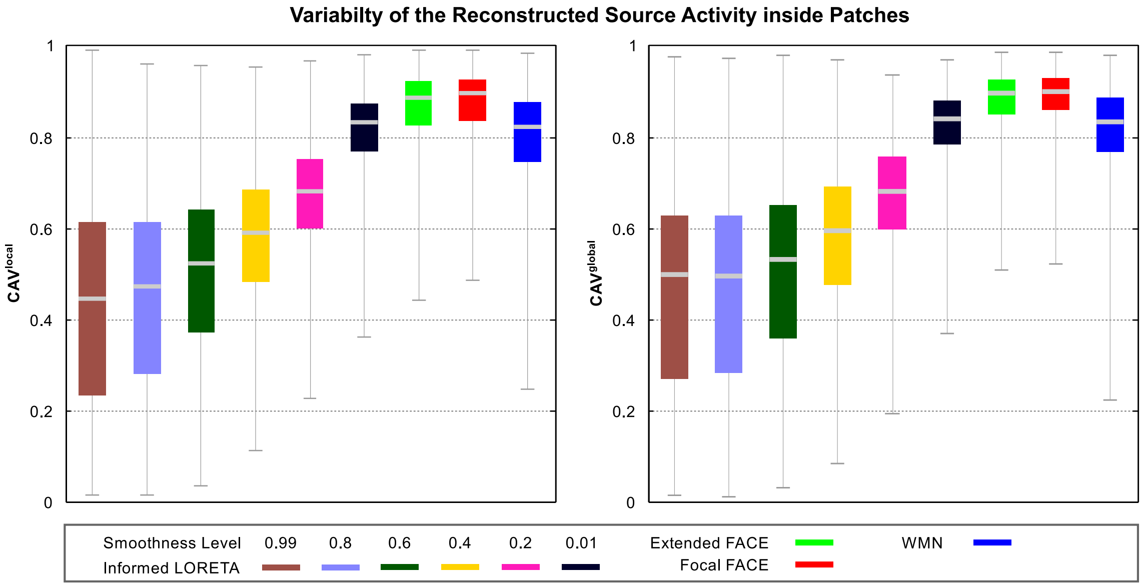

Figure 4.9: Distributions of CAV$^{\text{local}}$ (left) and CAV$^{\text{global}}$ (right), observations from all homogeneous parcellations are grouped together for each method. Active cluster size and patch are size are not considered. The boxplots indicate first and last quartile, median, and extreme points of the CAV distributions.

duced. The standard deviation of both distributions is rather large. This implies that the reconstruction quality is very good for certain patches, but other patches are affected by the bias. The bias effect seems to have almost vanished at a smoothness level of 0.8. These findings are in agreement with the analysis of the PRFI presented above.

Spatial extent of reconstructed activity: The next analysis focuses on the spatial distribution of reconstructed activity inside patches. The analysis is restricted to homogeneous parcellations to minimize any side-effects as, for instance the patch size depend bias. First, the CAV results derived on the basis of these parcellations were combined for each reconstruction method ($N = 35\,000$ per method). Figure 4.9 shows CAV$^{\text{global}}$ and CAV$^{\text{local}}$. The patch sizes and the extent of the activated areas are not taken into account. For each of the two metrics all distributions are statistically different from each other ($P < 1 \times 10^{-8}$). Note that the CAV is a quadratic measure. That means, only values very close to zero indicate a homogeneous activation of all sources within a patch[5].

First, the results clearly reflect that the source strengths inside patches are generally more similar when the smoothness contraint is stronger. Nonetheless, rugged solutions, which are certainly in a contradiction with the smoothness constraint, even appear for the levels 0.6, 0.8, and 0.99. This emphasizes that the smoothness constraint is not overestimated, that means the homogeneous activation of sources inside a patch must explain the data. Second, the results show that reconstruction methods with only a weak smoothness constraint (including FACE and WMN) cannot produce homogeneous solutions.

The distributions for higher smoothness levels exhibit a particularly large variance. Figure

---

[5] Considering two sources, a CAV value of 0.1 already corresponds to a rather large difference of around 45 % between their normalized energies.

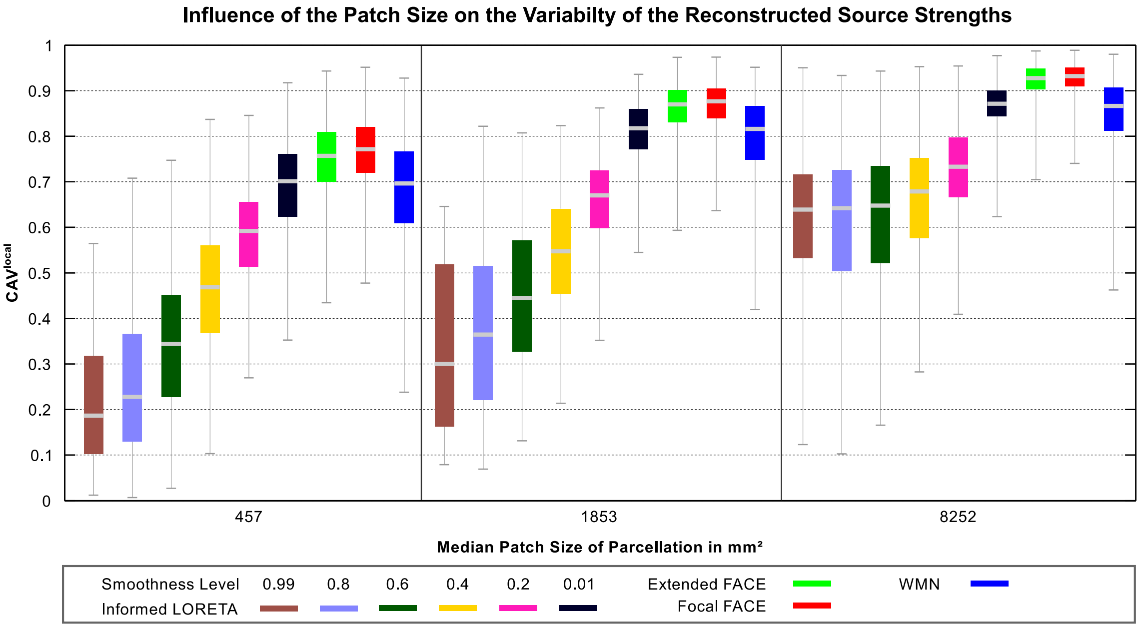

Figure 4.10: Distributions of $\mathrm{CAV}^{\mathrm{local}}$ derived on the basis of three homogeneous parcellations. Sizes of activated clusters are not considered. The boxplots indicate first and last quartile, median, and extreme points of the CAV distributions.

4.10 illustrates that this variance can be explained with the different patch sizes. Shown are the CAV measures derived for three homogeneous parcellations consisting of differently sized patches (the analysis was limited to $\mathrm{CAV}^{\mathrm{local}}$). The distributions obtained for each parcellation are statistically different from each other ($N = 5000$ per method, $P < 2 \times 10^{-4}$). First, the figure shows a considerable shift of the distributions towards higher CAV values for larger patches. It is obvious, however, that the strength of this effect depends on the smoothness level. Second, very focal solutions ($\mathrm{CAV} \geq 0.9$) only appear for the coarsest parcellation. In contrast, homogeneously activated patches ($\mathrm{CAV} \approx 0$) can only be found for the fine-grained parcellation. This can be explained as follows. It is very likely that the homogeneous activation of all sources in a large patch leads to a strong mismatch between predicted and recorded data. This is different for small patches since the limited spatial extent of the activity also limits the potential prediction error. Consequently, solutions with fully activated patches are more unlikely to occur for coarse parcellations if these solutions are not supported by data.

The location of the activated cluster and the cluster size employed to generate simulation data are certainly other aspects that can explain the variance in the CAV distributions. Studying the influence of the cluster size is particularly interesting since the ratio between cluster and patch size defines an optimal CAV that can be measured for a particular simulation. Therefore, the following section examines the reconstruction quality with respect to this ratio more closely.

Spatial extent of simulated activity: The final analysis in this section focuses on the dependence of the reconstruction quality on both activated cluster and patch size. The analysis is carried out on the basis of the ratio between these two parameters. This allows to combine the results derived for all homogeneous parcellations. Figure 4.11 shows scatter plots of the AUC

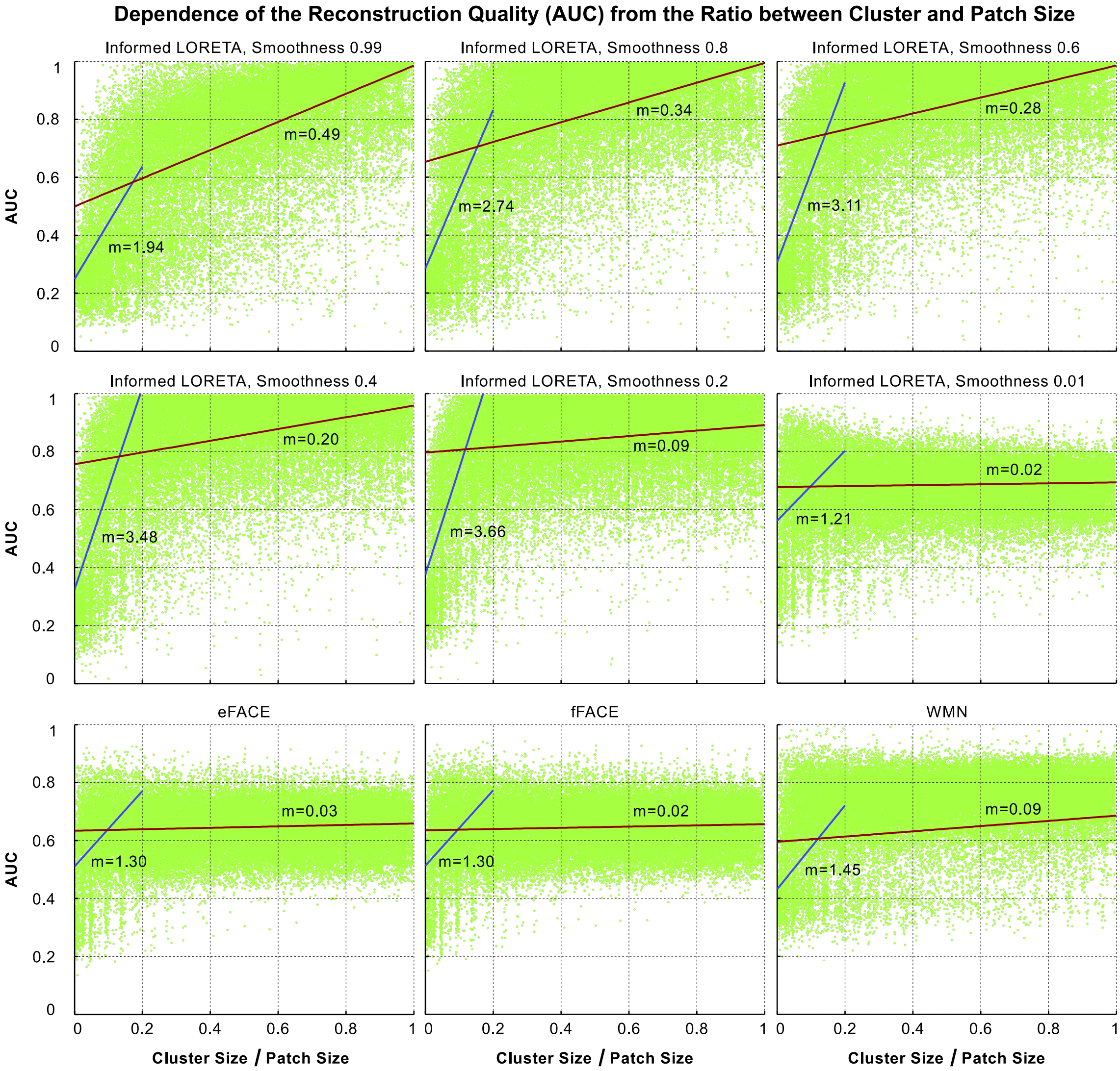

Figure 4.11: Scatter plots of the AUC metric (green dots) derived on the basis of homogeneous parcellations. Red/Blue lines are derived from a linear fit of the observations in the range from 0-0.1/0.1-1 on the abscissa. Values close to the lines denote the slopes. Axis labels apply to all figures in a row/column.

observations and two linear functions for each reconstruction method ($N = 35\,000$ samples per method). Their meaning is discussed below. Apart from eFACE and fFACE (statistically similar, $P = 0.36$) all AUC distributions are statistically different from each other ($P < 1 \times 10^{-8}$).

All plots in Fig. 4.11 exhibit a high concentration of small AUC values (AUC < 0.5) at small ratios between cluster and patch size. This is even the case for WMN. Therefore, the effect must be explained with the minimum norm constraint. The AUC values smaller than 0.5 imply that the originally activated sources are explained by activity in other areas. For WMN, this is usually the case for small clusters at the walls and the bottom of sulci. Sources in these regions usually have a smaller leadfield norm than superficial sources. As a consequence, it is particularly difficult to reconstruct activity using any of the evaluated methods if the cluster is small compared to the patch size and if the cluster is located in the mentioned regions. The

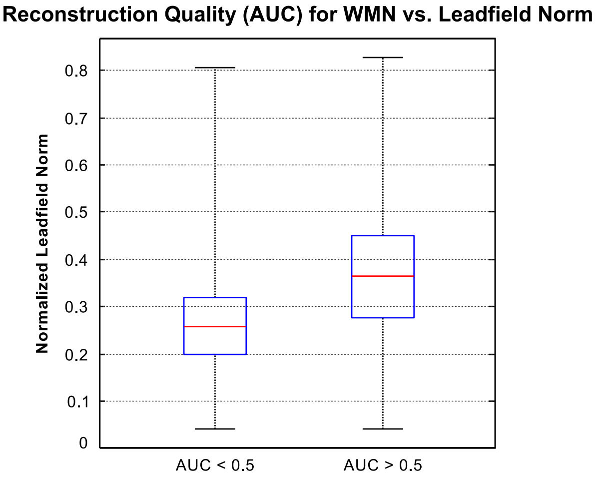

Figure 4.12: Distributions of the normalized leadfield norm of cluster seed points (the euclidean norm of each leadfield vector is divided by the strongest leadfield vector on the cortex) for AUC observations lower and higher 0.5. Results are derived on the basis of all homogeneous parcellations. The boxplots indicate first and last quartile, median, and extreme points of the distributions.

two distributions displayed in Fig. 4.12 (statistically different, $P < 1 \times 10^{-8}$) illustrate that small AUCs in fact coincide with small leadfield norms of the seed points of active clusters. It can therefore be assumed that the increased number of AUCs lower than 0.5 at small ratios in Fig. 4.11 are caused by small active clusters surrounding such seeds. Obviously, this bias effect even occurs when a smoothness constraint is applied. Therefore, it is useful to focus on larger ratios (e.g. AUC ≥ 0.1) to assess the reconstruction quality.

Due to the large variance of the observations in Fig. 4.11 the analysis of trends seems reasonable. Two linear functions are used for this purpose. The first is used for the range from 0 to 0.1 (blue line) and the second for the range from 0.1 to 0.9 (red line). The latter is particularly important since the above mentioned bias is reduced. It can be seen that the relationship between AUC and the cluster-to-patch size ratio significantly reduces towards lower smoothness levels. High smoothness levels for informed LORETA provide the best reconstruction quality for clusters in the range of the patch size. Interestingly, the performance for the levels 0.8 and 0.6 is very similar to level 0.99 at high ratios while it is much better at medium and lower ratios. Lowering the smoothness constraint even further (levels 0.4 and 0.2) mainly reduces the performance (i.e. variance increased) at higher ratios. For level 0.01, however, AUC values drop significantly. This leads to results that are comparable to the results of eFACE, fFACE and WMN. Except for small ratios there is only a weak relationship between AUCs and the size of a cluster inside a patch. It can be summarized that only the results for informed LORETA at smoothness level 0.2 and higher exhibit a dependence of the reconstruction quality on the ratio between cluster and patch size. Note that similar conclusions can be drawn for the COR metric which is shown in Fig. B.1 in appendix B.2.

4.4.4 Discussion

The simulations aimed at studying the spatial characteristics of source distributions derived from different informed linear reconstruction methods. The simulations were conducted under reasonably controlled conditions to isolate the influence of prior knowledge. That means, (1) the source space and forward model were kept constant, (2) prior information was derived from artificial parcellations, (3) the prior assumptions were consistent to the generated source patterns, (4) observations from both homogeneous and inhomogeneous parcellations were combined to prevent an overestimation of potential errors in individual parcellations, and (5) simulations were carried out under noise-free conditions.

The first simulation revealed that informed LORETA only produced a noticeable but still relatively small bias towards small patches at high smoothness levels (i.e. larger than 0.8). The bias is much weaker for lower smoothness levels and nonexistent for the two FACE methods. Therefore, it is no reason to expect any serious negative side-effects resulting from patch size differences when using realistic parcellations (as, for example, the two shown in Fig. 4.1). Of course, this also applies when only a subset of patches from such a parcellation is used. This would be the case for a local parcellation. However, in this case the size of the non-parcelled region(s) can be much larger than the patches in the subset. As a consequence, no bias between the patches in the parcelled area but a bias towards the whole parcelled region can reasonably be expected. The use of local parcellation is subject of Sec. 4.5.

The results for informed LORETA with the lowest smoothness level, for the two FACE methods, and for WMN exhibit a clear tendency to a more frequent activation of sources in large patches. The discussion revealed that this is not a bias induced by prior knowledge but directly results from the intrinsic minimum norm effect (i.e. sources with a strong leadfield norm are preferred). Since it is more likely that a large patch covers a superficial region, it is also more likely that activity is reconstructed in larger patches. Note that this is not a general finding but rather depends on the particular properties of the parcellation. The inhomogeneous parcellations employed here consist of patches whose sizes belong to discrete patch size levels. The conclusion from above can be drawn since the number of patches in each level is equal. The two FACE methods are most vulnerable to this effect since, in contrast to all other methods, their implementation according to Sec. 2.5.5 does not include leadfield normalization. This is particularly problematic for the simulation setup employed here since activity can be located on the whole cortex. The effect is less relevant in a scenario in which activity is mainly located in superficial regions. For example, this is the case for the analysis of brain responses in visual areas as done by Cottereau et al. (2012).

The aim of the second simulation was to evaluate the coupling between the spatial extent of the reconstructed source distribution and the imposed smoothness constraint. The simulations based on homogeneous parcellations revealed a considerable tendency to wide-spread solutions for high smoothness levels. It is important to note, however, that a strong smoothness constraint enables both focal and wide-spread solutions, whereas a weak constraint, for instance imposed by FACE, always leads to focal activity patterns. From this perspective, the latter are rather unsuited for the analysis of spatially wide-spread correlated data. Another finding was that strong variations concerning the spatial extent of reconstructed activity inside patches can be explained with the patch size. This is particularly the case at high smoothness levels. At a first glance, this implies that the patch size has a strong impact on the particular spatial extent of the reconstructed activity. However, further analysis using homogeneous parcellations (each with differently sized patches) revealed that the spatial extent of a reconstruction is rather independent of the patch size. This is an important result since it underpins that solutions are not dominated by the imposed smoothness constraint.

Based on these findings, the third analysis in this section aimed at evaluating the influence of the ratio between the size of an active cluster and the patch size on the source localization results. It turned out that algorithms with a weak smoothness constraint provide results that are very much independent of this ratio. In contrast, the reconstruction quality of algorithms with a considerably strong smoothness constraint is related to this ratio. Nonetheless, good reconstruction results were observed for both low and high ratios between cluster and patch size. That means that the algorithms were able to reconstruct both focal and wide-spread activity inside patches. Again, this underpins that the incorporation of patches does not impose a particular constraint of the shape of the activity, even not in case of a very strong smoothness constraint (in which the full activation of patches is certainly preferred). Note that the dependence of the reconstruction quality on this ratio also explains a considerable part of the variance of the observed spatial extent of reconstructed distributions (Fig. 4.10). The main conclusion is that high smoothness levels are particularly suited for the reconstruction of large ratios and moderate levels for moderate ratios. However, a more precise relationship between quality and the cluster-to-patch size ratio, for instance a certain maximum quality for each smoothness level, could not be identified.

In summary, the simulations carried out in this section provide inside into the effect of constraining linear inversion frameworks with different combinations of a smoothness assumption with prior knowledge drawn from parcellations. It turned out that, first, none of the methods induces a strong bias towards particular brain regions, and, second, no method strictly overestimates the smoothness constraint. From this perspective, any of these methods (i.e. any smoothness level for informed LORETA) could generally be employed for the reconstruction of brain activity. The benefit of utilizing prior knowledge on the functio-anatomical organization for smoothness based linear inversion frameworks is evaluated in the following section.

4.5 Evaluation of Parcellation-based Functio-Anatomical Constraints

4.5.1 Objective

This section deals with the evaluation of different prior assumptions regarding the shape and the structure of brain activity for linear source reconstruction approaches. These prior assumptions are derived from a combination of prior knowledge given by parcellations with a belief on the general smoothness of the solution. Therefore, various simulation scenarios are set up using both full and local parcellations. The evaluation is based on MC simulations. Firstly, it is particularly interesting whether one can expect an improved performance for informed reconstruction methods in comparison to uninformed methods given that prior information is correct. Therefore, several parameters are systematically varied to control the complexity of the simulated source patterns. These parameters are location and size of active clusters, the noise level, and the number of concurrently active clusters. Secondly, the simulations focus on misspecified prior knowledge. For example, this comprises simulations in which the course of functional boundaries is assumed to be inaccurate. But some simulations also imply the assumption that the course of boundaries is in principle accurate but that no activity in their vicinity contributes to the data. As a result, the data lacks any information on these boundaries. This use case (i.e assuming borders between regions which are not contributing to data) can be understood as misplacing boundaries. A typical scenario where this issue matters is the analysis of evoked responses using boundaries between regions in which spontaneous activity cancels out due to averaging.

4.5.2 Simulation Setup

The MC simulations are based on the realistic forward model (see Sec. 4.2.2 for details). Two artificial parcellations (HP8 and HP18, see Sec. 4.2.3) were used as prior knowledge. Additionally, a total of 10 local parcellation (subsequently denoted with the prefix LP) were derived given these full parcellations. This was done as follows. The first two parcellations were generated based on HP8 by selecting a compact set of adjacent patches from the left (LP1a) and the right hemisphere (LP1b). Another two were derived by extending LP1a (which results in LP1c) and LP1b (resulting in LP1d) with surrounding patches. Finally, the combination of LP1a with LP1b provided the 5th local parcellation, i.e. LP1e. Similarly, HP18 was used to derive another five local parcellations, i.e. LP2a-e.

The general procedure to generate compact activity clusters (see 4.2.4) was as follows: (1) 1-3 seed points were selected from the set of patches from the employed parcellation (only one seed per patch). Sources close to or even inside the interhemispheric fissure were not activated. (2) A cluster size between $48\,\mathrm{mm}^2/96\,\mathrm{mm}^2$ (HP8, LP1a-e / HP18, LP2a-e) and 1.1 times the size of the patch where the seed is located was randomly selected. (3) Active clusters were generated and a unique source strength was randomly assigned to each cluster. Possible values were 2, 4, 6, and 8. Depending on the simulation scenario (see below), patch boundaries were used to confine the the spatial extent of each cluster. (4) The forward solution was computed for SNR levels 1, 4, 9, 20, 50, 100, and 10^9. This procedure was used to generate a total of 5000 trials for each full parcellation and 1000 trials for each local parcellation in each of the following three simulation scenarios.

In the first scenario, the simulated activity is consistent with prior knowledge. An active cluster cannot overlap patch boundaries. Generation and reconstruction of brain activity is carried out with the same parcellation. The second scenario deals with the misspecifications of the course of boundaries. That means that functional boundaries which do not accurately follow the real borders between distinct functional regions are used. Activity is generated similarly as before, except that activity is allowed to spread over borders. The third scenario considers the misplacement of boundaries. Now, the generation and reconstruction of activity is performed with different parcellations. Two cases are distinguished. The first one is based on activity that is generated using the small ROI (i.e. LP1a, LP1b, LP2a, LP2b) and reconstructed using the corresponding extended version (i.e. LP1c, LP1d, LP2c, LP2d). The second one is based on generating activation using the extended ROI and reconstructing using the small ROI. Importantly, activity is not allowed to overlap patch boundaries.

Source reconstruction was performed using focal and extended FACE, informed and uninformed LORETA (see appendix B.1 for Laplacian regularization parameters), and WMN. Details are given in Sec. 4.2.5. Finally, the size of the activated area and the metrics AUC, RE and DE were computed for each reconstruction result.

4.5.3 Results

The simulation results are presented by means of rather similar figures. Hereafter, some general details on their appearance are summarized. The different observations are illustrated using boxplots. The white bar in each colored box denotes the median. Lower and upper bounds of the box denote the 25th and 75th percentile, and the gray whiskers indicate extreme points. The latter are cropped in parts of the figures in favour of a better visualization of all distributions. The results of statistical comparisons (i.e. Kolmogorov-Smirnov tests) with the reference method (i.e. WMN) are given in the text in a condensed manner and only for the relevant distributions.

The results presented in this section are grouped according to the previously outlined scenarios. That means, Sec. 4.5.3.1 presents the results based on prior consistent activation (i.e. scenario 1), Sec. 4.5.3.2 shows the results for misaligned boundaries (i.e. scenario 2), and Sec. 4.5.3.3 shows the reconstruction performance for misplaced functio-anatomical boundaries (i.e. scenario 3).

4.5.3.1 Scenario 1: Prior Consistent Activation

The first analysis aims at evaluating the performance of informed linear inverse methods with respect to the noise level given a prior consistent activation of source activity that can appear anywhere on the cortical sheet. The results obtained for the two incorporated full parcellations (i.e. HP8 and HP18) are combined for the analysis. Figure 4.13 shows the results for simulations with one active cluster. AUC and RE distributions indicate that all methods perform better at higher SNR levels. According to DE, however, the performance of informed LORETA with smoothness level 0.01, of the two FACE methods, and of WMN slightly decreases. Informed LORETA with smoothness level 0.4 and above outperforms WMN for AUC ($P < 1 \times 10^{-8}$) and RE ($P < 1 \times 10^{-8}$), and is slightly inferior according to DE ($P < 1 \times 10^{-8}$). Compared to WMN, the two FACE methods produce higher AUC values ($P<1 \times 10^{-8}$), RE distributions with similar median but a larger variance ($P < 1 \times 10^{-8}$), and significantly higher DE values ($P < 1 \times 10^{-8}$). The results for uninformed LORETA reflect the strong contradiction between the prior assumption (i.e. a large spatial extent of source activity) and the simulated source patterns, whose spatial extent is limited by the patch boundaries. For that reason, uninformed LORETA with smoothness level 0.2 and above is inferior to WMN. In contrast, uninformed LORETA with level 0.01 outperforms WMN regarding AUC ($P < 1 \times 10^{-8}$) and RE ($P < 1 \times 10^{-8}$) throughout all SNR levels. This emphasizes the need for a careful adjustment of the Laplacian regularization parameter. Figure B.2 and B.3 in appendix B.3.1 display the performance for two and three concurrently active clusters, respectively. These results are consistent to the findings presented here and, therefore, they are not analyzed in more detail.

The second analysis focuses on the reconstruction quality according to the number of active clusters. The results for all informed methods, WMN, and uninformed LORETA with smoothness level 0.01 shown in Fig. 4.14 can be summarized as follows. An increased number of active clusters leads to a slight performance reduction according to AUC and DE measures, but to slightly improved RE measures. Obviously, the ability of these methods to reconstruct shape and location of the activity reduces the more clusters are concurrently active, that means the more complex the patterns are. Informed LORETA (particularly with smoothness level 0.2

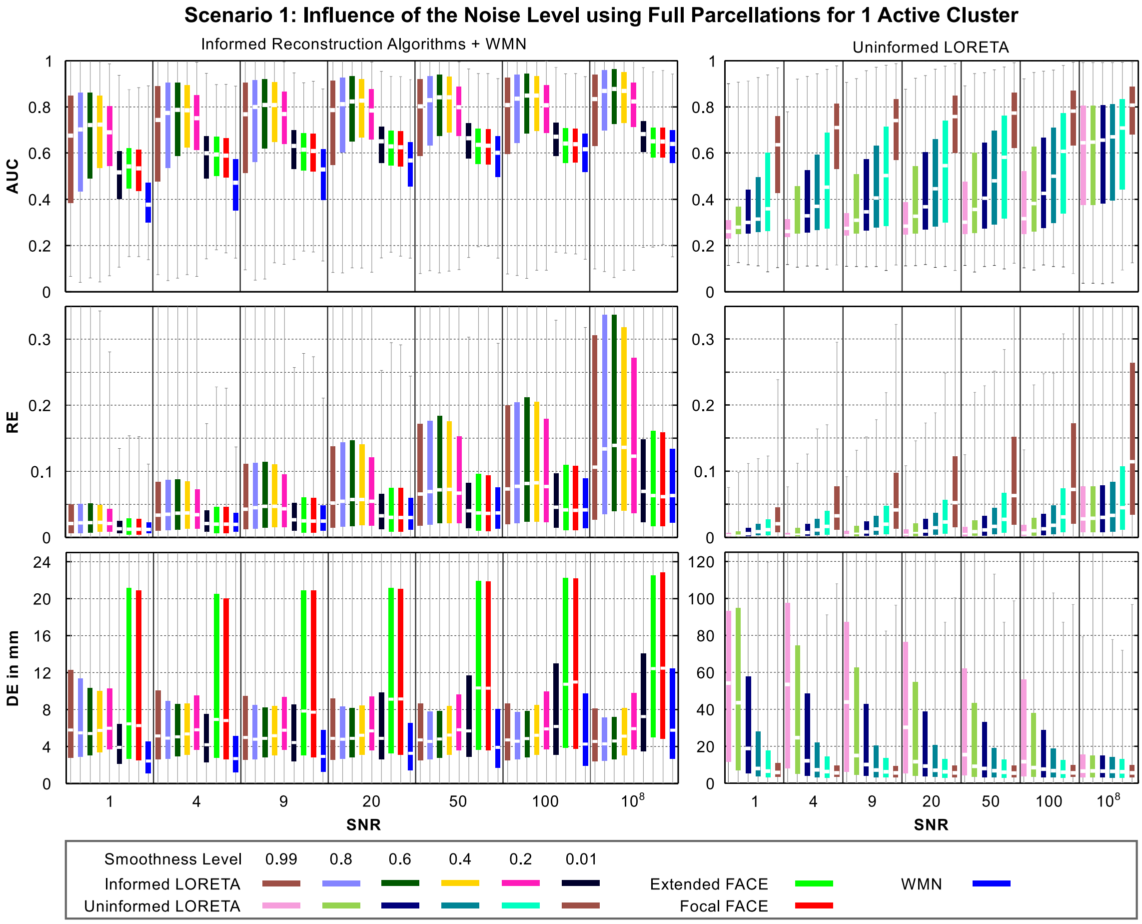

Figure 4.13: Performance of informed and uninformed linear reconstruction methods with respect to the noise level. Prior information was derived from full parcellations. Single clusters were activated, the activation was consistent with the boundaries. See page 82 for details on the box plots.

and above) clearly outperforms WMN according to AUC ($P < 1 \times 10^{-8}$) and RE ($P < 1 \times 10^{-6}$). Its results according to DE are similar even though the distributions are statistically different ($P < 1 \times 10^{-4}$). The FACE results are statistically different from the WMN results according to each of the three performance measures (i.e. AUC: $P < 1 \times 10^{-5}$, RE: $P < 1 \times 10^{-8}$, DE: $P < 1 \times 10^{-8}$). It is obvious, however, that FACE results are not better compared to WMN, especially not for complex source patterns with multiple clusters. Uninformed LORETA performs significantly worse than WMN (i.e. AUC: $P < 1 \times 10^{-5}$, RE: $P < 1 \times 10^{-8}$, DE: $P < 1 \times 10^{-8}$), except for smoothness level 0.01. In contrast to all other methods, the AUC obtained for uninformed LORETA improves the more clusters are active. This can be explained with the strong smoothness constraint which is imposed by most of the uninformed LORETA methods used here. A strong smoothness favours solutions with a large spatial extent (i.e. independently of the underlying activity). As a consequence, a higher number of truly active sources increases the true positive rate (cmp. Sec 4.2.6) and, therefore, improves the AUC measure. Uninformed LORETA with smoothness level 0.01 clearly outperforms WMN for ($P < 1 \times 10^{-8}$) and RE ($P < 1 \times 10^{-8}$). The method obviously imposes a much more meaningful smoothness assumption. According to DE, WMN performs slightly better ($P < 1 \times 10^{-7}$).

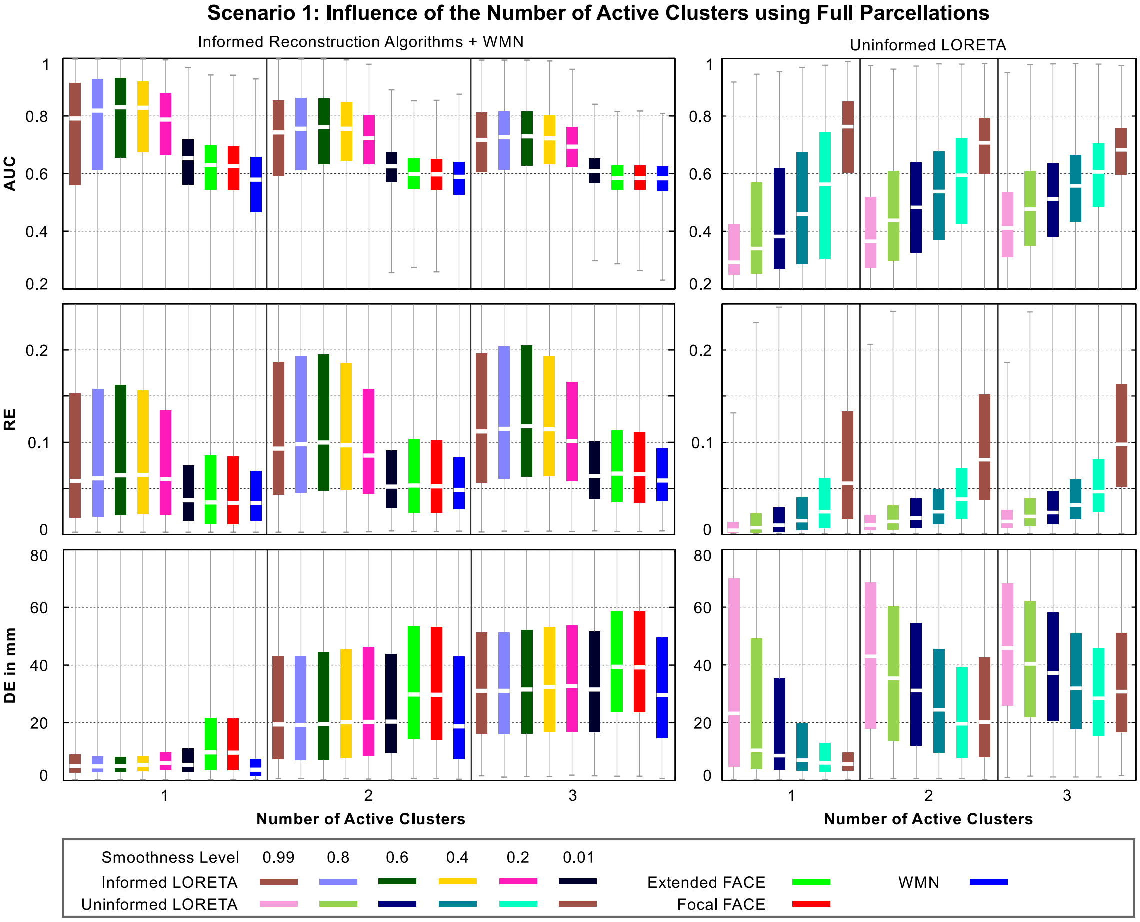

Figure 4.14: Performance of informed and uninformed linear reconstruction methods according to the number of concurrently active clusters. Prior information was derived from full parcellations, up to 3 clusters were activated. The activation was consistent with the boundaries. Results are integrated over SNR levels 9, 20, 50, and 100. See page 82 for details on the box plots.

The last analysis using full parcellations and a prior consistent activation evaluates the influence of differences between the strengths of multiple active clusters on the reconstruction quality. The analysis is based on the ratio between the weakest and strongest cluster in each source pattern. This ratio defines as $\|\hat{q}_i \cdot l_i^c\|_2 \big/ \|\hat{q}_j \cdot l_j^c\|_2$ with $\|\hat{q}_i \cdot l_i^c\|_2 \le \|\hat{q}_k \cdot l_k^c\|_2 \le \|\hat{q}_j \cdot l_j^c\|_2$, $k \in [1, N_A]$. N_A corresponds to the number of concurrently active clusters, $l_k^c \in \mathbb{R}^n$ is the sum of leadfield vectors in cluster k, and $\hat{q}_k \in \mathbb{R}$ is the unique source amplitude in cluster k. Figure 4.15 displays the reconstruction quality according to this ratio.

None of the algorithms exhibits a significant dependence on the difference between cluster strengths according to AUC and RE. As before, informed LORETA methods with smoothness level 0.2 and above outperform WMN according to AUC ($P < 1 \times 10^{-8}$) and RE ($P < 1 \times 10^{-8}$). Informed LORETA with level 0.01 ($P < 1 \times 10^{-8}$), eFACE ($P < 1 \times 10^{-3}$), fFACE ($P < 1 \times 10^{-2}$), and uninformed LORETA 0.01 ($P < 1 \times 10^{-8}$) only outperform WMN according to the AUC. In contrast to AUC and RE, DE provides a recognizable trend in this figure. The lowest DE values can be observed when the cluster strengths are balanced. This means that the occurrence of similarly strong clusters reduces the localization error. The two FACE methods and unin-

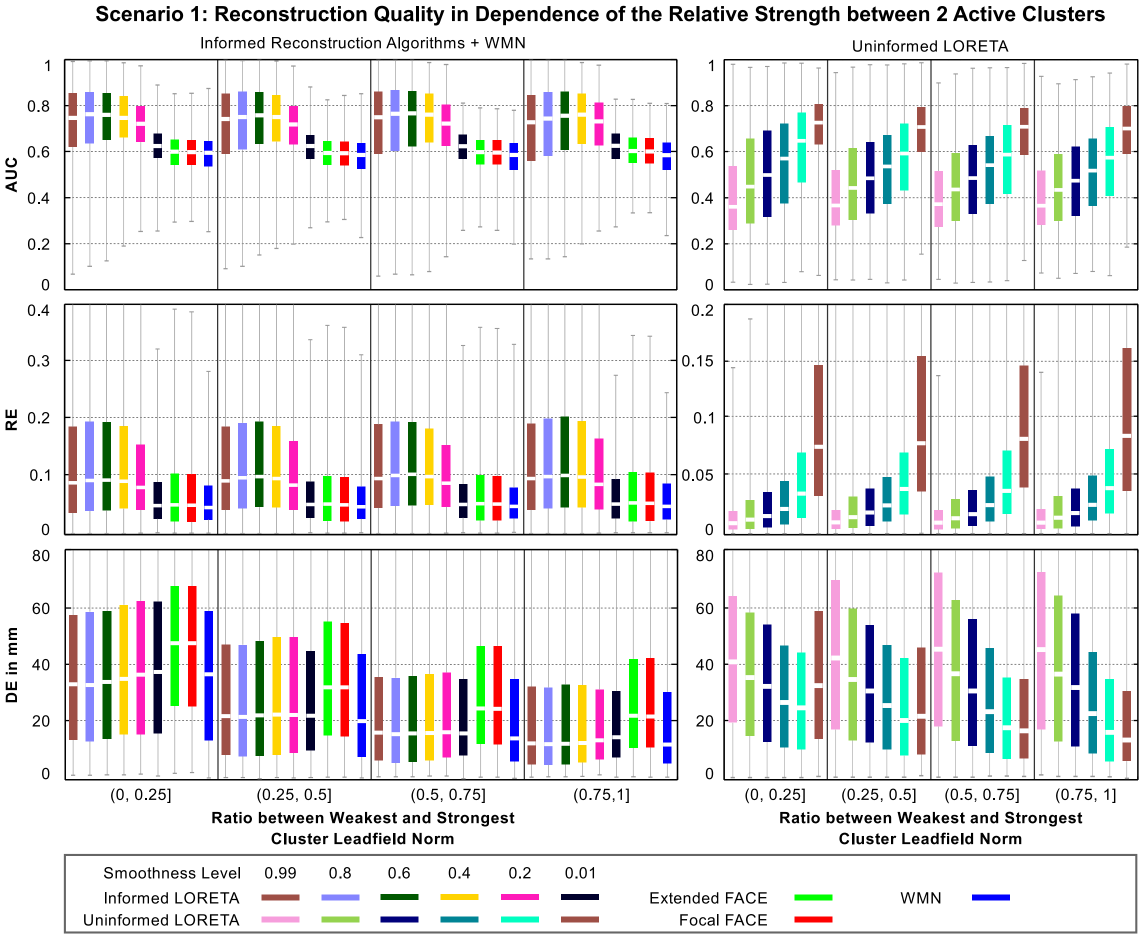

Figure 4.15: Performance of localization methods with respect to the ratio between weakest and strongest cluster for two active clusters. The measures are grouped according to four ratio intervals. Prior information was derived from full parcellations, two clusters were activated. The activation was consistent with the boundaries. The results are integrated over SNR levels 9, 20, 50, and 100. See page 82 for details on the box plots. Details on the cluster strength ratio are given in the text.

formed LORETA with smoothness level 0.2 and above lead to significantly higher localization errors compared to WMN ($P < 4 \times 10^{-2}$). The results of all other methods are similar to the WMN results. The large errors for FACE are likely to occur due to the missing leadfield normalization. The errors for uninformed LORETA can be explained with the strong smoothness constraint (see explanation above). Figure B.4 in appendix B.3.1 displays the analysis results for three concurrently active clusters. The conclusion that can be drawn from these results are very similar. General conclusions that can be drawn with respect to the use of full parcellations are discussed in Sec. 4.5.4.

The analysis now focuses on local parcellations. That means that activity is expected to be localized to a certain region for which the functio-anatomical structure is known. The analysis results obtained for all local parcellations consisting of a single ROI are combined (i.e. LP1e and LP2e are not used here). Figure 4.16 shows the influence of noise for simulations with one active cluster. Interestingly, the performance of uninformed LORETA and WMN according to the AUC improves towards higher SNR levels. In contrast, the FACE results are dis-

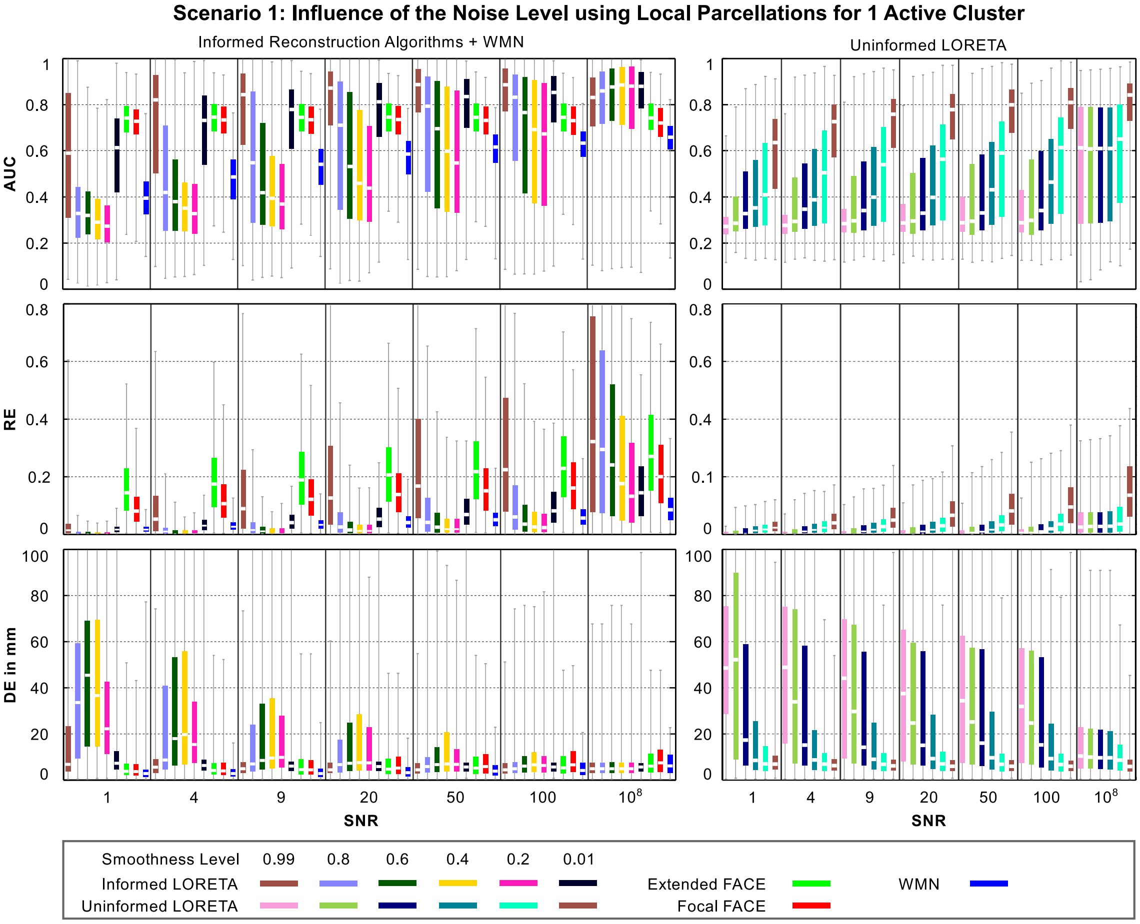

Figure 4.16: Performance of informed linear reconstruction methods with respect to the noise level. Prior information was derived from local parcellations with a single ROI. Single clusters were activated. The activation was consistent with the boundaries. See page 82 for details on the box plots.

tributed around a more or less constant median of 0.74 (eFACE) and 0.72 (fFACE). WMN is consistently outperformed by informed LORETA with smoothness levels 0.99 ($P < 1 \times 10^{-8}$) and 0.01 ($P < 1 \times 10^{-8}$), eFACE ($P < 1 \times 10^{-8}$), fFACE ($P < 1 \times 10^{-8}$), and uninformed LORTEA with level 0.01 ($P < 1 \times 10^{-8}$). It should be pointed out that both FACE methods are not only inferior to the two above mentioned informed LORETA derivatives given an SNR of at least 9, but also to uninformed LORETA with smoothness level 0.01. In contrast to the AUC measure, the RE metric improves for all methods towards high SNR levels. Again, only informed LORETA with level 0.99 ($P < 1 \times 10^{-8}$) and level 0.01 ($P < 1 \times 10^{-2}$), eFACE and fFACE ($P < 1 \times 10^{-8}$), and uninformed LORETA with smoothness level 0.01 ($P < 1 \times 10^{-8}$) consistently outperform WMN. The median obtained for eFACE and fFACE for the lowest SNR ratio is 0.14 and 0.08. This is remarkably high compared to all other methods. For example, informed LORETA with smoothness level 0.99 requires an SNR of at least 9 to provide a similar median. For high SNR levels, however, informed LORETA 0.99 provides very high SNR values and performs even better than FACE. According to DE, the performance of FACE and WMN slightly drops towards higher SNR levels, whereas it increases for all other methods. All distributions are statistically different from WMN (informed LORETA 0.01 and 0.99: $P < 1 \times 10^{-8}$, eFACE: $P < 1 \times 10^{-2}$, fFACE: $P < 1 \times 10^{-6}$, uninformed

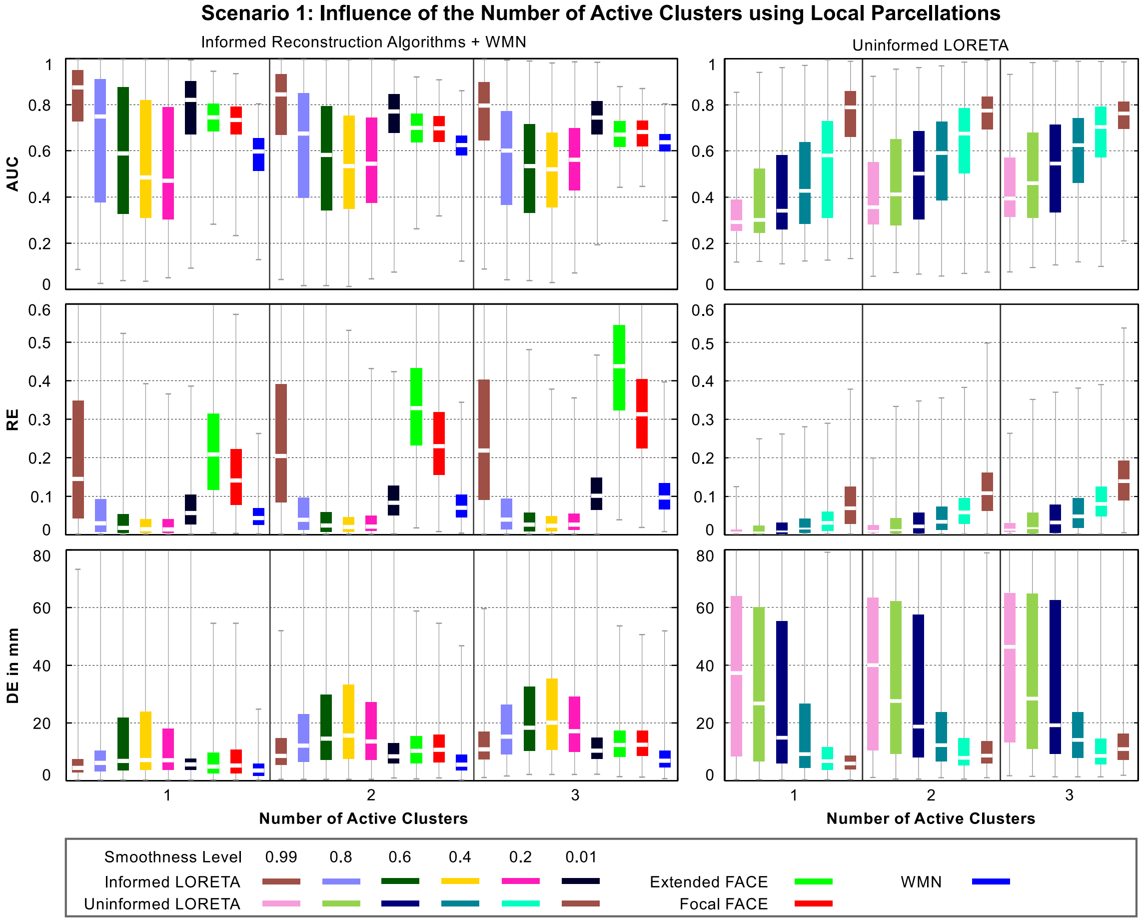

Figure 4.17: Performance of informed and uninformed linear reconstruction methods with respect to the number of concurrently active clusters. Prior information was derived from local parcellations with a single ROI, up to 3 clusters were activated. The activation was consistent with the boundaries. Results are integrated over SNR levels 9, 20, 50, and 100. See page 82 for details on the box plots.

LORETA: $P < 1 \times 10^{-8}$). More importantly, informed LORETA 0.99 leads to smaller localization errors in comparison to both FACE methods ($\mathrm{SNR} \geq 9$). For the sake of completeness, Fig. B.5 and B.6 in appendix B.3.1 display the performance for two and three concurrently active clusters. The main conclusion that can be drawn from the presented results is as follows. Given an SNR of at least 4, informed LORETA with smoothness level 0.99 provides the best compromise between (1) the reconstruction of the original shape of the activity (AUC), (2) the concentration of most of the reconstructed energy close to the truly active region, and (3) a smallest possible localization error. For lower SNR levels, FACE provides the best reconstruction results.

Figure 4.17 shows the reconstruction performance with respect to the number of concurrently active clusters. The results for informed LORETA with smoothness levels 0.99 and 0.01, the FACE methods, uninformed LORETA with level 0.01, and WMN, can be summarized as follows. The reconstruction quality consistently reduces according to AUC and DE but increases according to RE. Informed LORETA with level 0.99 provides the best AUC results ($P < 1 \times 10^{-8}$), followed by informed ($P < 1 \times 10^{-8}$) and uninformed LORETA ($P < 1 \times 10^{-8}$) with smoothness level 0.01, the two FACE methods ($P < 1 \times 10^{-8}$), and WMN. According to RE, the best results are achieved using eFACE ($P < 1 \times 10^{-8}$) followed by fFACE ($P < 1 \times 10^{-8}$), informed LORETA 0.99 ($P < 1 \times 10^{-8}$), uninformed ($P < 1 \times 10^{-8}$) and informed LORETA with level 0.01 ($P < 1 \times 10^{-8}$), and WMN. The DE observations of these algorithms are roughly in the same range. The lowest localization error is given by WMN ($P < 1 \times 10^{-8}$ for each method). As before, informed LORETA with smoothness level 0.99 provides a reasonable compromise between all performance measures when multiple clusters in a localized functional area have to be reconstructed. The method leads to the best results in terms of reconstructing the original shape of the activity (i.e. according to the AUC). Extended FACE might be the method of choice if one is interested in solutions for which most of the energy is reconstructed in originally active regions. However, this is mainly relevant when multiple clusters are active. The differences according to RE are much smaller for only one active cluster.

The last analysis with a prior consistent activation is carried out using local parcellations with two distinct ROIs. This mimics the reconstruction of brain activity that is generated in a functional network, which consists of areas in distinct brain regions. The simulation results obtained for the parcellations LP1e and LP2e are combined for the analysis. Figure 4.18 shows the reconstruction performance according to the noise level for one active cluster. That means that activity is located either in the one or in the other ROI. Figure B.8 and B.9 in appendix B.3.1 show results for simulations in which up to three clusters are concurrently active in both regions. Finally, Fig. B.7 in appendix displays the reconstruction quality according to the number of concurrently active clusters. It turned out that there is no principal difference between the reconstruction results for local parcellations with either one or multiple ROIs. Of course, this conclusion might be different if the underlying functio-anatomical structure is unknown or if at least uncertainties must be expected. This is subject of the following sections.

Finally, it is worth to note that informed LORETA with smoothness level 0.2 to 0.8 and uninformed LORETA with level 0.2 to 0.99 provide a very weak reconstruction performance. Uninformed LORETA imposes a smoothness constraint that is not consistent with the simulated patterns. The weak performance for the informed LORETA methods can be explained with the huge differences between the patch sizes inside the ROI and the rather large areas outside the ROI. The combination of this cortical organization structure with a moderate smoothness level leads to a complex correlation structure (cmp. chapter 3). The actual effect on source estimation is difficult to predict. For example, a level of 0.2 for informed LORETA corresponds to a high correlation between all sources inside each patch within the ROI, while the sources located outside the ROI (i.e. the areas which are not part of the local parcellation) are not correlated at all to each other (cmp. Sec. 3.4.3). The effect reduces the reconstruction bias towards parceled regions (which, however, is necessary to reconstruct activity in certain regions). Due to this, the reconstruction performance for the majority of simulations is weak.

4.5.3.2 Scenario 2: Misaligned Boundaries

The analysis in this section is focused on the evaluation on how discrepancies between the real and the *a priori* assumed course of functio-anatomical boundaries affect the reconstruction performance. According to the simulation design presented in Sec. 4.5.2, the generated activity may overlap patch boundaries. This implies, however, that not each of the simulated patterns contains activity that deviates from the prior information. This is a realistic scenario.

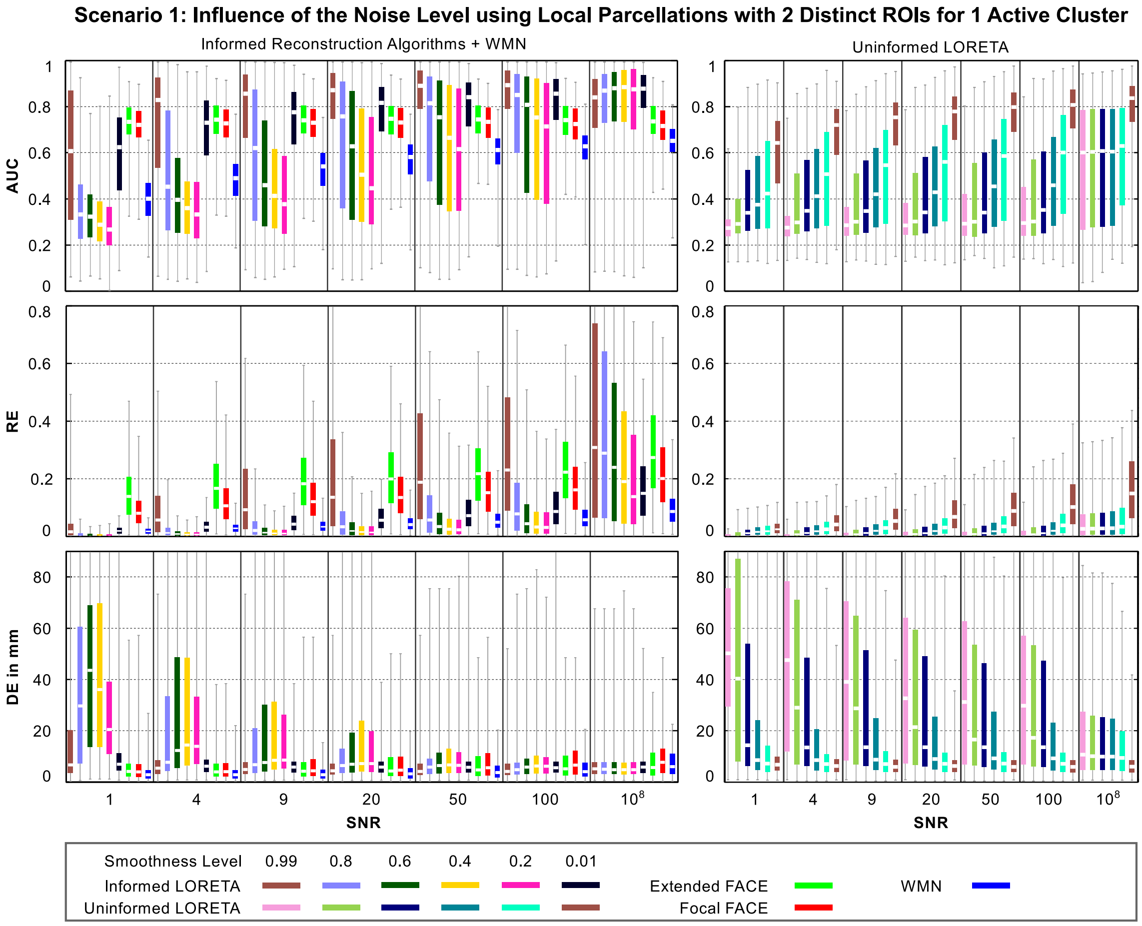

Figure 4.18: Performance of informed linear reconstruction methods with respect to the noise level. Prior information was derived from local parcellations with two distinct ROIs, single clusters were activated. The activation was consistent with the boundaries. See page 82 for details on the box plots.

In practice, it is reasonable to expect that the prior knowledge only has minor uncertainties rather than that the prior is completely wrong. Otherwise, using this kind of prior knowledge would not make much sense. These uncertainties are not relevant for uninformed LORETA. Therefore, the analysis is restricted to informed linear reconstruction methods and to WMN as reference. As above the simulation results obtained for HP8 and HP18 are combined.

Figure 4.19 shows the reconstruction performance with respect to the noise level. The AUC and DE distributions obtained for the informed methods are all statistically different from WMN (AUC: $P < 1 \times 10^{-8}$, DE: $P < 1 \times 10^{-8}$). According to RE, informed LORETA with smoothness level 0.99 performs very similar to WMN at each SNR level and is not statistically independent ($P \geq 0.17$). All others are statistically different from the reference method (i.e. $P < 1 \times 10^{-4}$). The performance with respect to the number of concurrently active clusters is displayed in Fig. 4.20. Here, all distributions are statistically independent of the results for the uninformed reference method (AUC: $P < 1 \times 10^{-7}$, RE: $P < 1 \times 10^{-2}$, DE: $P < 1 \times 10^{-4}$). The main conclusions that can be drawn from these results are as follows. In principle, the reconstruction results obtained for informed LORETA methods are of lower quality compared to the prior consistent activation, which was presented in the previous section. The strength of

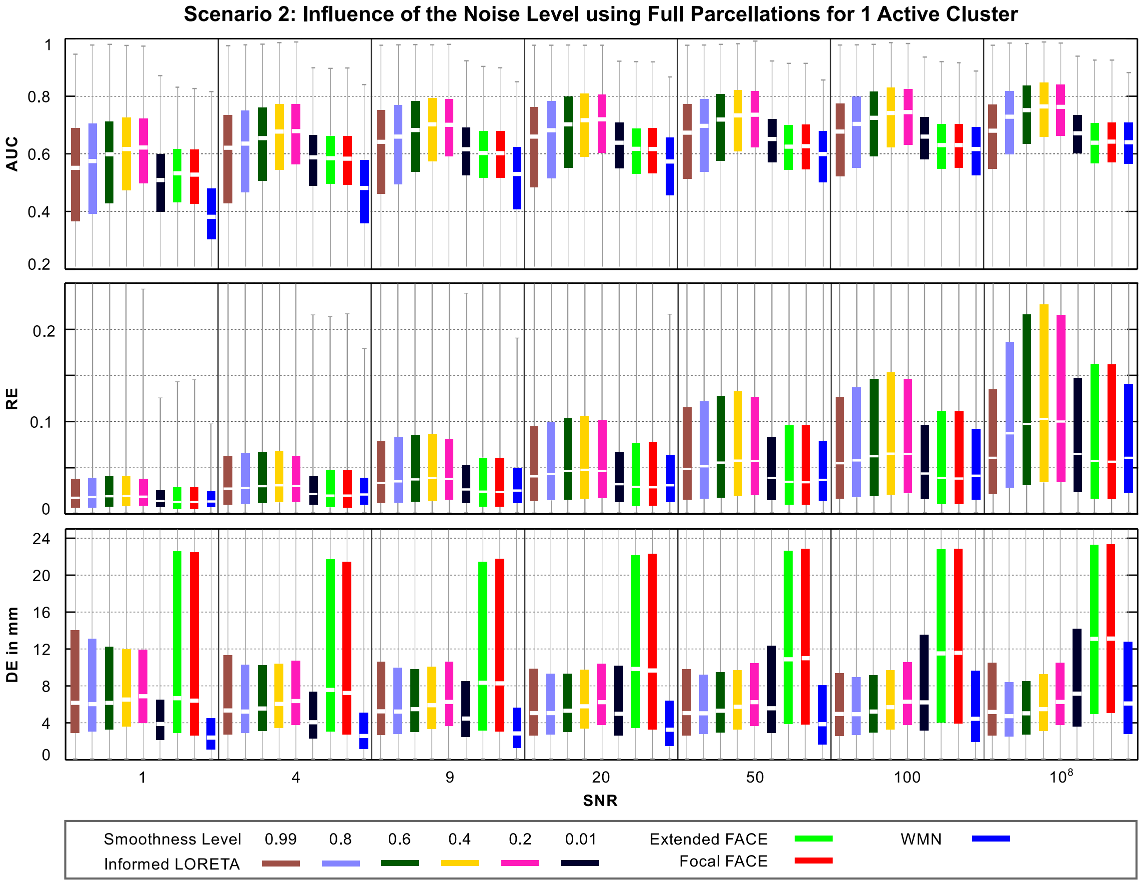

Figure 4.19: Performance of informed linear reconstruction methods with respect to the noise level. Prior information was derived from full parcellations, single clusters were activated without considering boundaries. See page 82 for details on the box plots.

the performance reduction depends on the noise level. It is highest at the lowest SNR level. In contrast, the performance of the two FACE methods is only hardly reduced in the present scenario. The reason for these two rather different findings is the difference between there smoothness constraints. The stronger the constraint is, the more likely do these boundaries influence the reconstructed source pattern (because a stronger smoothness constraint leads to a larger spatial extent of activity). Hence, the FACE methods are much less affected by misaligned functio-anatomical boundaries (i.e. uncertainties in prior knowledge) since they are based on a very weak smoothness constraint. The constraint is even weaker than for informed LORETA with smoothness level 0.01. Nonetheless, all informed methods (including FACE) perform better than WMN even though the prior knowledge is partly incorrect. This is for two reasons. First, as already mentioned above, not each simulated source pattern deviates from prior knowledge. Second, each informed method embodies a smoothness constraint which is, in principle, much more consistent to the employed simulation patterns (that means activity is explained by means of compact clusters) than the assumption of uncorrelated sources. Further results are discussed below.

Simulations using misaligned boundaries were also carried out for local parcellations. Therefore, the analysis results for all parcellations consisting of a single ROI are combined (i.e. LP1e

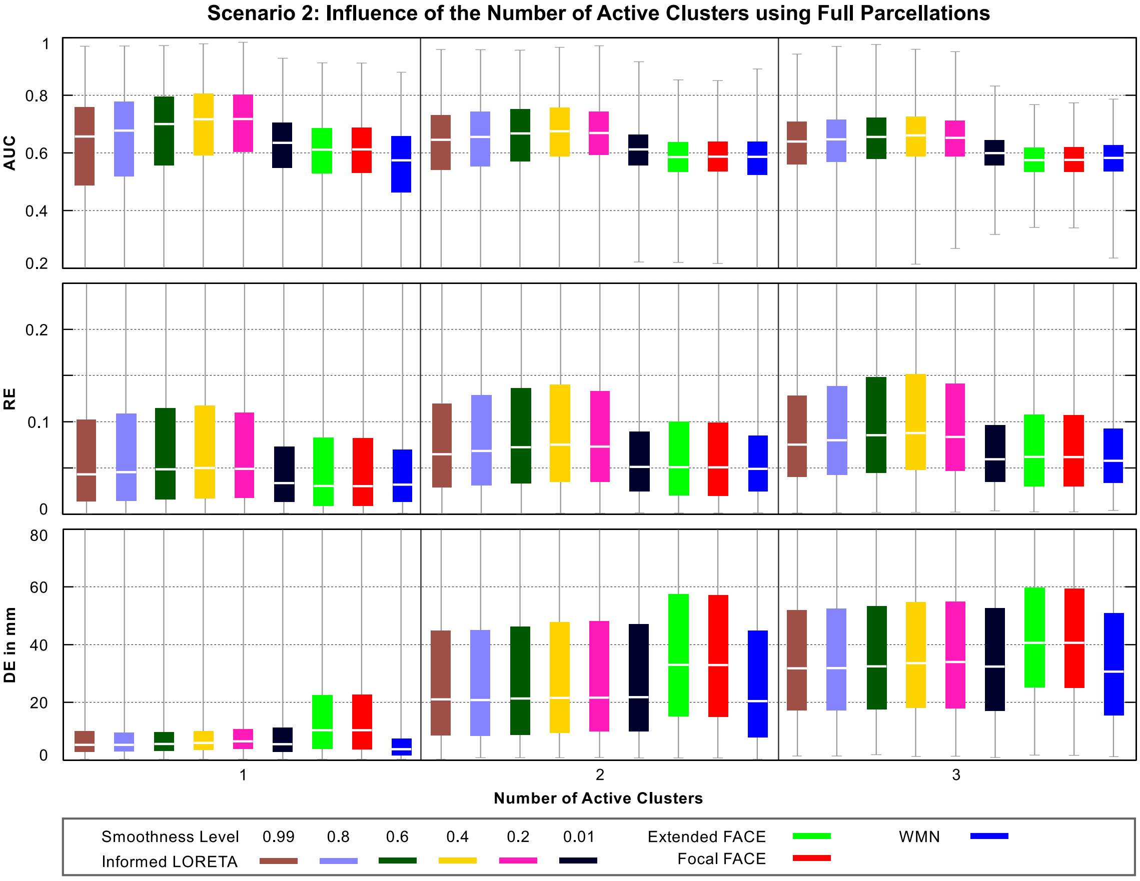

Figure 4.20: Performance of informed linear reconstruction methods with respect to the number of concurrently active clusters. Prior information was derived from full parcellations, up to 3 clusters were activated without considering the boundaries. Results are integrated over SNR levels 9, 20, 50, and 100. See page 82 for details on the box plots.

and LP2e are not used here). The performance results according to the noise level are displayed in Fig. 4.21. The distributions of the informed linear inverse methods are all statistically independent of the WMN distributions (AUC: $P < 1 \times 10^{-3}$, RE: $P < 4 \times 10^{-2}$, DE: $P < 1 \times 10^{-3}$). The simulation results according to the number of clusters are shown in Fig. 4.22. As before, the distributions for the informed methods are statistically independent of WMN (AUC: $P < 1 \times 10^{-8}$, RE: $P < 1 \times 10^{-5}$, DE: $P < 1 \times 10^{-8}$). The only exception is the AUC distribution for the fFACE method for three concurrently active clusters. This distribution is statistically similar to the WMN distribution ($P = 5.1 \times 10^{-2}$). The results can be summarized as follows.

In contrast to the results for full parcellations presented above, each informed method (i.e. also FACE) exhibits a clearly reduced reconstruction quality according to all performance measures in comparison to prior consistent simulations. Obviously, the two FACE methods and informed LORETA with smoothness level 0.01 are least affected by the introduced uncertainties (i.e. the have the smallest performance reduction). Of course, this is due to their weak smoothness constraints, for which uncertainties in prior knowledge are only of minor importance. The methods perform significantly better than WMN. Informed LORETA with smoothness level 0.99 performs better than WMN at most SNR levels as well. As above, it generally implies a more consistent assumption on the shape of the active clusters, even though uncertainties in prior

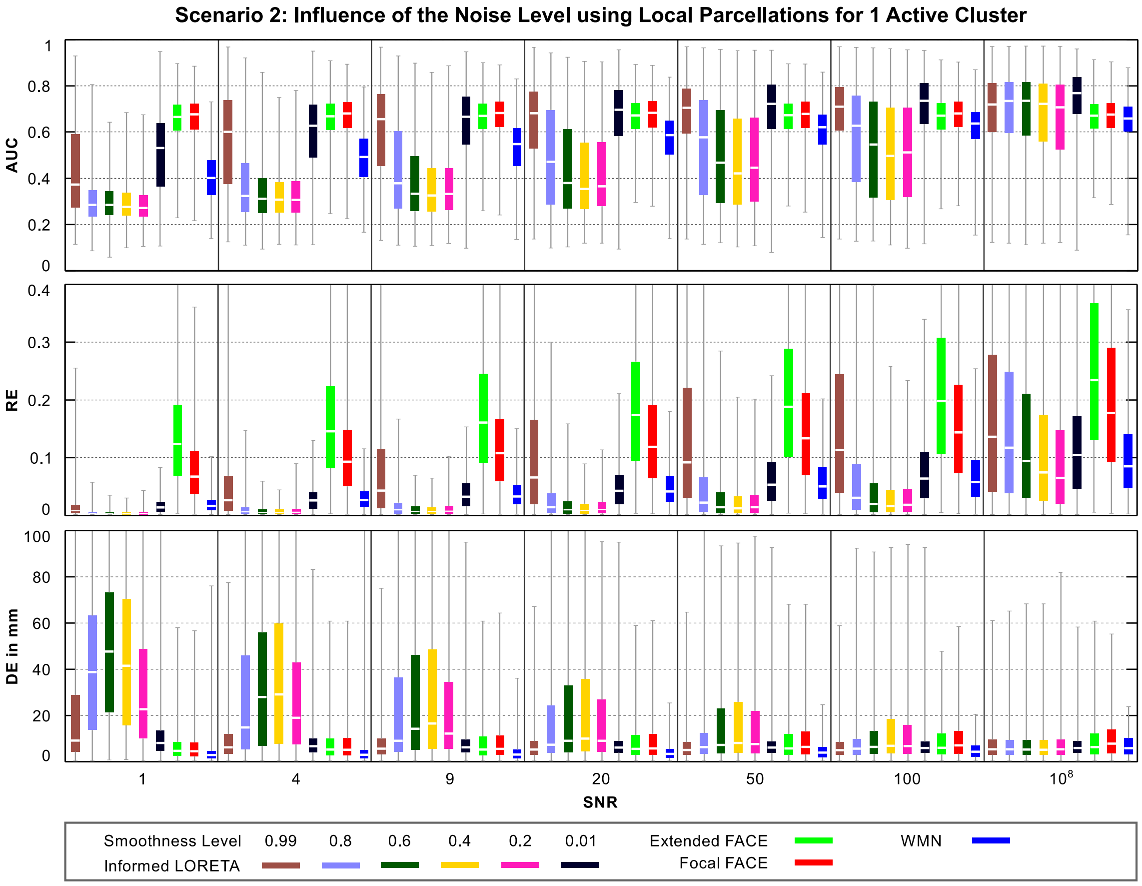

Figure 4.21: Performance of informed linear reconstruction methods with respect to the noise level. Prior information was derived from local parcellations, single clusters were activated without considering boundaries. See page 82 for details on the box plots.

knowledge have a rather strong impact. More importantly, the strong smoothness constraint introduces a bias towards the parceled areas. In contrast, informed LORETA with smoothness levels in the range from 0.2 to 0.8 are clearly inferior to WMN. Their smoothness constraints are weaker compared to informed LORETA with smoothness level 0.99. This results in a less efficient suppression of activity outside the region of interest. In other words, activity is systematically reconstructed outside the ROI in the unlabeled area of the local parcellation. This is also indicated by AUC values smaller than 0.5 and by large localization errors. This is obviously not consistent with the simulated source patterns.

4.5.3.3 Scenario 3: Misplaced and Ignored Boundaries

This section aims at analyzing the influence of ignored and misplaced boundaries on the reconstruction performance. The former represents the case that prior information does not include all functio-anatomical boundaries that are relevant to explain the actual source activity. In other words, data may contain information on the functional organization that is not reflected in prior knowledge. In contrast, the latter represents the case that not all incorporated boundaries are involved in activity generation. More precisely, the boundaries are invisible in the data since there is no activity in their vicinity (see Sec. 4.5.4 for a short discussion on this is-

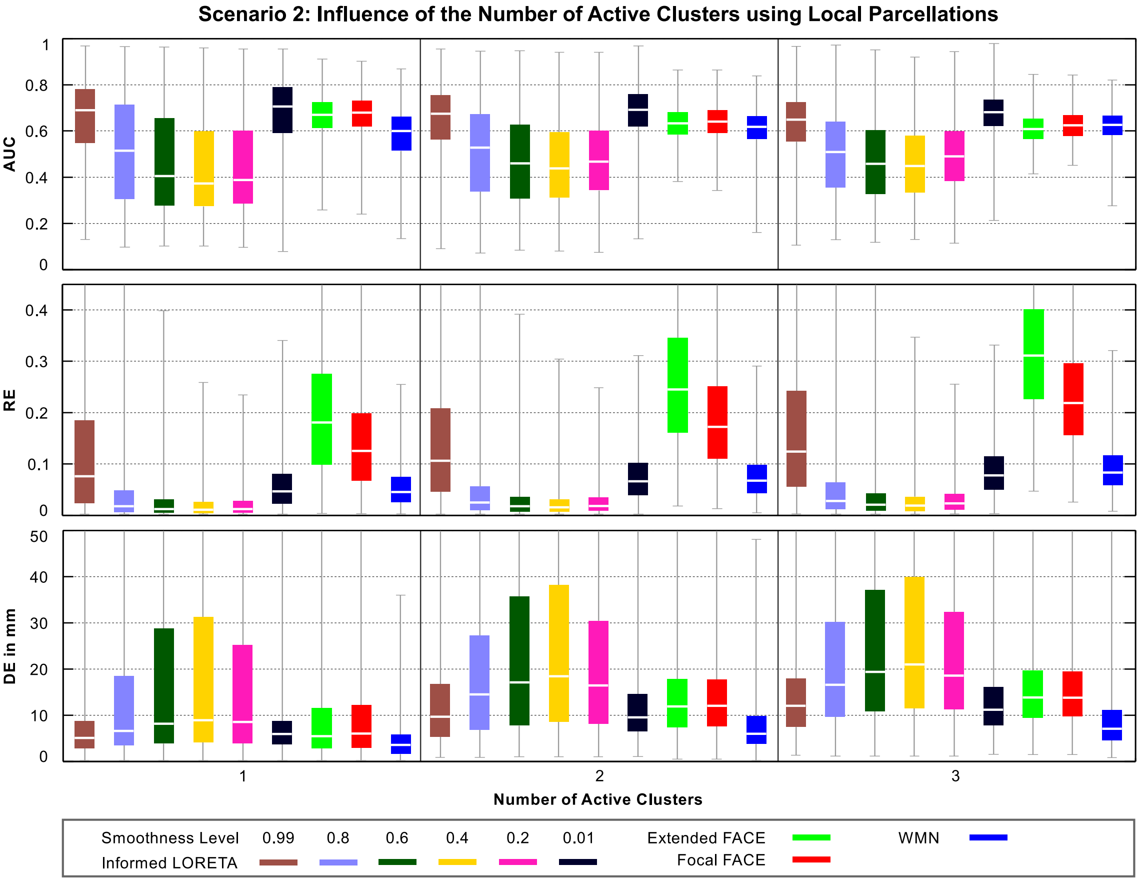

Figure 4.22: Performance of informed linear reconstruction methods with respect to the number of concurrently active clusters. Prior information was derived from local parcellations, up to 3 clusters were activated without considering the boundaries. Results are integrated over SNR levels 9, 20, 50, and 100. See page 82 for details on the box plots.

sue). Either way, the courses of the incorporated boundaries match the real functio-anatomical borders.

First, the use case of ignored boundaries is considered. Therefore, all results obtained for simulations with data generation on the basis of the large ROI and source reconstruction using the small ROI are combined (see Sec. 4.5.2 for details). Given this setup, the simulated source patterns are not necessarily located inside the ROI that is used to inform the reconstruction methods. Figure 4.23 shows the reconstruction performance with respect to the noise level for one active cluster. Figure 4.24 shows the performance in dependence on the number of concurrently active clusters. All distributions are statistically different from WMN (AUC: $P < 1 \times 10^{-5}$, DE: $P < 1 \times 10^{-5}$, RE: $P < 1 \times 10^{-8}$). The results provide the following insights.

The majority of the AUC samples observed for informed LORETA with smoothness levels 0.2 to 0.99 are generally close or even below 0.5 (except for noise-free simulations). As already mentioned above, a value below 0.5 means that active sources in the generated simulation pattern are systematically inactive in the corresponding reconstructed source pattern. This is exactly what happens here. Activity is generated using the large ROI, which contains certain regions that are not part of the small ROI. If activity is generated in these particular regions, the data is explained in the small ROI. This results from the bias effect that was observed for

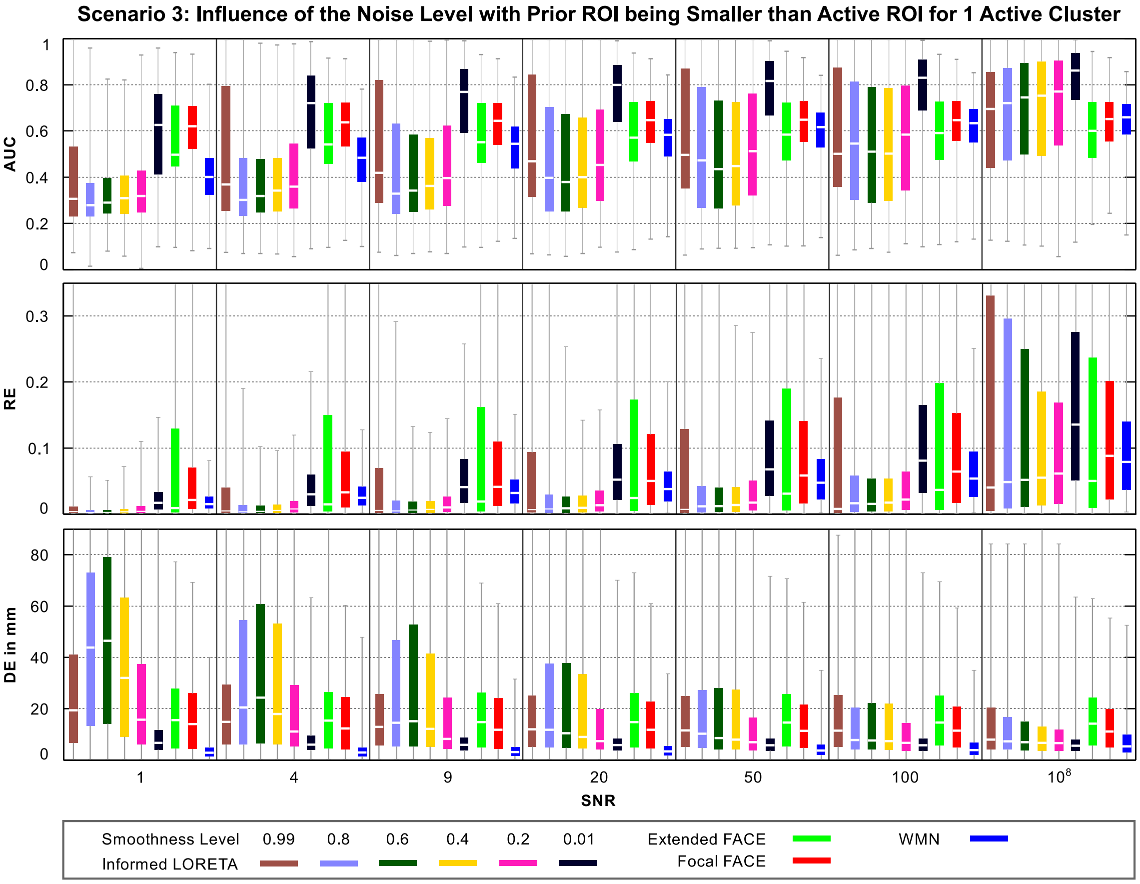

Figure 4.23: Performance of informed linear reconstruction methods with respect to the noise level. Prior information was derived from local parcellations (i.e. parcellations with a small ROI), single clusters were activated inside the corresponding large ROI area. The activation was consistent with the boundaries. See page 82 for details on the box plots.

local parcellations (i.e. activity is biased towards the parceled regions, see Sec. 4.5.3.1). In fact, informing LORETA with only a subset of the relevant functio-anamotical borders can be understood as a misinformation on the location of boundaries (or, in other words, on the existence of boundaries). This effect is also reflected in high DE values (i.e. high localization errors) and particularly low RE values (i.e. much of the energy is explained by sources outside the activated area).

It is obvious that this bias effect depends on the strength of the smoothness constraint. As a consequence, source reconstruction methods with a weak smoothness constraint (i.e. informed LORETA with smoothness level 0.01, eFACE, fFACE) provide much better results, in particular according to AUC and RE. However, it has to be pointed out that the performance difference between informed LORETA and the two FACE derivatives is rather strong. This is caused by different assumptions on the correlation structure outside the incorporated patches. FACE only imposes correlations between neighboring sources inside patches. That means that sources are expected to be uncorrelated in areas outside the small ROI. Informed LORETA imposes a general smoothness constraint everywhere on the cortex. This constraint is only lifted at boundaries. Hence, the general smoothness constraint provides a high consistency to any active cluster in the large ROI (i.e. outside the small ROI). This leads to high AUC values, the

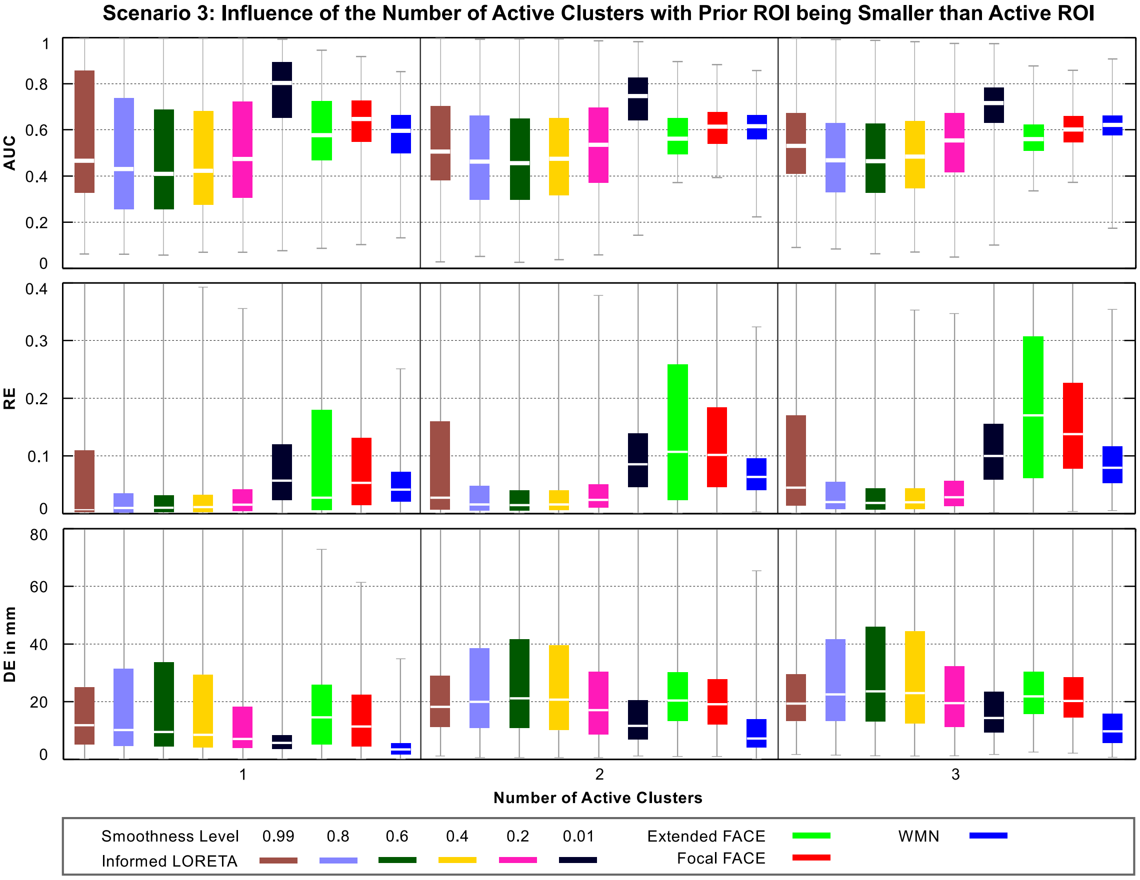

Figure 4.24: Performance of informed linear reconstruction methods with respect to the number of concurrently active clusters. Prior information was derived from local parcellations (i.e. parcellations with a small ROI), up to three clusters were activated inside the corresponding large ROI area. The activation was consistent to boundaries. Results are integrated over SNR levels 9, 20, 50, and 100. See page 82 for details on the box plots.

lowest localization errors compared to all other informed methods, and to moderate RE values compared to informed LORETA with higher smoothness levels. In fact, a comparison with the reconstruction performance of uninformed LORETA 0.01 (cmp. Fig. 4.17, Sec. 4.5.3.1) reveals a high similarity. This suggests that, here, the functional separation of the cortex according to incorporated boundaries is only of minor importance. Another interesting aspect is the comparison of the two FACE methods. Here, focal FACE generally outperforms extended FACE in case of one active cluster. When multiple clusters are active, the performance difference between these two methods reduces and even reverses for RE and DE (cmp. B.10 and Fig. B.11 in appendix B.3). In other words, the method with the stronger correlation constraint (i.e. inside the predefined ROI) is usually inferior to the method with the weaker smoothness constraint. This seems somewhat contrary to fact that a certain minimal smoothness level seems reasonable to explain compact clusters. One could expect that eFACE implies a better correspondence to the activated source patterns. However, this is obviously not the case. The performance differences between eFACE and fFACE is rather a matter of the degrees of freedom in each method. Focal FACE implies higher degrees of freedom since the smoothness constraint is weaker than in eFACE. This allows an easier deviation from solutions which are placed inside the small ROI.

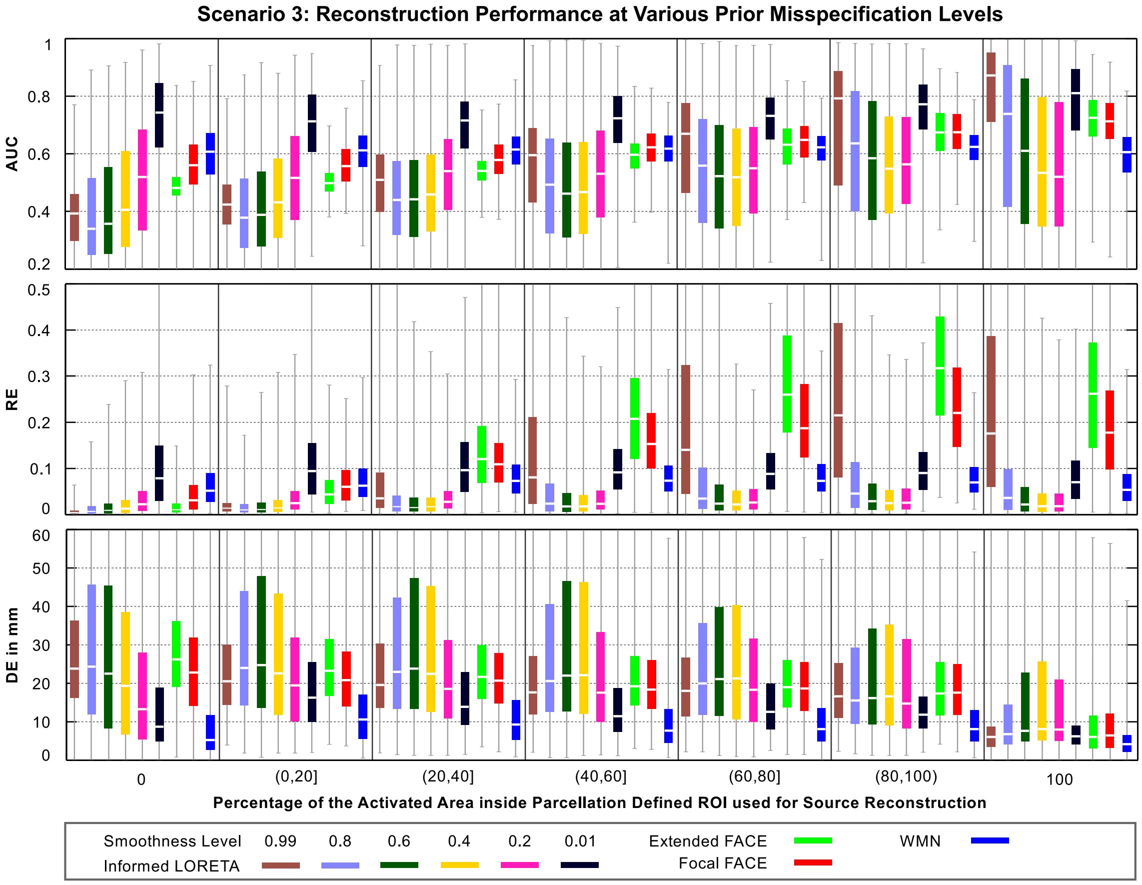

Figure 4.25: Performance of informed linear reconstruction methods with respect to the overlap between the total activated area and prior knowledge. Prior information was derived from local parcellations (i.e. parcellations with a small ROI). Up to three clusters were activated inside the corresponding large ROI. Results integrated over SNR levels 9, 20, 50, and 100. See page 82 for details on the box plots.

This is in fact similar to the bias effect observed for informed LORETA.

The final analysis focuses on the overlap between prior and activation. Therefore, the overlap between the area that is covered by activated clusters and the small ROI (which is used as prior knowledge) is determined for each simulation pattern. The overlap indicates how well the prior fits potential locations of brain activity. Figure 4.25 displays the performance in dependence of the overlap (in percent). The overlap is grouped according to two fixed levels (i.e. 0 % and 100 %) and 5 intervals. As above, the distributions obtained for informed methods are statistically different from the WMN distributions (AUC: $P < 1 \times 10^{-3}$, RE: $P < 1 \times 10^{-3}$, DE: $P < 1 \times 10^{-8}$).

First, the results for an overlap of 0 % (i.e. all activated clusters are located outside the small ROI) are considered. Informed LORETA with smoothness level 0.01 outperforms all methods according to AUC and RE and all informed methods according to DE. The majority of AUC samples for informed LORETA with level 0.4 and higher are considerably below 0.5 (that means, sources are systematically inactive during reconstruction) and the localization error (DE) is large. This clearly indicates that the activity is biased towards the *a priori* defined regions. As before, the largest bias can be observed for the strongest smoothness level. Moreover, it can be seen that fFACE performs better than eFACE. This underpins the above mentioned discussion that a bias effect towards parceled areas can also be observed for FACE.

Second, the results for higher overlap ratios are considered (except the results for 100 %). It can be seen that the performance of the informed LORETA methods with smoothness level 0.4 and higher, and of the two FACE methods steadily increases the more the prior and the activated source areas coincide. Nonetheless, informed LORETA 0.01 outperforms all methods according to AUC and, as above, all informed methods according to DE. It is obvious that the strongest effects (i.e. the strongest change of the reconstruction performance) can be found for the highest smoothness levels. This is particularly interesting for the two FACE methods. The performance gap between both methods according to AUC and DE converges towards zero. According to RE, eFACE is inferior to fFACE when the overlap is small but clearly outperforms fFACE even for moderate overlap ratios. This can be explained as follows. First, the more activity is located inside the *a priori* defined regions, the lower is the above mentioned bias effect. Second, the relevance of the smoothness constraint increases when more activity is located inside patches. Therefore, the eFACE method, which is based on a stronger smoothness constraint compared to fFACE, is more suited in this case.

Finally, a 100 % fit between activity and prior knowledge is considered. This effectively corresponds to the simulations carried out in scenario 1. The general drop of the RE performance in comparison to the preceding interval results from the fact that the distributions for 100 % overlap mainly consist of results for simulations with only one active cluster (because it is very likely that at least one cluster deviates from prior knowledge when multiple clusters are generated). It turned out before that the reconstruction performance according to RE is generally lower if less clusters are active (cmp. Fig. 4.14). Informed LORETA with smoothness level 0.99 provides the best reconstruction results (i.e. the best compromise between AUC, DE, and RE).

In summary, this analysis reveals that the reconstruction performance of informed methods whose correlation structure strongly depends on prior knowledge (i.e. all informed LORETA methods with smoothness level 0.2 and higher, and the two FACE methods) significantly drops when activity is located outside the *a priori* defined region. This is particularly relevant for informed LORETA with smoothness level 0.99 and for the two FACE methods. In both cases, the absence of important boundaries in prior knowledge leads to a location bias of the reconstructed activity. In contrast, informed LORETA with smoothness level 0.01 is much less prone to such errors. However, the poor impact of prior knowledge of course also leads to a lower reconstruction performance when prior and activity are consistent (cmp. scenario 1).

So far it turned out that the lack of relevant boundaries in prior information is a serious issue for most informed methods. Therefore, the second use case analyzes the reconstruction performance for simulations where to many functio-anatomical boundaries are defined. In other words, the prior knowledge contains boundaries that are irrelevant for the generation of the data (i.e. activity is not generated in their vicinity). As a consequence, these boundaries are not visible in data space. All results obtained for simulations with data generation on the basis of the small ROI (i.e. using parcellations LP1a, LP1b, LP2a, LP2b) and source reconstructions using the corresponding large ROI (i.e. LP1c, LP1d, LP2c, LP2d) are considered for the analysis. The results from the 4 parcellations are combined. Figure 4.26 displays the performance with respect to the noise level. Figure 4.27 shows the reconstruction quality in dependence of the number of active clusters. The distributions obtained for the informed methods are all

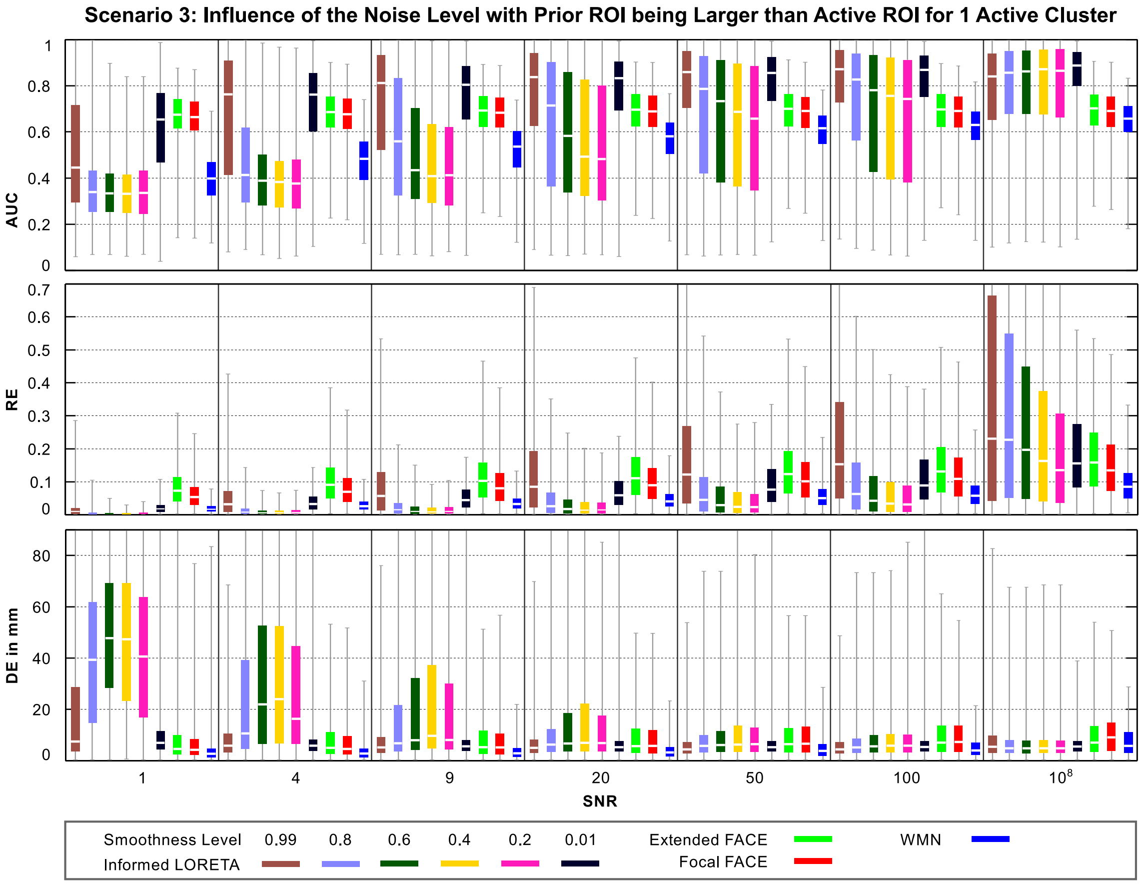

Figure 4.26: Performance of informed linear reconstruction methods with respect to the noise level. Prior information was derived from local parcellations (i.e. parcellations with a large ROI). Single clusters were activated inside the corresponding small ROI (prior consistent activation). See page 82 for details on the box plots.

statistically different from the WMN distributions (AUC: $P < 1 \times 10^{-8}$, RE: $P < 1 \times 10^{-4}$, DE: $P < 1 \times 10^{-7}$). B.12 and B.13 in appendix additionally show the performance for two and three concurrently active clusters.

It is mainly interesting how the misinformation influences the reconstruction performance in comparison to scenario 1 (i.e. in comparison to an optimally defined prior). However, it must be considered that the prior knowledge is different in both scenarios. As a consequence, the inverse algorithms are different as well (for example, the eFACE method used in both scenarios is not identical). It is therefore not possible to perform a direct comparison of the results obtained for each method in these two scenarios. It is rather useful to compare the performance differences that can be found between these methods separately for each scenario. This is done here. The results obtained for scenario 1 have shown that the use of informed LORETA with the strongest smoothness constraint promises the best reconstruction performance. A much lower smoothness constraint (smoothness level 0.01) still leads to acceptable AUC results but also to relatively low RE values (particularly in comparison to informed LORETA 0.99 and to the FACE methods). In contrast, the results obtained in the current scenario show that the use of the highest smoothness level is not superior to the use of the lowest level. The median in both AUC distributions is approximately the same. The RE values are more similar as well. In other

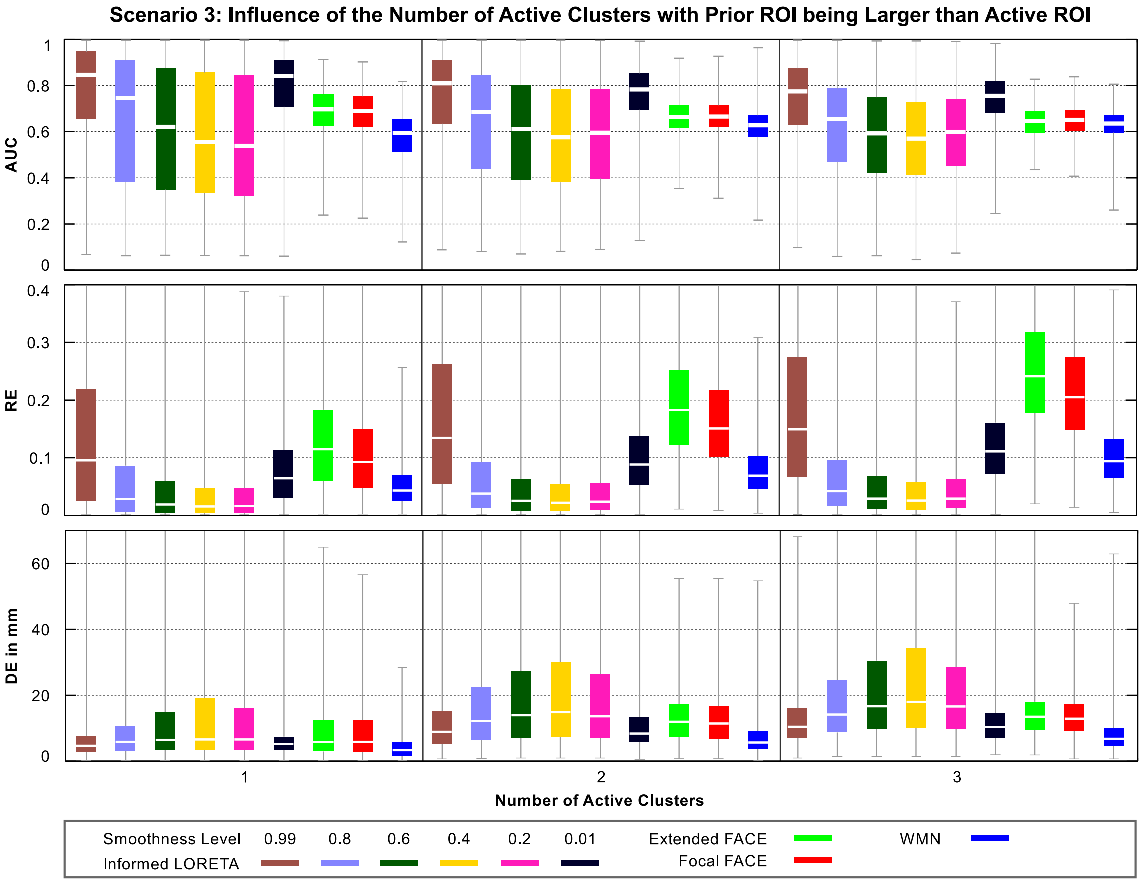

Figure 4.27: Performance of informed linear reconstruction methods with respect to the number of concurrently active clusters. Prior information was derived from local parcellations (i.e. parcellations with a large ROI). Up to three clusters were activated inside the corresponding small ROI (prior consistent activation). Results integrated over SNR levels 9, 20, 50, and 100. See page 82 for details on the box plots.

words, the performance difference between informed LORETA with smoothness level 0.99 and informed LORETA with smoothness level 0.01 is much smaller in the present scenario. Likewise, the performance difference between informed LORETA 0.01 and the two FACE methods is much smaller as well (particularly according to RE). This effect can be explained with the incorporation of irrelevant boundaries. These boundaries reduce the bias effect towards the region of interest[6] (i.e. the small ROI in this case; a bias effect towards the large ROI is still present but is irrelevant for the simulations scenario). As a consequence, some data is obviously explained by activity outside the small ROI (otherwise, the reconstruction quality would not be reduced).

Two main conclusion can be drawn from the results presented in this section. On the one hand, the comparison with results obtained for scenario 1 provides the essential insight that an extension of the ‘optimal’ ROI with irrelevant boundaries leads to a significant reduction of the reconstruction performance for methods where the prior knowledge has a strong impact

---

[6] For informed LORETA, the use of these boundaries drastically reduces the penalty of solutions with activity outside the small ROI. For FACE, the boundaries introduce a general smoothness assumption in regions outside the small ROI. Both effects result in a reduced bias towards the small ROI.

(i.e. informed LORETA 0.99 and FACE). On the other hand, the previous use case has shown that the reconstruction performance is even worse if relevant boundaries are omitted when defining prior knowledge. It is obvious that both cases should be prevented. However, this might be difficult in practice since the optimal ROI is usually not know. Therefore, the results emphasize that the priors must carefully be selected. The following section provides a further discussion on this issue.

4.5.4 Discussion

The aim of this section was the evaluation of various different functio-anatomical prior assumptions incorporated into linear inverse reconstruction methods. This included the use of different types of parcellations, i.e. local and full ones, and the variation of the validity of the prior information. The latter was realized by varying the consistency between brain activity and prior information. The evaluation was carried out subject to two aspects. The first is to provide insight in the potential performance of informed methods given that the prior fits to the actual brain activity (i.e. this was subject of simulation scenario 1). The second aspect is to examine how potential errors in prior knowledge affect the reconstruction performance (i.e. this is subject of scenario 2 and 3).

Before the results obtained for the different scenarios are discussed in more detail, it is first reasonable to put the focus on the terminology ‘correct’ and ‘incorrect’ prior knowledge, which is used in various contexts throughout this chapter. All algorithms employed for the simulations presented above are based on different assumptions on the source correlations. These assumptions are expressed by means of the source covariance matrix. The estimation of this matrix is based on the combination of a general smoothness assumption (i.e. even for the FACE methods) with prior knowledge. Importantly, the prior knowledge in a particular scenario is always the same for all reconstruction methods. As a result, each source covariance matrix expresses an assumptions on the covariance structure that is expected to underlie the data. This is the actual starting point to distinguish between correct and incorrect prior information. For example, the prior assumption is meant to be wrong if the covariance matrix implies correlation between sources which are uncorrelated in the data. This is, however, a situation that can easily occur when the prior assumption is based on (individual) structural information such as it is provided by functio-anatomical boundaries. For example, employing a full parcellation using informed LORETA with smoothness level 0.99 implies highly correlated activity in each patch. Likewise, employing a local parcellation implies a strong correlation inside the patches and in the outer patch area (i.e. the unlabeled region) as well. It is, however, very unlikely that such a correlation structure occurs in a realistic data set. In fact, it does even not occur in any of the simulations carried out in this section. Obviously, the intended and the actually imposed prior assumption can be in a blunt contradiction. Depending on the particular activation, this can lead to a corrupted reconstruction and to the generation of spurious sources. In fact, any of the employed reconstruction methods poses prior constraints that are incorrect in a certain manner. Therefore, the categorization of correct and incorrect priors does not relate to the particular prior assumption. It is rather based on the fact whether the simulated activity is consistent with the functio-anatomical boundaries (i.e. with the real underlying prior knowledge). That means, prior knowledge is meant to be correct if (1) the *a priori* defined patches fully cover the cortical area where activity might be generated and if (2) the incorporated boundaries confine the outline of active clusters (i.e. no overlap). Otherwise, prior knowledge is meant to be incorrect.

1$^{\text{st}}$ simulation scenario: The first scenario in this section dealt with correct prior knowledge. The simulations were based on the generation of compact clusters that were randomly distributed on the whole cortical sheet. Source reconstruction was performed using full parcellations. As a result, the whole cortex is subdivided into approximately equally sized areas. This leads to a rather balanced correlation structure in each cortical area for both informed LORETA and FACE. The analysis revealed that the combination of functio-anatomical prior knowledge with a moderate smoothness constraint (i.e informed LORETA with levels 0.4 to 0.8) provides the best reconstruction performance. The performance obtained for the strongest smoothness level is slightly lower (most likely because the intrinsic assumption of fully active patches is usually in conflict with the actual activation pattern). Nonetheless, the method still outperforms uninformed methods and informed methods with a weak smoothness constraint (i.e. informed LORETA 0.01, eFACE, and fFACE). Finally, these informed methods of a weak constraint outperform the uninformed reference methods WMN, but are inferior to uninformed LORETA with smoothness level 0.01 (i.e. the best uninformed reconstruction method). This means that the use of a general smoothness constraint is more effective than the use of constraint that is based on the combination of prior knowledge with a weak smoothness assumption in this particular scenario. This emphasizes the importance of the smoothness constraint regarding the impact of prior knowledge on source reconstruction.

Another analysis on the basis of correct prior knowledge was performed using local parcellations. The results confirm the importance of the smoothness constraint. In contrast to full parcellations, the cortex is subdivided into rather small parceled areas and usually much larger unlabeled regions. Compared to the use of full parcellations, this leads to a very different correlation structure between informed LORETA and FACE. In the FACE method, the correlation constraint is completely removed in unlabeled regions. In contrast, informed LORETA introduces a strong smoothness constraint for unlabeled regions. Depending on the actual smoothness level, this introduces long distant correlations in these areas, while the smoothness inside patches is limited by the patch size. Either way, the use of local parcellations introduces a correlation constraint that depends on the particular source location. These are important aspects that must be considered for the performance analysis.

According to the results, informed LORETA is only useful with the highest and lowest possible smoothness level. They provide much better results than informed LORETA for any other smoothness level and, more importantly, outperform the best uninformed reconstruction method (i.e. uninformed LORETA with smoothness level 0.01). This is interesting since the two informed LORETA derivatives imply totally different correlation structures. The highest smoothness level implies a very strong correlation between all sources in the outer-patch area (i.e. unlabeled regions). As a consequence, activity in these regions are effectively penalized. In other words, solutions are forced to be located inside the *a priori* defined patches. In contrast, the lowest smoothness level imposes correlations on a very small spatial scale (i.e. only a small fraction of the patch sizes) that is comparable to that in uninformed LORETA with smoothness level 0.01. Hence, the good performance obtained for smoothness level 0.01 cannot be explained with a bias of the solution towards *a priori* defined patches, but rather with a generally good correspondence between the prior assumption and the generated activity. All other smoothness levels seem unsuited for informed LORETA. The high localization errors that are observed with these methods indicate that the reconstructed activity is located in outer patch areas. It should be noted that the correlation structures obtained for these smoothness levels are very complex. It is therefore difficult to predict their actual effect on source reconstruction. It is obvious, however, that the imposed assumptions are usually inconsistent to the true activity.

The reconstruction results obtained for FACE demonstrate as well that the definition of the smoothness constraint is crucial. In FACE, the correlation structure inside patches can generally be compared to informed LORETA with smoothness level 0.01. That means that only a small scale intra-patch correlation is imposed on the solution. Outside patches, however, FACE assumes uncorrelated sources. It turned out that extended FACE outperforms focal FACE. A slightly stronger smoothness constraint as imposed by eFACE is obviously more consistent with compact activity (i.e. activity which has a certain spatial extent) than a much weaker smoothness constraint (as provided by fFACE). This is similar to the findings presented by Cottereau et al. (2012) who also carried out simulations using a local parcellation. It is, however, rather difficult to conclude how strong prior knowledge, i.e. the limitation of the correlation constraint by means of boundaries, actually contributes to the performance gain in comparison to WMN. Particularly the fact that FACE is still inferior to uninformed LORETA 0.01 emphasizes that a general correlation assumption has a major impact on the solution. Therfore, it is very likely that the limitation of this constraint (i.e. prior knowledge) is only of minor importance. Nonetheless, it should also be noted that FACE performs particularly well according to the RE measure. This, in turn, indicates that the incorporation of the boundaries is, in fact, relevant. Hence, the particular effect of the prior knowledge for FACE remains somewhat unclear. A final assessment cannot be made on the basis of these results. Another problem is that FACE as originally proposed by Cottereau et al. (2012) (and as used in this thesis) does not include leadfield normalization. In contrast, all LORETA methods include this kind of normalization to prevent an overestimation of superficial sources. Based on the conducted data it is, therefore, not possible to draw the conclusion whether FACE is inferior to LORETA-based approaches due to its weak smoothness constraint or due to the lack of depth normalization.

In summary, the results obtained for scenario 1 provide evidence that the incorporation of functio-anatomical prior information into linear inverse methods can improve source reconstruction in comparison to uninformed localization methods. The particular meaning of the terminology ‘correct prior knowledge’ was discussed above. It is obvious from the results that the use of local parcellations provides the best reconstruction performance. However, it is not possible to state that the use of a local parcellation generally provides better results than using a full parcellation. It is rather a question whether activity must be expected on the whole cortical surface (which usually seems to be unlikely), or if the activity is localized to certain regions (which is usually the case in many practical applications and which allows to use a local parcellation).

2$^{\text{nd}}$ simulation scenario: The second scenario dealt with inaccurate prior knowledge in the sense that the course of the boundaries is incorrect. Hence, boundaries incorporated as prior knowledge do not match the boundaries between distinct functional units. As stated above, such inaccuracies are likely to occur in realistic scenarios for multiple reasons. For example, the spatial resolution of any parcellation based on in vivo data is certainly limited[7]. The results for these simulations clearly show that the use of incorrect prior knowledge (i.e. incorrect with respect to the course of functio-anatomical boundaries) leads to a clearly reduced reconstruction performance compared to the use of correct prior information. It is obvious that methods based on a strong smoothness constraint are much more affected by uncertainties than methods with a weaker smoothness constraint.

The strength of the performance reduction depends on the particular measure that is used to asses the reconstruction quality. The strongest reduction can be found for the AUC measure. The definition of the sensitivity and the specitivity according to Eq. 4.5, which are the basic measures for the AUC, imply that differences between the shape of simulated and reconstructed source patterns have very a strong impact. In contrast, RE determines the amount of energy in the original activated regions and DE measures differences according to the location. Therefore, they are less dependent on the particular shape of the reconstructed source pattern. This explains why both measures are much less sensitive to the inaccuracies introduced in this scenario compared to the AUC.

It is particularly interesting that uninformed LORETA with smoothness level 0.01 outperforms all informed reconstruction methods. This emphasizes the importance of correctly aligned boundaries. However, it must also be noted that the simulation setup implies very strong uncertainties regarding the course of boundaries (because the maximum overlap of boundaries is not limited). In fact, this assumption implies that the course might be completely wrong. This can be interpreted as a worst case scenario. In practice one should expect much smaller uncertainties since, otherwise, the prior knowledge would not reflect any prior knowledge (i.e. it would be useless). From this point of view it can be argued that the course of the employed functio-anatomical boundaries exhibits only minor inaccuracies under practical conditions and, therefore, only a weak reduction of the reconstruction performance must be expected.

3rd simulation scenario: A different aspect of inaccurate prior knowledge was subject of the third simulation scenario. It dealt with both the use of borders that are not relevant for the particular simulation, and with the absence of borders that are relevant to explain the data. Although it turned out that both issues lead to a reduction of the reconstruction performance, the latter one is particularly problematic. More precisely, the results revealed that the reconstruction performance drastically reduces even if only a minor part of the active brain area is located in regions that are not incorporated as prior knowledge. This underpins the importance of a correct definition of boundaries. In practice, however, it is often difficult to specify only those borders that are actually relevant to explain the data. Therefore, it seems reasonable that local parcellations should consist of all patches that might contain any relevant activity.

The analyses carried out in this section have shown that the reconstruction quality essentially depends on two key factors: the prior knowledge defined by the course of the functio-anatomical boundaries, and the smoothness assumption. Although both are combined with each other in informed reconstruction methods, the latter one is of particularly importance.

---

[7] The estimation of functio-anatomical boundaries by means of some structural information as, for instance, the strength of fibers, which connect distinct regions, depends, first, on the accurate estimation of structural data and, second, on applying thresholds. This implies that it is unlikely to achieve a perfect match between the true and the estimated functional borders in a certain experimental paradigm.

The smoothness assumption expresses a general believe on the spatial extent of active clusters. Its importance is confirmed, for instance, by the enhanced reconstruction performance that can be achieved using uninformed LORETA with smoothness level 0.01 in comparison to the use of WMN.

Another important finding in this section is the use of local parcellations provides good reconstruction results in many situations. From a practical perspective, local parcellations are very useful. They allow to constrain activity to a particular region (without the need to adjust the variance of sources in order to increase their likelihood for being activated). Finally, informed LORETA with smoothness level 0.99 provides a very good reconstruction performance if the prior knowledge is correct. However, this method is also strongly prone to errors caused by inaccurate prior knowledge. In contrast, informed LORETA with smoothness level 0.01 leads to slightly lower reconstruction performance but is also more robust to errors in prior knowledge. Therefore, both methods can be useful in practical situations.

4.6 Influence of Spatial Inaccuracies in Forward Modeling

4.6.1 Objective

The simulations in the previous sections were carried out using the same forward model for data generation and source reconstruction (i.e. under ideal conditions). In fact, using the same model for both procedures is referred to as an inverse crime because it might cause the overestimation of performance measures (i.e. of the reconstruction quality). The subject of the present section is the evaluation of informed linear inverse methods using different forwards models for the generation of EEG data and its reconstruction. Two aspects are evaluated. The use of different source models for forward and inverse calculations is subject of the first simulation scenario (see below). This ensures a shift of the source locations. The impact of inaccuracies of the electrode positions (for example resulting from co-registration errors) on the solution is evaluated in the second scenario.

According to Kaipio and Somersalo (2005) even the use of different forward models which, however, are based on exactly the same underlying discretization of the solution space does not avoid inverse crime. In relation to EEG/MEG source reconstruction, this means that a different source space must be defined (for example by means of another tessellation of the cortical surface) for each forward model in order of effectively prevent inverse crime. In fact, this is an efficient technique that has already been employed in many studies (see, for instance, Auranen et al., 2005, Chang et al., 2010, 2013, Lucka et al., 2012, Ou et al., 2009). However, it limits the analysis to the use of performance measures which do not depend on source indexing. For example, this is necessary for correlation and AUC analysis, which rely on before/after comparisons. Common metrics that are used in this case are dipole localization error (DLE) or spatial dispersion (SD).

An alternative technique to generate a second source space is to shift each source to a new source position. This ensures that the same source indexing can be applied in both grids. It is then possible to carry out before/after comparisons at each source index, given that the shift of each source is in a sufficiently small range (for instance in the range of less than the half of the mean spatial resolution). This kind of shift can easily be realized on a regular cubic source space (for instance by means of a parallel shift of all source positions). The simulations in this thesis are based, however, on source models which are defined along the heavily folded cortical sheet. This requires another technique in order to shift each source to a new position. It is particularly important to preserve the general geometrical properties of the grid. The technique used here is outlined in the following section. It is the basis for subsequent simulations which aim at analyzing the relevance of inverse crime for informed LORETA based source localization.

4.6.2 Simulation Setup

The simulations in the present section are based on the realistic forward model presented in Sec. 4.2.2. This forward model was employed for the computation of the inverse operators of the different inverse methods. A modified version of this model was used for the prediction of EEG data. The forward model was modified in two different ways. For the first scenario, the source space was replaced by a shifted version (see below). Other components (e.g. the surfaces used to model the boundaries between different brain compartments) were kept constant. The shifted source space was generated by adding zero-mean Gaussian noise ($\sigma = 0.3\,\text{mm}$) to all source coordinates in the original source space. This way, all source locations are shifted by a reasonable distance, while the index of each source is preserved. The latter aspect is not only important to perform before/after comparisons but also ensures that prior knowledge (i.e. patch definitions) does not have to be readjusted. The minimum, maximum, and mean euclidian distance between the new and the original source positions are $5.8 \times 10^{-5}\,\text{mm}$, 2.82 mm, and 0.27 mm, respectively.

In the second scenario, only the sensor model was modified, while other components of the forward model (i.e. also the source space) were the same as presented in Sec. 4.2.2. Four different sensor models were generated. Now, the electrode positions were shifted by adding zero-mean Gaussian noise with the standard deviations $\sigma = 0.5\,\text{mm}/1\,\text{mm}/2\,\text{mm}/3\,\text{mm}$. This leads to a minimum, maximum, and mean euclidean distance between the electrode positions in the original and modified sensor model of 0.26 mm, 2.18 mm, 0.80 mm / 0.29 mm, 2.84 mm, 1.5 mm / 0.47 mm, 6.69 mm, 3.2 mm / 0.59 mm, 9.85 mm, 4.71 mm. Each of these sensor models embodies a different level of co-registration errors.

The full parcellations HP8 and HP18 (see Sec. 4.2.3) as well as the local parcellations LP1a, LP1b, LP2a, and LP2b (see Sec. 4.5.2) were employed as prior knowledge. Source activity was generated just like before (see p. 61). Only the prior consistent activation was considered here[8]. A total of 1500 trials for each full parcellation and 500 trials for each local parcellation were generated for each scenario. Source reconstruction was performed using focal and extended FACE, informed and uninformed LORETA (see appendix B.1 for Laplacian regularization parameters), and WMN. It was done on the basis of the original forward models[9]. Details on the inverse methods are given in Sec. 4.2.5. Finally, the size of the activated area and the metrics AUC, RE and DE were computed for each reconstruction result.

---

[8] Prior knowledge is assumed to be correct. However, the redefinition of the source space as mentioned above introduces minor uncertainties regarding the shape of the patches.

[9] Hence, a recalculation of the Laplacian regularization parameters is not necessary.

4.6.3 Results

The analyses carried out here are similar as those in Sec. 4.5.3. General details on the boxplots and on the statistical tests can be reviewed there. Section 4.6.3.1 presents the results for the use of different source models for forward and inverse calculation (i.e. scenario 1). Section 4.6.3.2 shows the reconstruction performance with respect to co-registration errors of the electrode positions (scenario 2).

4.6.3.1 Scenario 1: Different Source Models for Forward and Inverse Calculations

The very first analysis focuses on the use case that source reconstruction and data generation are based on different source models (i.e. no inverse crime). Activity can appear on the whole cortical sheet and is consistent with prior knowledge (i.e. full parcellations used for source localization). The results obtained for the two full parcellations (i.e. HP8 and HP18) are combined. Figure 4.28 shows the corresponding performance measures AUC, RE and DE in dependence of the signal-to-noise ratio (for trials with one active cluster). Almost all distributions obtained for informed and uninformed LORETA are statistically different from WMN (AUC: $P < 1 \times 10^{-3}$, RE: $P < 1 \times 10^{-2}$, DE: $P < 1 \times 10^{-2}$). The only exception is informed LORETA with smoothness level 0.01. The RE observations obtained for this methods are statistically similar to WMN ($P = 7.3 \times 10^{-2}$), particularly at low SNR levels. Figure 4.29 displays the performance according to the number of concurrently active clusters. Here, the DE distributions obtained for informed LORETA with levels 0.8 and 0.99 are statistically similar to the WMN observations ($P \geq 9.3 \times 10^{-2}$). All other distribution in the figure are statistically different from the WMN results (AUC: $P < 2 \times 10^{-2}$, RE: $P < 2 \times 10^{-2}$, DE: $P < 5 \times 10^{-2}$).

It is particularly informative to compare the performance results obtained here with those found in Sec. 4.3.3 (where inverse crime might be an issue). This comparison reveals no performance differences according to AUC and RE. The ability to localize the exact position of an active cluster is, however, slightly reduced here. Importantly, this is a general issue for all employed inverse methods and not only for informed reconstruction methods, which are of particular interest. Despite of this weak effect, it is reasonable to draw the conclusion that the performance in case of inverse crime and without inverse crime is approximately the same for any of the evaluated methods. For the sake of completeness, the reconstruction performance for two and three concurrently active clusters with respect to the SNR are displayed in appendix B.4 (i.e. Fig. B.14 and B.15).

The second analysis focuses on prior consistent source reconstruction using local parcellations. As above, data generation and source reconstruction are based on different source models. The results obtained for all local parcellations (i.e. LP1a, LP1b, LP2a, LP2b) are combined for this analysis. Figure 4.30 shows the reconstruction performance according to AUC, RE and DE with respect to the signal-to-noise ratio (for trials with one active cluster). The majority of the distributions obtained for informed and uninformed LORETA are statistically different from the WMN results (AUC: $P < 1 \times 10^{-8}$, RE: $P < 1 \times 10^{-2}$, DE: $P < 3 \times 10^{-2}$). However, the DE distributions for informed LORETA with smoothness levels 0.8 and 0.99 are statistically similar to the WMN results at various SNR levels ($P \geq 6.2 \times 10^{-2}$). Figure 4.31 displays the performance in dependence of the number of concurrently active clusters. Here, all distributions are statistically different from those provided by WMN AUC: $P < 1 \times 10^{-8}$, RE: $P < 1 \times 10^{-6}$, DE: $P < 1 \times 10^{-8}$).

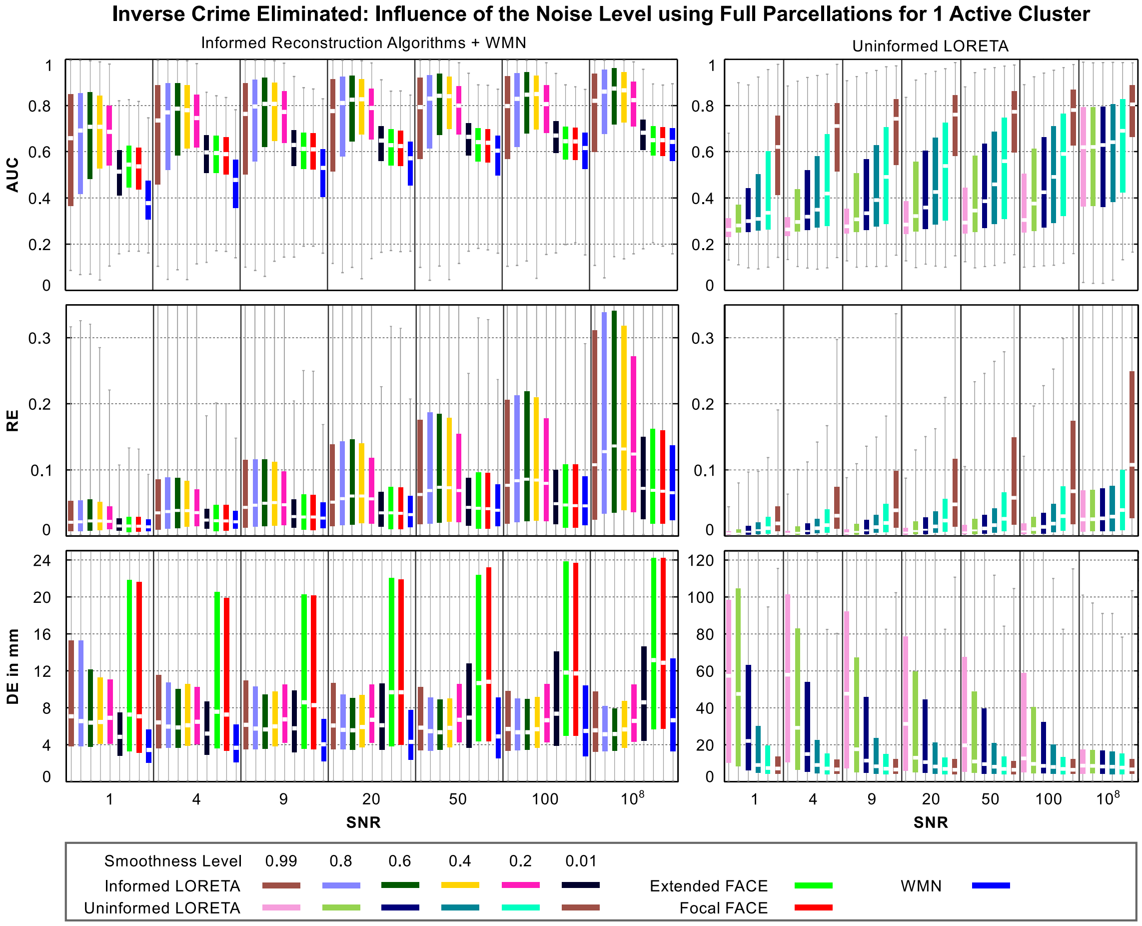

Figure 4.28: Performance of informed and uninformed linear reconstruction methods with respect to the noise level. Forward and inverse calculations are based on different source models. Prior information was derived from full parcellations, single clusters were activated. The activation was consistent with the boundaries. See page 82 for details on the box plots.

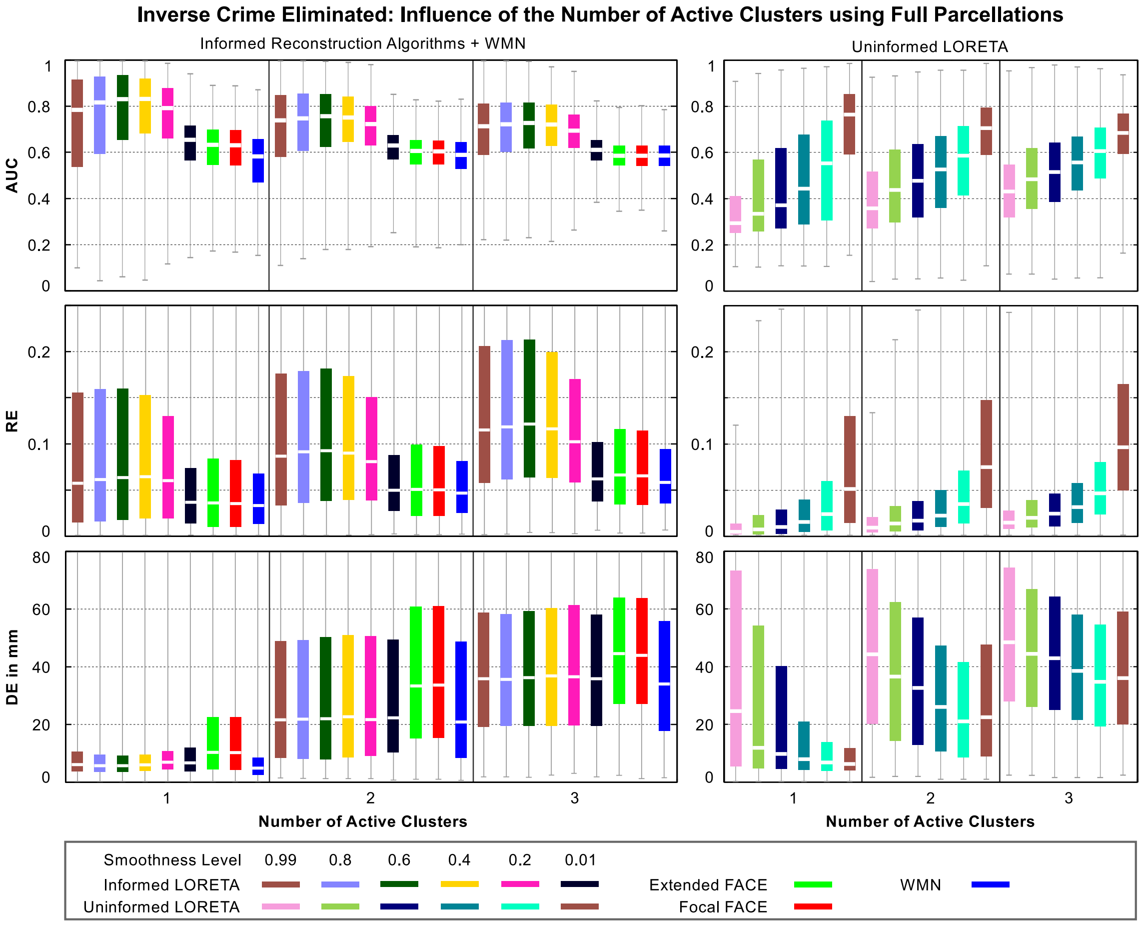

Figure 4.29: Performance of informed and uninformed linear reconstruction methods with respect to the number of concurrently active clusters. Forward and inverse calculations are based on different source models. Prior information was derived from full parcellations, up to 3 clusters were activated. The activation was consistent with the boundaries. Results are integrated over SNR levels 9, 20, 50, and 100. See page 82 for details on the box plots.

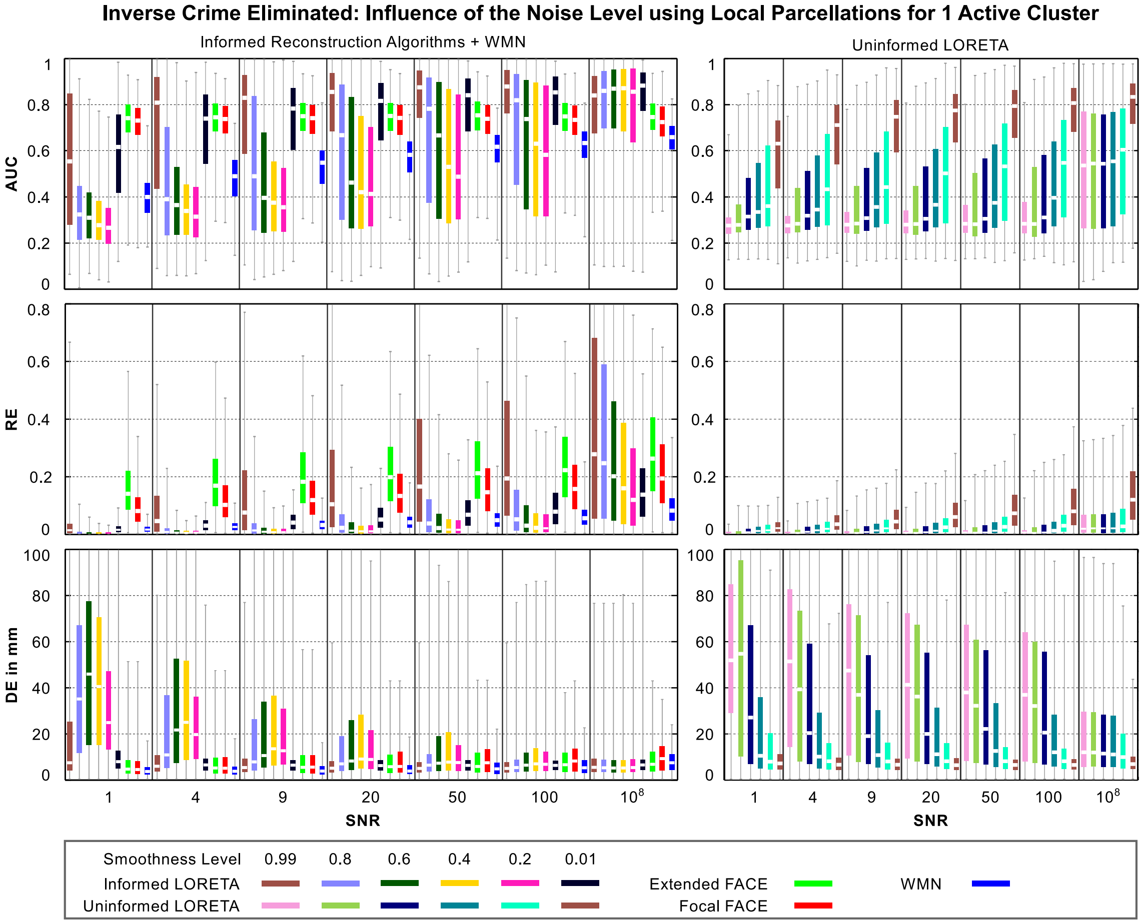

Figure 4.30: Performance of informed and uninformed linear reconstruction methods with respect to the noise level. Forward and inverse calculations are based on different source models. Prior information was derived from local parcellations, single clusters were activated. The activation was consistent with the boundaries. See page 82 for details on the box plots.

As above, it is particularly useful to compare the results with those obtained for simulations with local parcellations in Sec. 4.3.3. Similarly to the analysis with full parcellations, this comparison reveals the same performance according to AUC and RE and a slightly reduced performance according to DE for all methods. Likewise, it can be concluded that the correction for inverse crime does not change the general performance of the inverse methods to reconstruct activity that is localized to a confined region on the cortex. For the sake of completeness, the results for two and three concurrently active clusters are displayed in appendix B.4 (i.e. B.16 and B.17).

In summary, the results for simulations with both local and full parcellations have shown that the use of the same source space for forward and inverse calculations has only a marginal, if any, effect on the reconstruction performance. A short discussion on the results is provided in Sec. 4.6.4.

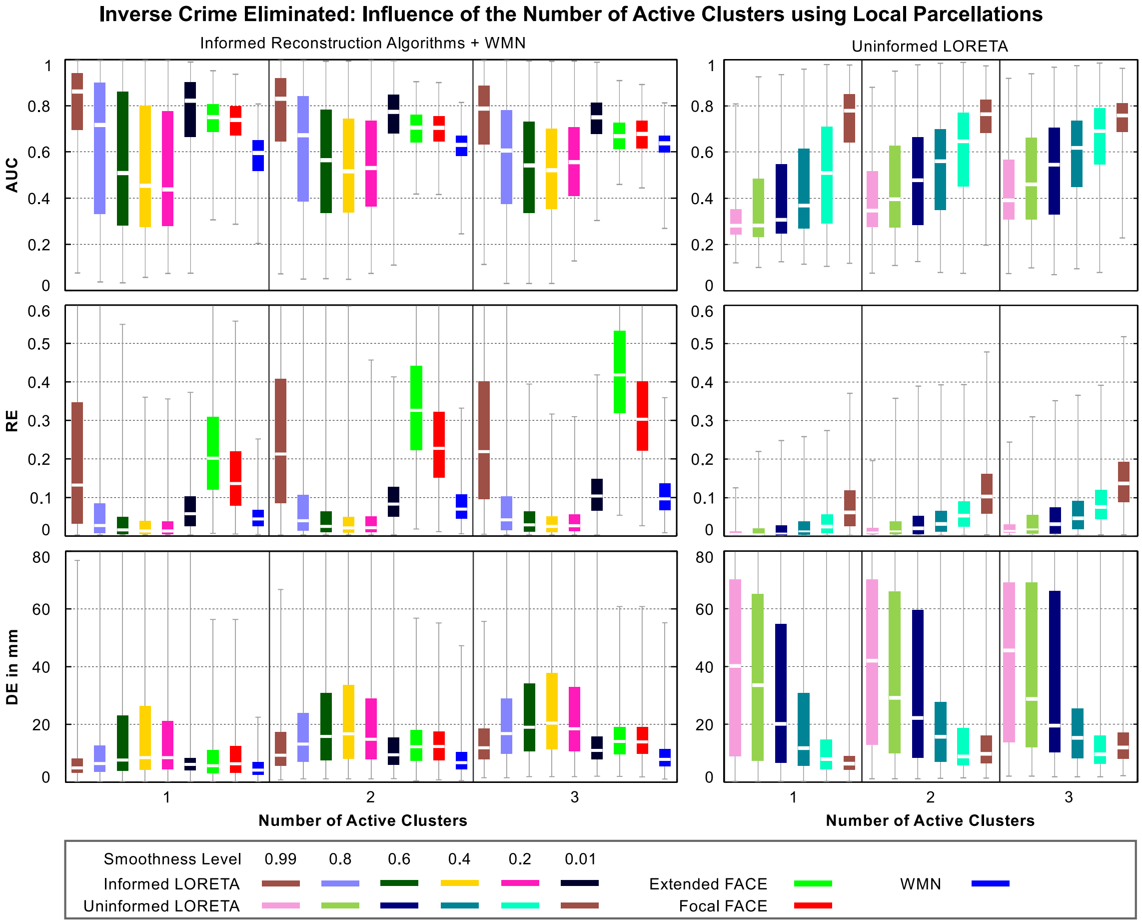

Figure 4.31: Performance of informed and uninformed linear reconstruction methods with respect to the number of concurrently active clusters. Forward and inverse calculations are based on different source models. Prior information was derived from local parcellations, up to 3 clusters were activated. The activation was consistent with the boundaries. Results are integrated over SNR levels 9, 20, 50, and 100. See page 82 for details on the box plots.

4.6.3.2 Scenario 2: Influence of Electrode Co-registration Errors

This section analyses the reconstruction performance of informed LORETA, extended FACE, and focal FACE in case of inaccurate EEG electrode positions due to co-registration errors. This is done separately for simulations on the basis of full and local parcellations. Figure 4.32 shows the combined results obtained for the two full parcellations (HP8 and HP18). The performance measures are displayed versus the strength of co-registration errors. These are indicated by the particular standard deviation of the Gaussian noise that was used to displace the electrode positions. All distributions are statistically different from the WMN samples (AUC: $P < 1 \times 10^{-8}$, RE: $P < 1 \times 10^{-4}$, DE: $P < 1 \times 10^{-8}$). Likewise, Figure 4.33 shows the combined results for all local parcellations. Again, all distributions of the informed methods are statistically different from the WMN observations (AUC: $P < 1 \times 10^{-8}$, RE: $P < 1 \times 10^{-8}$, DE: $P < 1 \times 10^{-8}$).

The results show that none of the performance measures is seriously affected by the co-registration errors. Neither any informed reconstruction method nor the uninformed reference method exhibits a reduced reconstruction performance at any of the tested co-registration

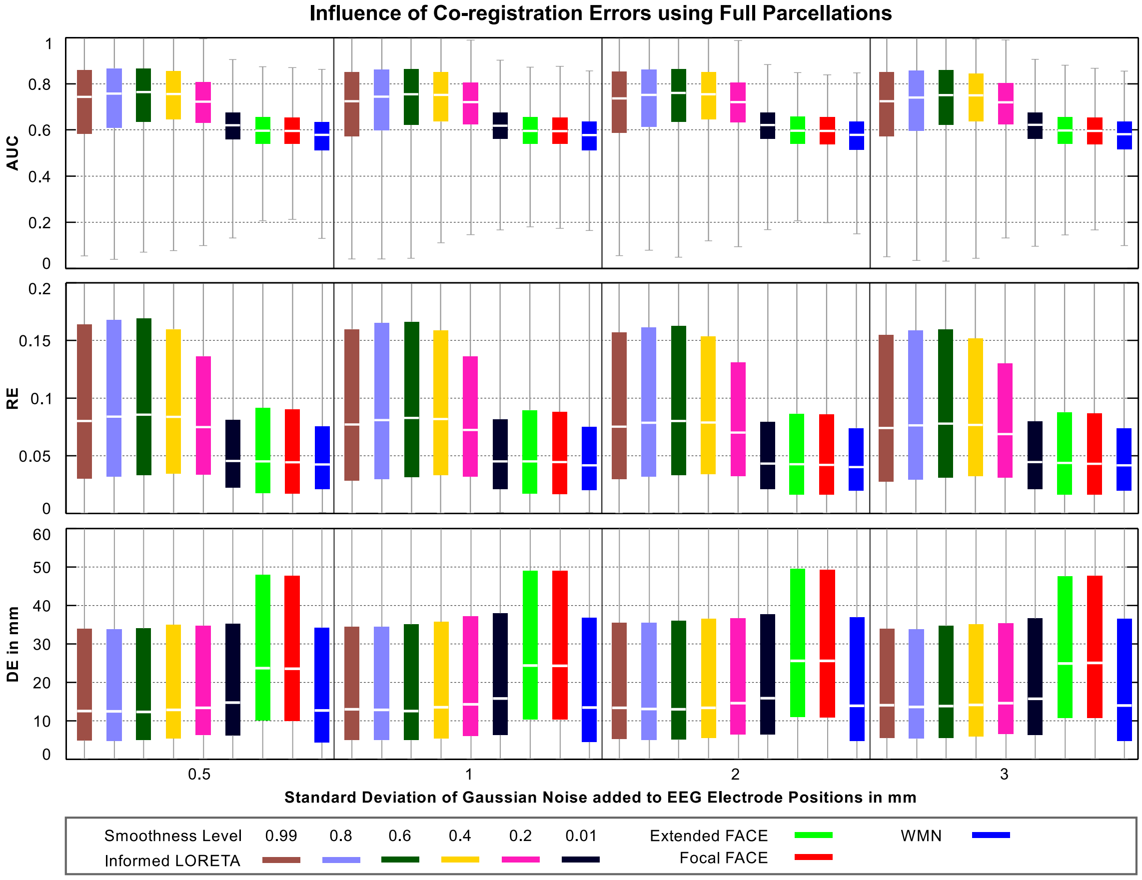

Figure 4.32: Performance of informed linear reconstruction methods with respect to the co-registration error of EEG electrodes. The strength of the error is indicated by the standard deviation of a Gaussian error function (see text). Prior information was derived from full parcellations, up to 3 clusters were activated. The activation was consistent with the boundaries. Results integrated over SNR levels 9, 20, 50, 100. See page 80 for details on the box plots.

error levels. These findings are consistent with the observations reported by Cottereau et al. (2012). Hence, it can be concluded that the utilization of functio-anatomical prior knowledge to constrain LORETA-based approaches does not increase the vulnerability to errors induced by inaccurate electrode positions. This was one of the questions to be answered in this section. Finally, it can be concluded that co-registration errors of the EEG electrode positions do not affect the simulation results presented in this work.

4.6.4 Discussion

The objective of the present section was the evaluation of the reconstruction performance of informed linear inverse methods given that the forward models used for the prediction (i.e. generation) and the reconstruction of EEG data are different. This is much more realistic than using identical models for these two procedures. In fact, these models are always different when analyzing real experimental data. However, all previous simulations carried out in chapter 4 employed the same forward model for inverse and forward calculations. It was therefore necessary to analyze whether this simplification of the simulation setup leads to an overesti-

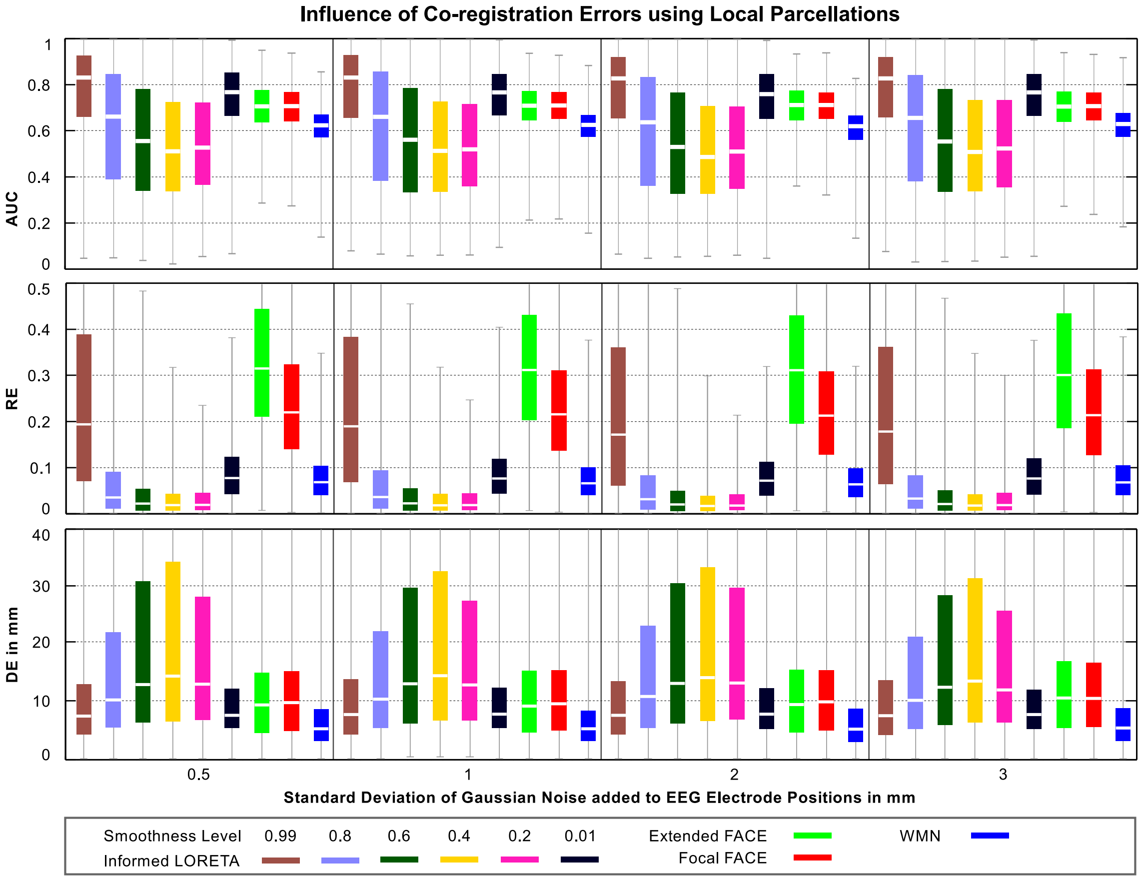

Figure 4.33: Performance of informed linear reconstruction methods with respect to the co-registration error of EEG electrodes. The strength of the error is indicated by the standard deviation of a Gaussian error function (see text). Prior information was derived from local parcellations, up to 3 clusters were activated. The activation was consistent with the boundaries. Results integrated over SNR levels 9, 20, 50, 100. See page 80 for details on the box plots.

mation of any performance measure (which might also have an impact on the conclusion that were drawn with regard to the reconstruction capabilities).

As before, several hundred source patterns of different complexity were randomly generated. Prior knowledge was derived from local and full parcellations and was assumed to be consistent to the generated activity. Two different types of simulations were carried out. The first approach was based on the use of different source models for the generation of the two forward models. More precisely, a new source space was generated by means of randomly shifting the source localizations in the original source space. This is an effective technique to prevent inverse crime. Moreover, it preserves source indexing. This allows to employ performance measures which rely on before/after comparisons of the spatial distributions (e.g. AUC, RE). This ensured that a potential overestimation of these performance measures, which were used in previous parts of this chapter, could in principle be detected. The evaluation revealed only a minor performance drop for DE and, more importantly, no performance reduction according to AUC and RE. The marginal drop of DE is a direct result of displacing each source to a new location. This shift renders a zero localization error virtually impossible. However, all reconstruction methods suffer from this effect. More importantly, the performance of the informed reconstruction methods is not overestimated compared to any other of the evaluated inverse methods. As a consequence, it can be concluded that inverse crime is not a problem at all for any of the simulations carried out in the previous sections.

Note that the weak relevance of inverse crime can explained with the high spatial resolution of the source space. This high resolution renders the leadfield of neighboring sources highly similar. That means, a shift between the true and the modeled source locations is per se unlikely to seriously affect any performance measure. Therefore, it can reasonably be argued that a sufficiently high spacial resolution of the source space effectively prevents inverse crime. This is consistent to Lamus et al. (2012) who reported the use of a source space with approximately 150 000 nodes per hemisphere to minimize the effect of inverse crime. This is in a similar range as for the realistic source models employed in this work.

The second approach in this section assessed the impact of EEG electrode co-registration errors. This addressed the problem that the accuracy of the modeled electrode positions is usually limited. For example, uncertainties introduced by the digitization process, the segmentation of the scalp surface (i.e. and all other volume components as well), and the matching between EEG/MEG and MRI coordinates are relevant steps in EEG/MEG processing in which uncertainties are likely to be introduced. Gaussian noise was added to the original electrode positions to generate a total of four different sensor models (each with a different co-registration error level). These errors are in a similar and even above the range as proposed in other studies that investigated the accuracy of electrode positions (see, for instance, Cottereau et al., 2012, Schwartz et al., 1996). The simulation results revealed no considerable influence of co-registration errors on the reconstruction performance. This emphasizes that linear inverse methods in general (and particularly informed reconstruction methods) are relatively robust against errors of the electrode positions. The robustness can be explained with the fact that this kind of error could also be modeled by means of adding uncorrelated noise at the *true* electrode location. The impact of noise is usually effectively minimized by means of regularization (see chapter 2). Hence, the effect of the modeled electrode localization errors are minimized by regularization as well. This is, of course, only true if the location errors at each electrode are linearly independent from each other. It can be concluded that potential errors between true and localized electrode position do not affect the results presented in this work.

5 Evaluation of Informed LORETA using Experimental Data

5.1 Motivation and Outline

This chapter demonstrates the application of informed LORETA for the reconstruction of real experimental EEG and MEG data. It aims at exploring the potential benefit of functio-anatomically informed linear source reconstruction methods under realistic conditions, that means for the analysis of a particular experimental paradigm. The analyzed EEG/MEG data was recorded in a language experiment in which multiple spoken sentences were presented to subjects. It is particularly interesting whether the use of informed reconstruction methods provides a plausible reconstruction of the likely generators of this kind of data.

EEG and MEG are commonly used techniques for studying the spatio-temporal organization of spoken language processing. Several neurocognitive models that explain the cortical organization of speech were presented in literature (e.g. Hickok and Poeppel, 2007, Knösche et al., 2005). These models are good candidates to derive functio-anatomical prior knowledge on the basis of individual parcellations. The subsequent chapter is structured as follows: Section 5.2 describes the experimental setup. This mainly includes the experimental paradigm, technical parameters, EEG/MEG signal processing, the derivation of functio-anatomical prior knowledge, and the estimation of noise and data (co-)variances, which are necessary to compute linear inverse solutions. The results are presented in section 5.3, separately for EEG and MEG measurements. Finally, the findings are discussed in sec. 5.4.

5.2 Methods

5.2.1 Experimental Setup

The basis for the evaluation of informed LORETA is EEG/MEG data of five subjects recorded in a spoken language experiment. A total of 192 sentences were presented to each subject. The task for each subject was to assess each sentence according to its grammatical structure and the prosody. The analysis carried out here does not focus on characteristic features of the brain response according to these two attributes, but rather on the brain processes which are triggered by a sentence onset. Therefore, the analysis is focused on the N100/N100m and P200/P200m components are. Data was simultaneously recorded at 60 EEG and 306 MEG channels with a sampling rate of 1 kHz using a Neuromag Vectorview device (Elekta Neuromag Oy, Helsinki, Finland).

The processing of the recorded signals comprised the following steps. At first, Neuromag's Max-Filter was applied to MEG data for interference suppression and head movement correction. Next, the raw signals were filtered using a bandpass (2-20 Hz). Afterwards, single trials (i.e. epochs, 200 ms before to 500 ms after sentence onset) were extracted from continuous data stream. Then, baseline correction was applied to each channel by subtracting the mean signal of the pre-stimulus interval from all samples in the corresponding trial. Next, disturbed channels and trials including artifacts were identified by means of visual inspection and discarded from further processing. The averaged evoked response of all trials was computed separately for EEG and MEG and, finally, all EEG signals were referenced to common average.

5.2.2 Forward model and Prior information

Freesurfer (Fischl et al., 2002) was used to construct triangulated grids for the folded cortical surface ($\approx$ 269.000 dipoles per subject), the inner and outer skull surfaces, and skin (each surface consists of 5120 vertices) based on individual MR images. The MNE toolbox (see `www.martinos.org/mne`) was used for the co-registration of these surfaces with the sensor coordinate system. The source space was built up by placing one ECD with perpendicular orientation on each vertex. Finally, a three-compartment BEM model with the conductivities 0.33 S/m for brain and skin, and 0.0042 S/m for the skull compartment, was constructed. The final EEG forward model was computed using SIMBIO (Fingberg et al., 2003) and the MEG leadfield using the MNE toolbox.

Prior information for the informed methods was derived from a parcellation according to the Destrieux-Atlas (Destrieux et al., 2010). An individual parcellation was generated from each subject's MRI data set by means of automated parcellation procedures provided by Freesurfer (Fischl et al., 2004). The individual prior models were constructed by selecting regions that are expected to be involved in the early processing of auditory signals and spoken language from each individual parcellation. The following regions were used (on both hemispheres): (1) areas close to or inside the superior temporal gyrus (STG), that means the transversal gyrus (Heschl's gyrus, BA 41, BA 42), the transverse temporal sulcus, planum polare, planum temporale, and the lateral STG; (2) additional areas in the temporal lobe as, i.e. the superior temporal sulcus and the middle temporal gyrus; (3) inferior frontal areas, that means orbital (BA 47), triangular (BA 45), and opercular (BA44) parts of the inferior frontal gyrus, the inferior frontal sulcus, and the lateral orbital sulcus. Major parts of these regions are involved in auditory processing (Fonaryova Key et al., 2005) and spoken language processing (Hickok and Poeppel, 2007, Knösche et al., 2005). The incorporated regions are of course only an approximation for the *true* underlying functional entities. For example, the automatic parcellation procedure is based on the sulcal depth, that means the accuracy of the boundaries is certainly limited. Moreover, some regions as, for instance, the lateral STG might consist of multiple distinct functional entities which are not contained in the prior model. Finally, additional regions (for example the transverse temporal sulcus) were used to account for the uncertainties regarding the course of the boundaries (this was done to ensure that any active region is covered by prior knowledge).

5.2.3 Reconstruction Methods and Assessment Criteria

The inverse solution presented in Eq. 2.13 and the estimate of the source variance defined in Eq. 2.15 are the basis for the analysis of experimental data. The noise covariance matrix C_ϵ and the total data variance $\mathrm{tr}(C_d)$ must be determined in order to solve these equations. These two quantities were estimated at each sample point of the averaged evoked response, separately for EEG and MEG. The data variance was approximated by summing up the squared amplitudes of all channels at each sample point in the averaged evoked response. The computation of C_ϵ was realized as follows: First, the averaged evoked response was subtracted from each single trial. Afterwards, the noise covariance matrix at sample point i was estimated on the basis of the inter-trial signals (see below) of all channels (that means, all inter-trial signals were correlated with each other). The inter-trial signal of channel x at a given sample point i defines as the concatenation of all single-trial amplitudes of channel x at sample point i. $C_\epsilon(i)$ turned out to be ill-conditioned in many cases. Therefore, additional regularization was applied (i.e. $C^*_\epsilon(i) = C_\epsilon(i) + \beta(i)I$, with $C^*_\epsilon(i)$ being the regularized noise covariance matrix and $\beta(i)$ the regularization parameter at sample point i) such that the goodness-of-fit (GOF, see below) of the solution reaches a maximum.

Informed LORETA and WMN (Eq. 2.20) were used for source reconstruction. The source correlation matrix for informed LORETA was determined according to Eq. 3.8. The highest smoothness level was selected for Laplacian regularization (Eq. 3.9). Note that the regularization parameter was individually calculated for each subject.

The reconstruction results were assessed by means of visual inspection and the GOF measure. The GOF defines as

$$\mathrm{GOF}(i) = 1 - \frac{\sum (L\hat{q}(i) - d(i))^2}{\sum d(i)^2}. \tag{5.1}$$

and describes how well the solution at sample point i, i.e. $\hat{q}(i)$, fits the of the averaged evoked response, i.e. $d(i)$, given the physical forward model defined by the leadfield. The value $\mathrm{GOF}(i) = 1$ implies a perfect fit. Smaller values indicate that not all spatial features of the data can be explained with the estimated solution. Good solutions are expected to provide a GOF of 0.8 and higher (Maurits, 2012).

For visual inspection, the absolute values of the estimated source strengths are mapped on each subjects inflated cortical surface. However, not the full spatial distribution but only the main spots of activity are visualized. Main activity is identified by discarding all sources with less than 97 % of the maximum source strength in the given solution. This value was determined from the explorative analysis of all histograms of the source strength. Sources with less than 3 % of the maximum value turned out to be a good approximation of significant activity.

5.3 Results

The analysis presented here focuses on the N100/N100m and P200/P200m component of the averaged evoked response (i.e. with respect to the sentence onset). The peak activity of these components consistently occurred at around 152 ms and 230 ms (median). The particular times for each subject, the number of rejected trials and channels, the estimated signal-to-noise-ratios, and the Laplacian regularization parameters are presented in Tab. 5.1. Figure 5.1-5.4 show the localization results for both components separately for EEG and MEG.

Table 5.1: Subject specific parameters of EEG/MEG data and informed LORETA Laplacian regularization parameters (i.e. for strongest smoothness constraint).

Subject	Peak N100 [ms]	Peak P200 [ms]	SNR N100		SNR P200		No. of rejected epochs		No. of rejected channels		λ_B
			EEG	MEG	EEG	MEG	EEG	MEG	EEG	MEG	
1	150	230	5	15	14	15	18	6	4	4	$1.4\cdot10^{-12}$
2	160	237	15	32	6	7	12	14	2	0	$1.6\cdot10^{-12}$
3	154	222	75	106	14	51	3	0	2	0	$1.6\cdot10^{-12}$
4	149	233	37	64	16	13	21	16	0	15	$1.6\cdot10^{-12}$
5	152	220	102	145	40	29	8	5	1	1	$1.4\cdot10^{-12}$

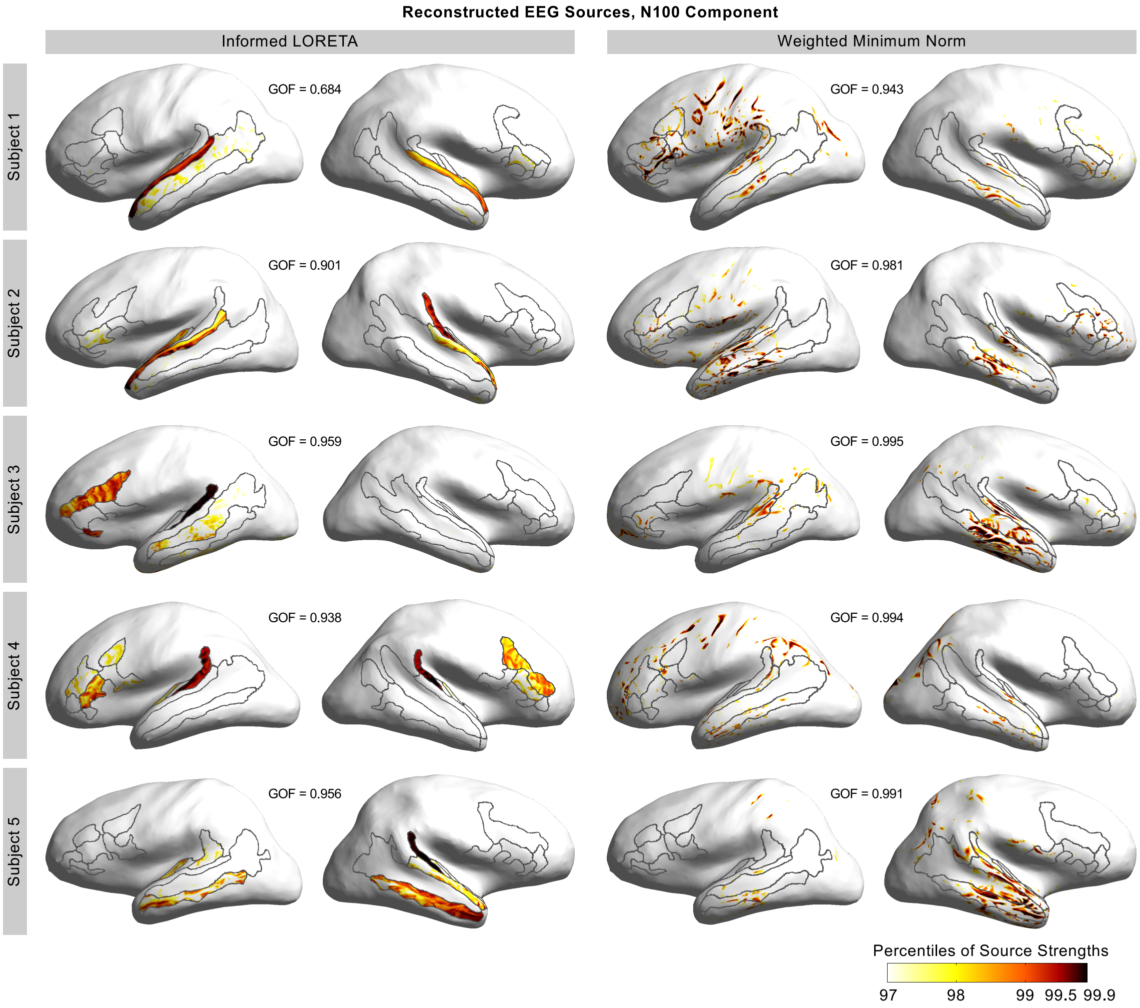

Figure 5.1: Shown are maps of significant N100 source activity on the individual inflated cortical surface derived from EEG data. Significant activity is indicated by the upper three percentiles of the absolute source strengths. Black edges denote prior knowledge.

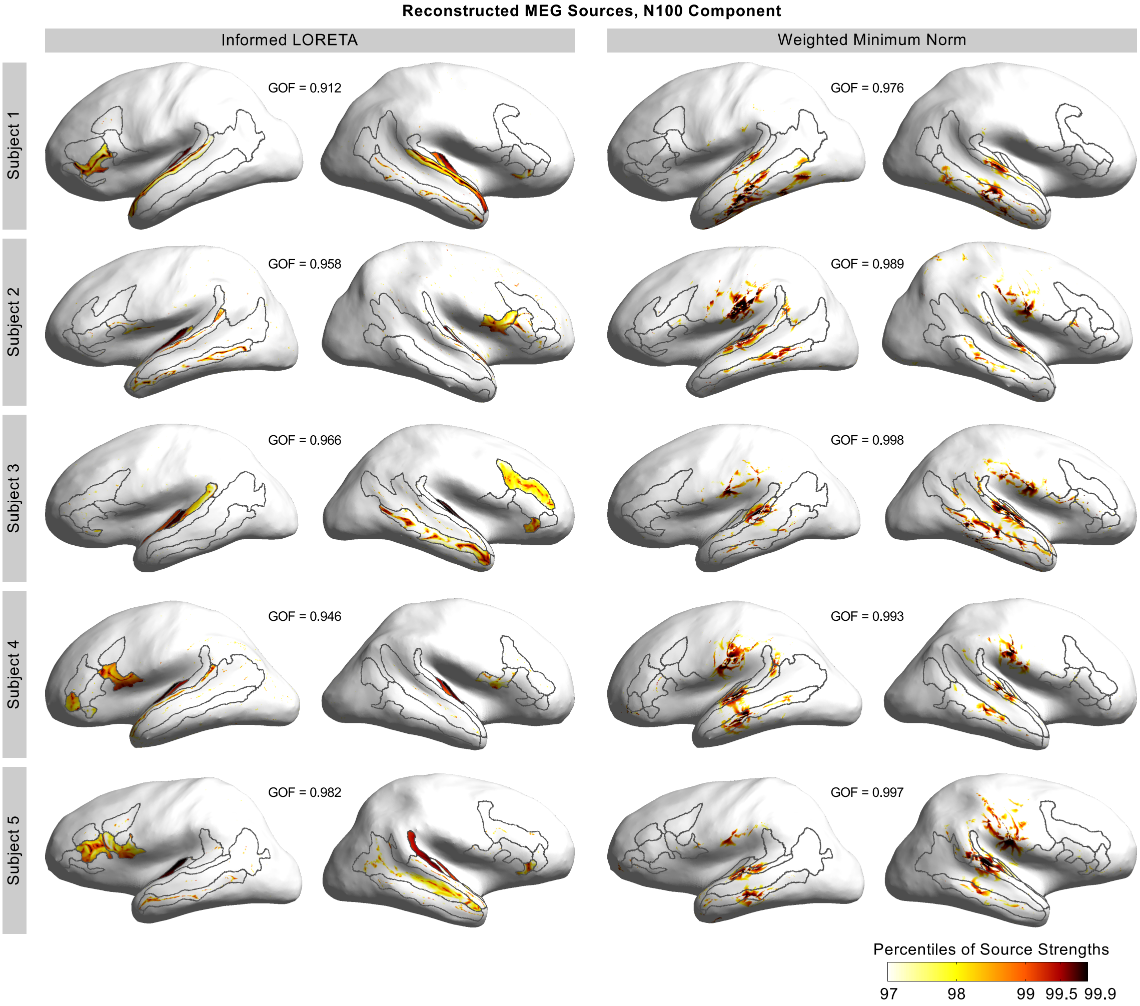

Figure 5.2: Shown are maps of significant N100 source activity on the individual inflated cortical surface derived from MEG data. Significant activity is indicated by the upper three percentiles of the absolute source strengths. Black edges denote prior knowledge.

First, the EEG reconstruction results obtained for the N100 component are considered. The GOF values indicate that the estimated solutions explain a sufficient amount of the data (GOF > 0.9, one exception). The WMN solutions are not very consistent over subjects. They indicate, at best, that main spots are located in the lateral STG (i.e. close to the transverse temporal gyrus) and in the right middle temporal gyrus. Activity on the left hemisphere is inconsistent between subjects and mainly distributed over frontal, central and parietal regions. The reconstructed source patterns for informed LORETA are much more compact, which is a straightforward consequence of the strong smoothness constraint. Likewise to WMN, however, the informed LORETA results are not very consistent over subjects as well. Three subjects exhibit significant activity in right planum temporale and left transverse temporal gyrus. In contrast to WMN, no activity is located outside *a priori* defined regions.

The MEG reconstruction results obtained for the N100 component are much more consistent. Besides that, all solutions explain the data with a GOF of at least 0.91. WMN reveals bilateral activity with main spots in the lateral STG (close to anterior part of planum temporale),

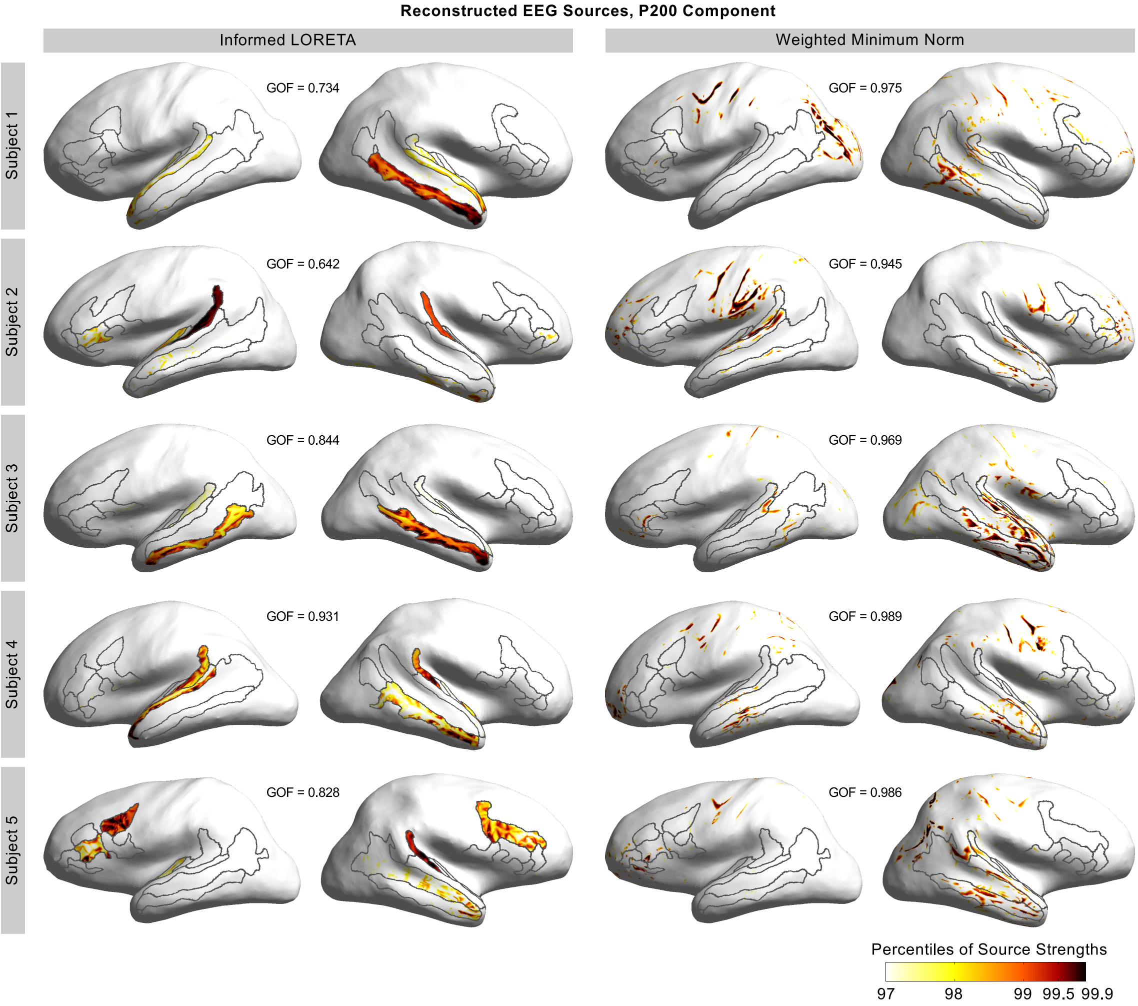

Figure 5.3: Shown are maps of significant P200 source activity on the individual inflated cortical surface derived from EEG data. Significant activity is indicated by the upper three percentiles of the absolute source strengths. Black edges denote prior knowledge.

the middle temporal gyrus, and the central gyrus. It seems obvious that the minimum norm effect projects the STG activity to the two adjacent gyri. As before, informed LORETA results are much more compact. Main spots are located in the left and right transverse temporal gyrus and sulcus, and (for three subjects) along the left lateral STG. Similarly to EEG, inconsistent activity also appears in other *a priori* defined regions but not outside these incorporated areas.

Generators of the N100 component have been reported in the superior temporal plane (Fonaryova Key et al., 2005), particularly in the primary auditory cortex in Heschl's gyrus (Hari et al., 1987), and in planum temporale Knösche et al. (2003). The results presented here are in general agreement to this level of knowledge. Particularly the informed LORETA source distributions obtained from MEG source reconstruction clearly indicate main activity in the transverse temporal gyrus. In contrast, WMN projects the solutions on top of superficial gyri and, therefore, provides no evidence that generators are located in the primary auditory cortex. The EEG results for informed LORETA provide some evidence that sources in planum temporale are active as well.

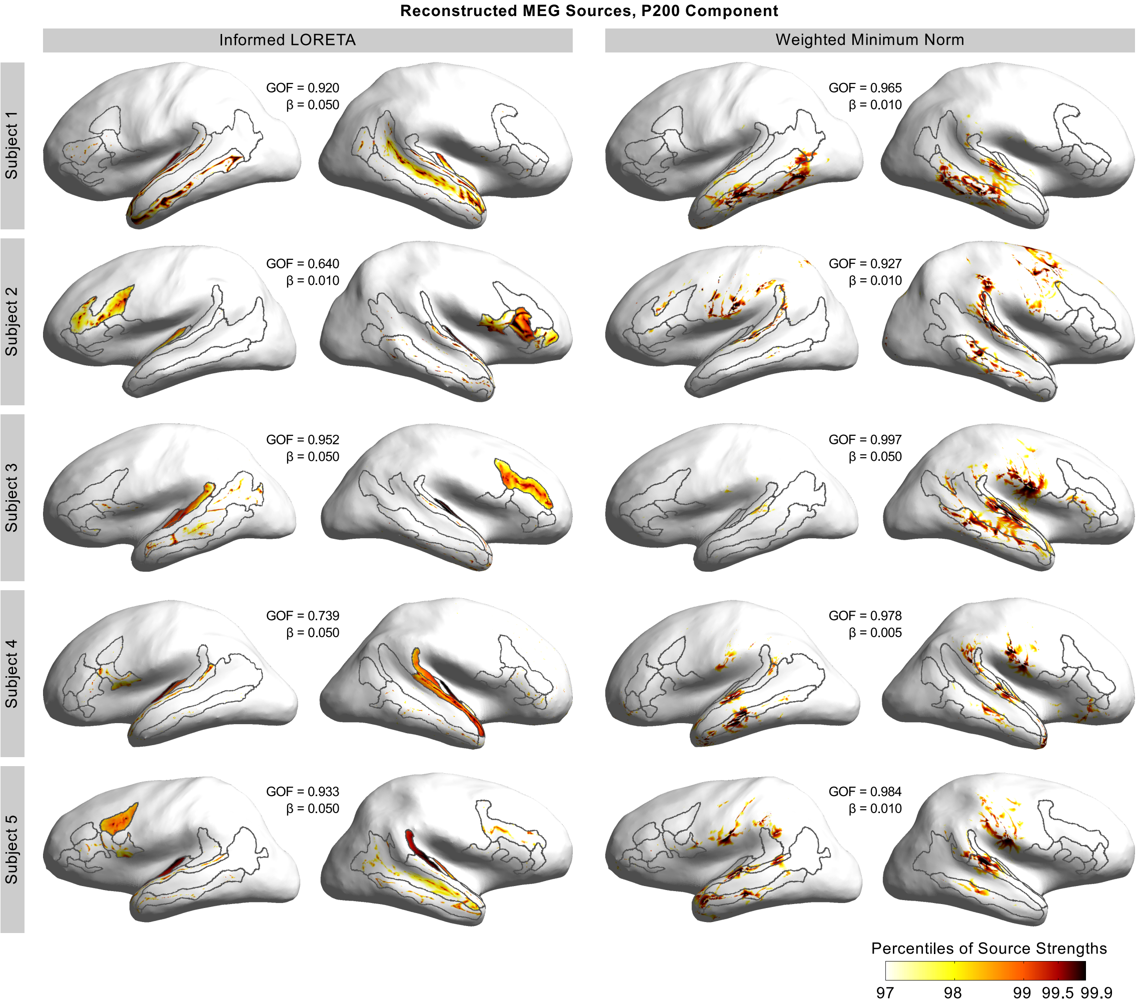

Figure 5.4: Shown are maps of significant P200 source activity on the individual inflated cortical surface derived from MEG data. Significant activity is indicated by the upper three percentiles of the absolute source strengths. Black edges denote prior knowledge.

The next analysis focuses on the P200 component. The GOF values for the EEG solutions are lower in comparison to the results obtained for the N100 component, particularly for informed LORETA. However, the values are still large enough to be considered as acceptable results (except for subject 1, whose GOF is lower 0.8). Like before, the WMN patterns exhibit a rather low consistency over subjects. The activity on the right hemisphere seems to be slightly more anterior in comparison to the N100. A consistent location on the left hemisphere cannot be found. For informed LORETA, a consistent activation in right planum temporale (in 3 of the 5 subjects) and in the anterior part of the right middle temporal gyrus (4 of 5 subjects) can be reported. Activity on the left hemisphere is inconsistent over subjects.

As before, MEG provides much more consistent spatial patterns of significant activity compared to EEG. For WMN, the P200 activity in temporal regions is slightly more distributed compared to the N100. Nonetheless, main spots are located in left and right lateral STG (close to the anterior part of planum temporale and the transverse temporal gyrus), the middle temporal gyrus, and, in most cases, the central gyrus. The informed LORETA results are widely consistent over subjects. The main spots are located in the lateral STG and the transverse temporal gyrus on both hemispheres. The GOF is less than 0.8 for two subjects.

Generators of the P200 component have been reported in the primary and secondary auditory cortices (Fonaryova Key et al., 2005). That means that some generators are slightly more anterior and posterior compared to the N100 component (Bosnyak et al., 2004). As before, particularly the informed LORETA solutions derived from MEG data are in good agreement with expected activity in the primary auditory cortex. In contrast, WMN does not provide sufficient evidence that these regions are active, neither for EEG nor for MEG. The existence of more anterior and/or posterior generators cannot be sufficiently verified on the basis of this data. While this could result from several issues, for instance the experimental design, data quality, uncertainties in prior knowledge, etc., it is of minor importance here. It can be summarized that the incorporation of individual functio-anatomical information into informed LORETA provides evidence on certain generators (i.e. activity in certain areas) of the N100/P200 components. Activity in these areas could not be reconstructed with the uninformed reference methods. This finding is crucial.

5.4 Discussion

In this chapter, informed LORETA and the uninformed reference method WMN were applied to the reconstruction of auditory event-related potentials recorded in a spoken language experiment. The analysis focused on the reconstruction of the N100 and the P200 components. These are supposed to have main generators in primary and secondary auditory cortices (Fonaryova Key et al., 2005). This partially comprises sources in deeper cortical structures, for instance Heschl's gyrus. These deeper regions can only be poorly reconstructed using classical linear inverse methods (e.g. WMN, LORETA). It should be demonstrated that the utilization of functio-anatomical similarity information by means of smoothness based linear inverse algorithms improves source reconstruction. Therefore, source reconstruction was carried out on realistically shaped folded cortical surfaces with high spatial resolution. Prior information was defined on the basis of individual anatomical data and its combination with general knowledge on the likely generators.

The EEG results obtained for the two tested algorithms are rather inconsistent over subjects. In contrast, the source patterns reconstructed from MEG data are widely consistent over subjects. Informed LORETA provides very plausible source distributions because main activity appears in the transverse temporal gyri (i.e. in the primary auditory cortex). This is also very plausible in the light of the WMN results. WMN reconstructs major parts of the activity on top of superficial gyri which are in the vicinity of Heschl's gyrus. This is a clear indication that the true sources might be located in deeper regions (e.g. transverse temporal gyri) which are enclosed by these adjacent gyri. The analysis does not focus on particular details of the N100/P200 components or even on differences between them. The results allow the conclusion that constraints on the correlation structure drawn from individual functio-anatomical prior information might be very helpful for the analysis of auditory evoked EEG/MEG data. Similarly, Cottereau et al. (2012) reported that the use of a functionally informed reconstruction methods (i.e. FACE) improves the localization visually evoked potentials. Besides the fact that informed LORETA and FACE are different according to some aspects, this emphasizes that information on the functional cortex organization is generally suited to improve EEG/MEG source localization of event related potentials.

The reconstruction results for PatchLORETA1 that were presented by Knösche et al. (2013) suggested that the incorporation of functio-anatomical prior knowledge into a local neighborhood-based smoothness operator defined on the folded cortical surface is ineffective. In contrast, the informed LORETA results presented here underpin that it is possible to achieve a significant effect on the reconstruction result by means of this technique (i.e. the combination of prior knowledge with a smoothness operator). In fact, the imposed constraint was even that strong that significant activity was only reconstructed inside *a priori* defined regions but not elsewhere. This, in turn, is actually very similar to the PatchLORETA2 results presented by Knösche and colleagues. The smoothness constraint in PatchLORETA2 is based on a patch neighborhood (i.e. all sources within a functional unit are correlated). These obvious discrepancies between PatchLORETA1 and the informed LORETA approach employed here can be explained with the Laplacian regularization parameter that controls the smoothness constraint. Here, the parameter was adjusted such that a high smoothness level is achieved. This is actually very similar as employing a patch based neighborhood constraint. In their study, the Laplacian regularization parameter for PatchLORETA1 was set to a fixed value. The resulting correlation structure was not considered. However, it is obvious that the selected regularization parameter imposes a smoothness level (i.e. a weak correlation constraint) which is unsuited for the source reconstruction on the folded cortical surface. This is particularly problematic if sources are expected in deeper cortical regions. The problem is that the smoothness constraint (i.e. the constraint on the similarity between reconstruction points) is in a contradiction to the minimum norm constraint imposed by leadfield similarity on the folded cortex. If the correlation constraint is not restrictive enough (which is the case for the fixed Laplacian regularization parameter in PatchLORETA1), it supports the co-activation of long-distant sources, for instance sources located on adjacent gyri. This is consistent with the minimum norm effect and eventually renders the functio-anatomical prior ineffective. Selecting a more restrictive correlation constraint (i.e. a smaller regularization parameter) renders the prior information more effective. Correlations between sources located in distinct functional regions are minimized, while the *a priori* correlation between adjacent sources becomes stronger. It has to be pointed out, however, that a co-activation of far distant sources would still be possible if it is supported by data.

Given that the incorporated areas represent homogeneous functional entities, the results produced by informed LORETA seem to be very plausible. The combination of a small regularization parameter with functio-anatomical boundaries imposes a correlation structure that is in a good agreement with the homogeneous activation of regions. However, this cannot be assumed in general. Particularly in larger areas such as the lateral STG it is likely that a more finegrained functional subdivision must be considered. Moreover, the parcellations employed here are estimated on the basis of certain anatomical properties and it is likely that the extracted boundaries do not exactly match the course of the true functional borders. On the one hand, the derivation of more precise and meaningful prior knowledge from, for example, fMRI could render its use even more powerful. On the other hand, the simulations in last chapter have shown that the incorporation of regions which do not contribute to the EEG/MEG data tends to reduce the reconstruction quality. This emphasizes that the regions that are used as prior information have to be carefully selected. Otherwise, implausible prior assumptions might not only reduce the reconstruction performance but also encourage the reconstruction of spurious sources.

6 Summary and Conclusions

This thesis deals with the reconstruction of neuroelectromagnetic sources from EEG/MEG data by means of spatially informed linear inverse methods. These methods employ so called distributed source models, which usually cover the cortical sheet, and whose free parameter are the source strengths (i.e. current densities). A unique solution to the inverse problem can be derived on the basis of a zero-mean shrinkage prior on the source strengths. This allows to encode independent prior information on the source variances and covariances. However, a reliable derivation of independent information on source variances is usually difficult. For example, it is not sufficiently understood how primary current densities can be inferred from BOLD intensities, which can be drawn from fMRI data. As already argued by Knösche et al. (2013), however, it is quite plausible that similar BOLD signals, similar long-range connectivity patterns, or similar cytoarchitectural properties of neighboring sources imply a certain functional similarity and, therefore, similar neuroelectric activity. This kind of functio-anatomical information can be encoded as *a priori* source correlations.

Recently, two independent studies reported the utilization of functio-anatomical prior knowledge for linear EEG/MEG source reconstruction[1]. The FACE method presented by Cottereau et al. (2012) allows to encode similarity information directly into the source correlation matrix[2]. The similarity information was derived from the separation of the cortex into distinct functional regions (i.e. parcellations). In contrast, PatchLORETA proposed by Knösche et al. (2013) employs a general smoothness assumption that is is lifted at functional boundaries. The boundaries were derived from parcellations as well. The method is essentially based on encoding smoothness between directly neighboring sources if they belong to the same functional region. Otherwise, the smoothness constraint is rejected. Besides the fact that it is only possible to encode binary similarity information (for instance, patch affiliation) into PatchLORETA, it was unclear whether the estimation of the source correlation matrix by means of Laplacian inversion (which is the essential core of this method) actually provides the intended correlation structure. A major subject of this thesis was the extension, the systematic evaluation, and the improvement of PatchLORETA.

The extension of PatchLORETA was presented in chapter 3 of this thesis. It allows the use

---

[1] The principal techniques presented to incorporate this knowledge could also be used with other approaches such as non-linear Bayesian inversion schemes (e.g. Daunizeau et al., 2006, Trujillo-Barreto et al., 2004)

[2] The general possibility to encoding functional information between cortical sources has already been proposed before (see, for instance, Dale and Sereno, 1993).

of more general, i.e. gradual similarity information. The subsequent analysis focussed on the Laplacian inversion based estimation of the source covariance matrix and revealed several issues. First, it turned out that the estimated variance of a source as well as the covariances in its vicinity depend on its geodesic distance to a discontinuity in the general similarity structure (e.g. introduced by functional borders). This effect causes undesired biases as, for instance, the preference of sources in smaller patches compared to large ones. Second, it was shown that in some cases negative entries appear in off-diagonal elements of the covariance matrix. This implies a phase shift of 180°, which is an implausible assumption on the basis of functio-anatomical priors. An additional normalization operator was introduced to ensure equal main diagonal entries in the source covariance matrix. While this effectively removes the bias effect, inhomogeneities in the covariance structure as well as negative covariances remain. However, they turned out to be of minor importance under practical conditions. Another major topic in chapter 3 was the evaluation of Laplacian regularization. It was demonstrated that the regularization is of crucial importance for the estimated source correlation structure. Moreover, a method was introduced that allows an efficient and, more importantly, an objective determination of a suitable parameter. The method indirectly accounts for the spatial resolution of the underlying source space and, finally, provides a dedicated source correlation patterns. The final method is referred to as informed LORETA.

In chapter 4, informed LORETA was evaluated by means of various simulations. A binary similarity measure rather than gradual similarity information was used to keep things simple. Although similarity information was defined on the basis of functional borders drawn from parcellations in most simulations, the use of boundaries drawn from major sulci was also demonstrated. Firstly, the chapter comprised an illustrative demonstration on how such priors actually affect source reconstruction. Secondly, informed linear inverse methods (i.e. informed LORETA and FACE) were evaluated in various simulation scenarios. The evaluation revealed general spatial characteristics of informed linear inverse estimates. Moreover, it provided important information on how the algorithms actually perform using parcellation-based functio-anatomical constraints in various situations. Among other things, the influence of noise, the complexity of activation patterns, and the consistency between prior knowledge and the activation was systematically varied. A main conclusion that can be drawn from the results is that the consistency between incorporated boundaries and the underlying activity is crucial for EEG/MEG source reconstruction. Not only is it important to employ all boundaries that are relevant in the particular condition, but also turned it out to be very helpful to eliminate those boundaries that are not visible in the data. Using boundaries that are not relevant (which might be the case when prior information is derived from a full parcellation) expresses a believe on the source correlation structure that is not supported by EEG/MEG data. For example, the fact that two areas can be separated by means of certain structural properties does not mean that their implicit common boundary is actually visible in the data set, particularly not if the function in these regions is not related to the stimulus used trigger evoked responses. As a result, the limitation to those boundaries which can be expected to contribute to the data seems very reasonable. The use of local parcellations is a step into this direction.

Subject of chapter 5 was the evaluation of informed LORETA for the reconstruction auditory event related potentials. The data used for the analysis was taken from a spoken language experiment. The analysis provided the main conclusion that the use of functio-anatomical prior information produces very plausible reconstruction results, particularly in comparison to uninformed methods. Knösche et al. (2013) reported that the use of smoothness-based prior assumptions (i.e. the incorporation of functio-anatomical prior knowledge into informed LORETA / PatchLORETA) might be less effective on the folded cortical surface. The authors argued that the interaction of the two contradicting constraints (i.e. the minimum norm constraint, which is based on leadfield similarity, and the local smoothness constraint) reduces the impact of prior knowledge. However, the evaluation presented here revealed a strong effect of smoothness-based prior assumptions. The results underpin the importance of Laplacian regularization. In other words, not only the functio-anatomical prior information itself but the effective source correlation structure imposed as a prior must be carefully considered before applying the method.

Likewise to FACE, informed LORETA represents a linear inverse method that constrains the solution by means of the *a priori* source correlation structure. This kind of prior assumption is usually a much weaker constraint than, for instance, restricting the source space to likely active regions (Baillet and Garnero, 1997) or than modulating the source variances with, e.g., BOLD intensities (Babiloni et al., 1998, Liu et al., 1998, Sato et al., 2004). For example, neighboring sources, whose functional similarity is low according to prior knowledge, can be activated independently of each other (i.e. independently of the smoothness constraint) if this is supported by the data. This would not be possible if one of these sources is either not available (i.e if the source is not included in the source space) or has a variance close to zero, which effectively minimizes their chance to be activated.

There are also some general differences between informed LORETA and FACE , which should be pointed out here. The main difference is the fact how the similarity information is actually encoded. While FACE allows to directly encode the correlation structure, informed LORETA is based on the estimation of this structure by means of Laplacian inversion. The Laplacian is used to expresses a general smoothness constraint (i.e. a general similarity assumption) between directly neighboring sources. Prior knowledge interrupts the spatial smoothness assumption at functio-anatomical boundaries. Finally, the Laplacian regularization parameter controls the smoothness constraint (i.e. the spatial extent). As a consequence, informed LORETA fully exploits the sparse nature of the Laplacian. That means that the number of non-zero off-diagonal elements in the Laplacian is independent of the spatial extent of the assumed (expected) spatial correlation. In contrast, FACE is currently based on encoding correlations up to the second order neighborhood. A stronger correlation constraint (i.e. a larger spatial extent) would require the definition of non-zero correlations with additional neighbors. As a result, the sparsity of the source correlation matrix reduces. Another difference is that informed LORETA employs the smoothness constraint everywhere on the cortex, whereas the similarity constraint in FACE is only applied inside functional units, i.e. only inside the patches of a parcellation. Sources are expected to be uncorrelated outside these areas. Note, however, that a stronger smoothness constraint implies a strong contradiction to the leadfield similarity based minimum norm constraint, particularly in large areas. In fact, the potential contradiction mainly depends on the patch size. This might be problematic for the use of local parcellations, which consist of small and large regions (i.e. unlabeled areas). Consequently, solutions in larger regions might be suppressed (however, this could also be intended in order to prefer certain regions for source localization). It is straightforward to propose an extension to informed

LORETA that eliminates this effect in unlabeled areas (see below).

The selection of patches (to generate a local parcellation, i.e. a unique prior model) for a certain experimental paradigm might be difficult in practice. An alternative to select one prior model, that means a certain combination of patches, might be the definition of multiple models and the evaluation of their evidence in the light of the data. This could effectively be done using Bayesian Model Averaging (BMA) (Trujillo-Barreto et al., 2004), which is essentially based on the definition of covariance components. Therefore, the specification of the covariance matrix could be replaced by the technique presented in this work, i.e. the estimation of a source correlation structure on the basis of a functio-anatomically informed Laplacian. Likewise, one could also employ a full parcellation with the Multiple Sparse Priors (MSP) approach (Friston et al., 2008). This non-linear Bayesian source reconstruction scheme is based on weighting several source covariance components based on their plausibility in the light of the data. The components could be derived from each patch in the parcellation (and a certain LORETA-bases smoothness assumption). Theoretically, no manual selection of a plausible prior model would be required. However, if such a more or less automatic prior selection leads to a plausible solution remains an open question.

The use of parcellations is not new and has already been proposed in other linear and non-linear EEG/MEG source reconstruction schemes. For example, Cottereau et al. (2007) described a multi resolution image selection approach. Parcellations, which span the whole cortical sheet, are the basis for an iterative search of an optimal parcellation that constitutes a best fitting source space. Other approaches did not directly employ parcellations but comprise the key assumption that brain activity can be described by correlated activation within several areas of a certain spatial extent (Chowdhury et al., 2013, Daunizeau et al., 2006, Friston et al., 2008). One has to keep in mind that the use of parcellations implies a relative exact knowledge on the location and the course of functional boundaries between neuronal sources. This implies a very high accuracy which, however, can certainly not be drawn from this kind of knowledge for the following reasons. First, assumptions on functional areas are drawn from knowledge on the anatomical structure. This information can only serve as an indicator for functional similarity. Second, the boundaries defined by, e.g., cytoarchitecture are often subtle and gradual (Kaas, 2002), that means not as strict as suggested by parcellations. Third, segmenting parcels on the individual cortical surface (no matter if this is done on the basis of individual anatomical information conducted in-vivo or based on the mapping of generic brain atlases to the cortex) is always prone to errors that might introduce uncertainties into the final parcellation. New techniques such as the hierarchical parcellation of the cortex, which are based on the similarity of long range connectivity patterns (Moreno-Dominguez et al., 2014), are very promising towards a more precise and more individual functional separation of the cortex.

An alternative to the use of parcellations would be the integration of gradual similarity information. For example, such information could be directly derived from the similarity between BOLD signals recorded during fMRI or rsMRI, between cytoarchitecture, or between long-range connectivity patterns. In principle, the extension proposed in this thesis allows to encode gradual mutual similarity information and, therefore, the use of the mentioned measures. The use of gradual information could, however, be problematic for the following reasons. As shown in chapter 3, the effect of prior information depends on the similarity contrast in the neighborhood of a source. Gradual similarity information reduces this contrast (compared to the use of binary information) and, therefore, the impact of prior knowledge on the solution. This effect could render the use of similarity priors ineffective with informed LORETA. A low similarity contrast might also imply a rather implausible correlation structure since it encourages long range correlations. Finally, the results presented in this thesis clearly indicate that even the use of binary similarity measures can lead to rather complex source correlation structures which are sometimes hard to predict. However, it is important to imagine the source correlation structure that may arise from the combination of prior knowledge with a smoothness assumption. Otherwise, a practical application of the method would be difficult. This might become even worse for gradual priors.

The informed LORETA method presented in this thesis can be extended in various ways, particularly with respect to the use of parcellations. First, it is straightforward to introduce an additional diagonal operator. Similarly to the already existing diagonal matrix which performs depth normalization, another diagonal matrix could be used to weight sources according to their plausibility of being active in the particular data set. This corresponds to the *a priori* definition of source variances. In fact, this would lead to a similar method as the *combined FACE* approach, which was also proposed by Cottereau et al. (2012). Increasing the weight for a particular source would lower its variance and vice versa. As already stated above, however, this is a more restrictive strategy than only defining similarity priors (i.e. correlation priors). Second, the Laplacian could be modified in a way that the general smoothness constraint between sources is only applied if they are located in a labeled area, that means in a patch of the parcellation. Otherwise, the off-diagonal elements can be set to zero, which leads to a diagonal weighting in this area, i.e. a minimum norm constraint. Moreover, one could even think about employing a regularization vector for the Laplacian rather than a unique regularization parameter. The entries of the vector could be used to encode the strength of the smoothness constraint separately for each patch. For example, this would allow to apply a much weaker smoothness constraint in unlabeled areas compared to other regions (i.e. patches). This way, the smoothness constraint in unlabeled areas could be reduced to a meaningful level. Finally, this would be an effective strategy to suppress the potential punishment of sources that was already discussed earlier in this work. Third, it is also straightforward to combine informed LORETA with the PatchLORETA2 approach. This allows to introduce a smoothness constraint between sources which are not directly connected in the underlying grid structure. This is the basis for incorporating inter-area correlations between functionally related regions.

Altogether, the results presented in this thesis emphasize that functio-anatomical priors can be incorporated into a smoothness-based linear inversion scheme in a very effective way. The technique seems suited to provide EEG/MEG source reconstruction results that are much more plausible compared to uninformed methods.

Appendix A Laplacian Inversion based Source Covariance Estimates

A.1 Occurrence of Negative Covariances

This section relates to the estimation of the normalized source covariance matrix $R_s = (B^T B + \lambda_B I)^{-1}$ (cmp. Sec. 3.3). It is shown that the regularization of the Laplacian can lead to a negative covariance $R_{s_{ij}}$ if the corresponding matrix element B_{ij} is zero. The effect is demonstrated using a test example.

Given is an annular grid consisting of $m = 4$ nodes. According to Eq. 3.1, and under the assumption that $\gamma_{ij} = 1 \;\; \forall i, j = 1 \dots m, \;\; i \neq j$, i.e. uniform geometrical properties, the Laplacian defines as

$$B = \begin{pmatrix} -1 & \frac{\mathrm{p}_{12}}{\mathrm{p}_{12}+\mathrm{p}_{14}} & 0 & \frac{\mathrm{p}_{14}}{\mathrm{p}_{12}+\mathrm{p}_{14}} \\ \frac{\mathrm{p}_{21}}{\mathrm{p}_{21}+\mathrm{p}_{23}} & -1 & \frac{\mathrm{p}_{23}}{\mathrm{p}_{21}+\mathrm{p}_{23}} & 0 \\ 0 & \frac{\mathrm{p}_{32}}{\mathrm{p}_{32}+\mathrm{p}_{34}} & -1 & \frac{\mathrm{p}_{34}}{\mathrm{p}_{32}+\mathrm{p}_{34}} \\ \frac{\mathrm{p}_{41}}{\mathrm{p}_{41}+\mathrm{p}_{43}} & 0 & \frac{\mathrm{p}_{43}}{\mathrm{p}_{41}+\mathrm{p}_{43}} & -1 \end{pmatrix}.$$

The structure of this matrix is representative for all Laplacians used in this work. Therefore, the conclusion which can be drawn from this example can easily be generalized for all invoked Laplacians.

First, the Laplacian for uninformed LORETA is considered. That means that the uniform similarity $p_{ij} = 1 \;\; \forall i, j = 1 \dots m, \;\; i \neq j$ is assumed between neighbors . Then, B simplifies and the matrix to be inverted writes as

$$B^T B + \lambda_B I = \begin{pmatrix} \lambda_B + 1.5 & -1 & 0.5 & -1 \\ -1 & \lambda_B + 1.5 & -1 & 0.5 \\ 0.5 & -1 & \lambda_B + 1.5 & -1 \\ -1 & 0.5 & -1 & \lambda_B + 1.5 \end{pmatrix}.$$

The explicit calculation of the inverse, for example using the adjoint method (i.e. the inverse of matrix A defines as $A^{-1} = 1/\det(A) \cdot \operatorname{adj}(A)$; see, e.g., Sharma (2004, p. 191)), yields the solution

$$R_s = \frac{1}{\lambda_B^4 + 6\lambda_B^3 + 9\lambda_B^2 + 4\lambda_B}$$

$$\times \begin{pmatrix} \begin{array}{c}\lambda_B^3 + 4.5\lambda_B^2 + \\ 4.5\lambda_B + 1\end{array} & \lambda_B^2 + 2\lambda_B + 1 & -0.5\lambda_B^2 + 0.5\lambda_B + 1 & \lambda_B^2 + 2\lambda_B + 1 \\ \lambda_B^2 + 2\lambda_B + 1 & \begin{array}{c}\lambda_B^3 + 4.5\lambda_B^2 + \\ 4.5\lambda_B + 1\end{array} & \lambda_B^2 + 2\lambda_B + 1 & -0.5\lambda_B^2 + 0.5\lambda_B + 1 \\ -0.5\lambda_B^2 + 0.5\lambda_B + 1 & \lambda_B^2 + 2\lambda_B + 1 & \begin{array}{c}\lambda_B^3 + 4.5\lambda_B^2 + \\ 4.5\lambda_B + 1\end{array} & \lambda_B^2 + 2\lambda_B + 1 \\ \lambda_B^2 + 2\lambda_B + 1 & -0.5\lambda_B^2 + 0.5\lambda_B + 1 & \lambda_B^2 + 2\lambda_B + 1 & \begin{array}{c}\lambda_B^3 + 4.5\lambda_B^2 + \\ 4.5\lambda_B + 1\end{array} \end{pmatrix}.$$

It can be seen that the elements $R_{s_{13}}$, $R_{s_{24}}$, $R_{s_{31}}$, and $R_{s_{42}}$ can become negative if $\lambda_B > 0$ exceeds a certain threshold. Note that these are the same elements which are zero in the Laplacian, i.e. $B_{13} = B_{24} = B_{31} = B_{42} = 0$. This procedure was replicated for examples with $m > 4$ nodes and it turned out that, indeed, each zero element in B can become negative in R_S.

To verify that this also holds for informed LORETA, another Laplacian is constructed by assuming that $p_{12} = p_{21} = 0$, and $p_{ij} = 1$ for all other similarities. This leads to the Laplacian

$$B = \begin{pmatrix} -1 & 0 & 0 & 1 \\ 0 & -1 & 1 & 0 \\ 0 & 0.5 & -1 & 0.5 \\ 0.5 & 0 & 0.5 & -1 \end{pmatrix},$$

and the expression

$$B^T B + \lambda_B I = \begin{pmatrix} \lambda_B + 1.25 & 0 & 0.25 & -1.5 \\ 0 & \lambda_B + 1.25 & -1.5 & 0.25 \\ 0.25 & -1.5 & \lambda_B + 2.25 & -1.0 \\ -1.5 & 0.25 & -1.0 & \lambda_B + 2.25 \end{pmatrix}.$$

Finally, the inverse for this informed LORETA example is given by

$$R_s = \frac{1}{\lambda_B^4 + 7\,\lambda_B^3 + 12.25\,\lambda_B^2 + 2.5\,\lambda_B} \times \begin{pmatrix} \lambda_B^3 + 5.75\,\lambda_B^2 + 7.375\,\lambda_B + 0.625 & 0.625 - 0.75\,\lambda_B & -0.25\,\lambda_B^2 + 0.625\,\lambda_B + 0.625 & 1.5\,\lambda_B^2 + 5\,\lambda_B + 0.625 \\ 0.625 - 0.75\,\lambda_B & \lambda_B^3 + 5.75\,\lambda_B^2 + 7.375\,\lambda_B + 0.625 & 1.5\,\lambda_B^2 + 5\,\lambda_B + 0.625 & -0.25\,\lambda_B^2 + 0.625\,\lambda_B + 0.625 \\ -0.25\,\lambda_B^2 + 0.625\,\lambda_B + 0.625 & 1.5\,\lambda_B^2 + 5\,\lambda_B + 0.625 & \lambda_B^3 + 4.75\,\lambda_B^2 + 4.875\,\lambda_B + 0.625 & \lambda_B^2 + 1.75\,\lambda_B + 0.625 \\ 1.5\,\lambda_B^2 + 5\,\lambda_B + 0.625 & -0.25\,\lambda_B^2 + 0.625\,\lambda_B + 0.625 & \lambda_B^2 + 1.75\,\lambda_B + 0.625 & \lambda_B^3 + 4.75\,\lambda_B^2 + 4.875\,\lambda_B + 0.625 \end{pmatrix}.$$

Now, the elements $R_{s_{12}}$ and $R_{s_{21}}$ can become negative in addition to $R_{s_{13}}$, $R_{s_{24}}$, $R_{s_{31}}$, and $R_{s_{42}}$. Again, the test was repeated several times for grids with $m > 4$ nodes. The result was always the same.

In a last test it should be examined if an element in R_s can be negative if its corresponding value in B is non-zero. For the examples above, this is obviously not possible. It could only be the case if the similarity contrast in a certain neighborhood exceeds some threshold. Therefore, the previous example was slightly modified. Now, the similarities $0 < p_{12} = p_{21} < 1$ were varied until the elements $R_{s_{12}}$ and $R_{s_{21}}$ only contained positive terms. Here, this was the case for $p_{12} = p_{21} > 0.1386$, which corresponds to a similarity contrast of $p_{13}/p_{12} \approx 7.22$. Hence, if the similarity to a neighbor is week with respect to all other neighbors, the covariance can be negative as well and the effect is not exclusively limited to zero elements in B.

The overall conclusion of this section is that covariances $R_{s_{ij}}$ between sources i and j can become negative if they have only a week or even no connection. In realistic problems, the number of sources which are not directly connected is huge in comparison to those which share a connection. For example, on a triangulated grid with 250 000 nodes and one source per node, each source is typically connected to 6 – 7 neighbors. This means that actually a huge number of elements in each row of R_s can become negative. The question under which conditions this can occur and whether this is problematic is subject of Sec. 3.3.

Appendix B Supplementary Material to MC Simulations

B.1 Laplacian Regularization Parameters for MC simulations

B.1.1 Informed LORETA Parameters for Full Parcellations

The following table lists Laplacian regularization parameters for informed LORETA. The parameters were used to adjust the smoothness level (cmp Eq. 3.9) in the simulations (in Sec. 4.4-4.6) which employed artificially generated full parcellations. See Sec. 4.2.3 for details on the parcellations and for the abbreviations used here.

Table B.1: Informed LORETA regularization parameters (λ_B) for full parcellations

		Smoothness Level					
		0.99	0.8	0.6	0.4	0.2	0.01
Parcellation	HP4	3.3×10^{-8}	1.4×10^{-6}	5.3×10^{-6}	2.0×10^{-5}	1.4×10^{-4}	7.9×10^{-2}
	HP8	1.1×10^{-8}	3.7×10^{-7}	1.4×10^{-6}	5.4×10^{-6}	3.8×10^{-5}	2.5×10^{-2}
	HP18	2.1×10^{-9}	7.4×10^{-8}	2.8×10^{-7}	1.1×10^{-6}	7.8×10^{-6}	6.0×10^{-3}
	HP26	1.2×10^{-9}	3.6×10^{-8}	1.3×10^{-7}	4.9×10^{-7}	3.6×10^{-6}	3.2×10^{-3}
	HP37	5.5×10^{-10}	1.7×10^{-8}	5.9×10^{-8}	2.2×10^{-7}	1.6×10^{-6}	1.5×10^{-3}
	HP56	2.3×10^{-10}	7.8×10^{-9}	2.8×10^{-8}	1.0×10^{-7}	7.1×10^{-7}	7.1×10^{-4}
	HP82	9.8×10^{-11}	3.2×10^{-9}	1.2×10^{-8}	4.1×10^{-8}	2.8×10^{-7}	3.2×10^{-4}
	IP1	2.4×10^{-10}	7.9×10^{-9}	3.2×10^{-8}	1.3×10^{-7}	9.6×10^{-7}	1.1×10^{-3}
	IP2	2.4×10^{-10}	7.8×10^{-9}	3.0×10^{-8}	1.2×10^{-7}	9.6×10^{-7}	1.1×10^{-3}
	IP3	2.6×10^{-10}	8.7×10^{-9}	3.4×10^{-8}	1.3×10^{-7}	1.0×10^{-6}	1.1×10^{-3}

B.1.2 Informed LORETA Parameters for Local Parcellations

Table B.2 contains Laplacian regularization parameters for informed LORETA. The parameters were used for the simulations with local parcellations in Sec. 4.5. See Sec. 4.5.2 for details on the parcellations and for the abbreviations used here.

Table B.2: Informed LORETA regularization parameters (λ_B) for local parcellations

		Smoothness Level					
		0.99	0.8	0.6	0.4	0.2	0.01
Parcellation	LP1a	3.0×10^{-12}	8.1×10^{-11}	2.6×10^{-10}	7.8×10^{-10}	3.6×10^{-9}	2.3×10^{-6}
	LP1b	3.0×10^{-12}	8.1×10^{-11}	2.6×10^{-10}	7.6×10^{-10}	3.6×10^{-9}	2.3×10^{-6}
	LP1c	2.8×10^{-12}	7.8×10^{-11}	2.5×10^{-10}	7.8×10^{-10}	3.7×10^{-9}	2.5×10^{-6}
	LP1d	2.9×10^{-12}	7.8×10^{-11}	2.5×10^{-10}	7.4×10^{-10}	3.6×10^{-9}	2.5×10^{-6}
	LP1e	2.9×10^{-12}	7.8×10^{-11}	2.5×10^{-10}	7.2×10^{-10}	3.6×10^{-9}	2.4×10^{-6}
	LP2a	2.7×10^{-12}	7.4×10^{-11}	2.4×10^{-10}	7.4×10^{-10}	3.6×10^{-9}	2.5×10^{-6}
	LP2b	3.0×10^{-12}	8.1×10^{-11}	2.6×10^{-10}	7.6×10^{-10}	3.6×10^{-9}	2.5×10^{-6}
	LP2c	2.5×10^{-12}	6.9×10^{-11}	2.3×10^{-11}	7.4×10^{-10}	3.7×10^{-9}	2.9×10^{-6}
	LP2d	2.6×10^{-12}	7.2×10^{-11}	2.4×10^{-10}	7.4×10^{-10}	3.7×10^{-9}	2.9×10^{-6}
	LP2e	2.5×10^{-12}	6.8×10^{-11}	2.2×10^{-10}	6.9×10^{-10}	3.6×10^{-9}	2.8×10^{-6}

B.1.3 Uninformed LORETA Laplacian Regularization Parameters

The following table lists Laplacian regularization parameters for uninformed LORETA. The parameters were used to adjust the smoothness level (cmp Eq. 3.9) in the simulations in Sec. 4.5-4.6.

Table B.3: Laplacian regularization parameters (λ_B) for uninformed LORETA

Smoothness Level					
0.99	0.8	0.6	0.4	0.2	0.01
3.2×10^{-12}	8.5×10^{-11}	2.7×10^{-10}	7.9×10^{-10}	3.6×10^{-9}	2.2×10^{-6}

B.2 Additional Simulation Results to Section 4.4

B.2.1 Influence of the Spatial Extent of Simulated Activity inside Patches

The analysis in Sec. 4.4 revealed that AUC values obtained for informed LORETA with smoothness level 0.2 and higher depend on the ratio between patch and cluster size. It is analyzed here whether a similar relation can also be found for the COR metric. For details on the simulation setup see Sec. 4.4. Figure B.1 shows the correlations (COR) between simulated and reconstructed source distributions. All distributions are statistically different from each other ($N = 35\,000$ samples per method, $P < 1 \times 10^{-6}$). A bias effect at small ratios (i.e. values less than 0.1) was observed for the AUC measure. Obviously, this is not the case here. This can be explained with the fact that the COR metric is based on the comparison of simulated and

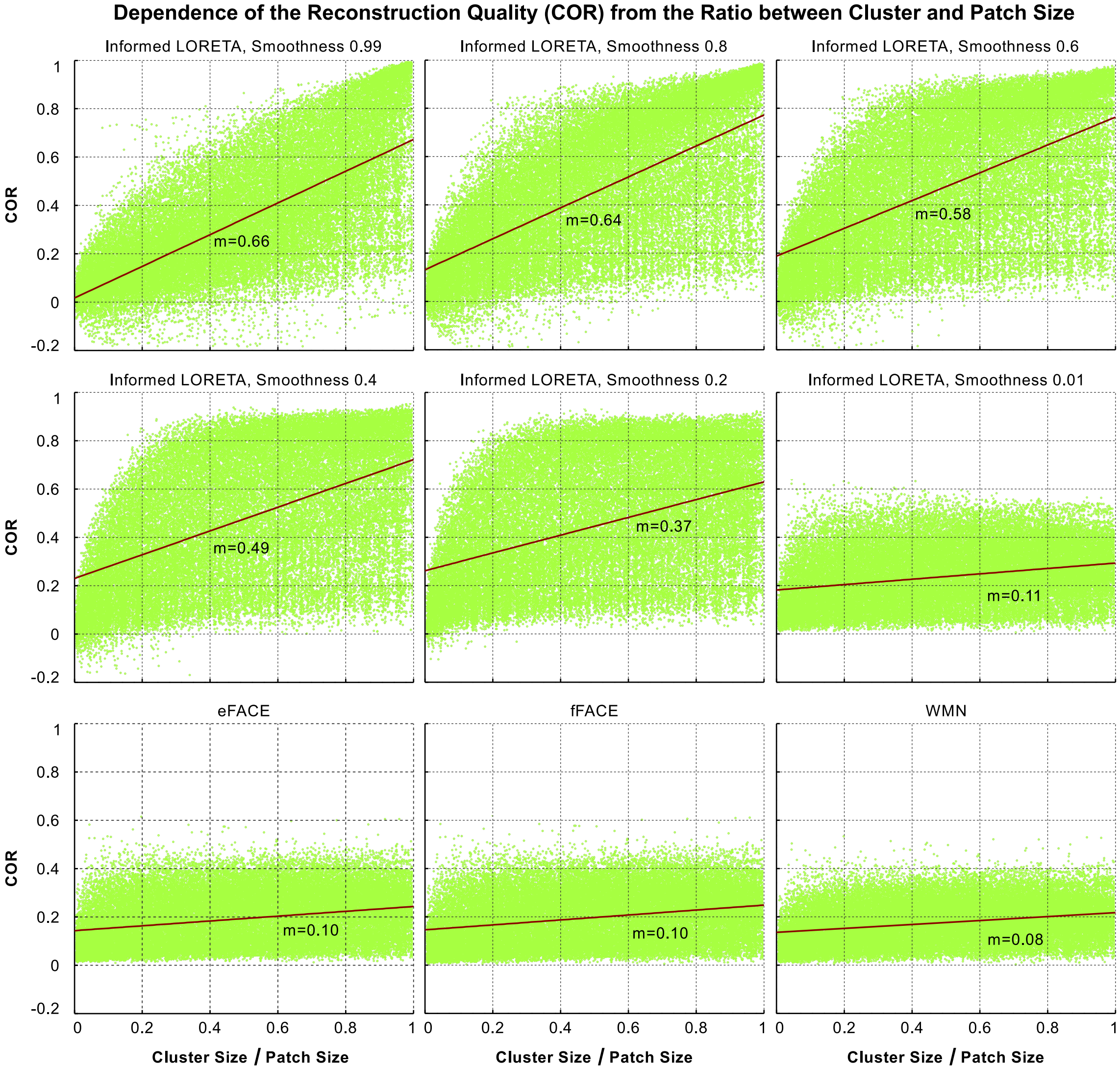

Figure B.1: Scatter plots of the COR metric (green dots) derived on the basis of homogeneous parcellations. Red lines are derived from a linear fit of the observations, values close to the lines denote the slopes. Axis labels apply to all figures in a row/column. See text for details (Sec. B.2.1).

reconstructed activity for all sources rather than on comparing only a small subset of sources (cmp. Sec. 4.4 on p. 78). Thus, the metric is much less sensitive to the mislocalization of tiny clusters, which were supposed to cause this bias. Among this, the results presented here confirm the dependence of the reconstruction quality from the ratio between cluster and patch size for informed LORETA with smoothness level 0.2 and higher.

B.3 Additional Simulation Results to Section 4.5

B.3.1 Scenario 1: Prior Consistent Activation

The results presented in this section refer to the performance analysis of informed linear inverse methods given a prior consistent activation (see 4.5.3.1). Details on the objective and the simulation setup can be found in Sec. 4.5.1 and 4.5.2.

Influence of the noise level, full parcellations: Figure B.2 shows the reconstruction quality with respect to the SNR level given that two clusters are concurrently active for data genera-

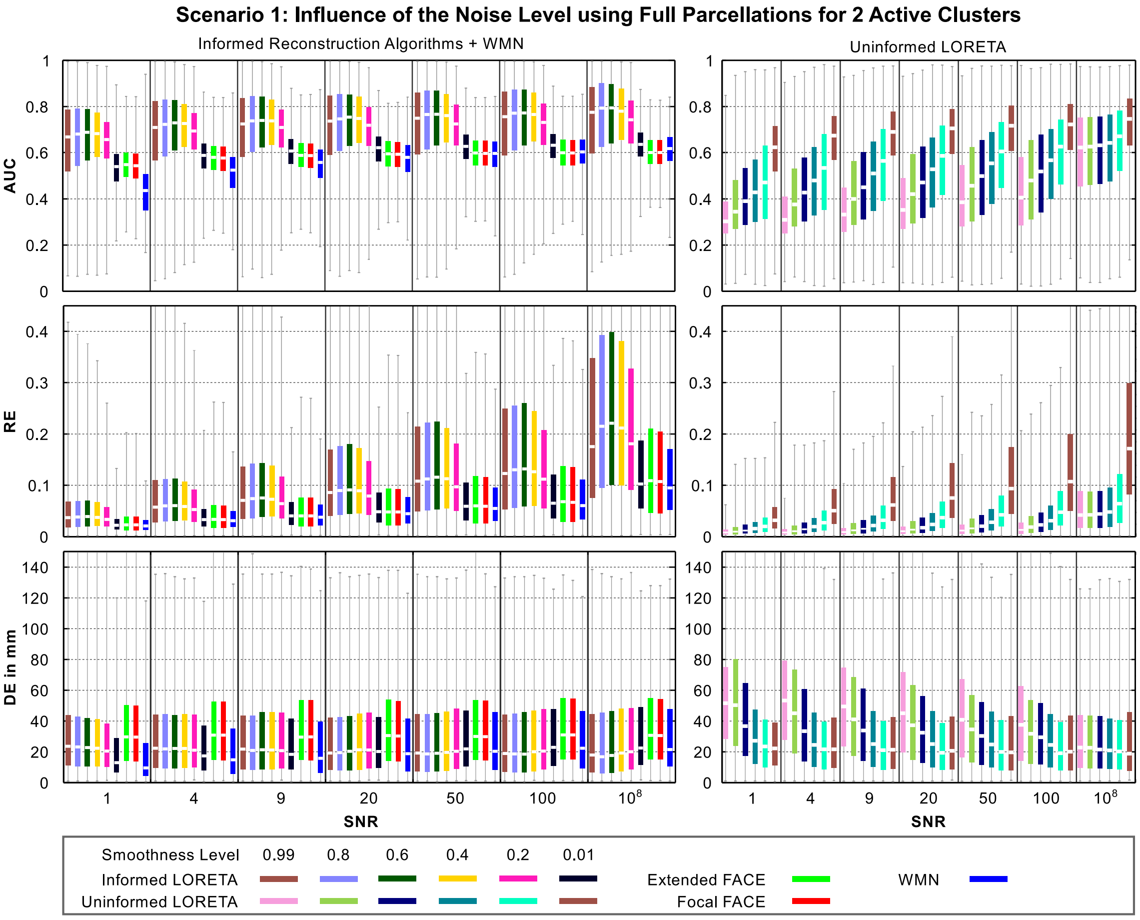

Figure B.2: Performance of informed and uninformed linear reconstruction methods with respect to the noise level. Prior information was derived from full parcellations, two separate clusters were activated. The activation was consistent with the boundaries. See page 82 for details on the box plots.

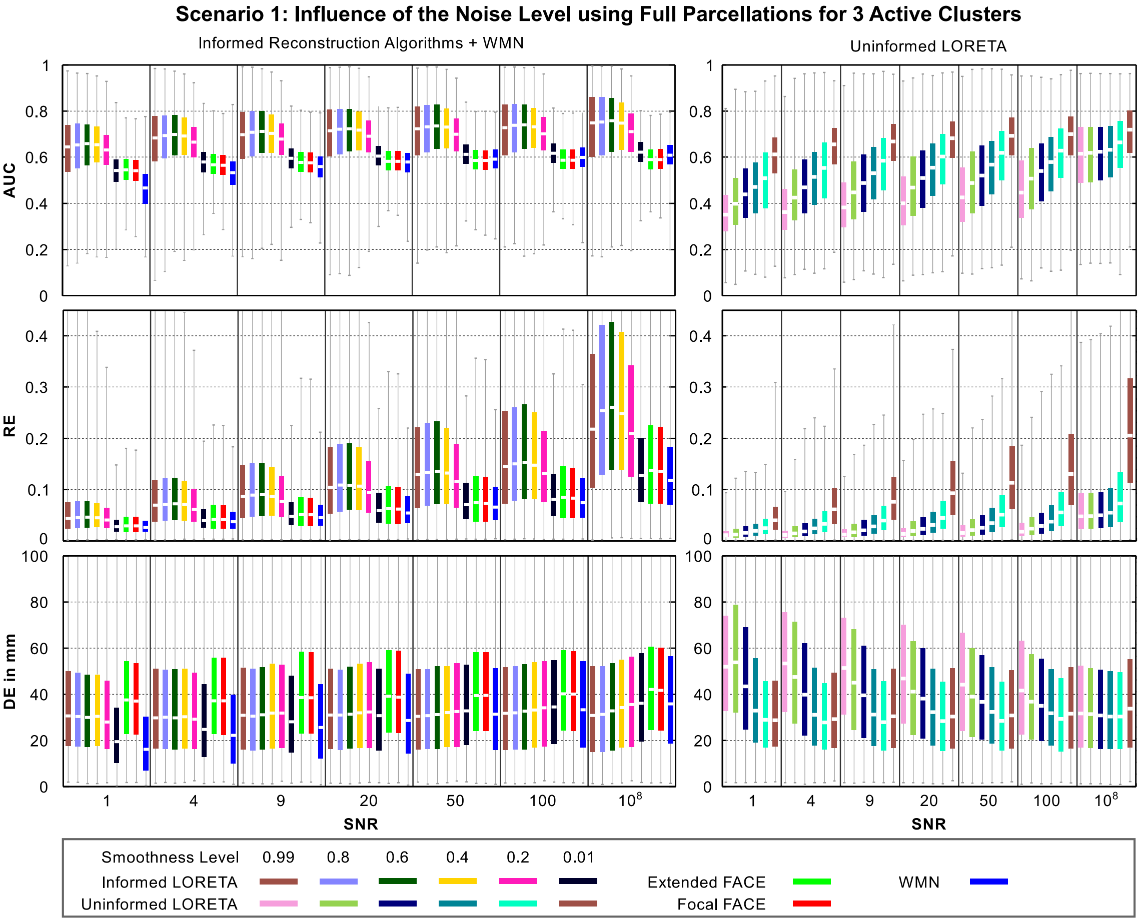

Figure B.3: Performance of informed and uninformed linear reconstruction methods with respect to the noise level. Prior information was derived from full parcellations, three separate clusters were activated. The activation was consistent with the boundaries. See page 82 for details on the box plots.

tion. Full parcellations were employed as prior knowledge. Likewise, Fig. B.3 shows the results for three concurrently active clusters. The main conclusions are as follows. AUC and RE measures improve for higher SNR levels for all methods, whereas DE seems to be relatively constant (i.e. except for uninformed LORETA with high smoothness levels). This is similar to simulations with one active cluster. Informed LORETA with smoothness level 0.2 and higher generally outperforms WMN according to AUC (for 2 clusters: $P < 1 \times 10^{-8}$; for 3 clusters: $P < 1 \times 10^{-6}$) and RE ($P < 1 \times 10^{-2}$ for 2 and 3 active clusters). For DE, the results of informed LORETA and WMN are in a very similar range. In fact, many of the distributions are statistically similar. The performance of FACE is very different. The AUC is consistently higher for SNR levels up to 20 ($P < 1 \times 10^{-2}$) and becomes more and more similar to the WMN results towards a better signal-to-noise ratio. The RE distributions exhibit a similar median but a larger variance (for 2 clusters: $P < 1 \times 10^{-7}$; for 3 clusters: $P < 1 \times 10^{-8}$) compared to WMN distributions. Moreover, FACE is inferior to WMN with respect to the DE metric (for 2 clusters: $P < 1 \times 10^{-8}$, for 3 clusters: $P < 1 \times 10^{-6}$). Finally, uninformed LORETA results for smoothness level 0.2 and higher are inferior to WMN (AUC: $P < 1 \times 10^{-8}$, RE: $P < 1 \times 10^{-8}$, DE: $P < 2 \times 10^{-2}$). In contrast, uninformed LORETA for level 0.01, which employs a very weak correlation constraint, outperforms WMN according to AUC (for 2 clusters: $P < 1 \times 10^{-8}$; for 3 clusters: $P < 1 \times 10^{-6}$) and RE ($P < 1 \times 10^{-2}$). All results are generally consistent with the findings revealed for simulations with one active cluster.

Relative strength between multiple clusters: Figure B.4 displays the reconstruction quality with respect to the relative strength between the weakest and the strongest cluster when three active clusters are activated. The AUC and the RE metric seem to be largely independent from this parameter. This in accordance with the results for two active clusters presented in Sec. 4.5.3.1. At best, a minor reduction of RE can generally be observed towards a more balanced activation. Informed LORETA with smoothness level 0.2 and higher outperforms WMN according to AUC ($P < 1 \times 10^{-8}$) and RE ($P < 1 \times 10^{-8}$). The DE results of both methods are similar. Informed LORETA with smoothness level 0.01 provides a slightly better AUC ($P < 1 \times 10^{-7}$) and very similar results for the two other measures. The AUC results obtained for the two FACE methods are similar to WMN. The localization error is significantly larger ($P < 1 \times 10^{-8}$). The

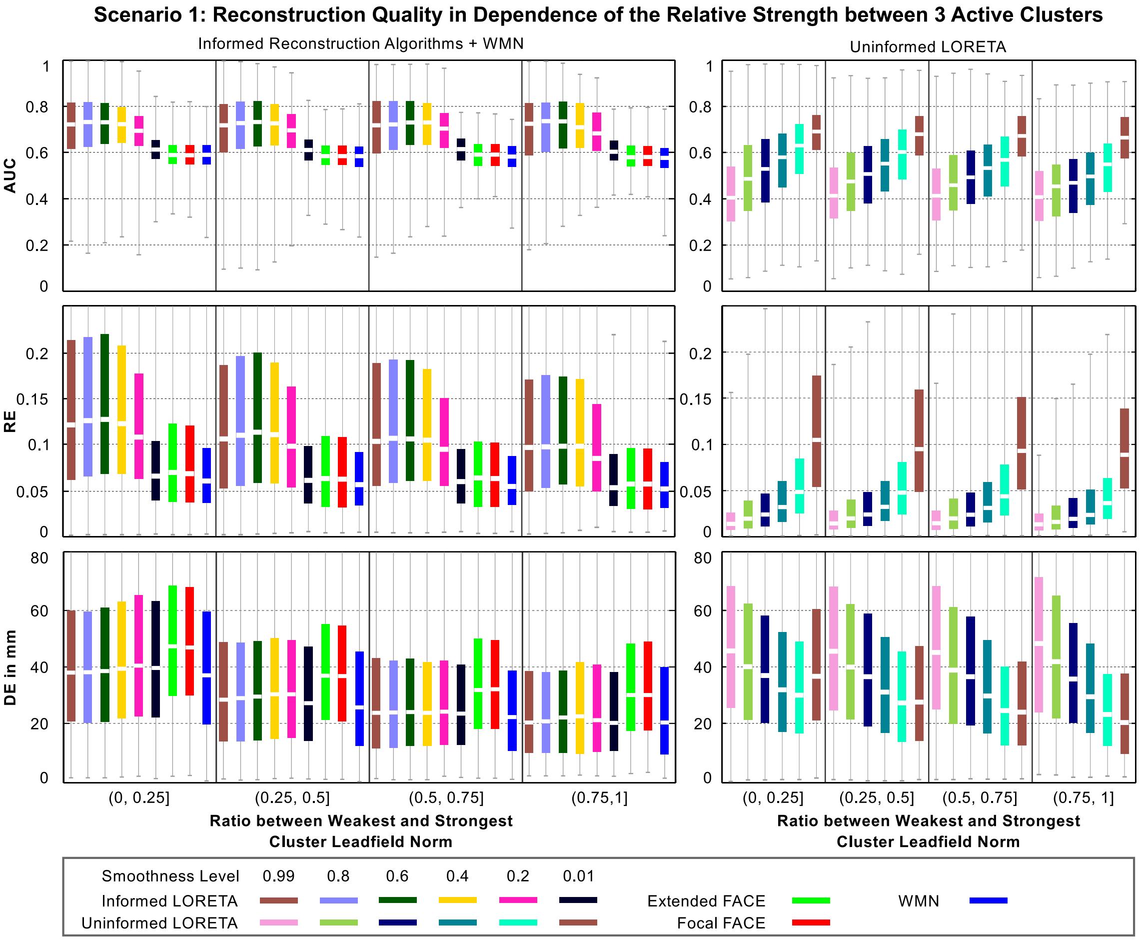

Figure B.4: Performance of localization methods with respect to the ratio between weakest and strongest cluster for three active clusters. The measures are grouped according to four ratio intervals. Prior information was derived from full parcellations, three clusters were activated. The activation was consistent with the boundaries. The results are integrated over SNR levels 9, 20, 50, and 100. See page 82 for details on the box plots. Details on the cluster strength ratio are given in the text on page 83.

corresponding RE distributions are characterized by a significantly higher median but also by a larger variance ($P < 1 \times 10^{-2}$). In summary, all results are consistent to the results obtained for two activated clusters.

Influence of the noise level, local parcellations: Figure B.5 shows the reconstruction quality with respect to the SNR level given that two clusters are concurrently active for data generation. Here, local parcellations were employed as prior knowledge. Likewise, Fig. B.6 shows the results for three concurrently active clusters. Obviously, the AUC generally increases for a higher signal-to-noise levels. For the two FACE methods, however, a rather stable distribution independent of the SNR can be observed. WMN is consistently outperformed by informed LORETA with smoothness level 0.99 ($P < 1 \times 10^{-8}$) and 0.01 ($P < 1 \times 10^{-8}$), eFACE ($P < 1 \times 10^{-8}$), fFACE (for 2 clusters: $P < 1 \times 10^{-8}$, for 3 clusters: $P < 1 \times 10^{-5}$), and uninformed LORTEA with level 0.01 ($P < 1 \times 10^{-8}$). The RE metric generally improves for higher SNR levels. WMN is outperformed by informed LORETA 0.99 ($P < 1 \times 10^{-8}$), informed LORETA 0.01 for SNR above 9 (for 2 clusters: $P < 1 \times 10^{-3}$, for 3 clusters: $P < 4 \times 10^{-2}$), eFACE ($P < 1 \times 10^{-8}$), fFACE ($P < 1 \times 10^{-8}$), and uninformed LORETA 0.01 ($P < 1 \times 10^{-8}$). As for one active cluster, the performance of

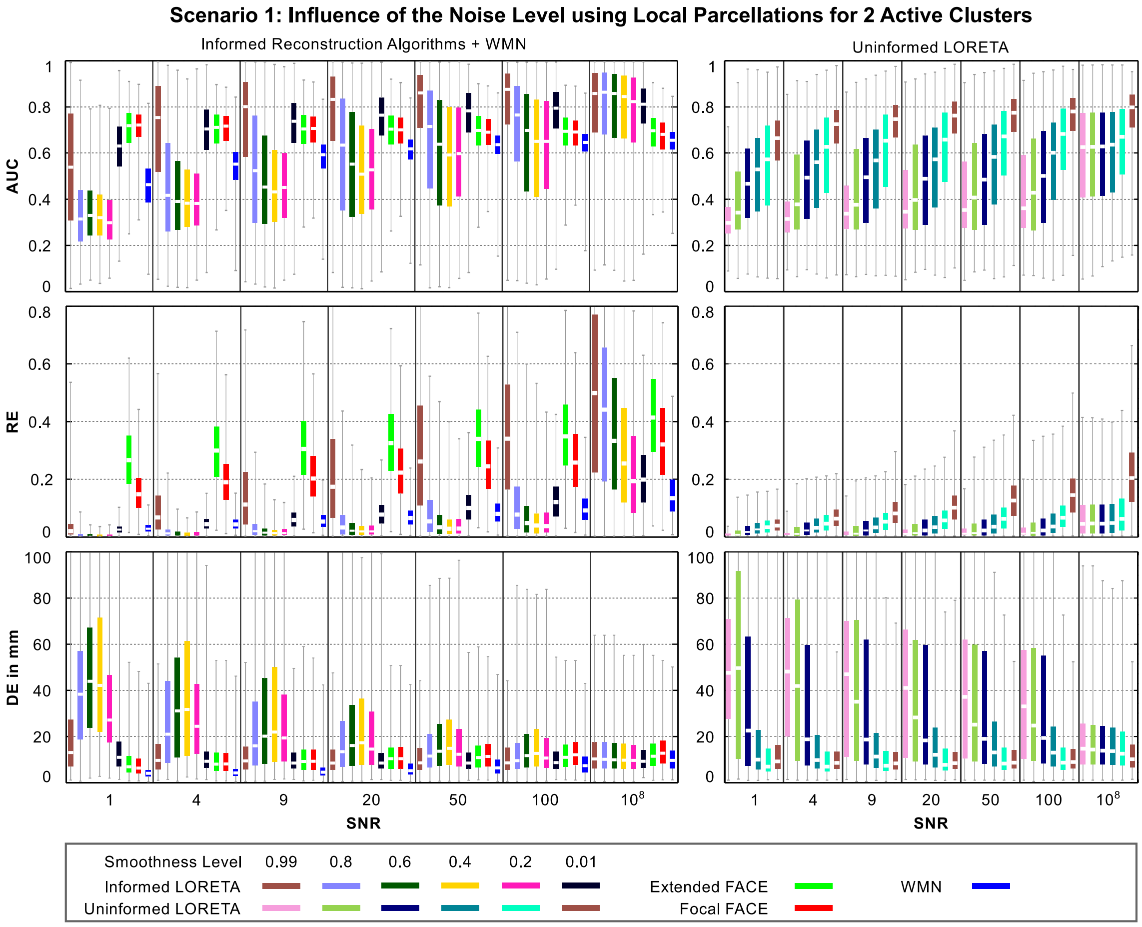

Figure B.5: Performance of informed linear reconstruction methods with respect to the noise level. Prior information was derived from local parcellations with a single ROI. Two clusters were activated. The activation was consistent with the boundaries. See page 82 for details on the box plots.

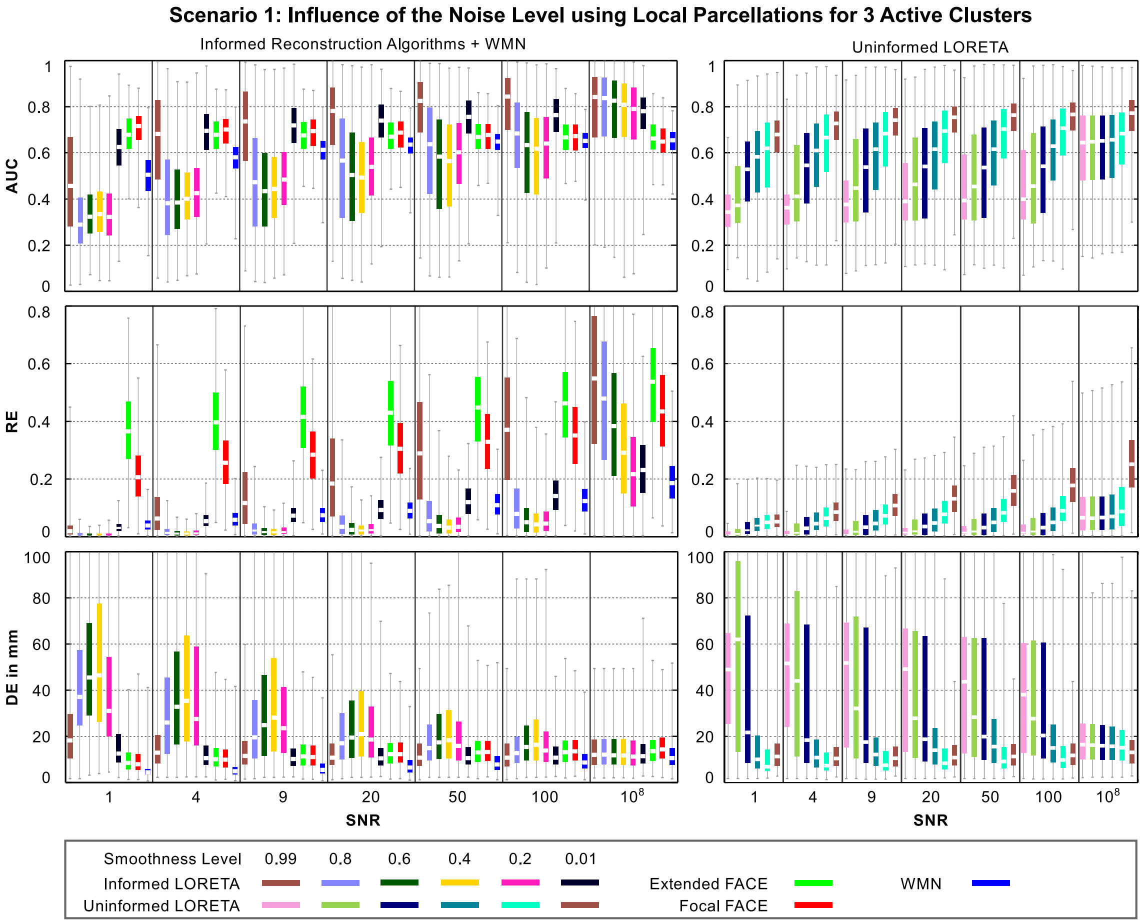

Figure B.6: Performance of informed linear reconstruction methods with respect to the noise level. Prior information was derived from local parcellations with a single ROI. Three clusters were activated. The activation was consistent with the boundaries. See page 82 for details on the box plots.

FACE according to RE is relatively high even for low SNR values. The performance of FACE and WMN according to DE slightly reduces for high SNR levels. In contrast, the performance of informed LORETA increases in this case. All distributions are statistically different from the WMN observations (for 2 clusters: informed LORETA: $P < 2 \times 10^{-2}$, eFACE: $P < 1 \times 10^{-8}$, fFACE: $P < 1 \times 10^{-8}$, uninformed LORETA: $P < 1 \times 10^{-5}$; for 3 clusters: informed LORETA: $P < 1 \times 10^{-2}$, eFACE: $P < 1 \times 10^{-8}$, fFACE: $P < 1 \times 10^{-8}$, uninformed LORETA: $P < 1 \times 10^{-8}$). As before, all findings are generally consistent with the results obtained for one active cluster. Moreover, it can be seen that the performance of all methods increases according to RE the more clusters are active. In contrast, the performance according to the AUC and DE slightly reduces.

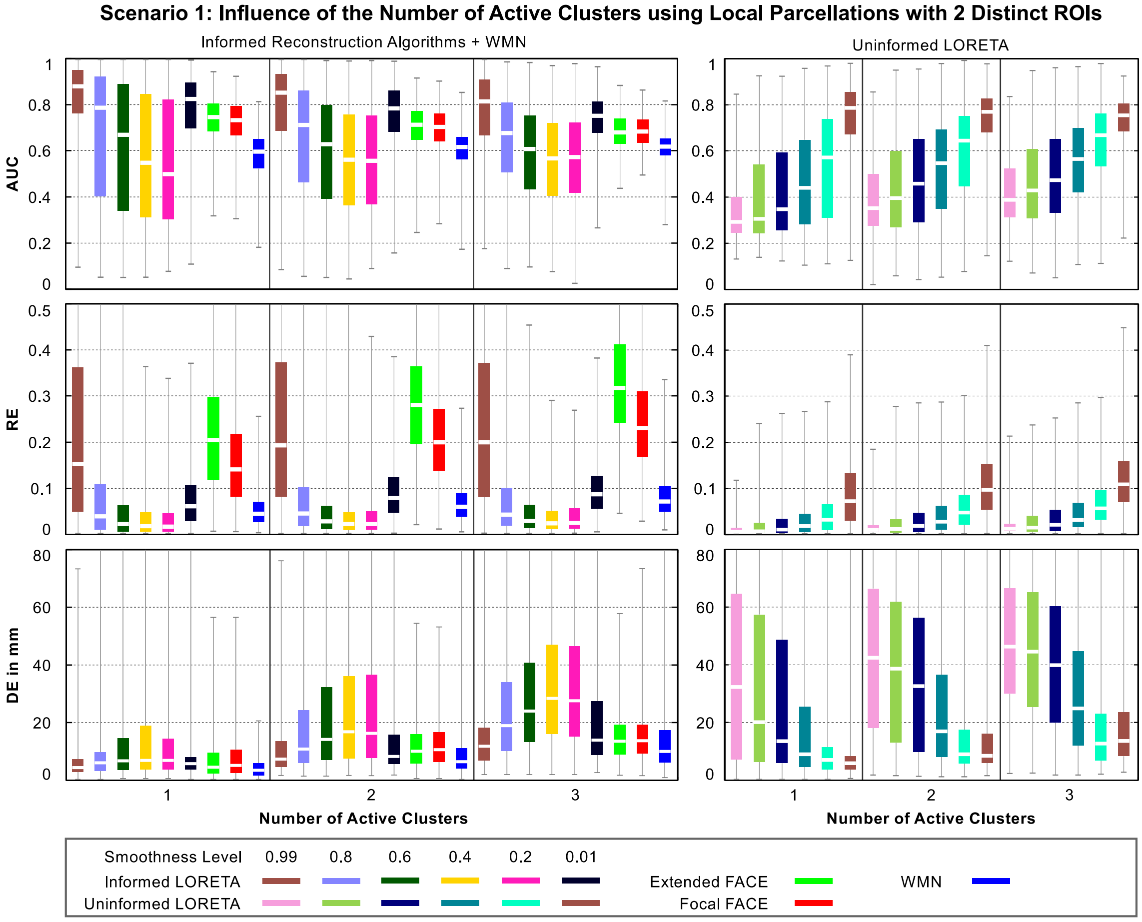

Figure B.7: Performance of informed and uninformed linear reconstruction methods with respect to the number of concurrently active clusters. Prior information derived from local parcellations with two distinct ROIs, up to 3 clusters were activated. The activation was consistent with the boundaries. Results are integrated over SNR levels 9, 20, 50, and 100. See page 82 for details on the box plots.

Simulations with distinct ROIs as prior information: Another important aspect is the performance analysis when multiple distinct brain regions are involved in data generation. Simulations concerning this issue were undertaken in this work by combining two distinct regions, i.e. two local parcellations, to generate prior knowledge. Figure 4.18 in Sec. 4.5.3.1 displays the performance of the evaluated methods with respect to the noise level given that a unique compact cluster is active in one of the incorporated regions. The results are very similar to simulations with a single ROI (cmp. Fig. 4.16). Figure B.7 presents the reconstruction quality with respect to the number of clusters that are activated within these ROIs. A comparison to Fig. 4.17 reveals that these results are similar to the simulations with a single ROI as well. The reconstruction quality of the informed methods, WMN, and uninformed LORETA with smoothness level 0.01 consistently reduces according to AUC and DE the more clusters are active. In contrast, the reconstruction quality according to RE increases. According to AUC and RE, WMN is outperformed by informed LORETA with smoothness level 0.99 ($P < 1 \times 10^{-8}$) and 0.01 ($P < 1 \times 10^{-8}$), both FACE methods ($P < 1 \times 10^{-8}$), and uninformed LORETA 0.01 ($P < 1 \times 10^{-8}$). The localization error for informed LORETA 0.99 is approximately in the same range as for WMN, while the

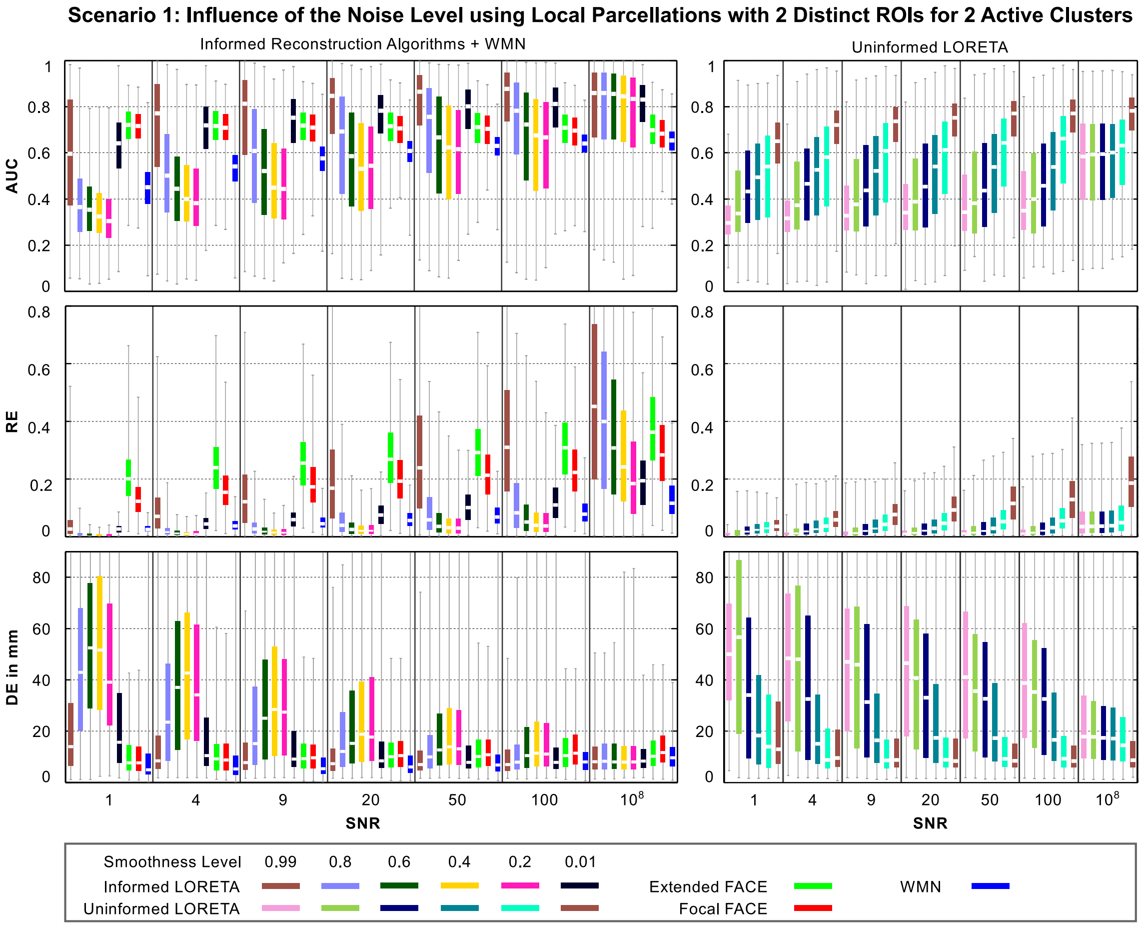

Figure B.8: Performance of informed linear reconstruction methods with respect to the noise level. Prior information was derived from local parcellations with two distinct ROIs, two clusters were activated. The activation was consistent with the boundaries. See page 82 for details on the box plots.

errors for informed LORETA 0.01 ($P < 1 \times 10^{-8}$), eFACE ($P < 1 \times 10^{-8}$), fFACE ($P < 1 \times 10^{-8}$), and uninformed LORETA 0.01 ($P < 1 \times 10^{-8}$) are slightly larger.

For the sake of completeness, Fig. B.8 and B.9 show the performance with respect to the noise level for two and three active clusters, respectively. Again, these results are very similar to the results obtained for simulations with one ROI (cmp. Fig. B.5 and B.6). Informed LORETA with smoothness levels 0.99 and 0.01, the two FACE methods, and uninformed LORETA with smoothness level 0.01 outperform WMN according to the AUC ($P < 1 \times 10^{-3}$) and RE ($P < 5 \times 10^{-2}$). The localization error for informed LORETA 0.99 is very similar to WMN for higher SNR levels (i.e. SNR $\geq$ 20) and slightly higher for lower levels (for 2 active clusters: $P < 5 \times 10^{-2}$, for 3 clusters: $P < 1 \times 10^{-2}$). Informed LORETA with level 0.01 produces larger errors compared to WMN for SNR = 50 and lower ($P < 1 \times 10^{-2}$). This is also true for uninformed LORETA with smoothness level 0.01 ($P < 1 \times 10^{-2}$). Finally, the two FACE methods are generally inferior to WMN regarding DE (for 2 cluster: $P < 1 \times 10^{-2}$, for 3 clusters: $P < 1 \times 10^{-6}$).

It can be summarized that an increased number of concurrently active sources coincides with a slightly reduced AUC performance (particularly for moderate SNR values), with a relatively strong improvement of the RE performance, and with a moderate reduction of the DE

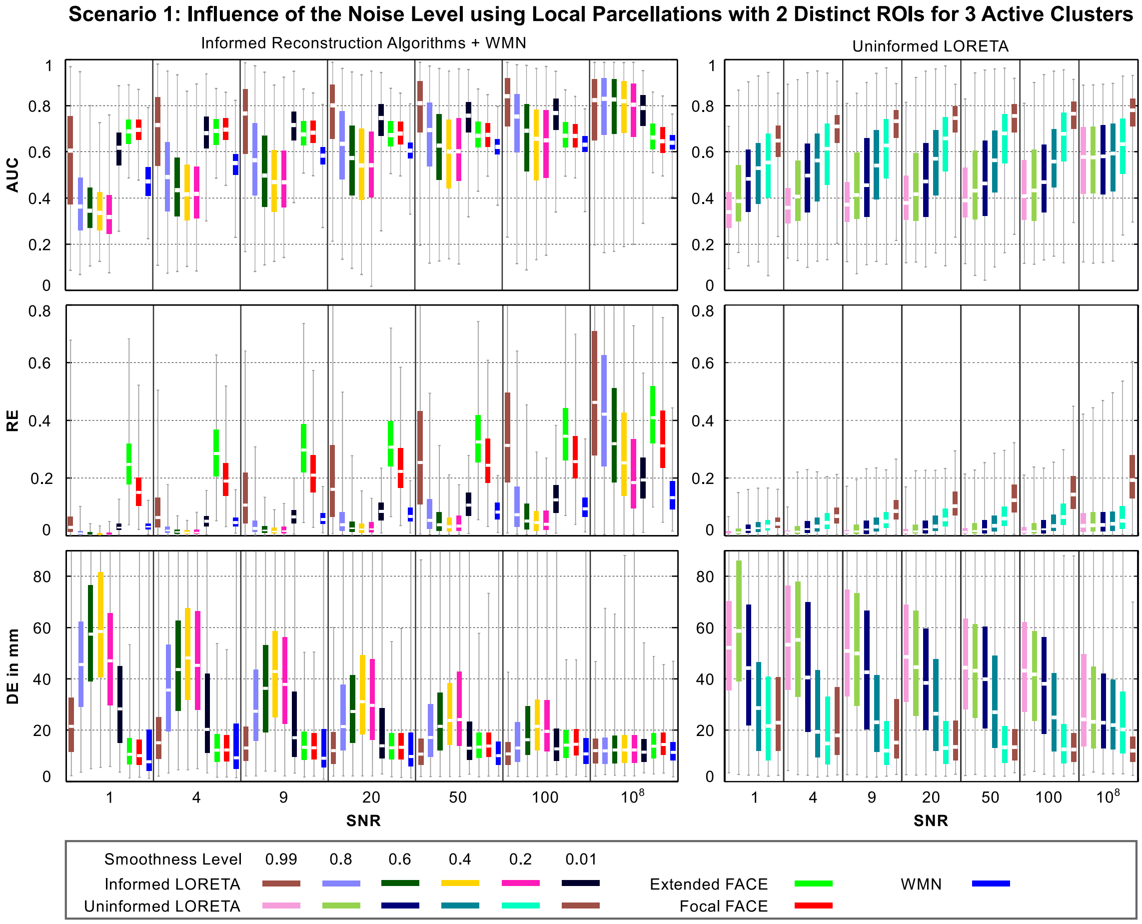

Figure B.9: Performance of informed linear reconstruction methods with respect to the noise level. Prior information was derived from local parcellations with two distinct ROIs, three clusters were activated. The activation was consistent with the boundaries. See page 82 for details on the box plots.

performance. Importantly, this seems to be independent on the fact whether only a single ROI or, as in this case, two distinct ROIs are incorporated as prior knowledge. It is likely that the incorporation of another one or two distinct ROIs (that means, a total of three or four ROIs within on parcellation) is still unproblematic with respect to the reconstruction quality. If, however, the total area covered by these ROIs becomes large with respect to the whole cortical area, the prior might become ineffective. This is similar to the use of a local parcellation that covers a huge area or even the full parcellation. It was shown in this work that the use of a full parcellation is ineffective if activity outside an *a priori* defined area can safely be excluded. In this case, a locale parcellation is more appropriate. Similarly, the use of parcellations consisting of multiple distinct local areas seems only useful if activity must be expected in each of the incorporated regions.

B.3.2 Scenario 3: Misplaced and Ignored Boundaries

The results presented in this section refer to the performance analysis of informed linear inverse methods given a prior inconsistent activation (see 4.5.3.3). Different situations are distinguished. (1) Boundaries are ignored for data generation. This mimics the case that the course of boundaries is inaccurate. (2) Important boundaries are omitted for the prior definition. (3) The prior contains information on boundaries which are not reflected in the data. More details on these use cases, the objective, and the simulation setup can be found in Sec. 4.5.1 and 4.5.2.

Ignored boundaries: This use case implies that the simulated source patterns might be located outside the ROI that is used to inform the inverse method. Figure B.10 shows the reconstruction quality with respect to the SNR level given that two clusters are concurrently active for data generation. Likewise, Fig. B.11 shows the results for three concurrently active clusters. The distributions of the metrics obtained for FACE and LORETA methods are statistically different from the results for obtained for the WMN method. The P-values are as follows. AUC: informed LORETA $P < 1 \times 10^{-8}$, eFACE $P < 1 \times 10^{-5}$, fFACE $P < 1 \times 10^{-6}$, uninformed LORETA $P < 1 \times 10^{-8}$; RE: informed LORETA $P < 1 \times 10^{-5}$, eFACE $P < 1 \times 10^{-8}$, fFACE $P < 1 \times 10^{-8}$, un-

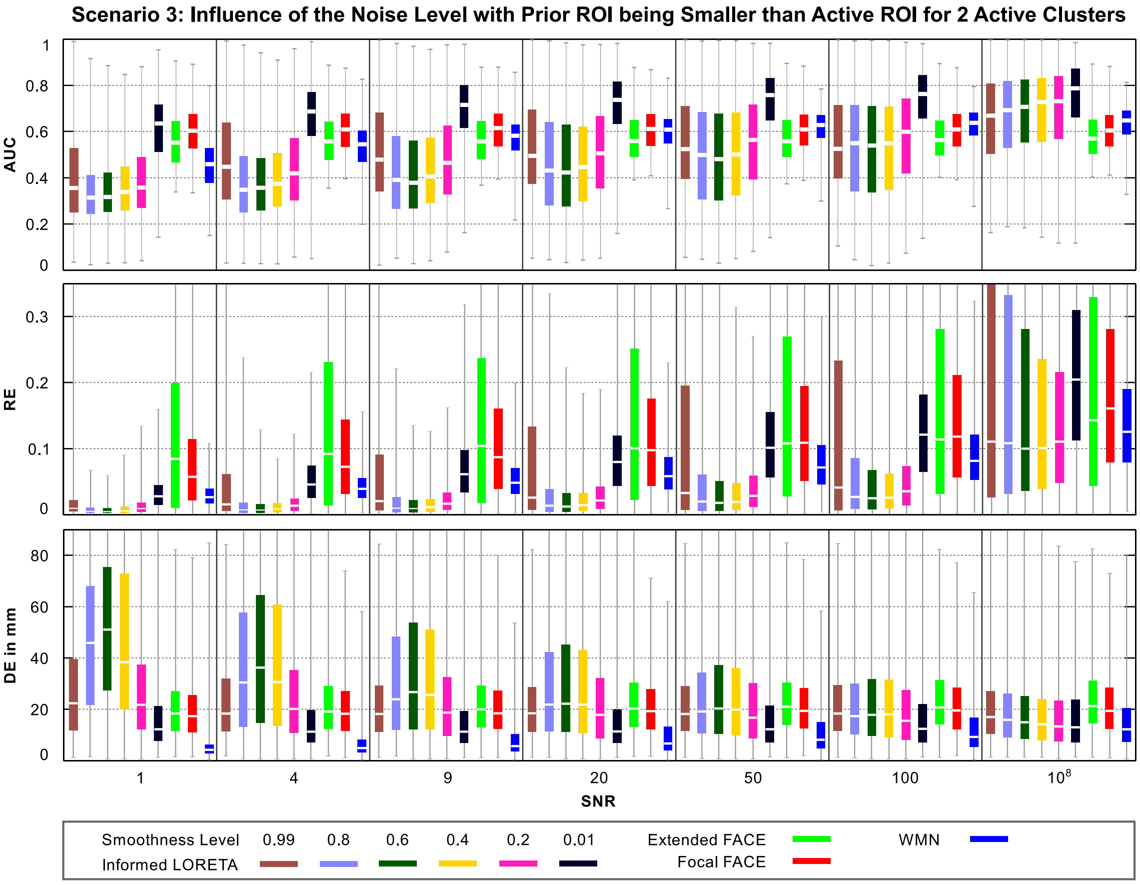

Figure B.10: Performance of informed linear reconstruction methods with respect to the noise level. Prior information was derived from local parcellations (i.e. parcellations with a small ROI), two clusters were activated inside the corresponding large ROI area. The activation was consistent with the boundaries. See page 82 for details on the box plots.

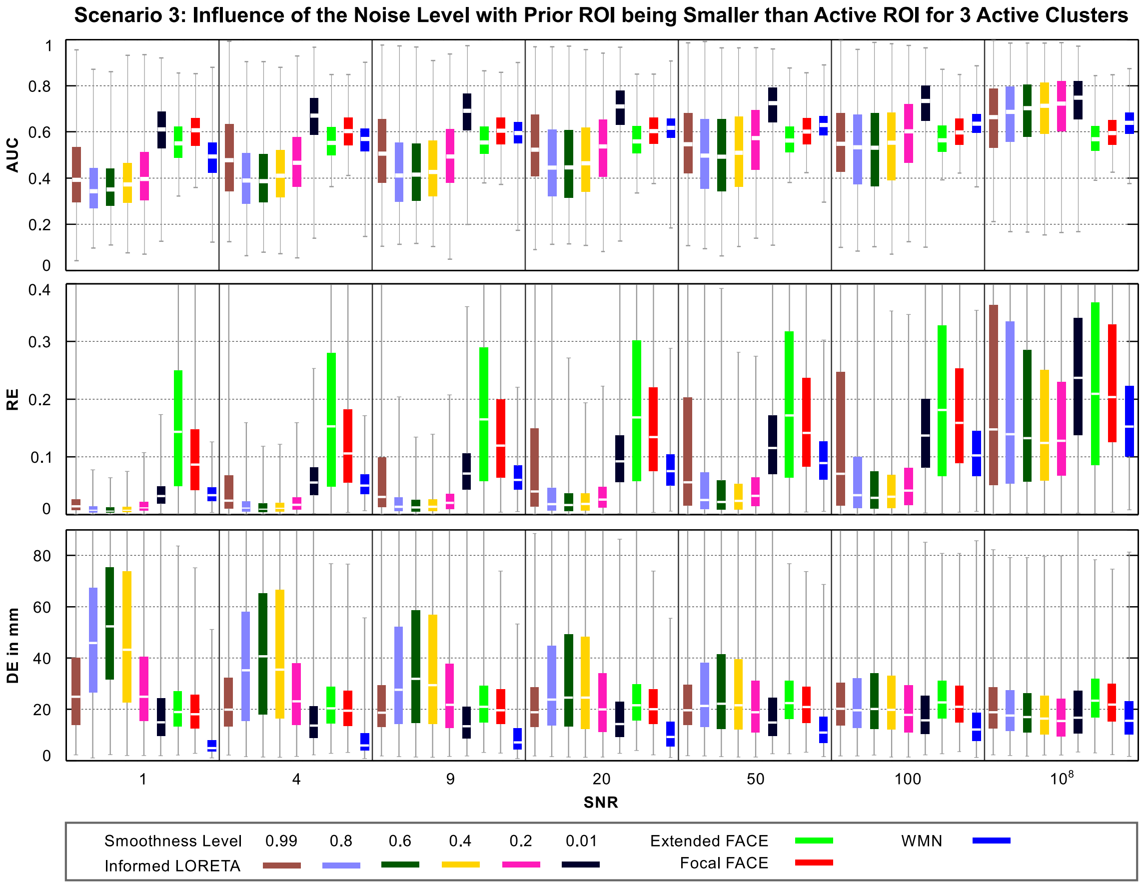

Figure B.11: Performance of informed linear reconstruction methods with respect to the noise level. Prior information was derived from local parcellations (i.e. parcellations with a small ROI), three clusters were activated inside the corresponding large ROI area. The activation was consistent with the boundaries. See page 82 for details on the box plots.

informed LORETA $P < 1 \times 10^{-7}$; DE: informed LORETA $P < 1 \times 10^{-2}$, eFACE $P < 1 \times 10^{-8}$, fFACE $P < 1 \times 10^{-8}$, uninformed LORETA $P < 1 \times 10^{-4}$. Compared to the results obtained for one active cluster (see 4.23), the AUC distributions tend to have a lower median and also a smaller variance the more clusters are active. The localization error increases, that means that the reconstruction performance reduces as well. In contrast, RE results have higher medians and a larger variance the more clusters are active. This is consistent to simulation results for consistent priors presented above.

Misplaced boundaries: In these simulations source patterns were generated in the subset of patches that was also used to inform the linear inverse methods. This means that the ROI used for reconstruction (i.e. prior knowledge) is larger than the ROI in which activity is generated. Thus, several functio-anatomical boundaries are not relevant for source reconstruction, that means they are misplaced. Importantly, clusters do not overlap patch boundaries. Hence, the course of the boundaries is assumed to be correct. Figure B.12 shows the reconstruction quality with respect to the SNR level given that two clusters are concurrently active for data generation. Likewise, Fig. B.13 shows the results for three concurrently active clusters. The distributions obtained for all informed and uninformed LORETA methods as well as for the

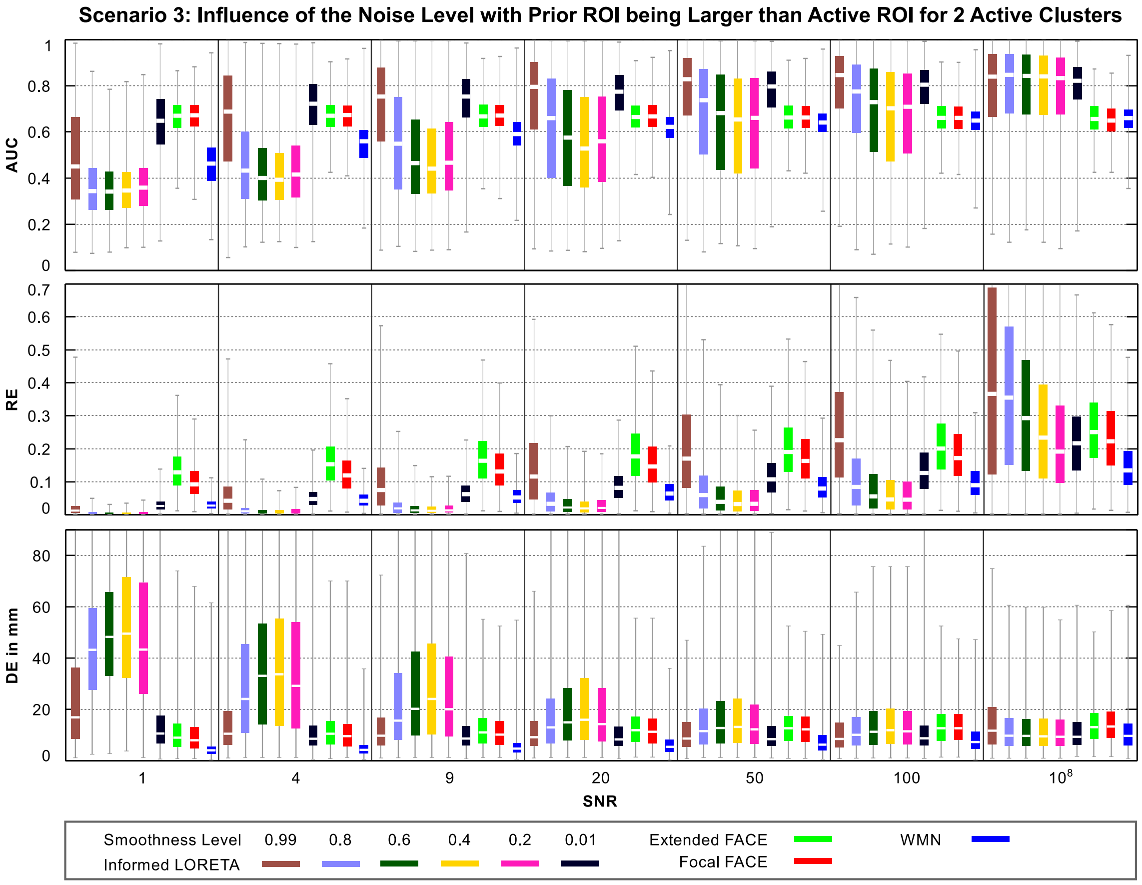

Figure B.12: Performance of informed linear reconstruction methods with respect to the noise level. Prior information was derived from local parcellations (i.e. parcellations with a large ROI), two clusters were activated inside the corresponding small ROI area. The activation was consistent with the boundaries. See page 82 for details on the box plots.

two FACE methods are almost all statistically different from the WMN results (for 2 clusters: AUC: $P < 1 \times 10^{-3}$, RE: $P < 1 \times 10^{-2}$, DE: $P < 1 \times 10^{-2}$; for 3 clusters: AUC: $P < 1 \times 10^{-3}$, RE: $P < 1 \times 10^{-3}$, DE: $P < 1 \times 10^{-3}$). Only the RE results for informed LORETA with smoothness level 0.01 at for SNR = 4 are similar to WMN ($P = 0.34$). It can be seen that the reconstruction quality slightly reduces according to AUC and DE and slightly increases according to RE when the number of concurrently active clusters increases. That is similar to the results obtained for the prior consistent simulations. Moreover, the reconstruction performance for two and three active clusters is generally consistent to that of simulations with only one cluster.

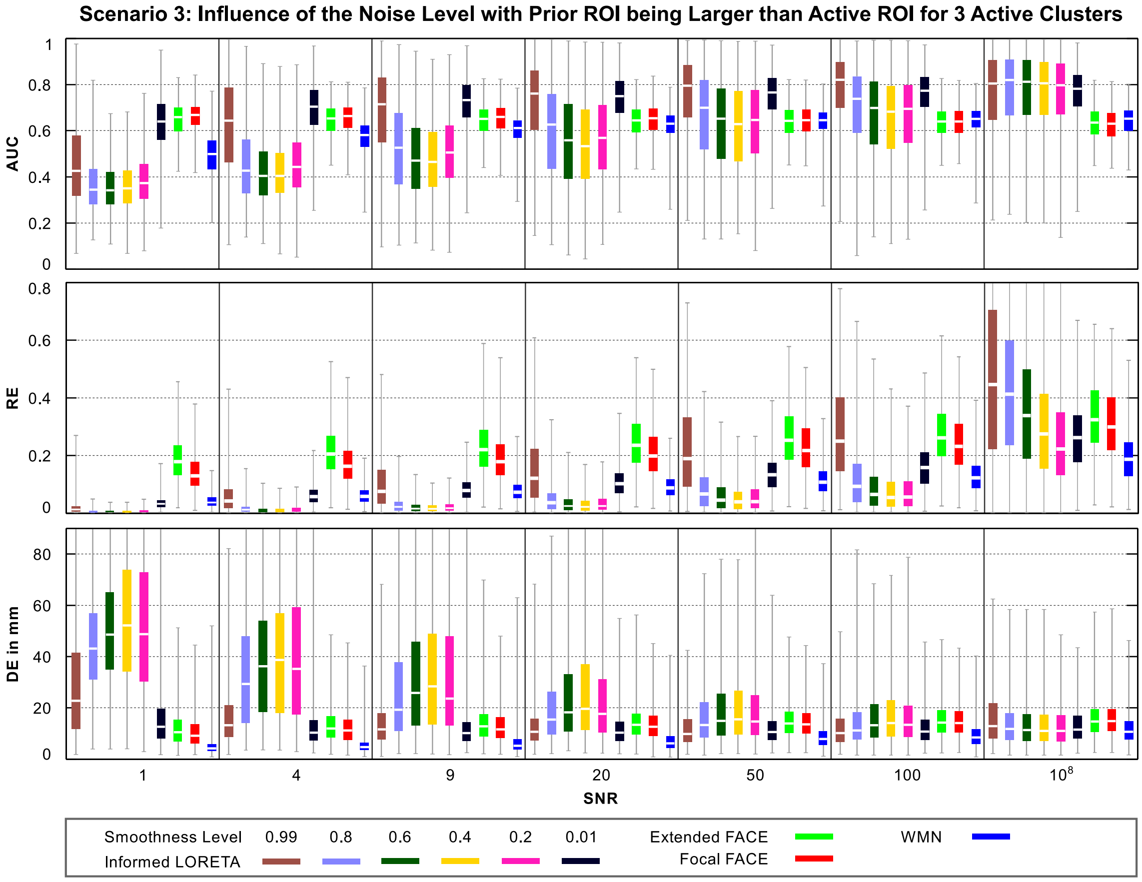

Figure B.13: Performance of informed linear reconstruction methods with respect to the noise level. Prior information was derived from local parcellations (i.e. parcellations with a large ROI), three clusters were activated inside the corresponding small ROI area. The activation was consistent with the boundaries. See page 82 for details on the box plots.

B.4 Additional Simulation Results to Section 4.6

B.4.1 Scenario 1: Different Source Spaces for Forward and Inverse Calculations

The results presented in this section refer to the performance analysis of informed linear inverse methods using different forward models (i.e. leadfield matrices) for forward and inverse calculations (see 4.6.3.1). The generated source patterns were consistent with the functio-anatomical boundaries employed as prior knowledge. More details on the objective and the simulation setup can be found in Sec. 4.6.1 and 4.6.2.

Influence of the noise level, full parcellations: Figure B.14 shows the reconstruction quality with respect to the SNR level given that two clusters are concurrently active for data generation. Full parcellations were used as prior knowledge. Likewise, Fig. B.15 shows the results for three concurrently active clusters. AUC and RE improves for higher SNR levels for all methods. In contrast, DE seems to be relatively constant for most methods. Informed LORETA with smoothness level 0.2 and higher generally outperforms WMN according to AUC ($P < 1 \times 10^{-8}$

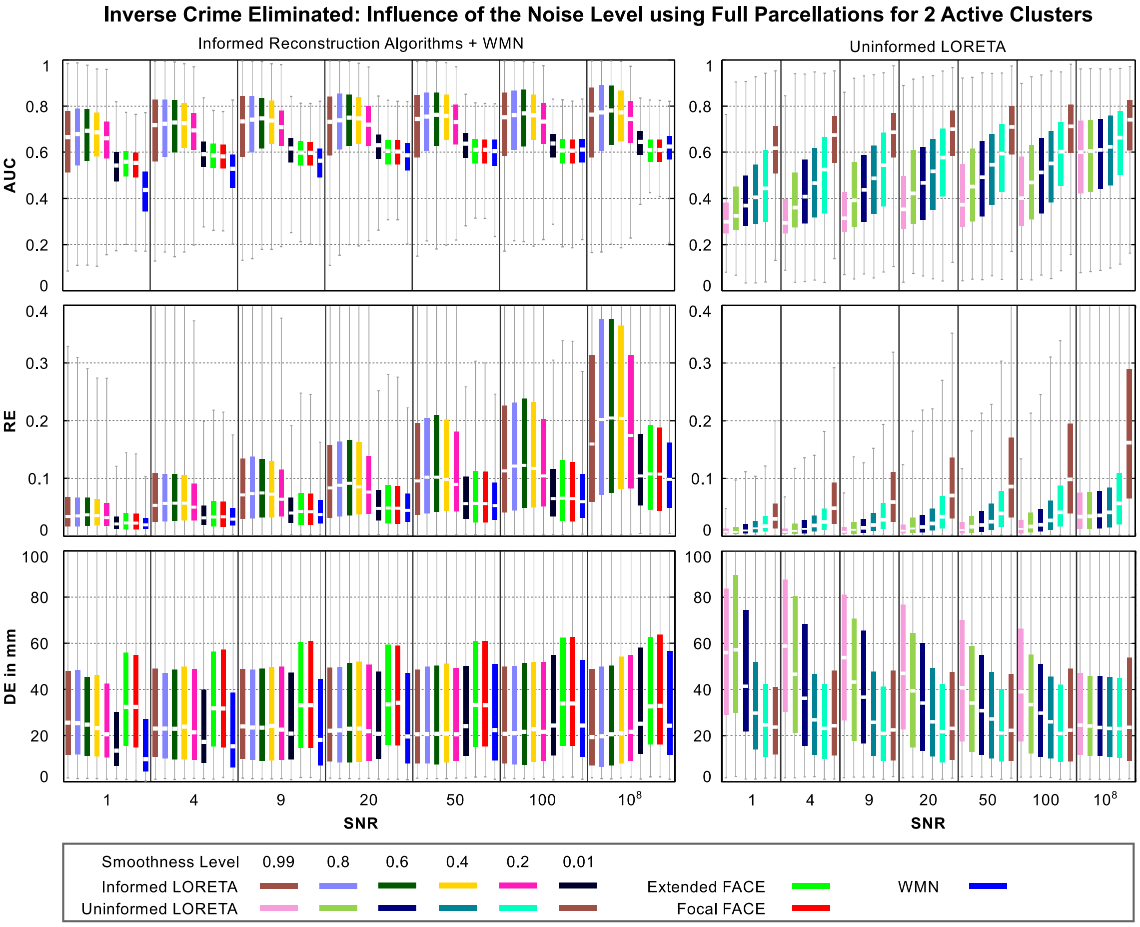

Figure B.14: Performance of informed and uninformed linear reconstruction methods with respect to the noise level. Distinct source models were used for forward and inverse calculations. Prior information was derived from full parcellations, two clusters were activated. The activation was consistent with the boundaries. See page 82 for details on the box plots.

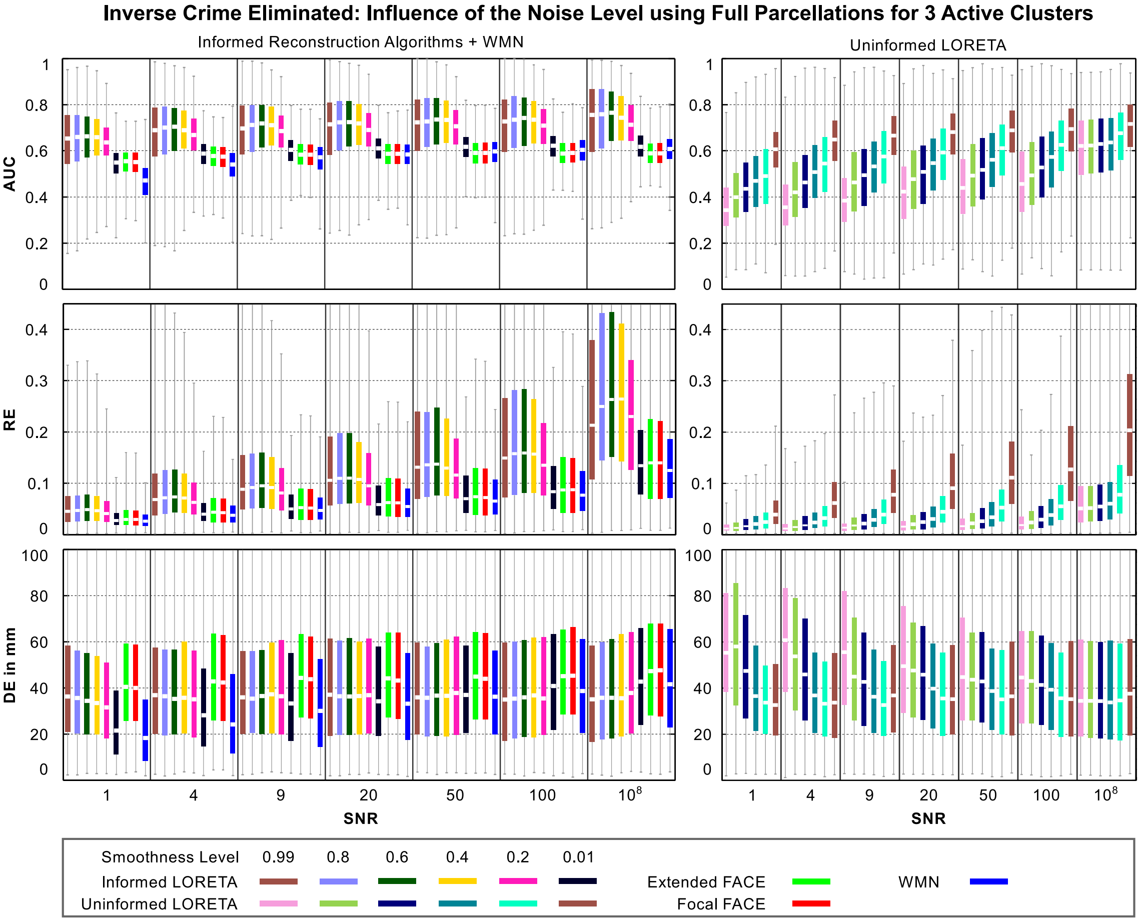

Figure B.15: Performance of informed and uninformed linear reconstruction methods with respect to the noise level. Distinct source models were used for forward and inverse calculations. Prior information was derived from full parcellations, three clusters were activated. The activation was consist with the boundaries. See page 82 for details on the box plots.

for 2 and 3 active clusters) and RE ($P < 1 \times 10^{-8}$ for 2 and 3 active clusters). The DE results obtained for informed LORETA and WMN are in a very similar range. In fact, many of the distributions are statistically similar. FACE provides a very different performance. The AUC is consistently higher for SNR levels up to 20 (for 2 clusters: $P < 1 \times 10^{-3}$, for 3 clusters: $P < 5 \times 10^{-2}$) and becomes more and more similar to the WMN results for higher signal-to-noise ratios. The RE distributions have a slightly higher median but and a significantly larger variance (for 2 clusters: $P < 2 \times 10^{-2}$; for 3 clusters: $P < 1 \times 10^{-3}$) compared to WMN distributions. Moreover, FACE is inferior to WMN with respect to the DE metric (for 2 clusters: $P < 1 \times 10^{-5}$, for 3 clusters: $P < 4 \times 10^{-2}$). Finally, uninformed LORETA results for smoothness level 0.2 and higher are inferior to WMN (AUC: $P < 1 \times 10^{-8}$, RE: $P < 1 \times 10^{-7}$). In contrast, uninformed LORETA for level 0.01, which employs a very weak correlation constraint, outperforms WMN according to AUC ($P < 1 \times 10^{-8}$) and RE ($P < 1 \times 10^{-8}$). All results are generally consistent with the findings revealed for simulations with one active cluster. More importantly, the results are very similar to the results obtained for simulation in which the simulation setup does not account for inverse crime (cmp. Fig B.2 and B.3).

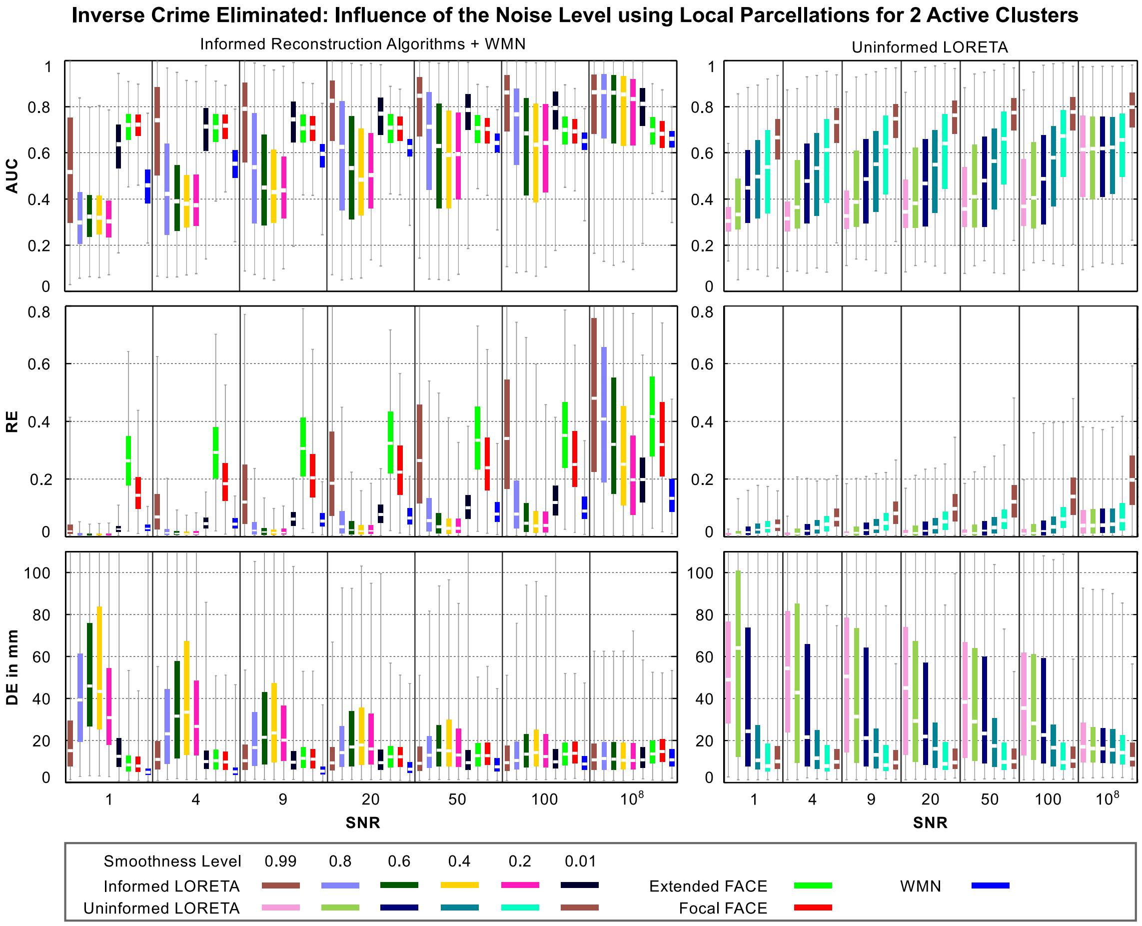

Figure B.16: Performance of informed and uninformed linear reconstruction methods with respect to the noise level. Distinct source models were used for forward and inverse calculations. Prior information was derived from local parcellations, two clusters were activated. The activation was consistent with the boundaries. See page 82 for details on the box plots.

Influence of the noise level, local parcellations: Figure B.16 shows the reconstruction quality with respect to the SNR level given that two clusters are concurrently active for data generation. Local parcellations were used as prior knowledge. Likewise, Fig. B.17 shows the results for three concurrently active clusters. The AUC generally increases for higher signal-to-noise levels. For the two FACE methods, however, the AUC results are rather independent of the SNR level. The WMN method is consistently outperformed by informed LORETA with smoothness level 0.99 ($P < 1 \times 10^{-8}$) and 0.01 ($P < 1 \times 10^{-8}$), eFACE ($P < 1 \times 10^{-8}$), fFACE (for 2 clusters: $P < 1 \times 10^{-8}$, for 3 clusters: $P < 1 \times 10^{-4}$), and uninformed LORTEA with level 0.01 ($P < 1 \times 10^{-8}$). The RE metric improves for all methods for higher SNR levels. WMN is outperformed by informed LORETA 0.99 ($P < 1 \times 10^{-8}$), eFACE ($P < 1 \times 10^{-8}$), fFACE ($P < 1 \times 10^{-8}$), and uninformed LORETA 0.01 ($P < 1 \times 10^{-8}$). Moreover, informed LORETA 0.01 for SNR above 4 in case of two active clusters ($P < 1 \times 10^{-2}$), and for SNR above 20 in case of three active clusters ($P < 1 \times 10^{-5}$), outperforms WMN as well. As for one cluster, the performance of FACE according to RE is relatively high, even for low SNR values. According to DE, the performance of FACE and WMN slightly reduces for higher SNR levels. In contrast, the results obtained for informed LORETA with smoothness level 0.2 and higher improve for higher SNR levels. All dis-

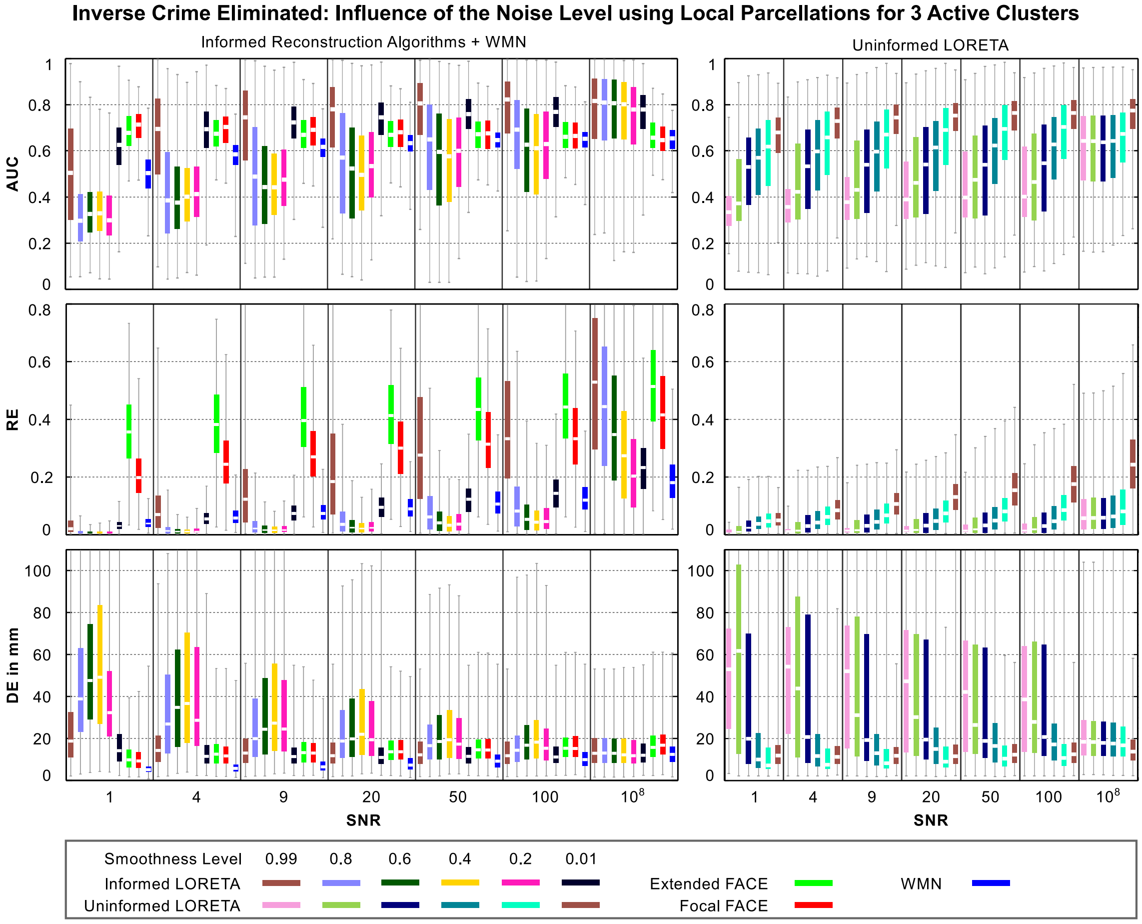

Figure B.17: Performance of informed and uninformed linear reconstruction methods according to the noise level. Distinct source models were used for forward and inverse calculations. Prior information was derived from local parcellations, three clusters were activated. The activation was consistent with the boundaries. See page 82 for details on the box plots.

tributions are statistically different from the WMN results (for 2 clusters: informed LORETA smoothness level 0.2 and larger: $P < 1 \times 10^{-3}$, eFACE: $P < 1 \times 10^{-8}$, fFACE: $P < 1 \times 10^{-8}$, uninformed LORETA: $P < 1 \times 10^{-2}$; for 3 clusters: informed LORETA smoothness level 0.2 and larger: $P < 1 \times 10^{-3}$, eFACE: $P < 1 \times 10^{-8}$, fFACE: $P < 1 \times 10^{-8}$, uninformed LORETA: $P < 1 \times 10^{-6}$). Informed LORETA with smoothness level 0.01 is statistically different from the WMN results as well, but not in the noise-free case (for 2 clusters: $P < 1 \times 10^{-4}$, for 3 clusters: $P < 1 \times 10^{-5}$). Again, all findings are generally consistent with the results obtained for simulations with one active cluster. The results presented here clearly indicate that the use of identical source models for forward and inverse calculations does not cause an overestimation of the performance measures. This is consistent with the findings for full parcellations (see above).

Bibliography

Z. A. Acar and S. Makeig. Neuroelectromagnetic forward head modeling toolbox. *Journal of Neuroscience Methods*, 190(2):258–270, 2010. doi: 10.1016/j.jneumeth.2010.04.031.

S. P. Ahlfors and G. V. Simpson. Geometrical interpretation of fMRI-guided MEG/EEG inverse estimates. *NeuroImage*, 22(1):323–332, May 2004. doi: 10.1016/j.neuroimage.2003.12.044.

W. Andrä and H. Nowak. *Magnetism in Medicine. A Handbook*. Wiley-VCH, second edition edition, October 2006. ISBN: 978-3527405589.

A. Anwander, M. Tittgemeyer, D. Y. von Cramon, A. D. Friederici, and T. R. Knösche. Connectivity-based parcellation of Broca's area. *Cerebral Cortex*, 17(4):816–825, 2007. doi: 10.1093/cercor/bhk034.

T. Auranen, A. Nummenmaa, M. S. Hämäläinen, I. P. Jääskeläinen, J. Lampinen, A. Vehtari, and M. Sams. Bayesian analysis of the neuromagnetic inverse problem with ℓp-norm priors. *NeuroImage*, 26(3):870–884, 2005. doi: 10.1016/j.neuroimage.2005.02.046.

T. Auranen, A. Nummenmaa, M. S. Hämäläinen, I. P. Jääskeläinen, J. Lampinen, A. Vehtari, and M. Sams. Bayesian inverse analysis of neuromagnetic data using cortically constrained multiple dipoles. *Human Brain Mapping*, 28(10):979–994, 2007. doi: 10.1002/hbm.20334.

A. Babajani and H. Soltanian-Zadeh. Integrated MEG/EEG and fMRI model based on neural masses. *IEEE Transactions on Biomedical Engineering*, 53:1794–1801, 2006. doi: 10.1109/TBME.2006.873748.

F. Babiloni, F. Carducci, C. Del Gratta, C. Babiloni, G. M. Roberti, G. L. Romani, C. Caltagirone, P. M. Rossini, and A. Urbano. Combined high resolution EEG and functional MRI data for modeling of cortical sources of human movement-related potentials. In *Annual International Conference of the IEEE Engineering in Medicine and Biology Society*, volume 4, 1998. doi: 10.1109/IEMBS.1998.747031.

F. Babiloni, C. Babiloni, F. Carducci, C. Del Gratta, G. L. Romani, P. M. Rossini, and F. Cincotti. Cortical source estimate of combined high resolution EEG and fMRI data related to voluntary movements. *Methods of Information in Medicine*, 41:443–450, 2002.

F. Babiloni, C. Babiloni, F. Carducci, G. L. Romani, P. M. Rossini, L. M. Angelone, and F. Cincotti. Multimodal integration of high-resolution EEG and functional magnetic resonance imaging data: A simulation study. *NeuroImage*, 19(1):1–15, 2003. doi: 10.1016/S1053-8119(03)00052-1.

S. Baillet and L. Garnero. A bayesian approach to introducing anatomo-functional priors in the EEG/MEG inverse problem. *IEEE Transactions on Biomedical Engineering*, 44(5): 374–385, May 1997. doi: 10.1109/10.568913.

S. Baillet, J. C. Mosher, and R. M. Leahy. Electromagnetic brain mapping. *IEEE Signal Processing Magazine*, 18:14–30, 2001. doi: 10.1109/79.962275.

H. Barbas and N. Rempel-Clower. Cortical structure predicts the pattern of corticocortical connections. *Cerebral Cortex*, 7(7):635–646, 1997. doi: 10.1093/cercor/7.7.635.

C. Beaulieu. The basis of anisotropic water diffusion in the nervous system - a technical review. *NMR in Biomedicine*, 15(1):435–455, 2002. doi: 10.1002/nbm.782.

T. E. J. Behrens, M. W. Woolrich, S. M. Smith, C. A. M. Wheeler-Kingshott, P. A. Boulby, G. J. Barker, E. L. Sillery, K. Sheehan, O. Ciccarelli, A. J. Thompson, J. M. Brady, P. M. Matthews, and H. Johansen-Berg. Non-invasive mapping of connections between human thalamus and cortex using diffusion imaging. *Nature Neuroscience*, 6(7):750–757, 2003. doi: 10.1038/nn1075.

R. R. Benson, W. J. Logan, G. R. Cosgrove, A. J. Cole, H. Jiang, L. L. LeSueur, B. R. Buchbinder, B. R. Rosen, and V. S. Jr. Caviness. Functional MRI localization of language in a 9-year-old child. *The Canadian Journal of Neurological Sciences*, 23:213–219, 1996. doi: 10.1017/S0317167100038543.

D. Le Bihan, C. Poupon, C. A. Clark, S. Pappata, N. Molko, and H. Chabriat. Diffusion tensor imaging: Concepts and applications. *Journal of Magnetic Resonance Imaging*, 13(4): 534–546, 2001. doi: 10.1002/jmri.1076.

B. Biswal, F. Z. Yetkin, V. M. Haughton, and J. S. Hyde. Functional connectivity in the motor cortex of resting human brain using echo-planar mri. *Magnetic Resonance in Medicine*, 34 (4):537–541, October 1995.

F. R. Bommel, R. Rockelein, and L. Urankar. Boundary element solution of biomagnetic problems. *IEEE Transactions on Magnetics*, 29(2):1395–1398, 1993. doi: 10.1109/20.250663.

D. J. Bosnyak, R. A. Eaton, and L. E. Roberts. Distributed auditory cortical representations are modified when non-musicians are trained at pitch discrimination with 40 hz amplitude modulated tones. *Cerebral Cortex*, 14(10):1088–1099, 2004. doi: 10.1093/cercor/bhh068.

V. Braitenberg. A note on myeloarchitectonics. *The Journal of Comparative Neurology*, 118: 141–156, 1962. doi: 10.1002/cne.901180202.

K. Brodmann. *Vergleichende Lokalisationslehre der Grosshirnrinde in ihren Prinzipien dargestellt auf Grund des Zellenbaues.* Leipzig: Barth, 1909.

M. Catani, R. J. Howard, S. Pajevic, and D. K. Jones. Virtual in vivo interactive dissection of white matter fasciculi in the human brain. *NeuroImage*, 17(1):77–94, 2002. doi: 10.1006/nimg.2002.1136.

W.-T. Chang, A. Nummenmaa, J.-C. Hsieh, and F.-H. Lin. Spatially sparse source cluster modeling by compressive neuromagnetic tomography. *NeuroImage*, 53(1):146–160, 2010. doi: 10.1016/j.neuroimage.2010.05.013.

W.-T. Chang, S. P. Ahlfors, and F.-H. Lin. Sparse current source estimation for MEG using loose orientation constraints. *Human Brain Mapping*, 34(9):2190–2201, 2013. doi: 10.1002/hbm.22057.

G. E. Chatrian, E. Lettich, and P. L. Nelson. Ten percent electrode system for topographic studies of spontaneous and evoked eeg activities. *American Journal of EEG Technology*, 25 (2):83–92, 1985.

R. A. Chowdhury, J. M. Lina, E. Kobayashi, and C. Grova. MEG source localization of spatially extended generators of epileptic activity: Comparing entropic and hierarchical Bayesian approaches. *PLoS ONE*, 8(2):e55969, February 2013. doi: 10.1371/journal.pone.0055969.

D. L. Collins, P. Neelin, T. M. Peters, and A. C. Evans. Automatic 3D intersubject registration of MR volumetric data in standardized Talairach space. *Journal of Computer Assisted Tomography*, 18(2):192–205, 1994. doi: 10.1097/00004728-199403000-00005.

B. R. Cottereau, K. Jerbi, and S. Baillet. Multiresolution imaging of MEG cortical sources using an explicit piecewise model. *NeuroImage*, 38(3):439–451, 2007. doi: 10.1016/j.neuroimage.2007.07.046.

B. R. Cottereau, J. M. Ales, and A. M. Norcia. Increasing the accuracy of electromagnetic inverses using functional area source correlation constraints. *Human Brain Mapping*, 33 (11):2694–2713, 2012. doi: 10.1002/hbm.21394.

C. W. Crowley, R. E. Greenblatt, and I. Khalil. Minimum norm estimation of current distributions in realistic geometries. In S. J. Williamson, M. Hoke, G. Stroink, and M. Kotani, editors, *Advances in Biomagnetism*, pages 603–606. Springer US, 1990. ISBN 978-1-4612-7876-4. doi: 10.1007/978-1-4613-0581-1_133.

F. H. L. da Silva. The impact of EEG/MEG signal processing and modeling in the diagnostic and management of epilepsy. *IEEE Reviews in Biomedical Engineering*, 1:143–156, 2008. doi: 10.1109/RBME.2008.2008246.

F. L. da Silva and A. van Rotterdam. Biophysical aspects of EEG and magnetoencephalogram generation. In E. Niedermeyer and F. L. da Silva, editors, *Electroencephalography, Clinical Applications, and Related Fields*, pages 93–109. Williams & Wilkins, Baltimore, Basic Principles, 1999.

A. M. Dale and E. Halgren. Spatiotemporal mapping of brain activity by integration of multiple imaging modalities. *Current Opinion in Neurobiology*, 11(2):202–208, 2001. doi: 10.1016/S0959-4388(00)00197-5.

A. M. Dale and M. I. Sereno. Improved localization of cortical activity by combining EEG and MEG with MRI cortical surface reconstruction: A linear approach. *Journal of Cognitive Neuroscience*, 5:162–176, 1993. doi: 10.1162/jocn.1993.5.2.162.

A. M. Dale, A. K. Liu, B. R. Fischl, Y. L. Buckner, J. W. Belliveau, J. D. Lewine, and E. Halgren. Dynamic statistical parametric neurotechnique mapping: Combining fMRI and MEG for high-resolution imaging of cortical activity. *Neuron*, 26:55–67, April 2000. doi: 10.1016/S0896-6273(00)81138-1.

M. Dannhauer, B. Lanfer, C. H. Wolters, and T. R. Knösche. Modeling of the human skull in EEG source analysis. *Human Brain Mapping*, 32(9):1383–1399, 2011. doi: 10.1002/hbm.21114.

J. Daunizeau, J. Mattout, D. Clonda, B. Goulard, H. Benali, and J.-M. Lina. Bayesian spatio-temporal approach for EEG source reconstruction: conciliating ECD and distributed models. *IEEE Transactions on Biomedical Engineering*, 53(3):503–516, 2006. doi: 10.1109/TBME.2005.869791.

J. Daunizeau, C. Grova, G. Marrelec, J. Mattout, S. Jbabdi, M. Pélégrini-Issac, J.-M. Lina, and H. Benali. Symmetrical event-related EEG/fMRI information fusion in a variational Bayesian framework. *NeuroImage*, 36(1):69–87, 2007. doi: 10.1016/j.neuroimage.2007.01.044.

T. Davis. SPARSEINV: A MATLAB toolbox for computing the sparse inverse subset using the Takahashi equations, November 2011. URL `http://www.mathworks.com/matlabcentral/fileexchange/33966`.

R. G. de Peralta Menendez and S. L. Gonzalez Andino. Basic limitations of linear inverse solutions: A case study. In S.L. Gonzalez Andino, editor, *Proceedings of the 20th Annual International Conference of the IEEE Engineering in Medicine and Biology Society*, volume 20, pages 2143–2146, 1998. doi: 10.1109/IEMBS.1998.747033.

R. G. de Peralta Menendez and S. L. Gonzalez Andino. Discussing the capabilities of laplacian minimization. *Brain Topography*, 13:97–104, 2000. doi: 10.1023/A:1026603017734.

R. G. de Peralta Menendez and S. L. Gonzalez Andino. Comparison of algorithms for the localization of focal sources: Evaluation with simulated data and analysis of experimental data. *International Journal of Bioelectromagnetism*, 4(1), 2002.

R. S. Desikan, F. Ségonne, B. Fischl, B. T. Quinn, B. C. Dickerson, D. Blacker, R. L. Buckner, A. M. Dale, R. P. Maguire, B. T. Hyman, M. S. Albert, and R. J. Killiany. An automated labeling system for subdividing the human cerebral cortex on MRI scans into gyral based regions of interest. *NeuroImage*, 31(3):968–980, 2006. doi: 10.1016/j.neuroimage.2006.01.021.

C. Destrieux, B. Fischl, A. Dale, and E. Halgren. Automatic parcellation of human cortical gyri and sulci using standard anatomical nomenclature. *NeuroImage*, 53(1):1–15, 2010. doi: 10.1016/j.neuroimage.2010.06.010.

R. Durbin and G. Mitchison. A dimension reduction framework for understanding cortical maps. *Nature*, 343(6259):644–647, 1990. doi: 10.1038/343644a0.

D. J. Felleman and D. C. van Essen. Distributed hierarchical processing in the primate cerebral cortex. *Cerebral Cortex*, 1(1):1–47, 1991. doi: 10.1093/cercor/1.1.1-a.

J. Fingberg, G. Berti, H. Hartmann, A. Basermann, C. H. Wolters, A. Anwander, A. McCarthy, and S. Woods. Bio-numerical simulations with SimBio. In *NEC Research and Development*, volume 40, pages 140–145, 2003.

B. Fischl. FreeSurfer. *NeuroImage*, 62(2):774–781, 2012. doi: 10.1016/j.neuroimage.2012.01.021.

B. Fischl, D. H. Salat, E. Busa, M. Albert, M. Dieterich, C. Haselgrove, A. van der Kouwe, R. Killiany, D. Kennedy, S. Klaveness, A. Montillo, N. Makris, B. Rosen, and A. M. Dale. Whole brain segmentation: Automated labeling of neuroanatomical structures in the human brain. *Neuron*, 33(3):341–355, 2002. doi: 10.1016/S0896-6273(02)00569-X.

B. Fischl, A. van der Kouwe, C. Destrieux, E. Halgren, F. Ségonne, D. H. Salat, E. Busa, L. J. Seidmanand, J. Goldstein, D. Kennedy, V. Caviness, N. Makris, B. Rosen, and A. M. Dale. Automatically parcellating the human cerebral cortex. *Cerebral Cortex*, 14(1):11–22, 2004. doi: 10.1093/cercor/bhg087.

B. Fischl, N. Rajendran, E. Busa, J. Augustinack, O. Hinds, B. T. T. Yeo, H. Mohlberg, K. Amunts, and K. Zilles. Cortical folding patterns and predicting cytoarchitecture. *Cerebral Cortex*, 18 (8):1973–1980, August 2008. doi: 10.1093/cercor/bhm225.

A. P. Fonaryova Key, G. O. Dove, and M. J. Maguire. Linking brainwaves to the brain: An ERP primer. *Developmental Neuropsychology*, 27(2):183–215, 2005. doi: 10.1207/s15326942dn2702_1.

K. J. Friston, D. E. Glaser, R. N. A. Henson, S. Kiebel, C. Phillips, and J. Ashburner. Classical and Bayesian inference in neuroimaging: Applications. *NeuroImage*, 16(2):484–512, 2002. ISSN 1053-8119. doi: 10.1006/nimg.2002.1091.

K. J. Friston, L. Harrison, J. Daunizeau, S. Kiebel, C. Phillips, N. Trujillo-Barreto, R. Henson, G. Flandin, and J. Mattout. Multiple sparse priors for the M/EEG inverse problem. *NeuroImage*, 39(3):1104–1120, 2008. doi: 10.1016/j.neuroimage.2007.09.048.

M. Fuchs, M. Wagner, T. Köhler, and H. A. Wischmann. Linear and nonlinear current density reconstructions. *Journal of Clinical Neurophysiology*, 16(3):267–295, May 1999. doi: 10.1097/00004691-199905000-00006.

M. Fuchs, M. Wagner, and J. Kastner. Boundary element method volume conductor models for EEG source reconstruction. *Clinical Neurophysiology*, 112(8):1400–1407, 2001. doi: 10.1016/S1388-2457(02)00030-5.

M. Fuchs, B. Maess, and T. R. Knösche. LineLORETA: A method for linear source reconstruction based on EEG and MEG data using functio-anatomical similarity priors. In

Biomedical Engineering/Biomedizinische Technik 2012, volume 57, page 654, Jena, Germany, August 2012. doi: 10.1515/bmt-2012-4294.

N. Fujimaki, T. Hayakawa, M. Nielsen, T. R. Knösche, and S. Miyauchi. An fMRI-constrained MEG source analysis with procedures for dividing and grouping activation. *NeuroImage*, 17 (1):324–343, 2002. doi: 10.1006/nimg.2002.1160.

G. H. Golub and C. F. van Loan. *Matrix Computations*. The Johns Hopkins University Press, 3rd edition, 1996. doi: 10.1137/1028073. ISBN 0-8018-5418-8.

I. F. Gorodnitsky, B. D. Rao, and J. George. Source localization in magnetoencephalography using an iterative weighted minimum norm algorithm. In *Conference Record of the Twenty-Sixth Asilomar Conference on Signals, Systems and Computers*, pages 167–171. IEEE, 1992. doi: 10.1109/ACSSC.1992.269280.

I. F. Gorodnitsky, J. S. George, and B. D. Rao. Neuromagnetic source imaging with FOCUSS: A recursive weighted minimum norm algorithm. *Electroencephalography and Clinical Neurophysiology*, 95:231–251, 1995. doi: 10.1016/0013-4694(95)00107-A.

G. Le Goualher, E. Procyk, D. L. Collins, R. Venugopal, C. Barillot, and A. C. Evans. Automated extraction and variability analysis of sulcal neuroanatomy. *IEEE Transactions on Medical Imaging*, 18(3):206–217, March 1999. doi: 10.1109/42.764891.

R. Grech, T. Cassar, J. Muscat, K. P. Camilleri, S. G. Fabri, M. Zervakis, P. Xanthopoulos, V. Sakkalis, and B. Vanrumste. Review on solving the inverse problem in EEG source analysis. *Journal of Neuroengineering and Rehabilitation*, 5(25):25–33, 2008. doi: 10.1186/1743-0003-5-25.

A. Grinvald, E. Lieke, R. D. Frostig, C. D. Gilbert, and T. N. Wiesel. Functional architecture of cortex revealed by optical imaging of intrinsic signals. *Nature*, 324:361–364, November 1986. doi: 10.1038/324361a0.

C. Grova, J. Daunizeau, J.-M. Lina, C. G. Bénar, H. Benali, and J. Gotman. Evaluation of EEG localization methods using realistic simulations of interictal spikes. *NeuroImage*, 29(3): 734–753, 2006. doi: 10.1016/j.neuroimage.2005.08.053.

A. Grunwald. *Das Verteilte-Quelle-Modell bei der Analyse von MEG-Daten - Kritische Betrachtungen zur Quellenanalyse*. PhD thesis, Westfälische Wilhelms-Universität Münster, 1996.

D. Güllmar, J. Haueisen, M. Eiselt, F. Giessler, L. Flemming, A. Anwander, T. R. Knösche, C. H. Wolters, M. Dümpelmann, D. S. Tuch, and J. R. Reichenbach. Influence of anisotropic conductivity on EEG source reconstruction: Investigations in a rabbit model. *IEEE Transactions on Biomedical Engineering*, 53(9):1841–1850, 2006. doi: 10.1109/TBME.2006.876641.

R. Hari, M. Pelizzone J. P. Mäkelä, J. Hällström, L. Leinonen, and O. V. Lounasmaa. Neuromagnetic responses of the human auditory cortex to on-and off-sets of noise bursts. *International Journal of Audiology*, 26(1):31–43, 1987.

M. K. Hasnain, P. T. Fox, and M. G. Woldorff. Structure-function spatial covariance in the human visual cortex. *Cerebral Cortex*, 11:702–716, 2001. doi: 10.1093/cercor/11.8.702.

J. Haueisen. *Methods of numerical field calculation for neuromagnetic source localization*. PhD thesis, Technical University of Ilmenau, 1996.

O. Hauk. Keep it simple: A case for using classical minimum norm estimation in the analysis of EEG and MEG data. *NeuroImage*, 21:1612–1621, April 2004. doi: 10.1016/j.neuroimage.2003.12.018.

R. N. Henson, G. Flandin, K. J. Friston, and J. Mattout. A parametric empirical Bayesian framework for fMRI-constrained MEG/EEG source reconstruction. *Human Brain Mapping*, 31(10):1512–1531, 2010. doi: 10.1002/hbm.20956.

R. N. Henson, D. G. Wakeman, V. Litvak, and K. J. Friston. A parametric empirical Bayesian framework for the EEG/MEG inverse problem: Generative models for multisubject and multimodal integration. *Frontiers in Human Neuroscience*, 5(76), 2011. doi: 10.3389/fnhum.2011.00076.

G. Hickok and D. Poeppel. The cortical organization of speech processing. *Nature Reviews Neuroscience*, 8(5):393–402, 2007. doi: 10.1038/nrn2113.

O. Hinds, J. R. Polimeni, N. Rajendran, M. Balasubramanian, K. Amunts, K. Zilles, E. L. Schwartz, B. Fischl, and C. Triantafyllou. Locating the functional and anatomical boundaries of human primary visual cortex. *NeuroImage*, 46(4):915–922, 2009. doi: 10.1016/j.neuroimage.2009.03.036.

G. Huiskamp. Difference formulas for the surface laplacian on a triangulated surface. *Journal of Computational Physics*, 95(2):477–496, August 1991. doi: 10.1016/0021-9991(91)90286-T.

M. S. Hämäläinen. Discrete and distributed source estimates. In *Source Localization: Continuing Discussion of the Inverse Problem*, number 6 in ISBET Newsletter, pages 16–28. 1995. ISSN 0947-5133.

M. S. Hämäläinen and R. J. Ilmoniemi. Interpreting measured magnetic fields of the brain: Estimates of current distributions. Technical Report TKK-F-A559, Helsinki University of Technology, December 1984.

M. S. Hämäläinen and R. J. Ilmoniemi. Interpreting magnetic fields of the brain: Minimum norm estimates. *Medical and Biological Engineering and Computing*, 32(1):35–42, 1994. doi: 10.1007/BF02512476.

M. S. Hämäläinen and J. Sarvas. Realistic conductivity geometry model of the human head for interpretation of neuromagnetic data. *IEEE Transactions on Biomedical Engineering*, 36(2): 165–171, 1989. doi: 10.1109/10.16463.

R. J. Ilmoniemi. Estimating brain source distributions: Comments on LORETA. In *Source Localization: Continuing Discussion of the Inverse Problem*, number 6 in ISBET Newsletter, pages 12–14. 1995. ISSN 0947-5133.

C.-H. Im, K.-O. An, H.-K. Jung, H. Kwon, and Y.-H. Lee. Assessment criteria for MEG/EEG cortical patch tests. *Physics in Medicine and Biology*, 48(15):2561–73, 2003. doi: 10.1088/0031-9155/48/15/320.

C.-H. Im, H.-K. Jung, and N. Fujimaki. fMRI-constrained MEG source imaging and consideration of fMRI invisible sources. *Human Brain Mapping*, 26(2):110–118, 2005a. doi: 10.1002/hbm.20143.

C.-H. Im, H.-K. Jung, and N. Fujimaki. Anatomically constrained dipole adjustment (ANACONDA) for accurate MEG/EEG focal source localizations. *Physics in Medicine and Biology*, 50(20):4931–4953, 2005b. doi: 10.1088/0031-9155/50/20/012.

B. Jeffs, R. Leahy, and M. Singh. An evaluation of methods for neuromagnetic image reconstruction. *IEEE Transactions on Biomedical Engineering*, 34:713–723, 1987. doi: 10.1109/TBME.1987.325996.

H. Johansen-Berg, T. E. Behrens, M. D. Robson, I. Drobnjak, M. F. Rushworth, J. M. Brady, S. M. Smith, D. J. Higham, and P. M. Matthews. Changes in connectivity profiles define functionally distinct regions in human medial frontal cortex. *Proceedings of the National Academy of Sciences of the United States of America*, 101:13335–13340, 2004. doi: 10.1073/pnas.0403743101.

H. Johansen-Berg, T. E. J. Behrens, E. Sillery, O. Ciccarelli, A. J. Thompson, S. M. Smith, and P. M. Matthews. Functional-anatomical validation and individual variation of diffusion tractography-based segmentation of the human thalamus. *Cerebral Cortex*, 15(1):31–39, 2005. doi: 10.1093/cercor/bhh105.

S. C. Jun, J. S. George, W. Kim, J. Paré-Blagoev, S. Plis, D. M. Ranken, and D. M. Schmidt. Bayesian brain source imaging based on combined MEG/EEG and fMRI using MCMC. *NeuroImage*, 40(4):1581–1594, 2008. doi: 10.1016/j.neuroimage.2007.12.029.

J.H. Kaas. Cortical areas and patterns of cortico-cortical connections. In A. Schüz and R. Miller, editors, *Cortical areas: unity and diversity*, pages 179–191. London: Taylor & Francis, 2002. doi: 10.1201/9780203299296.ch9.

J. P. Kaipio and E. Somersalo. *Statistical and Computational Inverse Problems*, volume 160 of *Applied Mathematical Sciences*. Springer New York, 2005. doi: 10.1007/b138659.

C.-Y. Kao, M. Hofer, G. Sapiro, J. Stern, K. Rehm, and D. A. Rottenberg. A geometric method for automatic extraction of sulcal fundi. *IEEE Transactions on Medical Imaging*, 26(4):530–540, March 2007. doi: 10.1109/TMI.2006.886810.

W. E. Kincses, C. Braun, S. Kaiser, and T. Elbert. Modeling extended sources of event-related potentials using anatomical and physiological constraints. *Human Brain Mapping*, 8(4): 182–193, 1999. doi: 10.1002/(SICI)1097-0193(1999)8:4<182::AID-HBM3>3.0.CO;2-M.

T. R. Knösche. *Solutions of the Neuroelectromagnetic Inverse Problem. An Evaluation Study.* PhD thesis, University of Twente, 1997. ISBN: 9036509734.

T. R. Knösche and M. Tittgemeyer. The role of long-range connectivity for the characterization of the functional-anatomical organization of the cortex. *Frontiers in Systems Neuroscience*, 5 (58), 2011. doi: 10.3389/fnsys.2011.00058.

T. R. Knösche, C. Neuhaus, J. Haueisen, and K. Alter. The role of the planum temporale in the perception of musical phrases. In *Proceedings of 4th International Conference on Noninvasive Functional Source Imaging (NFSI)*, Chieti, Italy, 2003.

T. R. Knösche, B. Maess, A. Nakamura, and A. D. Friederici. Human communication investigated with magnetoencephalography: Speech, music, and gestures. *International review of neurobiology*, 68:79–120, 2005. doi: 10.1016/S0074-7742(05)68004-X.

T. R. Knösche, M. Gräser, and A. Anwander. Prior knowledge on cortex organization in the reconstruction of source current densities from EEG. *NeuroImage*, 67(0):7–24, 2013. doi: 10.1016/j.neuroimage.2012.11.013.

M. A. Koch, D. G. Norris, and M. Hund-Georgiadis. An investigation of functional and anatomical connectivity using magnetic resonance imaging. *NeuroImage*, 16(1):241–250, 2002. doi: 10.1006/nimg.2001.1052.

T. Köhler, M. Wagner, M. Fuchs, H.-A. Wischmann, R. Drenckhahn, and A. Theissen. Depth normalization in MEG/EEG current density imaging. In *Proceedings of the 18th Annual International Conference of the IEEE Engineering in Medicine and Biology Society*, volume 2, pages 812–813, Amsterdam, Netherland, 1996. doi: 10.1109/IEMBS.1996.651989.

C. Lamus, M. S. Hämäläinen, S. Temereanca, E. N. Brown, and P. L. Purdon. A spatiotemporal dynamic distributed solution to the MEG inverse problem. *NeuroImage*, 63(2):894–909, 2012. doi: http://dx.doi.org/10.1016/j.neuroimage.2011.11.020.

B. Lanfer, M. Scherg, M. Dannhauer, T. R. Knösche, M. Burger, and C. H. Wolters. Influences of skull segmentation inaccuracies on EEG source analysis. *NeuroImage*, 62(1):418–431, 2012. ISSN 1053-8119. doi: 10.1016/j.neuroimage.2012.05.006.

P.S. Lewis, J. C. Mosher, and R. M. Leahy. Neuromagnetic source reconstruction. In *International Conference on Acoustics, Speech, and Signal Processing (ICASSP)*, volume 5, pages 2911–2914, May 1995. doi: 10.1109/ICASSP.1995.479454.

F.-H. Lin, T. Witzel, M. S. Hämäläinen, A. M. Dale, J. W. Belliveau, and S. M. Stufflebeam. Spectral spatiotemporal imaging of cortical oscillations and interactions in the human brain. *NeuroImage*, 23(2):582–595, 2004. doi: DOI:10.1016/j.neuroimage.2004.04.027.

F.-H. Lin, J. W. Belliveau, A. M. Dale, and M. S. Hämäläinen. Distributed current estimates using cortical orientation constraints. *Human Brain Mapping*, 27(1):1–13, 2006a. doi: 10.1002/hbm.20155.

F.-H. Lin, T. Witzel, S. P. Ahlfors, S. M. Stufflebeam, J. W. Belliveau, and M. S. Hämäläinen. Assessing and improving the spatial accuracy in MEG source localization by depth-weighted minimum-norm estimates. *NeuroImage*, 31(1):160–171, 2006b. doi: 10.1016/j.neuroimage.2005.11.054.

A. K. Liu, J. W. Belliveau, and A. M. Dale. Spatiotemporal imaging of human brain activity using functional MRI contrained magnetoencephalography: Monte Carlo simulations. *Proceedings of the National Academy of Sciences of the United States of America*, 95: 8945–8950, 1998. doi: 10.1073/pnas.95.15.8945.

A. K. Liu, A. M. Dale, and J. W. Belliveau. Monte Carlo simulation studies of EEG and MEG localization accuracy. *Human Brain Mapping*, 16:47–62, 2002. doi: 10.1002/hbm.10024.

Z. Liu and B. He. fMRI–EEG integrated cortical source imaging by use of time-variant spatial constraints. *NeuroImage*, 39(3):1198–1214, 2008. doi: 10.1016/j.neuroimage.2007.10.003.

Z. Liu, L. Ding, and B. He. Integration of EEG/MEG with MRI and fMRI. *IEEE Engineering in Medicine and Biology Magazine*, 25:46–53, 2006. doi: 10.1109/MEMB.2006.1657787.

N. K. Logothetis, J. Pauls, M. A. Augath, T. Trinath, and A. Oeltermann. Neurophysiological investigation of the basis of the fMRI signal. *Nature*, 412:150–157, 2001. doi: 10.1038/35084005.

G. Lohmann. Extracting line representations of sulcal and gyral patterns in MR images of the human brain. *IEEE Transactions on Medical Imaging*, 17(6):1040–1048, December 1998. doi: 10.1109/42.746714.

F. Lucka, S. Pursiainen, M. Burger, and C. H. Wolters. Hierarchical Bayesian inference for the EEG inverse problem using realistic FE head models: Depth localization and source separation for focal primary currents. *NeuroImage*, 61(4):1364–1382, 2012. doi: 10.1016/j.neuroimage.2012.04.017.

B. Lütkenhöner, E. Menninghaus, O. Steinsträter, C. Wienbruch, H. M. Gißler, and T. Elbert. Neuromagnetic source analysis using magnetic resonance images for the construction of source and volume conductor model. *Brain Topography*, 7(4):291–299, 1995. doi: 10.1007/BF01195255.

P. J. Magistretti, L. Pellerin, D. L. Rothman, and R. G. Shulman. Energy on demand. *Science*, 283(5401):496–497, 1999. doi: 10.1126/science.283.5401.496.

D. Malonek and A. Grinvald. Interactions between electrical activity and cortical microcirculation revealed by imaging spectroscopy: Implications for functional brain mapping. *Science*, 272(5261):551–554, 1996. doi: 10.1126/science.272.5261.551.

D. W. Marquardt. An algorithm for least-squares estimation of nonlinear parameters. *Journal of the Society for Industrial & Applied Mathematics*, 11(2):431–441, 1963. doi: 10.1137/0111030.

N. Maurits. *From Neurology to Methodology and Back: An Introduction to Clinical Neuroengineering*. Springer New York, 2012. doi: 10.1007/978-1-4614-1132-1. ISBN: 978-1-4614-1131-4 (Print) 978-1-4614-1132-1 (Online).

C. Metz. ROC methodology in radiologic imaging. *Investigative Radiology*, 21(9):720–733, September 1986. doi: 10.1097/00004424-198609000-00009.

A. Molins, S. M. Stufflebeam, E. N. Brown, and M. S. Hämäläinen. Quantification of the benefit from integrating MEG and EEG data in minimum $\ell 2$-norm estimation. *NeuroImage*, 42(3): 1069–1077, 2008. doi: 10.1016/j.neuroimage.2008.05.064.

D. Moreno-Dominguez, A. Anwander, and T. R. Knösche. A hierarchical method for whole-brain connectivity-based parcellation. *Human Brain Mapping*, 35(10):5000–5025, October 2014. doi: 10.1002/hbm.22528.

S. Mori and P. C. van Zijl. Fiber tracking: Principles and strategies - a technical review. *NMR in Biomedicine*, 15:468–480, 2002. doi: 10.1002/nbm.781.

J. C. Mosher, P. S. Lewis, and R. M. Leahy. Multiple dipole modeling and localization from spatio-temporal MEG data. *IEEE Transactions on Biomedical Engineering*, 39(6):541–557, June 1992. doi: 10.1109/10.141192.

J. C. Mosher, R. M. Leahy, and P. S. Lewis. EEG and MEG: Forward solutions for inverse methods. *IEEE Transactions on Biomedical Engineering*, 46(3):245–259, 1999. doi: 10.1109/10.748978.

J. C. Mosher, S. Baillet, and R. M. Leahy. Equivalence of linear approaches in bioelectromagnetic inverse solutions. In *Proceedings on the IEEE Workshop on Statistical Signal Processing 2003*, pages 294–297, 2003. doi: 10.1109/SSP.2003.1289402.

J. C. De Munck. *A mathematical and physical interpretation of the electromagnetic field of the Brain.* PhD thesis, University of Amsterdam, 1989.

S. S. Nagarajan, O. Portniaguine, D. Hwang, C. Johnson, and K. Sekihara. Controlled support MEG imaging. *NeuroImage*, 33(3):878–885, 2006. doi: 10.1016/j.neuroimage.2006.07.023.

J. Neumann, D. Y. von Cramon, B. U. Forstmann, S. Zysset, and G. Lohmann. The parcellation of cortical areas using replicator dynamics in fMRI. *NeuroImage*, 32(1):208–219, 2006. doi: 10.1016/j.neuroimage.2006.02.039.

P. L. Nunez. Comments on LORETA. In *Source Localization: Continuing Discussion of the Inverse Problem*, number 6 in ISBET Newsletter, pages 14–16. 1995. ISSN 0947-5133.

P. L. Nunez and R. B. Silberstein. On the relationship of synaptic activity to macroscopic measurements: Does co-registration of EEG with fMRI make sense? *Brain Topography*, 13 (2):79–96, 2000. doi: 10.1023/A:1026683200895.

P. L. Nunez and R. Srinivasan. *Electric Fields of the Brain - The Neurophysics of EEG.* Oxford University Press, 2nd edition, 2006. doi: 10.1093/acprof:oso/9780195050387.001.0001. ISBN: 978-0-19-505038-7.

W. Ou, M. S. Hämäläinen, and P. Golland. A distributed spatio-temporal EEG/MEG inverse solver. *NeuroImage*, 44(3):932–946, 2009. doi: http://dx.doi.org/10.1016/j.neuroimage.2008.05.063.

R. D. Pascual-Marqui. Reply to comments by hämäläinen, ilmoniemi and nunez. In *Source Localization: Continuing Discussion of the Inverse Problem*, number 6 in ISBET Newsletter, pages 16–28. 1995. ISSN 0947-5133.

R. D. Pascual-Marqui, C. M. Michel, and D. Lehmann. Low resolution electromagnetic tomography - a new method for localizing electrical activity in the brain. *International Journal of Psychophysiology*, 18(1):49–65, October 1994. doi: 10.1016/0167-8760(84)90014-X.

R. E. Passingham, K. E. Stephan, and R. Kötter. The anatomical basis of functional localization in the cortex. *Nature Reviews Neuroscience*, 3(8):606–616, 2002. doi: 10.1038/nrn893.

C. Phillips, M. D. Rugg, and K. J. Friston. Anatomically informed basis functions for EEG source localization: Combining functional and anatomical constraints. *NeuroImage*, 16(3): 678–695, 2002. doi: 10.1006/nimg.2002.1143.

C. Pierpaoli, P. Jezzard, P. J. Basser, A. Barnett, and G. D. Chiro. Diffusion tensor mr imaging of the human brain. *Radiology*, 201(3):637–648, 1996. doi: 10.1148/radiology.201.3.8939209.

R. Pohlmeier, H. Buchner, G. Knoll, A. Rienäcker, R. Beckmann, and J. Pesch. The influence of skull-conductivity misspecification on inverse source localization in realistically shaped finite element head models. *Brain Topography*, 9(3):157–162, 1997. doi: 10.1007/BF01190384.

A. Puce, R. T. Constable, M. L. Luby, G. McCarthy, A. C. Nobre, D. D. Spencer, J. C. Gore, and T. Allison. Functional magnetic resonance imaging of sensory and motor cortex: Comparison with electrophysiological localization. *Journal of Neurosurgery*, 83(2):262–270, 1995. doi: 10.3171/jns.1995.83.2.0262.

A. Puce, T. Allison, S. S. Spencer, D. D. Spencer, and G. McCarthy. Comparison of cortical activation evoked by faces measured by intracranial field potentials and functional mri: Two case studies. *Human Brain Mapping*, 5(4):298–305, 1997. doi: 10.1002/(SICI)1097-0193(1997)5:4<298::AID-HBM16>3.0.CO;2-A.

J. Riera, E. Aubert, P. Waldes, R. Casanova, and O. Lins. Discrete spline electric-magnetic tomography (DSPET) based on realistic neuroanatomy. In C. Wood., editor, *Proceedings of the 10th International Conference on Biomagnetism*, 1996.

S. E. Robinson and J. Vrba. Functional neuroimaging by synthetic aperture magnetometry (SAM). In T. Yoshimoto, M. Kotani, S. Kuriki, H. Karibe, and N. Nakasato, editors, *Recent advantages in biomagnetism: Proceedings of the 11th International Conference on Biomagnetism*, pages 302–305, Sendai, Japan, 1999. Tohoku University Press.

M. F. S. Rushworth, T. E. J. Behrens, and H. Johansen-Berg. Connection patterns distinguish 3 regions of human parietal cortex. *Cerebral Cortex*, 16:1418–1430, 2006. doi: 10.1093/cercor/bhj079.

F. Sanides. *Die Architektonik des menschlichen Stirnhirns.* Monographien aus dem Gesamtgebiete der Neurologie und Psychiatrie. Springer, 1962. doi: 10.1007/978-3-642-86210-6.

J. Sarvas. Basic mathematical and electromagnetic concepts of the biomagnetic inverse problem. *Physics in Medicine and Biology*, 32(1):11, 1987. doi: 10.1088/0031-9155/32/1/004.

M. Sato, T. Yoshioka, S. Kajihara, K. Toyama, N. Goda, K. Doya, and M. Kawato. Hierarchical Bayesian estimation for MEG inverse problem. *NeuroImage*, 23(3):806–826, 2004.

M. Scherg and P. Berg. Use of prior knowledge in brain electromagnetic source analysis. *Brain Topography*, 4(2):143–150, 1991. doi: 10.1007/BF01132771.

M. Scherg and D. von Cramon. Two bilateral sources of the late AEP as identified by a spatio-temporal dipole model. *Electroencephalography and Clinical Neurophysiology/evoked Potentials Section*, 62:32–44, 1985. doi: 10.1016/0168-5597(85)90033-4.

M. Scherg and D. von Cramon. Evoked dipole source potentials of the human auditory cortex. *Electroencephalography and Clinical Neurophysiology*, 65(5):344–60, 1986. doi: 10.1016/0168-5597(86)90014-6.

D. M. Schmidt, J. S. George, and C. C. Wood. Bayesian inference applied to the electromagnetic inverse problem. *Human Brain Mapping*, 7(3):195–212, 1999. doi: 10.1002/(SICI)1097-0193(1999)7:3<195::AID-HBM4>3.0.CO;2-F.

D. Schwartz, D. Lemoine, E. Poiseau, and C. Barillot. Registration of MEG/EEG data with 3D MRI: Methodology and precision issues. *Brain Topography*, 9(2):101–116, 1996. doi: 10.1007/BF01200710.

J.-K. Seong, K. Im, S. W. Yoo, S. W. Seo, D. L. Na, and J.-M. Lee. Automatic extraction of sulcal lines on cortical surfaces based on anisotripic geodesic distances. *NeuroImage*, 49(1): 293–302, January 2010. doi: 10.1016/j.neuroimage.2009.08.013.

A. K. Sharma. *Text Book of Matrix*. Discovery Publishing Pvt.Ltd, September 2004. ISBN: 978-8171418947.

M. Singh, D. Doria, V. W. Henderson, D. C. Huth, and J. Beatty. Reconstruction of images from neuromagnetic fields. *IEEE Transactions on Nuclear Science*, 31(1):585–589, February 1984. doi: 10.1109/TNS.1984.4333324.

W. E. Smith. Estimation of the spatio-temporal correlations of biological electrical sources from their magnetic fields. *IEEE Transactions on Biomedical Engineering*, 39(10):997–1004, October 1992. doi: 10.1109/10.161331.

R. C. Sotero and N. J. Trujillo-Barreto. Biophysical model for integrating neuronal activity, EEG, fMRI and metabolism. *NeuroImage*, 39(1):290–309, 2008. doi: 10.1016/j.neuroimage.2007.08.001.

K. Takahashi, J. Fagan, and M. S. Chen. Formation of a sparse bus impedance matrix and its application to short circuit study. *IEEE Power Industry Computer Applications Conference*, (8):63–69, June 1973.

A. Tarantola. *Inverse Problem Theory and Methods for Model Parameter Estimation.* SIAM, 2005. doi: 10.1137/1.9780898717921. ISBN: 978-0-89871-572-9.

A. N. Tikhonov and V. Y. Arsenin. *Solutions of Ill-Posed Problems.* Winston & Sons, 1977. doi: 10.1137/1021044.

G. Tononi, O. Sporns, and G. M. Edelman. Reentry and the problem of integrating multiple cortical areas: Simulation of dynamic integration in the visual system. *Cerebral Cortex*, 2(4): 310–335, 1992. doi: 10.1093/cercor/2.4.310.

R. Toro and Y. Burnod. A morphogenetic model for the development of cortical convolutions. *Cerebral Cortex*, 15:1900–1913, 2005. doi: 10.1093/cercor/bhi068.

A. Le Troter, G. Auzias, and O. Coulon. Automatic sulcal line extraction on cortical surfaces using geodesic path density maps. *NeuroImage*, 61(4):941–949, 2012. doi: 10.1016/j.neuroimage.2012.04.021.

N. J. Trujillo-Barreto, E. Aubert-Vázquez, and P. A. Valdés-Sosa. Bayesian model averaging in EEG/MEG imaging. *NeuroImage*, 21(4):1300–1319, 2004. doi: 10.1016/j.neuroimage.2003.11.008.

N. J. Trujillo-Barreto, E. Aubert-Vázquez, and W. D. Penny. Bayesian M/EEG source reconstruction with spatio-temporal priors. *NeuroImage*, 39(1):318–335, January 2008. doi: 10.1016/j.neuroimage.2007.07.062.

Z. Tu, S. Zheng, A. L. Yuille, A. L. Reiss, R. A. Dutton, A. D. Lee, A. M. Galaburda, I. Dinov, P. M. Thompson, and A. W. Toga. Automated extraction of the cortical sulci based on a supervised learning approach. *IEEE Transactions on Medical Imaging*, 26(4):541–552, April 2007. doi: 10.1109/TMI.2007.892506.

K. Uutela, M. S. Hämäläinen, and E. Somersalo. Visualization of magnetoencephalographic data using minimum current estimates. *NeuroImage*, 10(2):173–180, 1999. doi: 10.1006/nimg.1999.0454.

B. D. van Veen, W. van Drongelen, M. Yuchtman, and A. Suzuki. Localization of brain electrical activity via linearly constrained minimum variance spatial filtering. *IEEE Transactions on Biomedical Engineering*, 44(9):867–880, 1997. doi: 10.1109/10.623056.

O. Vogt. Die myeloarchitektonische Felderung des menschlichen Stirnhirns. *Journal für Psychologie und Neurologie*, 15:221–232, 1910.

O. Vogt. Die Myeloarchitektonik des Isocortex parietalis. *Journal für Psychologie und Neurologie*, 18:379–390, 1911.

H. von Helmholtz. Über einige Gesetze der Vertheilung elektrischer Ströme in körperlichen Leitern mit Anwendung auf die thierisch-elektrischen Versuche. *Annalen der Physik*, 165(6): 211–233, 1853. doi: 10.1002/andp.18531650603.

J.-Z. Wang, S. J. Williamson, and L. Kaufman. Magnetic source imaging based on the minimum-norm least-squares inverse. *Brain Topography*, 5(4):365–371, June 1993. doi: 10.1007/BF01128692.

W. I. Welker. Why does the cerebral cortex fissure and fold. *Cerebral Cortex*, 8:3–135, 1990. doi: 10.1007/978-1-4615-3824-0_1.

W. I. Welker and G. B. Campos. Physiological significance of sulci in somatic sensory cerebral cortex in mammals of the family procyonidae. *Journal of Comparative Neurology*, 120(1): 19–36, February 1963. doi: 10.1002/cne.901200103.

K. Wendel, O. Vaisanen, J. Malmivuo, N. G. Gencer, B. Vanrumste, P. Durka, R. Magjarevic, S. Supek, M. L. Pascu, H. Fontenelle, and R. G. de Peralta Menendez. EEG/MEG source imaging: Methods, challenges, and open issues. *Computational Intelligence and Neuroscience*, 2009, April 2009. doi: 10.1155/2009/656092.

G. S. Wig, T. O. Laumann, and S. E. Petersen. An approach for parcellating human cortical areas using resting-state correlations. *NeuroImage*, 93 Pt 2(0):276–291, 2014. doi: 10.1016/j.neuroimage.2013.07.035.

C. H. Wolters, M. Kuhn, A. Anwander, and S. Reitzinger. A parallel algebraic multigrid solver for finite element method based source localization in the human brain. *Computing and Visualization in Science*, 5(3):165–177, 2002. doi: 10.1007/s00791-002-0098-0.

F. Zanow. *Realistically Shaped Models of the Head and Their Application to EEG and MEG.* PhD thesis, University of Twente, Enschede, The Netherlends, 1997.

F. Zanow and M. J. Peters. Individually shaped volume conductor models of the head in EEG source localisation. *Medical and Biological Engineering and Computing*, 33(4):582–588, 1995. doi: 10.1007/BF02522518.

K. Zilles, G. Schlaug, S. Geyer, G. Luppino, M. Matelli, M. Que, A. Schleicher, and T. Schormann. Anatomy and transmitter receptors of the supplementary motor areas in the human and nonhuman primate brain. In *Supplementary Sensorimotor Area.* Lippincott-Raven, Philadelphia, 1996. editor: Lueders, H. O.

K. Zilles, N. Palomero-Gallagher, and A. Schleicher. Transmitter receptors and functional anatomy of the cerebral cortex. *Journal of Anatomy*, 205:417–432, 2004. doi: 10.1111/j.0021-8782.2004.00357.x.

List of Figures

List of Tables

Erklärung

Ich versichere, dass ich die vorliegende Arbeit ohne unzulässige Hilfe Dritter und ohne Benutzung anderer als der angegebenen Hilfsmittel angefertigt habe. Die aus anderen Quellen direkt oder indirekt übernommenen Daten und Konzepte sind unter Angabe der Quelle gekennzeichnet.

Bei der Auswahl und Auswertung folgenden Materials haben mir die nachstehend aufgeführten Personen in der jeweils beschriebenen Weise ~~entgeltlich~~/unentgeltlich geholfen:

1. Dr. Burkhard Maeß und Maria Felber vom Max-Planck-Institut für Kognitions- und Neurowissenschaften stellten die experimentellen EEG/MEG-Daten sowie die zugehörigen anatomischen Daten (MRT-Segmentierung) zur Verfügung.

Weitere Personen waren an der inhaltlich-materiellen Erstellung der vorliegenden Arbeit nicht beteiligt. Insbesondere habe ich hierfür nicht die entgeltliche Hilfe von Vermittlungs bzw. Beratungsdiensten (Promotionsberater oder anderer Personen) in Anspruch genommen. Niemand hat von mir unmittelbar oder mittelbar geldwerte Leistungen für Arbeiten erhalten, die im Zusammenhang mit dem Inhalt der vorgelegten Dissertation stehen.

Die Arbeit wurde bisher weder im In- noch im Ausland in gleicher oder ähnlicher Form einer Prüfungsbehörde vorgelegt.

Ich bin darauf hingewiesen worden, dass die Unrichtigkeit der vorstehenden Erklärung als Täuschungsversuch bewertet wird und gemäß § 7 Abs. 10 der Promotionsordnung den Abbruch des Promotionsverfahrens zur Folge hat.

Leipzig, 30. November 2016